Development of Novel Ni-based Brazing Filler Metals

Liam Hardwick

The University of Sheffield
Department of Materials Science and Engineering

A thesis submitted in partial fulfilment of the requirements for the degree of

Doctor of Philosophy

November 2020

Abstract

The capability to join various metallic and non-metallic materials is crucial to the production of a wide array of components across many industries, ranging from the soldering of small scale electronics, to the welding of larger scale automotive and aircraft structures. Brazing is a distinct joining technique, involving the melting of a metallic filler metal introduced in between two or more materials to be joined. While welding requires the melting of the materials being joined, brazing does not, and as such the avoidance of welding-induced defects is important to many industries, including aerospace. Brazing bears similarities to soldering, and is distinguished from soldering in the temperatures at which it is conducted (typically above 450ºC). Filler metals used in brazing are usually tailored to the particular materials being joined, in terms of melting temperature and chemistry. Ni-based filler metals are widely used in the vacuum brazing of high temperature materials such as Ni-based superalloys. In order to ensure melting of the filler metal at a temperature below that of the base metal, Ni-based filler metals often contain elements such as B, Si and P, which act as so-called Melting Point Depressants (MPDs). The use of such elements, however, leave brazed joints susceptible to formation of brittle intermetallic phases, which may only be removed by prolonged time at the brazing temperature or lengthy heat treatments post-braze. In many cases, the current commercial Ni-based filler metals have seen little in the way of exploration into compositional changes that may alleviate such issues. In highlighting the need for more work in this area, this project was concerned with the development of novel Ni-based brazing filler metals, primarily for the brazing of Ni-based superalloys, employing alternative MPDs and other compositional changes. Using phase diagrams and CALPHAD (CALculation of PHase Diagrams)-based software, the use of elements In and Ge as alternative MPDs was investigated. Their use as sole alloying additions to Ni (i.e. wholly replacing elements B, Si or P) was deemed unsuitable due to the high liquidus temperatures, which were well in excess of those of commercial Ni-based filler metals. The use of In and Ge in conjunction with reduced B content was also investigated. While this strategy allowed lower liquidus temperatures, the potential for brittle boride formation meant such compositions were deemed unsuitable. CALPHAD predictions of the Ni-In and Ni-Ge systems were of limited accuracy, though were found to be useful in predicting general trends in liquidus as a function of composition. A further strategy, using concepts such as High Entropy Alloys (HEAs) and Multi-Principal Element Alloys (MPEAs), was used to design two Ni-based MPEA filler metals, including novel MPD elements In and Ge. The first filler metal, based on NiCrMnIn, was found to be unsuitable for the vacuum brazing of Inconel-718 (IN718) superalloy due to volatilisation and liquation, though was successfully applied to the belt furnace brazing of carbide-tipped drill bits. The second filler metal, based on NiCrFeGeB, was successful in the vacuum brazing of IN718. Average joint shear strength of 332 ± 15 MPa was recorded following brazing at 1100ºC for 60 minutes. While weaker than achievable using commercial AWS BNi-2 under similar conditions, the joint microstructure exhibited isothermal solidification of an MPEA-like NiCrFeGe solid solution, with limited boride formation in the IN718 base metal. Overall, this research demonstrated a design strategy for the development of novel Ni-based MPEA filler metals, and it was found that elements In and Ge may be incorporated into an MPEA-type filler metal, allowing the partial or complete replacement of conventional MPD elements while achieving a liquidus temperature comparable with commercial Ni-based filler metals (and below 1100ºC). It is suggested that future work should be focussed on the refinement of the developed compositions to address inferior mechanical properties as compared to joints produced using commercially available AWS BNi-2. Furthermore, it is proposed that the design strategy for such filler metals may be expanded to other brazing applications outside Ni-based superalloys, for example in nuclear reactors.

Acknowledgements

I have received tremendous support from many people throughout the course of this work. Firstly, I would like to thank EPSRC and VBC Group for jointly funding this project.

I have been extremely lucky to have had an amazing supervisory team throughout this project, to whom I wish to give my utmost thanks; first supervisor Professor Russell Goodall, for the continual advice, guidance, encouragement, and for always being available; second supervisor Dr Ed Pickering, for many useful suggestions and help with Manchester facilities; and industrial supervisor Pat Rodgers at VBC Group, for all the helpful chats, practical advice, and introducing me to many great people in industry. Likewise, I would like to thank Phil Webb at VBC Group, for providing many insights helping to guide this project and for advice at conferences.

I also owe huge thanks to departmental staff for their technical assistance and expertise, in particular Neil Hind and Lisa Hollands, without whom much of this work would not have been possible. I would also like to thank Dr Claire Utton for advice with Thermo-Calc software and DSC experiments. I also thank staff in Manchester, including Dr Jonathan Fellowes for help with EPMA. Thanks also to Sharon Brown, Lynn Li and Claire Hinchliffe, for organising much of the amazing experiences I had chance to experience throughout this project. I would also like to thank staff at Kepston Ltd and Armeg Ltd, for allowing me access to their facilities and for their technical advice.

I am infinitely grateful to my friends and family for their support and encouragement over the past four years. In particular, my parents, who always encouraged me to push myself, and whose constant support throughout my life is what has allowed me to be here today. I would also like to thank my fellow 2016 cohort colleagues for many visits to the pub; having such a great bunch starting this journey at the same time was an enormous help, and I wish them all the best for the future. To Matt, Danny, Chris, and all the lads at football, thanks for providing my much needed weekly escape. And finally, to my girlfriend Dhinisa, for endless patience, understanding, support and advice, and for keeping me going to the very end.

Table of Contents

Introduction

Brazing is a method for the joining of various materials, involving the melting of a filler material in between the unmelted materials to be joined. Practically any metallic material can be brazed, as can many other materials including ceramics, and brazing can also be used in the joining of components with complex geometries. As such, brazing is industrially important, and as advanced structural materials are developed to meet the needs for the future energy and aerospace industries, this capacity for producing metal-ceramic and even additively-manufactured metal joints is likely to prove increasingly valuable. The filler metal selected depends on the materials being joined, and is tailored as such. As the filler metal is required to melt at a lower temperature than the materials being joined, the chemical composition must allow for this, and can be achieved by addition of alloying elements that reduce the melting temperature of the filler metal. Consideration is also given to the mechanical properties of the filler metals and materials being joined, and so it is usually necessary to select a filler metal with a composition based around the same main element as in the alloy or other material being joined.

Brazing bears similarities to other joining techniques such as soldering (conducted at lower temperatures) and welding (involving the melting of the materials being joined). Brazing offers advantages, however; strengths of brazed joints can be substantially greater than for soldered joints, and difficult to weld materials can be joined, and without altering microstructure by melting. Welds are also susceptible to defects in the heat-affected zone. As such, brazing is an important joining method for many metallic materials, especially Ni-based superalloys. Despite this, there are long standing issues in the brazing of metallic materials, such as the formation of brittle intermetallic phases both within the joint, and in the regions in the vicinity of the joint. Often, this is a consequence of the inclusion of certain elements required to reduce the melting temperature of the filler metal. In Ni-based filler metals, used in the brazing of Ni-based superalloys and other high temperature materials, elements such as B, Si and P are alloying additions. The presence of such phases is detrimental to the mechanical properties of joints, providing crack initiation and propagation paths, and potentially compromising resistance to corrosion.

In order to alleviate such issues, the brazing process may be conducted at higher temperatures, or for longer times at temperature, or heat treatments of the joint may be conducted post-braze. These processes are conducted to allow the homogenisation of the joint chemistry, such that the concentration of undesired phases within and near the brazed region is reduced, or ultimately completely removed. There are economic costs with such procedures, however, as they require longer furnace operation times, often for many hours. Many of the filler metals used currently in industry for the brazing of Ni-based superalloys have been established for decades, with relatively little exploration of new compositions conducted in order to address these issues. This leaves a potential gap in the market, and attempts to address this (reported in Chapter 3 of this thesis), while often involving the investigation of novel compositions, generally place less emphasis on operating at the same brazing temperatures as current commercial Ni-based filler metals. There is motivation, therefore, for the development of novel brazing filler metal compositions that may also be used at temperatures often employed in industry, particularly for the brazing of Ni-based superalloys. This project aims to investigate novel filler metal compositions, and the strategy for designing such.

As is often the case in alloy development, balances must be struck for a development to be of merit. In the development of novel filler metals for the brazing of Ni-based superalloys, or indeed other high temperature materials, the balance is between the realisation of mechanical and microstructural improvements (such as the avoidance of brittle phases), and the melting temperature of the filler metal. One way in which this balance can be struck is through the identification of alternative elements for the reduction of filler metal melting temperature. By utilising equilibrium binary phase diagrams, as well as software (Thermo-Calc) for the modelling of thermodynamic properties of alloys, it may be possible to identify elements that can fulfil the role of lowering filler metal melting point, while reducing the potential for formation of brittle phases in brazed joints. Chapter 8 of this work details the investigation of two such elements, and their potential for use as replacements for conventionally used elements such as B and Si.

Another strategy involved the application of the concepts of High Entropy Alloys (HEAs) and Multi-Principal Element Alloys (MPEAs), introduced in Chapter 4, to the design of novel brazing filler metals. This relatively new class of alloys, in contrast to conventional alloys such as steels, use multiple elements in roughly equal concentrations. Such alloys have been the subject of significant interest since the early 2000s, due to the potential for forming solid solution phases with attractive mechanical properties. Aside from potential mechanical improvements, another result of such compositions is a lower melting temperature than the individual pure elements. The application of this strategy is detailed in Chapter 9 of this work, with Chapters 10 and 11 reporting the application of this strategy for developing novel Ni-based filler metals for the vacuum brazing of Ni-based superalloy Inconel 718.

In summary, the overall aims of this research are to develop novel Ni-based brazing filler metals, primarily for the brazing of Ni-based superalloys, as well as to assess to extent to which the properties of such filler metals may be accurately predicted, and designed for. This will be achieved by investigating the use of alternative elements for the suppression of filler metal melting temperature, and in the application of new alloy design concepts such as those used for HEAs and MPEAs. Assessments are also made as to the applicability and effectiveness of such strategies.

1. Introduction to Brazing

Brazing is a process for joining two or more metal or ceramic materials, using a filler metal whose liquidus is lower than that of the materials to be joined. As such, brazing differs from welding in that no melting of the materials to be joined is required. It closely resembles soldering in this way, though is distinguished from this in being defined as being used at temperatures above 450°C. This has obvious benefits in that the microstructure of the base metal is left largely uncompromised except for in the very near vicinity of the interface with the filler metal.

Unlike welding of metallic materials, brazing involves the use of an insert metal, or filler metal, which is usually placed in between, or applied to the vicinity of, the materials to be joined (referred to as the base metal). The filler metal is designed to melt somewhat below the brazing temperature, and the interaction between this melt and the base metal results in a metallic joint when solidified. The molten filler metal relies on capillary force in order to flow across the surface to be joined, particularly in cases where the filler metal is not applied directly on this surface. Fig. 1.1 shows some basic common geometries of joint assemblies. Tearing or cracking that can be a problem in welded joints can also be avoided, and joints whose composition and microstructure is similar to the base metal are possible. In addition, difficult to weld materials such as certain Ni-based superalloys, ceramics and carbides can be joined via brazing. Brazing even allows for the joining of dissimilar materials such as one alloy to another, or even an alloy to a ceramic, with selection of an appropriate filler metal. Compared to soldered joints, the mechanical properties required of brazed joints tend to be greater, and often allow for larger assemblies and batch processing. Disadvantages of the joining of materials via brazing relate to joint strength, which may be inferior to those achievable from welding. In addition, certain brazing techniques, and materials being brazed, can be very sensitive to cleanliness and surface preparation, moreso than for soldering or welding.

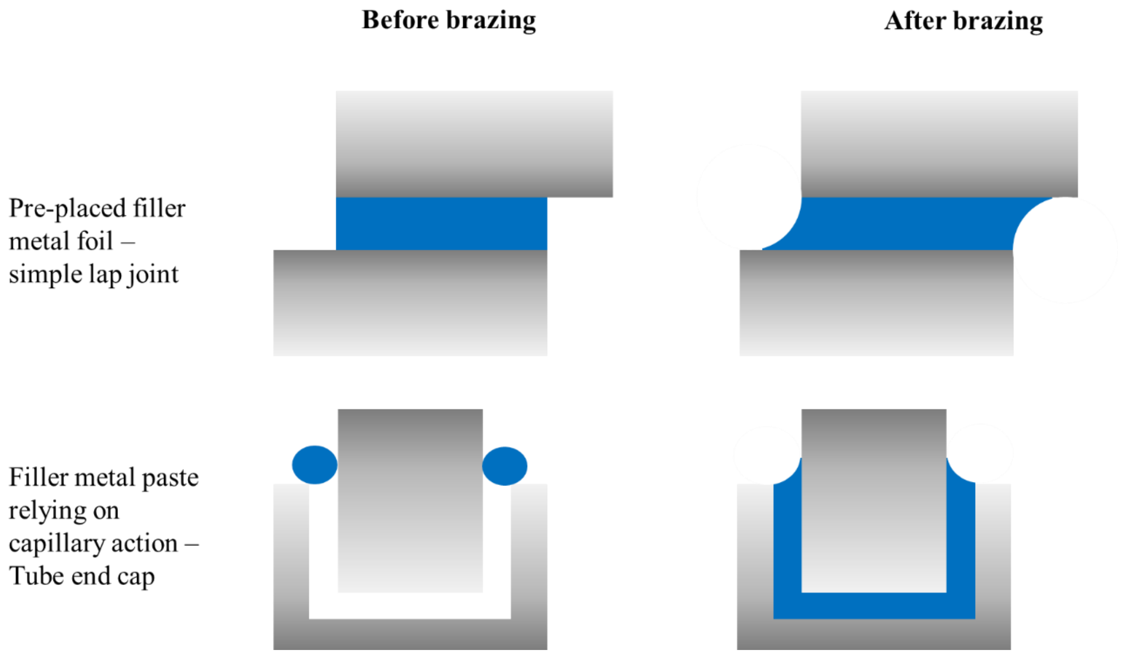

Figure 1.1: Schematic illustrating joint configurations relying on placement of a filler metal foil on the surfaces being bonded, and relying on flow of molten filler metal paste in to more complex gap geometries.

Brazing as a joining process has been used in some form since ancient times, for such things as Au jewellery and joining handles to ceramic pottery. As more and more elements were discovered and technology advanced through the middle ages to the industrial revolution and beyond, brazing developed into the key joining technology used today, in applications ranging from dentistry and jewellery, to gas turbines and jet engines.

1.1 Physical considerations for brazing

The brazing process relies on certain well documented physical phenomena in order to successfully join materials, and achieve joints with the required mechanical properties. One of the most important considerations is the wetting of the base materials by the filler metal, and, depending on joint geometry, capillary flow of the molten filler metal. Wetting is defined by the contact angle, θ, between the solid base metal surface and the liquid filler metal, and depends on the balance of surface tensions according to the Young equation:

$$\gamma_{SV} = \gamma_{LV} \cos\theta + \gamma_{SL} \qquad (1.1)$$

where γ_{SV}, γ_{LV} and γ_{SL} are the surface tensions between solid and vapour, liquid and vapour, and solid and liquid, respectively. Fig. 1.2(a) illustrates this schematically. The ability of a filler metal to wet a given base metal is influenced by various factors including surface roughness, surface oxidation, and presence of contaminants, as is discussed briefly in Chapter 2 (Section 2.2).

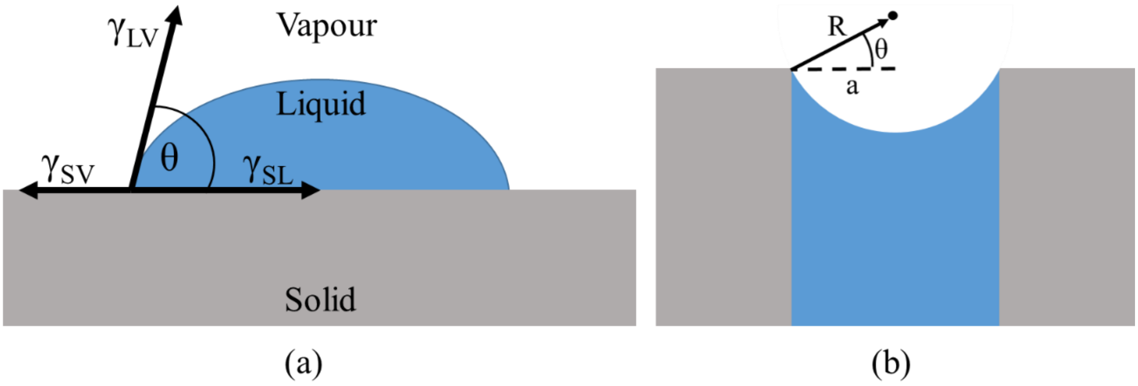

Figure 1.2: (a) Schematic of droplet on solid surface, indicating the three surface tensions related in the Young equation. (b) Schematic of capillary action of a molten filler metal between two base metals

Linked to wetting, capillary action is how a molten filler metal can flow and fill the joint gap or clearance between the base metals being joined. Generally, to achieve strongest brazed joint for a given system, the joint gap should be minimal particularly when relying on capillary action to achieve complete filling of the joint by the molten filler metal, as can be shown by considering the Young-Laplace equation, relating the pressure difference due to capillary action, Δp, with the surface tension of the particular filler metal, γ, and the radius of a spherical meniscus formed between the two base metals, R:

$$\Delta p = \frac{2\gamma}{R} \qquad (1.2)$$

R is itself a function of the contact angle between meniscus and base metal, and the half joint gap, a (see Fig. 1.2(b)):

$$R = \frac{a}{\cos\theta} \qquad (1.3)$$

Such that Equation 1.2 becomes:

$$\Delta p = \frac{2\gamma\cos\theta}{a} \qquad (1.4)$$

Hence the capillary pressure is greatest for narrower joint gaps.

Another important physical characteristic to consider, especially when brazing dissimilar materials, is the differences in coefficients of thermal expansion (CTE) of the materials. The thermal expansion (or contraction) in dimensions in response to changing temperature changes from material to material, and so this must be taken into account when designing joint assemblies where two materials being joined exhibit different CTEs. The difference in CTE can be large when brazing metals with ceramic materials, something which increasingly being explored for advanced applications. For example, materials such as alumina (approximately 4.5 µm/m·K) and W carbide (approximately 5.5 µm/m·K) have much lower CTEs than 304 stainless steel (approximately 17 µm/m·K) or Cu (approximately 16.5 µm/m·K). Fixturing of the assembly can help to prevent joint deformation during heating, but stresses can also build during different rates of contraction during cooling, possibly causing cracks in brazed joints. Therefore, ductile and more deformable filler metals are often preferred for joints with large differences in CTE, in order to accommodate such stresses.

1.1 Modern brazing techniques in industry

There are several types of modern day brazing, from simple manual torch brazing of single components, to batch furnace brazing and even induction brazing and laser brazing. Torch brazing is a common hands-on form of brazing, whereby typically a rod or wire of filler metal is applied and melted directly onto a fixture to be joined by a gas flame torch. Hand-held torch brazing, while suitable for small work volumes or otherwise unique and custom jobs, can have high costs in terms of labour, and often a lower level of quality control, with the final joint being heavily dependent on the skill of the worker. Some of this can be overcome by a fixed-position torch or automated versions of torch brazing. To overcome problems with oxidation due to the lack of controlled atmosphere, torch brazing often requires a flux, which also helps the molten rod or wire to flow evenly along the joint fixture. Otherwise, self-fluxing rods (that is, filler metal rods that contain a fluxing agent which is activated during brazing, and hence an additional flux is not required to be applied) or wires may be employed.

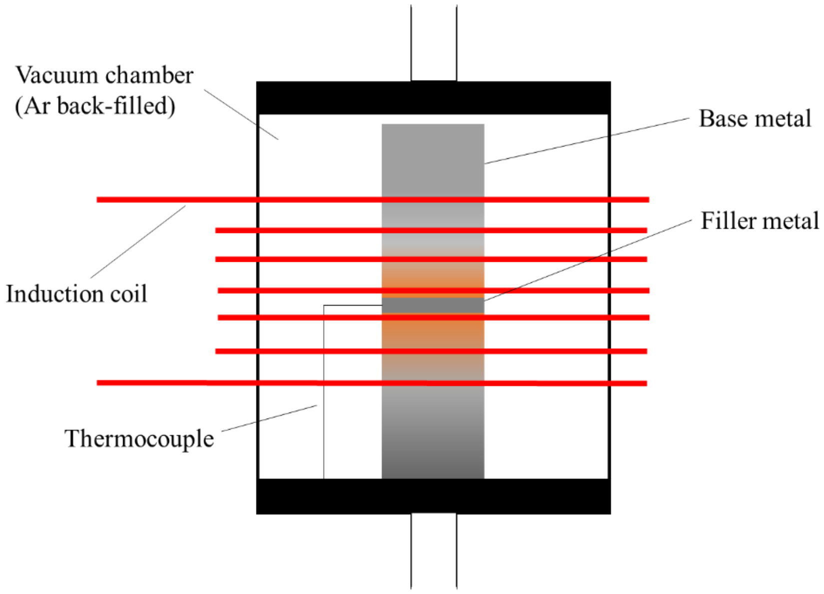

Figure 1.3: Schematic diagram of typical induction brazing set-up. Sample may be placed in a controlled-atmosphere vessel, often fused quartz, with heat applied from the exterior coils.

Induction brazing is a potentially very fast technique, and combined with a controlled atmosphere, it can be a very attractive option. As shown in Fig. 1.3, It involves the positioning of a joint assembly in an electric field produced by coils with an alternating current passed through. This induces a voltage in the sample, with its electrical resistance resulting in the production of heat, thus melting the filler metal. The assembly of coils may be arranged in such a way as to provide even heating over a larger area or targeted heating in a small area as required. Considering heating times, induction brazing coils can provide heating at a rate of the order of hundreds of ^{o}C per second, which can offer a significant time saving advantage over furnace brazing [1]. As furnace brazing often requires prolonged cooling, so altogether hours can be saved by using induction brazing. Industrial induction brazing can offer very consistent and high quality results, and the possibility of protective atmospheres give it a cleanliness advantage over torch brazing in open air. However, induction brazing does not have the same batch capacity as furnace brazing, and so may not be as quick a process when considering large production volumes. In addition, problems can arise when brazing dissimilar materials via induction brazing, due to different electrical resistances and coefficients of thermal expansion [2]. The resulting build-up of internal stresses can be a particular problem for the brazing of metal-to-carbide for tooling [2]. Another less common method that can offer extremely localised and controlled heat focus, as well as high heating and cooling rates potentially exceeding that of induction brazing [3], is laser brazing. It also offers extremely precise control of heat application through control of the laser power. Laser joining techniques are however more suitable for small-size precision components due to the small heating area, making it advantageous in applications such as brazing of thin sheets.

Of greater relevance to this thesis are two forms of furnace brazing. Continuous belt furnace brazing (Fig. 1.4) is important method employed widely across industry, particularly for tool and tool part manufacturing [4] and in many cases is the preferred method where shear volume is the primary need. It is especially suitable where high volumes of repeatable parts are to be brazed, such as in the production of small brazed tool parts. Benefits of continuous belt furnace brazing, as compared to typical vacuum furnace brazing, for the brazing of abrasive diamond grains have also been reported [4]. Parts are typically prepared and placed at one end of the belt, which are then carried at a controlled speed through the heating chamber or ‘hot zone’, containing a reducing atmosphere, where the brazing occurs. Parts continue through a cooling zone to the end of the belt where they can be removed. This method allows an effectively constant flow of brazed parts to be produced, with low labour costs and reasonable control of cleanliness. The reducing atmosphere used in the hot zone can be tailored to be suitable for the materials being brazed, such as pure hydrogen, N, a mix of these, or Ar. The limitation of this method of brazing however is its unsuitability for O-sensitive materials. All gaseous atmospheres used will not be completely free of O, and so reactive materials such as Ti may not be easily brazed using this method. Furthermore, the size and movement (albeit slow) of the furnace can limit what can be brazed to certain geometries, as assemblies above a certain height or width will simply not fit through the furnace.

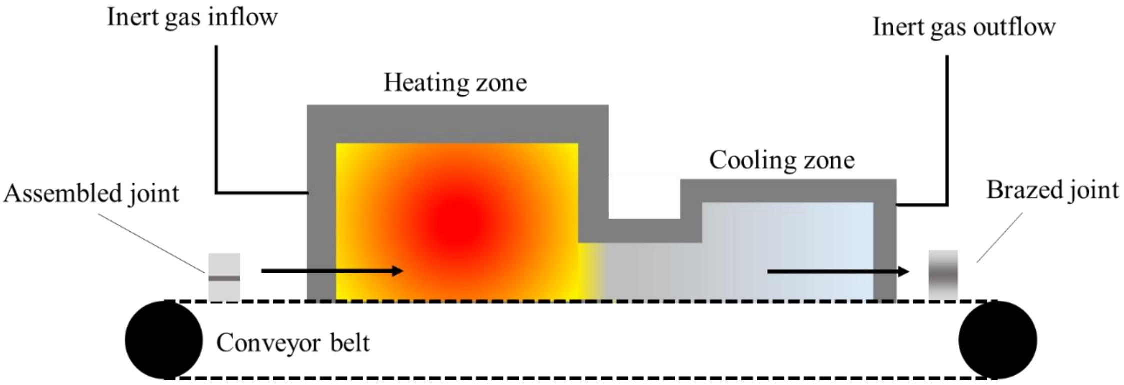

Figure 1.4: Schematic of basic continuous belt furnace set-up.

The final method discussed here is vacuum brazing, which offers several advantages for certain critical applications, mainly the reduced chance of contamination of the joint, and the ability to maintain excellent temperature uniformity, reducing stresses in the joint during the process. Vacuum brazing comes with large initial capital costs, and maintenance and cleaning can be time consuming and expensive. But despite this, the availability of large vacuum furnaces combined with excellent control over atmosphere and temperature, and the batch capability of vacuum brazing makes it one of the most commercially important forms of brazing (along with induction and belt furnace brazing) across multiple industries today, including the aerospace, power turbine, and Heating, Ventilation and Air Conditioning (HVAC) industries. As the majority of the research presented here uses vacuum brazing as the preferred method, it will be discussed in more detail here.

In contrast to continuous belt furnace brazing, vacuum brazing is used to process parts a batch at a time (with usually long cycle times), and so the work volume is typically less. Nonetheless, many parts can be brazed within one batch, and so has low labour costs (although the initial costs of the furnace itself can be large). The entire process of brazing in a vacuum furnace can be referred to as a ‘brazing cycle’, and is usually pre-programmed by the furnace control panel. The brazing cycle is comprised of several stages:

1. **Loading of parts to be brazed**. Parts may be placed on ceramic trays to avoid any damage from molten filler metal run-off, or bonding to the furnace floor. Thermocouples may at this point be placed such that accurate readings of temperature close to the parts are available.
2. **Inducing vacuum.** Using typically turbo-pumps or diffusion pumps, air is removed from the vacuum chamber in preparation for brazing. The best modern furnaces may achieve down to

10^{-6} torr (10^{-4} Pa). The time taken to achieve suitable vacuum depends on the capability of the pumps and the size of the vacuum chamber.

3. **Ramping up.** The heating elements are turned on and the radiating heat increases the internal temperature. This is done typically at a rate of 10 – 20°C per minute, depending on capability. Too slow a rate will make the process take too long to be economic, whereas to quickly may engage the next steps before achieving temperature homogeneity across the vacuum chamber. Generally, however, the ramp rate is as quick as possible.
4. **Outgassing hold.** This is an optional step which may be introduced if using brazing paste which contain a flux or other organics. This stage is usually a hold at 150 – 260°C to allow liquids contained in these pastes to vaporise and leave the braze joint. If the ramp rate is suitably slow, this stage may not be needed, but sudden outgassing bubbles may be left behind if the temperature is moved beyond this range too quickly.
5. **Temperature stabilisation hold.** This involves a hold, usually for at least 10 minutes, at a temperature up to around 40°C below the brazing temperature. This is performed to allow the temperature in any cooler spots to catch up, and to so ensure all thermocouples have reached the same temperature.
6. **Hold at brazing temperature.** This is the stage where the brazing takes place, at the pre-determined temperature and for the pre-set time, typically 10 – 60 minutes, depending on size and geometry of joints (time must be allowed for filler metal flow where required) and the filler metal composition.
7. **Cooling.** At this stage cooling can be allowed, either slowly by simple furnace cooling, or quickly through introduction of inert gas such as Ar. Again, this is usually determined by speed of production requirements, while balancing possible distortion of parts.

1.2 Forms of Filler Metal

In all brazing techniques, the basic steps include placement of the brazing filler metal depending on the form of the filler metal. Several forms of filler metal are recognised and employed in industry [5], most commonly including foils, wires and pastes. Some foils are traditionally produced by rolling, including Ag-based and Cu-based filler metals, as well as most Au and Pd-based filler metals. Annealing steps are often required due to work hardening during rolling. For Ni-based brazing filler metals, foils are typically produced via rapid solidification in melt spinning, resulting in an amorphous microstructure in the as-cast state. This is important, as the B, Si and P contents of such filler metals mean they would be too brittle for rolling in the cast state. Indeed, even some specific or specialised Cu-based, Pd-based and Ti-based filler metals, that contain brittle elements, require the strip casting method. Foils produced in this way are generally between 10 – 100 µm, with 50 µm thickness often being preferred (though this depends on the application and desired joint width) and are suitable for placement directly between the base metal components to be joined (not requiring the flow of the molten filler metal). Foils are often used in the brazing of Ni-based superalloys with Ni-based filler metals, as flow of the filler metal over these kinds of surface can often be hindered by oxide layers [6]. For example, BNi-2 (a typical commercially available and popular Ni-based filler metal), is often used in the form of 50 µm foil pre-placed between the materials to be joined. Other methods of foil production have been demonstrated for specific applications, for example rolling of mixed powders, followed by sintering, in order to produce Ti-Zr-Cu-Ni and Cu-Sn-Ti filler metals [7]. Typical atomisation production routes for these alloys can be cost ineffective and wasteful, and so this method is proposed to overcome this [7]. Standards for foil thickness, width, camber and tolerances are available [5].

Most filler metals available as foils are also available as powders, usually combined with a binder into a paste. Powders can be produced by milling, water atomisation, or for the most consistently spherical particles, gas atomisation (see Chapter 7 for more detail on this technique). Pastes are particularly useful in cases where multiple walls of a joint require brazing, where otherwise multiple foils in different orientations would be required. Pastes can be pre-placed in these situations, but they can also take advantage of the capillary force induced by the narrow gap and surface tension. Through careful joint design, a sound, defect-free joint can be produced from a single deposit of paste and allowing its flow throughout the cavity under capillary force.

Other less common physical forms of filler metals include preforms, and composite wires and foils. Preforms involve modifying the geometry of usually a filler metal foil to fit a certain component precisely. This may be advantageous for applications where good flow may not be possible, and so it is important that the filler metal is already in place where needed prior to brazing. Novel production routes of preforms in recent years have included injection moulding of Ni-based brazing alloy powder with thermoplastic polymers [8]. Composite wires and foils generally involve distinct microstructural regions, for example, a flexible Ni-rich wire core surrounded by a more brittle shell that contains the melting point depressant (MPD) element. Similar structures can be achieved for foils, and this is often useful for wider gaps. Also for wider gaps, the filler metal can actually be a pre-made mixture of filler metal powder with some percentage of base metal powder. This is often used in the braze repair of cracks occurring in single crystal components such as turbine blades. Another less common foil form is borided foils, where the required B content of a Ni-based filler metal is added to a pre-made foil via boriding (a process typically used for surface hardening) at high temperature and pressure.

1.3 Overview of Brazing Alloy Families

There are many different filler metal compositions in use for numerous applications today, often optimised for joining a certain type of alloy (though some filler metals can be used on several different types of alloy – see Table 1.1 for examples). These can be grouped according to the primary elemental component comprising the filler metal. As such, various filler metal ‘families’ are generally recognised, which have a composition-dependant range of brazing temperature required (Fig. 1.5 shows typical temperature ranges of common brazing alloy families). For the common families, at the lowest brazing temperatures are the Al-based filler metals, operating above 570^{o}C up to around 620^{o}C. At more intermediate temperatures are the Ag-based alloys (620^{o}C - 980^{o}C) and Cu-based alloys (705^{o}C - 1150^{o}C). At higher temperatures are the Au-based alloys (890^{o}C - 1230^{o}C) and Ni-based alloys (927^{o}C - 1205^{o}C). There are also some higher operating temperature filler metals in the form of Fe-based alloys (approx. 1100^{o}C - 1200^{o}C) and Co-based alloys (approx. 1150^{o}C - 1250^{o}C) for specific applications. Another precious metal filler family are the Pd-based alloys (approx. 850^{o}C - 1250^{o}C), initially developed as a slightly cheaper alternative to Au-based alloys. Table 1.1 summarises briefly the applications of these various families, as well as some common alloying additions comprising the filler metals. Of greater importance to this research are the Ni-based brazing alloys, particularly valued due to their combination of high temperature mechanical properties, high temperature corrosion resistance, and chemistry compatible with Ni-based superalloys being used across various industries. Ni-based brazing filler metals are discussed in depth in Chapter 2.

Table 1.1: Common applications and alloying additions in various brazing filler metal families.

Filler Metal Family	Joining Applications	Common Alloying Additions
Al-based	Al-based alloys, Ti-based alloys	Si, Zn, Cu
Ag-based	Various steels, Ni-based alloys, Cu-based alloys, Ti-based alloys, some ceramics	Cu, Zn, Sn, Ni, Mn
Cu-based	Cu-based alloys, Ni-based alloys, various steels	P, Ag, Sn
Au-based	Various steels, Ni-based alloys, Cu-based alloys	Cu, Ni, Pd
Ni-based	Ni-based alloys, Co-based alloys, various steels, Cu-based alloys	Cr, Fe, Si, B, P
Fe-based	Various steels (especially stainless and those used in automotive applications)	Cr, Ni, Si
Co-based	Co-based alloys	Cr, Ni, Si
Pd-based	Ni-based alloys, various steels, metallised ceramics	Ag, Cu, Ni

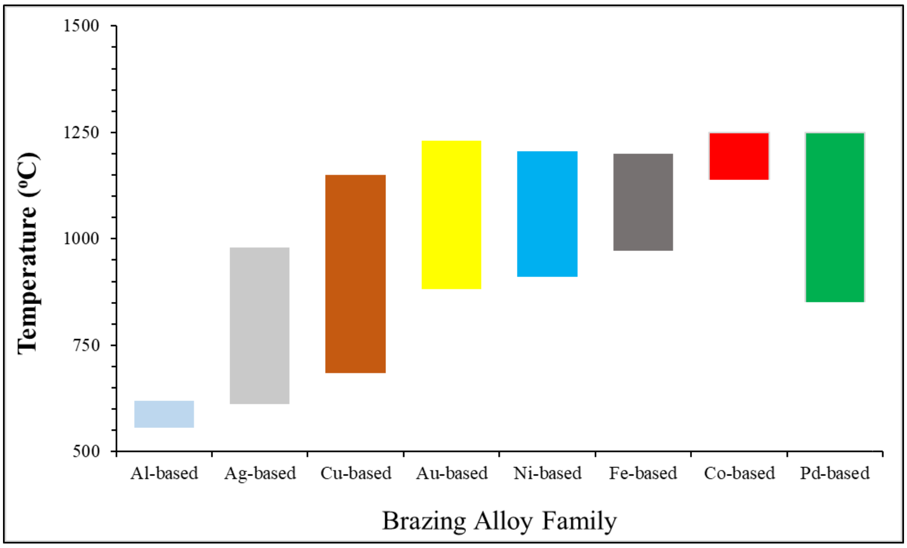

Figure 1.5: Summary of common brazing filler metal families, and the temperature range over which they are used.

2. Brazing of Ni-Based Superalloys

This section will proceed to take a closer look specifically at the brazing of Ni-superalloys with Ni-based filler metals, as well as the related technique of transient liquid phase bonding (TLPB). The filler metals selected to join these high performance materials in many ways have to exhibit properties similar to the base material they are to join. The best joints therefore are able to possess tensile or shear strengths near that of the base metal, as well as excellent corrosion resistance in service. As such, Ni-based filler metals are the preferred option for joining superalloy components across the aerospace and other industries.

2.1 Ni-Based Superalloys

It is first important to discuss the development, properties, and applications of the Ni-based superalloys employed in these industries (and which will be used as the base metal in the experimental sections of this thesis). Ni-based superalloys, so-named for their superior mechanical and corrosion properties at high temperatures, were first developed in the post-WWII period [9], where advances in turbochargers and turbine engines required materials capable of performing at very high temperatures. These were built upon earlier developments in Ni-alloys such as Ni-20Cr, the precursor to alloy families such as Nimonic and Inconel [10,11]. In particular, their ability to retain good strength over service lifetimes at temperatures often exceeding 600ºC was a key development. While the term 'superalloy' can in fact be used to describe various series of Ni-, Fe- or Co-based alloys, Ni-based superalloys emerged as a widespread solution to metallurgical demands in a diverse range of applications over decades since their development.

Compositionally, Ni-based superalloys are complex but generally comprise transition metals, with a majority Ni content in addition to significant contents of Cr, Co and Fe depending on the alloy group. Current Ni-based superalloys may contain upwards of nine or ten alloying elements, in weight percentages in the tens down to well below one. Some alloying additions, such as Al and Cr, are almost universal across Ni-based superalloys. Others, such as Co and Ti, are very common additions but their abundance may vary widely, being present only as trace elements in some alloys. Others that are almost universal, but in very small quantities, are grain boundary-migrating elements such as B, C and Zr. Fe is a major alloying addition for some wrought alloys (see below), but is not used at all in cast alloys. These Fe-bearing wrought alloys are therefore often referred to as Ni-Fe superalloys. Many other elements are present only in some Ni-based superalloys, from still relatively common Ta and W, to less common Ru.

The primary matrix phase found in Ni-based superalloys is the austenitic gamma (γ) phase. This is the FCC phase which accommodates much of the alloying additions with somewhat similar atomic radii to Ni, including Fe, Cr and Co (as well as elements such as W, Mo, Re and Ru where they are present) [9]. The primary source of the strength of many Ni-based superalloys is the gamma-gamma prime (γ-γ') microstructure. γ' precipitates are an intermetallic phase of the type $Ni_3(Al, Ti)$ (Fig. 2.1(a)), coherent with the γ matrix. It possesses an $L1_2$ cubic structure, which possesses a primitive cubic lattice with Ni at the face-centres and Al/Ti at the cube corners. A dispersion of such precipitates in the γ-matrix provides coherence strain in the lattice, impeding dislocation motion through the ductile FCC matrix. It is this phase which allows Ni-superalloys to maintain strength at elevated temperatures. Some Ni-based superalloys (generally the Ni-Fe superalloys) may instead rely on a secondary precipitate known as gamma-double-prime, or γ'', formed through the addition of Nb (particularly in the case of Inconel-718) or V. This is a body-centred tetragonal (D0_{22}) intermetallic of the form Ni_3Nb (Fig. 2.1(b)) or Ni_3V, with Nb or V at the cell centre and corners, and provides strength through coherence strain and order-hardening. However, the γ'' phase is metastable, and transforms to the orthorhombic δ (D0_a) phase after sufficient time at elevated temperature. Further minor, yet important phases found in Ni-superalloys are carbide and boride phases, which are typically precipitated at the grain boundaries of the γ matrix, and can reduce tendency for grain boundary sliding. The carbides are often referred to as MC carbides, forming with elements such as Hf and Ti, and during service other carbides of the form $M_{23}C_6$ may form with elements such as Cr and Mo. Similarly, Cr, Mo and W may form borides at the grain boundaries.

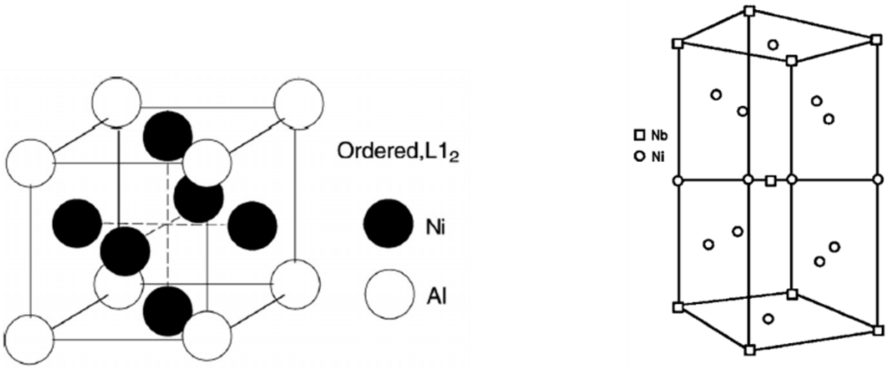

(a) (b)

Figure 2.1: Unit cells of (a) γ' Ni_3Al and (b) γ'' Ni_3Nb strengthening phases found in Ni-based superalloys. Images reproduced with permission from [9].

In total, this chemistry of the Ni-based superalloys imparts the properties that make them the material of choice for various demanding applications such as gas turbine engines, marine propulsion, nuclear reactors (including those on submarines), exhaust nozzles and pressure vessel containers. Aggressive hot gas erosion may be encountered, or extreme tensile loading due to centrifugal forces in gas turbines [12]. These are among the most demanding applications, and the Ni-based superalloys employed require high strength, high elevated temperature strength, high temperature creep resistance, high fatigue strength, provided by the careful precipitation of strengthening γ' and γ'' phases. In the extreme, Ni-based superalloys can be used at temperatures of up to 90 % of their melting temperature which may be experienced in the hottest sections of military-grade engines, above 1000^{o}C [11]. For example, the 6th generation Ru-bearing TMS-238 superalloy has a 1000-hour creep rupture life (137 MPa load) maximum temperature of up to 1120^{o}C [13]. Resistance to corrosion and oxidation in Ni-based superalloys is excellent, and achieved through formation of passive surface oxides such as Cr_2O_3 and Al_2O_3.

Reed [9] distinguished two groups of Ni-based superalloys; the cast (often single-crystal) aerofoil alloys used predominantly for turbine blades, and the wrought (polycrystalline) alloys used for turbine discs. However, such divisions can be somewhat broad, and alternatively another common classification might include cast aerofoils (commonly single-crystal and possessing the highest γ' fraction) and polycrystalline alloys (which can be cast or wrought, but possess typically lower γ' volume fraction). The former sets tend to have a greater content of the γ' forming elements Al and Ti, whereas the latter may have significant Fe content which is not used in the former. The use of W and

Ta is also somewhat reduced in wrought superalloys, whereas the Cr content is generally increased in wrought superalloys. A further significant difference is the presence of Re and Ru in the cast superalloys, which are not used in wrought alloys. For the cast single-crystal superalloys, these compositions are used with the intent of achieving certain properties such as outlined by Reed, namely; promoting a γ′ volume fraction of ~70% (the role of Al, Ti and Ta content); small γ/γ′ lattice misfit; sufficient concentrations of creep-strengthening elements (the role of Re, Ru, W and Mo); and a composition that prevents surface degredation through corrosive attack (the role of oxide formers Al and Cr). For the wrought superalloys, composition is equally important. The γ′ promoting elements Al, Ti and Ta are used, though the γ′ volume fraction is typically less at between 40 and 55 %. A further consideration for wrought superalloys is the presence of grain boundaries. Therefore, grain size should be tailored appropriately, as it correlates directly with creep strength and resistance to fatigue crack growth but inversely with yield strength and resistance to fatigue crack initiation. In addition, elements that tend to migrate to grain boundaries such as C and B are beneficial in small quantities, improving creep and low-cycle fatigue resistance. Zr may also provide some benefit at grain boundaries, capturing undesirable contaminants such as S and P [9].

Of particular interest to the brazing industry are the Inconel alloys, a family of Ni-Cr and Ni-Cr-Fe superalloys. They are employed in a wide range of applications and extreme envFements, from cryogenics, to pressure vessel containers, to high-temperature turbine discs and exhaust nozzles. Compositionally, the Inconel series varies from alloy to alloy, with common main alloying elements including Fe, Co, Mo, Ti, Al and Nb. In those containing Ti and Al, while promoting the γ′ phase, this also leaves the alloys susceptible to cracking in the heat-affected zone (HAZ) when welded, and so brazing is a crucial joining technology for these alloys. Of particular note for this thesis (see Chapters 10 and 11) is the aforementioned Ni-based superalloy Inconel-718 (IN718).

This is particularly the case for Inconel-718 (IN718), an alloy of particular note for this thesis (see Chapters 10 and 11). This alloy, whose composition is shown in Table 2.1, possesses a γ (FCC) Ni-Cr-Fe solid solution, and is primarily strengthened by the γ″ phase (making up approximately 20 % volume fraction), and contains only a small γ′ volume fraction (approximately 3 %, up to approximately 5 %, dependent on heat treatment). IN718 is noted for its retention of higher strength over the range 450ºC – 700ºC range, as well as excellent corrosion and oxidation resistance, and is generally considered to have good weldability [14]. It therefore sees wide usage in the cast form for hot-section components for aero engines, gas turbines, and applications in the nuclear and other high temperature industries. However, Nb, while the primary γ″ forming element with Ni, can exhibit segregation at grain boundaries [14, 15] and form Laves phase of the form $(Ni,Cr,Fe)_2Nb$, leading to microfissuring and liquation cracking in Inconel-718 weldments [14].

In summary, Ni-based superalloys see use in a wide variety of demanding applications and envFements, representing some of the greatest and most complex advances in alloying. Their high-temperature mechanical, corrosion and oxidation properties make them ideal materials for such components as those found in jet engines and high pressure vessel and containment applications. There is often a need to join Ni-based superalloys to produce such components, and difficulty arises in attempting to weld them due to their aforementioned susceptibily to the HAZ. The following section will discuss the use of brazing as the preferred method for joining Ni-based superalloys.

Table 2.1: Typical composition of Inconel-718 superalloy in weight percentage (atomic percentage), according to that provided by a supplier (Goodfellow Ltd, Cambridge, UK)

Ni	**Cr**	**Fe**	**Nb+Ta**	**Mo**	**Ti**	**Al**	**Co**
53.4 (52.8)	18.7 (20.8)	17.7 (18.3)	5.07 (3.16)	2.93 (1.75)	0.97 (1.17)	0.55 (1.18)	0.23 (0.22)
Mn	**Cu**	**Si**	**C**	**P**	**B**	**S**	
0.14 (0.15)	0.10 (0.09)	0.08 (0.16)	0.03 (0.14)	0.011 (0.05)	0.002 (0.01)	0.0004 (0.002)	

2.2 Ni-Based Brazing Filler Metals

Ni-based brazing alloys, as are commercially available today, are a family of brazing filler metals comprising mostly, as the name suggests, Ni, along with several other alloying additions. While numerous standardised compositions of these alloys see industrial application currently, their initial development dates back to the 1950s, just as for Ni-based superalloys. Due to the aforementioned difficulties in welding certain superalloys, brazing and related processes were instead considered as a solution for joining Ni-superalloy components. Perhaps the earliest alloy system that saw application as modern brazing filler metals was the Ni-Cu system. Lynch *et al.* [16] used such to join Ti, before a similar process was conducted by Owczarski *et al.* [17] to join Zircaloy 2 to 304 stainless steel.

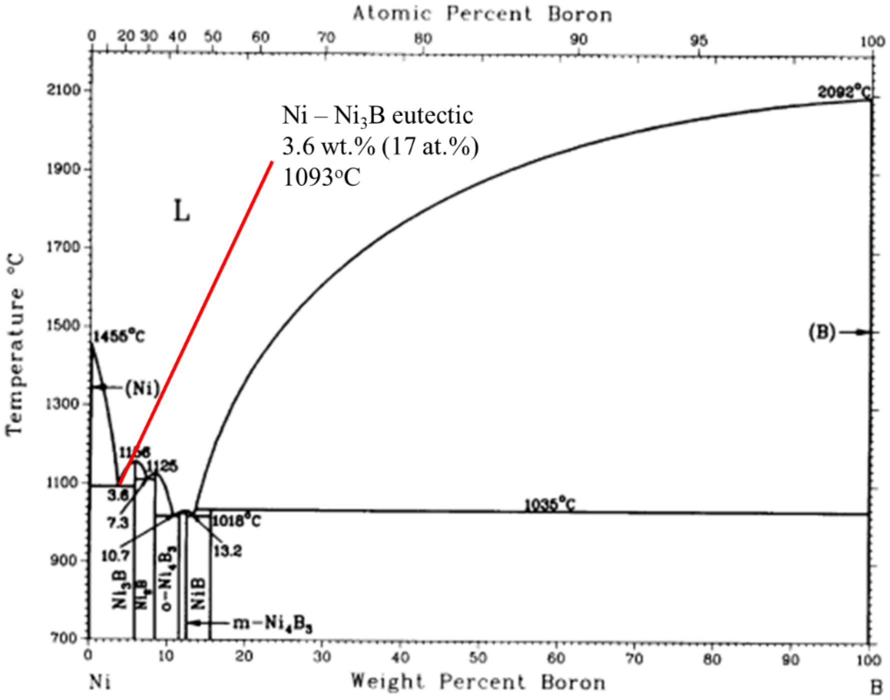

Figure 2.2: Ni-B binary phase diagram, from ASM Handbook [18], and based on [19]. Due to its relevance to Ni-based filler metals, the first eutectic point is indicated.

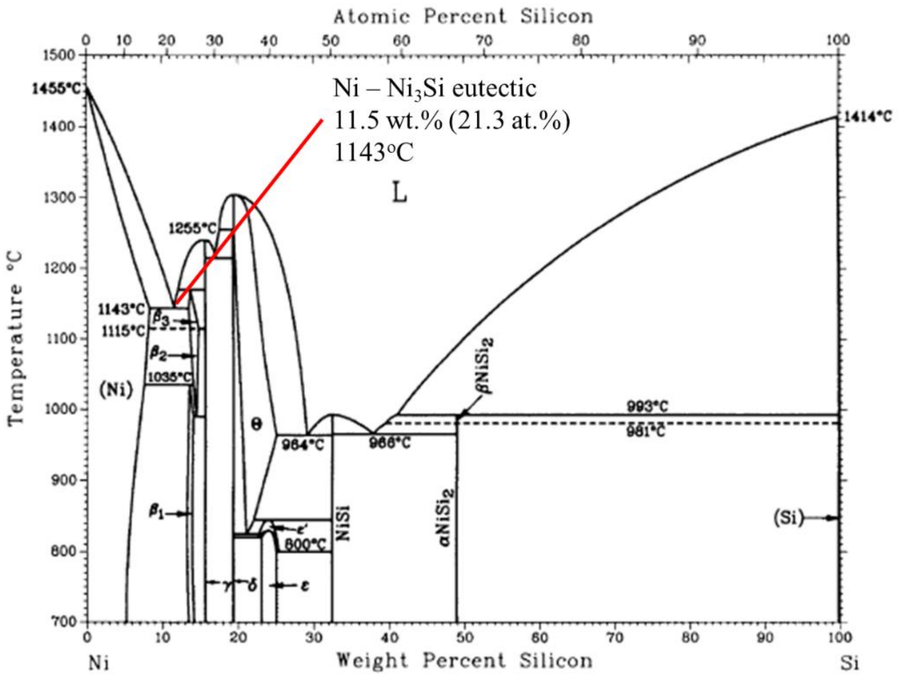

Figure 2.3: Ni-Si binary phase diagram, from ASM Handbook [18], and based on [19]. Due to its relevance to Ni-based filler metals, the first eutectic point is indicated.

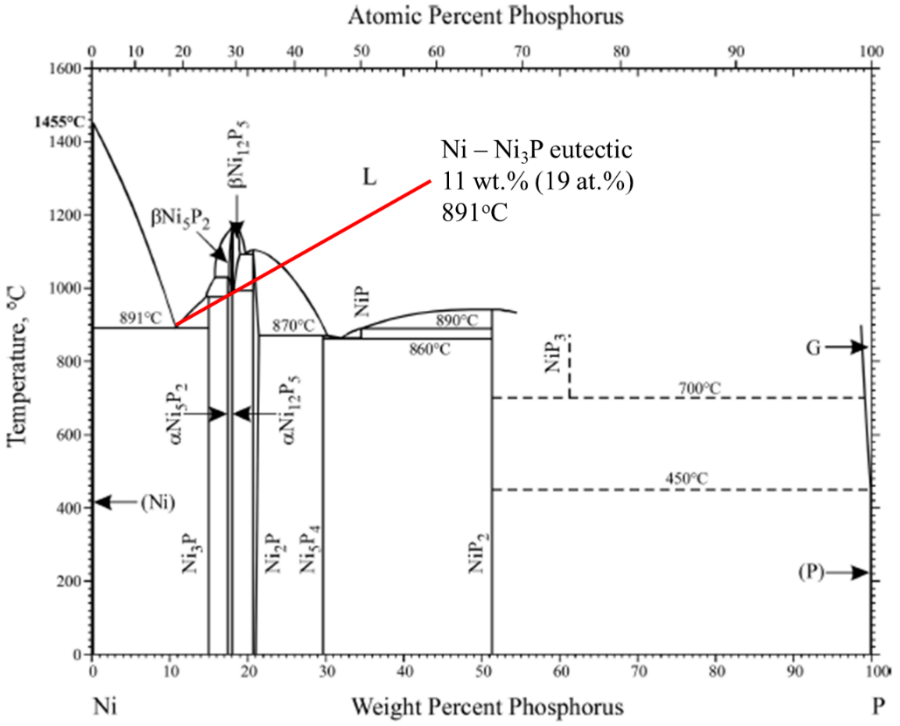

Figure 2.4: Ni-P binary phase diagram from ASM Handbook [18], and based on [20]. Due to its relevance to Ni-based filler metals, the first eutectic point is indicated.

One of the more important aspects of these alloys is the alloying additions of so-called melting point depressant (MPD) elements, necessary introductions to ensure melting of the filler metal before approaching the solidus temperature of the base metal. Across the vast majority of commercially available Ni-based filler metals, the elements used as MPDs are B, Si and P, based on the binary phase diagrams of Ni with these elements (see Figs. 2.2 – 2.4, [18 – 20]). The Ni-B and Ni-P systems were used by Duvall *et al*. [21] in a process was that was the first use of the term transient liquid phase bonding (TLPB) (see Section 2.3). Later, the Ni-Cr-B, Ni-Cr-Si and Ni-Cr-B-Si systems, which were originally developed for wear-resistant coatings, were touted for use in brazing [22], with these systems exploiting the phenomenon of diffusion of B, which, as a small radius element, can diffuse interstitionally and hence transport very quickly. This would also have the benefit of increasing the 're-melt' temperature of the joint, that is, the melting temperature of the filler metal left in the joint increases as B diffuses away, so can withstand higher service temperatures. Knotek and Lugscheider [22] proposed that alloys based on the Ni-Cr-Si-B system could be successfully applied to brazing production and repair, noting the temperature of the Ni-Ni_3B eutectic. It was also noted that the Ni-Cr-B ternary is the most important system to consider for these alloys, considering the greater effects of B on the melting temperature but also on its extremely limited solubility in Ni an Ni-Cr, in comparison to Si. Higher B content also results in a decrease in Si solubility, increasing the propensity for both borides as well as silicides. Both Cr and Si were deemed necessary for good wetting, while at the same time the lowest liquidus temperatures are found in the Ni-rich corner (the alternative, at high B contents, showed almost no plasticity). Therefore, Si and B were suggested to be added only to a level such that a desirably low melting temperature is exhibited.

Lugscheider *et al*. [23, 24] later investigated specifically B-free filler metals, which are necessary in some industries such as nuclear. Ni-Cr-Si-P alloys were suggested as a development on already existing Ni-Cr-Si alloys (such as BNi-5), which possess higher liquidus' than B-containing fillers BNi-2, BNi-3 and BNi-4. The use of P as a sole MPD in Ni was previously established as seen in the BNi-6 (Ni-P) and BNi-7 (Ni-Cr-P) alloys, but not in conjunction with Si. The effect of P additions to a ternary near-eutectic Ni-20.4Cr-11.6Si (wt. %) with liquidus approximately 1077^{o}C were investigated, with approximately 0.5 wt. % P reducing the liquidus to approximately 1060^{o}C, approximately 75^{o}C lower than for BNi-5. However, with P also possessing very poor solubility in Ni, phosphides were formed in this alloy. Lugscheider *et al*. [25] followed up on this work investigating three low-P containing Ni-Cr-Si-P alloys for brazing 321 stainless steel, with the low-P, high-Si compositions showing increased Ni-solid solution microhardness due to the higher solubility of Si in Ni. Lugscheider and Cosack [26] also later demonstrated the suitability of a Ni-20.3Cr-11.5Si-0.5P (wt. %) alloy as a substitute for BNi-5 for brazing this steel, achieving base metal tensile strength in the joint after brazing at 1070^{o}C for 10 minutes. Meanwhile, increasing the P content and decreasing the Si content resulted in inferior brazing results for this alloy system.

Today, the composition of alloys in the standardised family of Ni-based brazing alloys has remained largely constant for some years, as described in the latest AWS standard under the 'BNi-' designation. Table 2.2 shows the standard compositions of the main BNi- series alloys; these are generally given in weight percentage. As can be seen, all alloys share several main alloying additions, generally each having the role of either MPD as described above (B, Si, P) or solid solution former (Cr, Fe), with some also increasing wettability (Cr, Si). The most universal alloying addition among Ni-based filler metals is Cr. It is added typically in proportions from 7 (for example in AWS BNi-2) to 15 wt.% (for example in AWS BNi-5). Its primary role in brazing alloys is as it is in stainless steels and Ni-based superalloys – corrosion resistance, and has been included since early development in Ni-based filler metals [22 – 28]. The impact of obtaining this superior corrosion resistance is generally an increase in the brazing temperature necessary to ensure the alloy is fully molten, as can be seen in the different industry-quoted melting temperatures of 7 wt.% Cr BNi-2 (998ºC) versus 15 wt.% Cr BNi-9 (1055ºC) [5]. Other brazing filler metal families are known to possess excellent corrosion (and oxidation) resistance, notably the precious metal-based Ag, Au and Pd families [30, 31], as well as filler metals that simply contain some of these, in particular Pd-bearing filler metals [31-34]. Ag, however, is not used in Ni-based filler metals due to both cost and the tendency to reduce the wetting of Ni, while Au and Pd have been included in Ni-based filler metals but are less preferred due to cost [35]. Mo has been reported as contributing to the corrosion resistance [36, 37] but has seen little attention as an addition to Ni-based filler metals for corrosion purposes, perhaps due to the potential for undesirable phases, increasing melting temperature, or simply due to there being no demand for such additions.

Table 2.2: Compositions in weight percent of various commercially available Ni-based brazing filler metals from the AWS BNi- series of alloys [5].

Alloy		Ni	Cr	B	Si	Fe	P	Melting Range (ºC)
BNi-1	Wt. %	Bal.	14	3.1	4	4.5	-	980 – 1060
	At. %	Bal.	13.1	14	7	3.9	-	
BNi-2	Wt. %	Bal.	7	3.1	4.5	3	-	970 - 1000
	At. %	Bal.	6.6	14	7.9	2.6	-	
BNi-3	Wt. %	Bal.	-	3.1	4.5	1.5 (max)	-	980 - 1040
	At. %	Bal.	-	14.2	7.9	1.3 (max)	-	
BNi-4	Wt. %	Bal.	-	1.85	3.5	1.5 (max)	-	980 - 1070
	At. %	Bal.	-	9	6.5	1.4 (max)	-	
BNi-5	Wt. %	Bal.	19	trace	10.1	-	-	1080 - 1135
	At. %	Bal.	18.9	trace	18.6	-	-	
BNi-6	Wt. %	Bal.	-	-	-	-	11	875
	At. %	Bal.	-	-	-	-	19	
BNi-7	Wt. %	Bal.	14	-	-	-	10.1	890
	At. %	Bal.	14.3				17.3	
BNi-9	Wt. %	Bal.	15	3.6	-	-	-	1055
	At. %	Bal.	14.4	16.6	-	-	-	

While in-depth investigation of wettability was beyond the scope of this project, some points pertinent to the work here are mentioned (Gale and Butts [6], among others [31, 38], discuss wettability in greater detail). The wettability of the filler metal is crucial to ensure good flow of the molten filler metal over the entirety of the surface to be joined. From a compositional perspective, elements such as Cr (which can wet oxides can carbides) and Si in the filler metal improve the wettability on Ni-based superalloys [23], though Cr can also increase melting temperature, and so may have the opposite effect [39]. Again, this was established in early work on Ni-based filler metals, and so these elements are still common alloying additions. Other elements that were observed to improve wettability, either on Ni-based superalloys or difficult-to-wet surfaces in general, include Ti [40], Zr [31], and V [41].

It is worth looking briefly at other brazing applications of these alloys outside the joining of superalloys. Indeed, Ni-based brazing alloys have been demonstrated to successfully braze steels [42, 43], Co-based alloys [44], Mo to steel [45], and various ceramics [46, 47], to name a few examples of many. The two base materials being joined need not always be the same alloy; significant research has focused on the brazing of dissimilar materials, whether one superalloy to another (such as may be found in [48 – 53]), to a steel [54, 55], and to Co and Co-superalloys [56, 57]. Joints of higher cost superalloys to cheaper materials such as steels has been seen as an enabling technology for a strategy to reduce the costs for certain components in power plant and marine industries, without compromising on properties, and in some cases the combination offers technological advantages [55]. Ghaderi *et al*. [58] brazed IN718 to ultrafine-grained 304L stainless steel, using commercial filler metal BNi-2, and also using BNi-2, Baharzadeh *et al*. [55] brazed Inconel X-750 to 2205 duplex steel. Similarly, it may be desirable to combine small parts made from ceramics that can be difficult to produce in large or complex geometries, but that nonetheless have the required properties, with other materials. Ni-based brazing alloys have been applied even for this task. Lu *et al*. [59] successfully brazed Ti_2AlC ceramic to Ni using BNi-2 filler metal, achieveing approximately 90 % the strength of the ceramic. Lee *et al*. have successfully brazed yttria-stabilised zirconia (NiO-YSZ) cermets to 306L stainless steel using commercial filler metals BNi-2 [60] and BNi-3 [61].

2.3 Transient Liquid Phase Bonding

An important development in the design and implementation of brazing is the concept of transient liquid phase bonding (TLPB). This is essentially the process of brazing carried out to the extent that complete isothermal solidification (IS) of the joint takes place during the brazing process at the brazing temperature. That is, sufficient diffusion of the MPD element into the base material such that the liquidus of the melt increases and surpasses the brazing temperature, and so the solidification of the joint, commencing at the interface with the base material, is achieved at the brazing temperature. Throughout this project, as will be seen in later chapters, the term ‘brazing’ has been used rather than TLPB, even though the brazing conducted has been guided by the principles of TLPB. Gale and Butts [6] distinguish TLPB from brazing in its suitability for joining components used in high service temperatures, where joint properties close to the base material are required. Through careful consideration of the filler metal as well as the brazing parameters such as brazing temperature and holding time at temperature, it is therefore possible to achieve a joint whose microstructure is free of the centreline eutectic constituent that is often seen in cases where insufficient diffusion of the MPD has taken place. Other steps such as diffusion holding at a temperature below the brazing temperature, or even post-braze heat treatments, may also be included as part of the TLPB process. Duvall *et al*. [21] considered TLPB to be comprised of three steps: base metal dissolution, followed by isothermal solidification, followed by homogenisation of the joint. Later, in the model proposed by Tuah-Poku *et* *al*. [62], the base metal dissolution stage was considered to be actually composed of filler metal melting and widening of the liquid phase as discrete processes. MacDonald and Eagar [63] then proposed another prior stage to account for interdiffusion between filler and base metal during the heating stage, before full melting of the filler metal, which may be a problem at slow heating rates or for extremely thin filler metal inserts. In the review by Zhou *et al*. [64], four stages were discussed based on the previous works [21, 62, 63], and Gale and Butts summarised the process in three stages based on [62] with omission of some heating considerations. Considering the aforementioned works, three main stages of importance to this thesis are discussed for a simple filler metal of matrix element A with MPD element B:

- **Base metal dissolution / Liquid Homogenisation**
  Upon heating and eventual melting of the filler metal, diffusion of B from A into the base metal occurs at the interface, which has the effect of adjusting the composition of the adjacent base metal towards the solidus, while adjusting the composition of the adjacent liquid filler metal toward the liquidus, and so the width of the liquid increases Equilibrium is reached when the base metal reaches solidus composition, and molten filler reaches liquidus composition, and dissolution ceases with the maximum width of the liquid. This process usually completes quickly, from seconds to a few minutes depending on the system, as it does not rely on long-range solid diffusion [6].

  Zhou *et al*. [64] further defines two regimes in this stage for a eutectic filler metal composition. The first is during the temperature increase from filler metal liquidus to brazing temperature, where the concentration of solute B in the solid and liquid at the interface will follow the solidus and liquidus lines as the temperature rises. The second is the continuing isothermal dissolution at the brazing temperature, until equilibrium is achieved and dissolution ceases.

- **Isothermal Solidification**
  Following the dissolution stage, further diffusion of B into the base metal at the brazing temperature increases the liquidus of the melt. Meanwhile, according to most models, the concentration of solute B in the solid and liquid immediately adjacent to the interface remains constant at that of the solidus and liquidus respectively, which was achieved at the end of the dissolution stage [6]. When the liquidus reaches the brazing temperature, the liquid begins to solidify and the liquid width decreases as A-rich solid with B in solution advances toward the centre from both sides of the joint. From a technological point of view, the isothermal solidification stage is often considered the most important step in the brazing process, as the extent of its completion can greatly influence the performance of the resulting joint. This stage, however, typically takes much longer than the dissolution stage, as sufficient solid diffusion of B into the base metal must occur. Depending on the system (that is, on the amount of B that must be diffused, in turn determined by the composition and thickness of filler metal), this may take several minutes to several hours, for a given set of brazing conditions. As the brazing temperature is increased, so does the diffusivity, D, of B (according to the Arrhenius equation shown in Equation 2.1), thus isothermal solidification may proceed at a greater rate.

  $$D = D_0 \, e^{-Q/_{RT}} \qquad (2.1)$$

  where D_0 is the temperature-independent material constant, Q is the activation energy for diffusion, R is the gas constant, and T is the temperature. However, increasing the temperature may result in a greater degree of base metal dissolution in the first stage due to increased diffusion, which effectively creates a wider liquid layer which must solidify, thus prolonging the time at the brazing temperature required. Therefore, for a given system there exists a brazing temperature for which the time for isothermal solidification is minimum, which is of obvious technical importance [63].

With this in mind, it is unsurprising that a large amount of interest has been paid to analytical approaches to determining the time for isothermal solidification. The models of Tuah-Poku *et al*. [62] and Zhou *et al*. [64] based on a half-joint (for symmetry) with a semi-infinite base metal layer and a liquid layer, have been widely studied and applied elsewhere [65, 66]. Gale and Wallach [67] compared such models with two other approaches, one of which [68] was based on work by Nakagawa *et al*. [69]. This latter approach provided the best agreement with experimental observations of isothermal solidification when brazing Ni-Cr alloys with BNi-3 [67]. Meanwhile, using the model of Tuah-Poku *et al*. [62], the time for isothermal solidification was overestimated. Ojo *et al*. [70] also successfully applied the approach used by Gale and Wallach. Based on this approach, the MPD concentration, *C*, at location *y* and time *t* can be described by Equation 2.2 [67]:

$$C_{y,t} = C_s\left[1 + erf\left(\frac{y}{\sqrt{4Dt}}\right)\right] \qquad (2.2)$$

where C_s is the MPD solubility in the base metal at the solidus and D is the diffusivity of the MPD (given by Equation 1). Solving Equation 2.2 for the time taken for complete isothermal solidification, $t_{f,}$ gives Equation 2.3:

$$t_f = h^2 \frac{\pi}{4D}\left(\frac{C_l}{C_s}\right)^2 \qquad (2.3)$$

where h is the half-width of the filler metal and C_l is the MPD concentration in the liquid filler metal. This model, however, assumes a stationary solid-liquid interface for the MPD distribution described by Equation 2.2 to be accurate, and also that negligible MPD is diffused into the base metal before the base metal dissolution has ceased, which is unlikely to be the case for fast-diffusing MPDs such a B. This approach has been observed to overestimate t_f [67, 70]. Similar approaches have also been described by Nakao *et al*. [71].

Alternatives to the above instead treat the liquid layer and semi-infinite base metal as continuous without set compositions of the solid and liquid, based on work that suggested that the base metal dissolution stages occurred simultaneously rather than as discrete stages [69]. This approach has been found to provide good agreement with experimental results for B-containing filler metal, in the study by Gale and Wallach [67] and Ojo [70]. The MPD concentration distribution as a function of distance *y* away from the centre of filler metal with width *h,* and time *t,* is given by Equation 2.4:

$$C_{y,t} = C_m + \frac{1}{2}(C_0 - C_m)\left[erf\frac{y + w_0}{\sqrt{4Dt}} - erf\frac{y - w_0}{\sqrt{4Dt}}\right] \qquad (2.4)$$

where C_m and C_0 are the initial MPD concentrations in base metal and filler metal respectively, and w_0 is the full width of the filler metal. For the case of complete isothermal solidification after time t_f, the MPD concentration at the centre of the joint (i.e. at y = 0) can be assumed to have reached the solidus composition of the solidified phase, C_s, such that $C_{y,t} = C_s$, and Equation 2.4 reduces to Equation 2.5 (noting the property $\mathrm{erf}(-x) = -\mathrm{erf}(x)$) :

$$(C_s - C_m) = (C_0 - C_m)\left[erf\,\frac{w_0}{\sqrt{4Dt_f}}\right] \qquad (2.5)$$

Therefore, the time taken for complete isothermal solidification can be determined as in Equation 2.6:

$$t_f{}^2 = \frac{w_0}{\sqrt{4D}}\,\frac{1}{erf^{-1}\left[\frac{C_s - C_m}{C_0 - C_m}\right]} \qquad (2.6)$$

Deviations from the above models based on simple binary filler metals have been noted by several authors, generally for cases where more than one solute MPD element is in the filler metal, such as in alloys bearing both B and Si, which in practice is more often the case. This results in the presence of two regimes, as proposed by Sinclair *et al*. [72] due to the different solubilities and diffusion coefficients of the two MPDs: 1) A faster first regime controlled by diffusion of the faster-diffusing MPD (typically B); and 2) A slower second regime controlled by diffusion of the slower-diffusing MPD (such as Si). This was also considered to be the case by Yuan *et al*. [73] for two Ni-Si-B filler metals. In addition, while the above models would predict faster completion of isothermal solidification, it has been observed that at higher temperatures the isothermal solidification was taking longer, which has been attributed to a second, slower regime based not on slower diffusion of a second MPD, but on progressively increasing base metal element concentration in the remaining liquid, effectively acting as MPDs thus prolonging the solidification time [74]. As mentioned above, increased dissolution of base metal at higher temperatures has also been reported as playing a role in deviation from the conventional models [75, 76].

- **Solid Homogenisation**
  Upon completion of isothermal solidification, an additional hold at elevated temperature may be commenced. This may be at, but typically below, the brazing temperature, and its purpose is to allow further diffusion of solute B away from the bonded region. This can be especially important to ensure the concentration of B at the joint centre, where the diffusion distance of B into the base metal is greatest, is below the room temperature solubility limit in A, thus preventing the precipitation of B-rich intermetallic phases. Again, this process can be prolonged, as it relies on solid state diffusion and so the temperature of this homogenisation hold should still be high enough to achieve this in good time. When sufficient time is allowed, the concentration gradient of B across the joint may be negligible and so the microstructure may be largely indistinguishable from the base metal.

2.4 Microstructural Features of Brazed Joints

The evolution of the joint microstructure through the above stages, from the room temperature assembled fixture to the complete isothermally solidified and homogenised joint, has been extensively documented. For brazed joints that rely on the diffusion of an MPD element, common microstructural features or zones in relation to their position are almost universally observed to some degree. The presence of such changes with brazing time and temperature and joint composition (both filler metal and base metal). Fig. 2.5 shows optical micrographs of joints of IN718 brazed with commercial Ni-based filler metals (a) BNi-2 and (b) BNi-3, with the distinct microstructural zones that can be exhibited by a brazed joint indicated. Such zones can be explained as follows:

- **Isothermally Solidified Zone (ISZ)** – The ISZ is the area of the joint which has solidified at the brazing temperature due to the outward diffusion of the MPD into the base metal (as described above). The entire width of the joint region may be taken up by the solid solution of the ISZ if isothermal solidification has completed, otherwise two separate solidification fronts will be evident, having moved inwards from the interface with the base metal. These can be a single grain zones. The composition of this zone is the primary γ FCC matrix, rich in Ni with elements from both the initial filler metal and the base metal in solution.

- **Athermally Solidified Zone (ASZ)** – This zone forms in the case of incomplete isothermal solidification, where the onset of cooling occurs while liquid remains towards the joint centre. Elements with a partition coefficient with Ni of less than one ($k < 1$), are rejected from the advancing γ solid solution fronts during isothermal solidification, pushing the remaining liquid gradually towards eutectic composition. When the temperature decreases past the liquidus, this remaining liquid begins to freeze and may undergo a single or successive binary or ternary eutectic transformations. The resulting solid is typically comprised of intermetallic phases such as borides and silicides. Often, this can be observed as a continuous narrow band of brittle material along the centre line of the joint (the thickness determined by how much isothermal solidification had completed) [53, 77, 78]. This is an important feature to avoid, as it clearly provides a continuous crack path potentially leading to brittleness and premature joint failure. Further homogenisation may reduce or even eliminate the ASZ, though the time and temperature required may be excessive in some cases as diffusion in intermetallics is slow.

- **Diffusion Affected Zone (DAZ)** – The diffusion of MPD elements away from the filler metal during brazing often results in a region of high intermetallic concentration in the base metal adjacent to the joint region, formed with base metal elements. This is especially common with B containing filler metals used to braze Ni-based superalloys, due to the low solubility of B in the base metal γ matrix. It is undesirable to retain a region such as this in the final joint microstructure, as it can provide a low-resistance path for cracking [79], and boride-forming elements such as Cr, Mo, Ti and Nb can be effectively removed from the matrix thus impacting the local corrosion resistance [78, 80]. However, it has been noted that intermetallics in the DAZ may be less detrimental to joint strength than the ASZ, as they are not continuous [81]. Borides in this region may have various morphologies depending on where they precipitate, whether in the grains or along grain boundaries. Smaller, blocky morphology may be observed close to the joint interface, with elongated needle-like borides precipitating well into the base metal grains at increased bonding times [80, 82]. Grain boundary borides may in particular be observed well into the base metal due to the fast diffusion path provided along grain boundaries [83, 84].

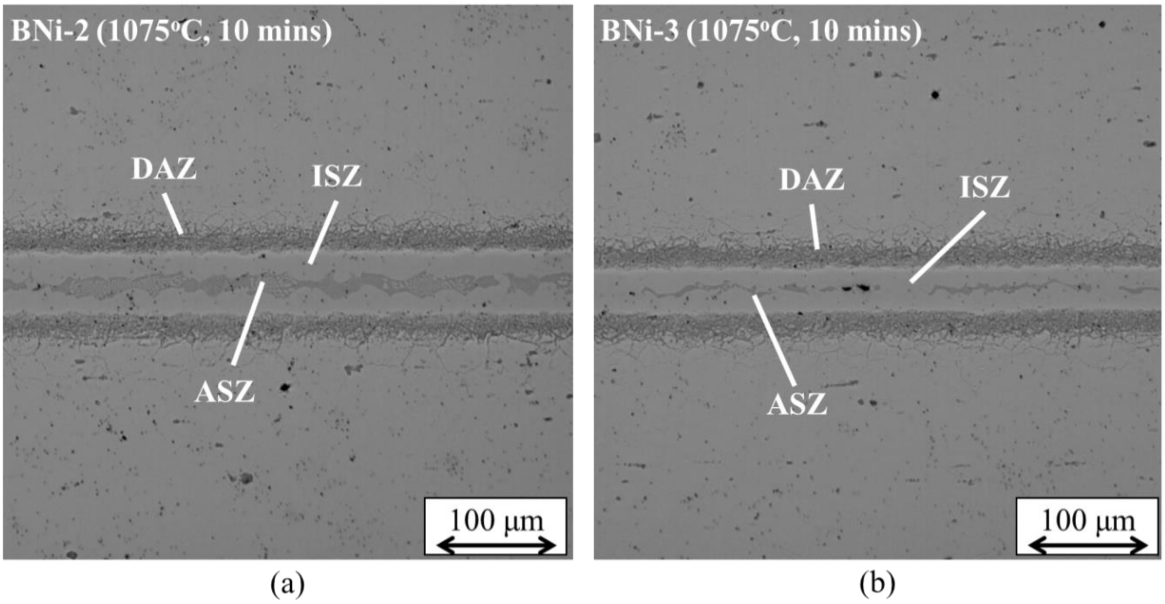

(a) (b)

Figure 2.5: Optical micrographs of typical joints of IN718 vacuum brazed with (a) AWS BNi-2 filler metal, and (b) AWS BNi-3 filler metal. Brazing temperature and time in each case was 1075°C and 10 minutes respectively, and filler metal foil thickness was 50 µm. Regions often observed in such joints are labelled, including athermally soldified zone (ASZ), isothermally solidified zone (ISZ) and diffusion affected zone (DAZ).

For this work, it is worth briefly discussing the above features in the context of brazing IN718. As described in Section 2.1, IN718 is one of the more widely used superalloys, and as such the joining of this material is often required. Despite this, brazing of IN718 in the literature appears to be far from the most widely reported. Such microstructural features are not particular to any one base metal – filler metal combination, but the compositions of the base and filler metals influence the composition of the phases in these features. For example, IN718 superalloy, which notably contains Fe and Nb, in addition to elements such as Cr, Ti and Mo, and borides containing these elements can form when using B-containing filler metals. These may be found in the DAZ, where outward-diffusing B encounters these elements, and in particular Nb and Mo which can be segregated in the IN718 base metal. They may also be observed in the joint region due to introduction via base metal dissolution, though more commonly is Cr-borides in the ASZ, as filler metals often contain Cr. Ni-silicides can also form in the ASZ, due to the high Ni concentration and the relatively slower Si diffusion away from the joint.

2.5 Properties of Brazed Joints

Having looked at the principles behind the brazing and TLPB of Ni-based superalloys, this section will look at the properties achievable in brazed and TLPB joints, evidenced in the extensive literature. Firstly, joining the same base metals together (often referred to as ‘similar joints’ in the literature) represents the simplest cases of brazing, with only two different compositions to consider (that is, the initial filler metal composition and initial base metal composition). Except for practical situations that may arise due to poor joint design, the interaction between the different chemistries will be essentially mirrored on both sides. ‘Dissimilar’ joints, using two difference base metals as opposed to similar joints, are likely to have a somewhat asymmetrical chemistry and final microstructure after brazing (depending on how different the base materials are). In either case, tensile and shear strengths of brazed joints have been common measures of the quality of a brazed joint because of the generally observed relationship between strength and degree to which isothermal solidification is complete. The joint strength required can differ depending on the application. For instance, in brazed joints for electronics, the joint strength might of less importance than electrical or thermal properties, and some joints may prioritise corrosion resistance over strength where aesthetics are a concern. Where a joint is formed in order to produce a single component, however, it is often desired to achive a joint shear or tensile strength close to that of the base metal(s) being joined, so as to avoid a weaker part of the component. Achieving this does not always appear to be of emphasis in the literature, and often a study may go only as far as maximising the strength achieved for a given filler metal and base metal combination, particularly by maximising isothermal solidification. Regardless, for the brazing of most Ni-based superalloys with typical commercially available Ni-based filler metals, the joint shear and tensile strengths achieved are generally of the order of hundreds of MPa.

Speaking generally, and considering the principles discussed so far, increasing hold time for a given temperature and filler metal thickness improves joint strength. Increasing bonding temperature for a given hold time and filler metal thickness will improve joint strength, up until a certain point past which the excessive initial base metal dissolution outweighs the increased diffusion rate of the MPD, by changing the chemistry of the melt (thus influencing the solidification) and increasing the diffusion distance during isothermal solidification. Examples of this can be seen in [85, 86]. For most cases regardless of brazing temperature or hold time, filler metal thickness is kept below 100 µm and above 25 µm to achieve best joint strength. Too thick, and the diffusion distance is greater thus isothermal solidification will be less complete after a given time. Too thin, and the MPD can be entirely consumed through diffusion in the heating stage, resulting in no liquid being available at the bonding temperature [87]. The interplay of these parameters, and the effect on the joint properties, is widely investigated across the literature for many different filler metal and base metal combinations.

Brazed joints involving just one type of Ni-based superalloy as the base metal are the simplest case. Binesh and Gharenbagh [86] systematically studied the effects of bonding temperature, bonding time and filler metal thickness on the isothermal solidification rate and shear strength when joining IN738 with MBF-15 (Ni-13Cr-4.2Fe-4.5Si-2.8B in wt. %). At a constant temperature of 1130°C and 35 µm thickness filler metal, shear strength increased with bonding time up to a maximum of almost 700 MPa after 90 minutes, with a corresponding decrease in ASZ width. In addition, for a constant bonding time of 30 minutes and 35 µm thickness filler metal, shear strength decreased with increasing temperature from 1130°C to 1170°C, from above 600 MPa to below 450 MPa. This was coincident with increasing ASZ width, attributed to increased base metal dissolution. Idowu *et al*. [74] also joined IN738, using Nicrobraz 150 (Ni-15Cr-3.5B in wt. %). Brazing temperatures were between 1130°C and 1175°C, with hold times from 1 hour to 8 hours, and joint width of 100 µm. The completion of isothermal solidification still took 5 hours at least, for a 1145°C temperature, and longer was required for lower and higher temperatures. Joint width was also studied at a constant 1160°C temperature, with isothermal solidification completing quicker for thinner gaps as expected. The authors also described deviation from traditional models of time required for isothermal solidification, proposing the two-regime model as described in Section 2.3. Amiri *et al*. [80] conducted investigations on the bonding of γ'-strengthened GTD-111 with MBF-20 filler metal (Ni-7.6Cr-3.4Fe-3.6Si-3B in wt. %). Shear strength increased from approximately 425 MPa to approximately 600 MPa when increasing hold time from 15 minutes to 105 minutes at 1120°C. Increasing bonding temperature from 1080°C to 1180°C (keeping hold time at 15 minutes) achieved complete isothermal solidification with an intermetallic-free joint, but intermetallics reappeared when temperature was further increased to 1200°C. Pouranvari *et al*. [78] studied the effect of TLPB temperature and hold time for joining IN718 with BNi-2. For temperatures of 1000°C, 1050°C and 1100°C, isothermal solidification completed after approximately 60, 40 and 20 minutes respectively, displaying low time and temperature requirements when compared to some other systems. Compared to a partially isothermally solidified joint, a fully isothermally solidified joint achieved almost twice the UTS and elongation at failure. Other similar systematic studies of similar joint investigating variation of hold time and hold temperature include [89] and [90].

While not the focus of this work, studies of dissimilar brazed joints and their properties are also common in the literature. Dissimilar joints involving combinations of Ni-based superalloys, steels, ceramics and other materials, while of growing importance in certain industries, they are beyond the scope of this work. Of more relevance are dissimilar joints involving two different Ni-based superalloys, as such joints still favour the use of Ni-based brazing filler metals. As mentioned, chemical asymmetry in the final joint is likely in these cases, and this is enhanced the more dissimilar the base materials are. Despite this, the same principles generally apply, and numerous studies have demonstrated that isothermal solidification is an important step for the mechanical properties [52, 53, 85, 90 – 94]. The effects of the different chemistry on either side of the joint can however be seen where isothermal solidification is not completed [85, 91], especially in cases where B may diffuse at different rates in the dissimilar base metals [85, 91].

Generally, therefore, whether similar or dissimilar joints, mechanical properties can be seen to improve with the degree of isothermal solidification completion, and joint strength close to that of the base metal(s) is achievable with appropriate brazing cycles. This is of clear importance, not just in brazed joints in general, but in braze repair applications where wide cracks in a base metals are filled with a mix of base metal powder and brazing filler metal powder [95, 96]. While the most significant improvements in joint strength tends to be made up until isothermal solidification is completed, this does not necessarily represent the maximum strength that can be achieved in a joint (see ‘Solid Homogenisation’ above). Shear strengths have been observed to increase with further heat treatment past the completion of isothermal solidification due to continued diffusion of MPD elements away from the joint [49, 57, 79, 97-99], as well as dissolved base metal elements within the joint, imparting solid solution strengthening [100]. In many cases, therefore, joint shear strengths upwards of 400 MPa are achievable when brazing generally between 1050°C and 1150°C, and for hold times less than 60 minutes. But to achieve the greater shear strengths observed, upwards of 600 MPa, prolonged hold times of over 60 minutes, and sometimes prolonged post-braze heat treatments, are required.

Given the environments in which Ni-based superalloys are employed, such as in temperatures in excess of 600°C, the mechanical properties of joints thereof at elevated temperatures are particularly important. Despite this, literature investigating mechanical properties of joints at these temperatures is more scarce, likely a result of the difficulty in performing such tests, namely high-temperature shear and tensile tests, which requires specialist equipment in order to heat the sample and testing rig. That which does exist is generally still concerned with the shear or tensile strength behaviour at higher temperatures, and how they compare to room temperature strength. Luo *et al*. [101] brazed Hastelloy-C276 with BNi-2 filler metal for 25 minutes at 1060°C, and tensile testing the joint at 625°C revealed a reduction in UTS and yield strength compared to room temperature results (for example, maximum room and high temperature UTS of 403 MPa and 340 MPa respectively). Pilehrood *et al*. [79] conducted high temperature tensile testing (at 650°C, 750°C and 850°C) on IN738LC joints brazed with BNi-2 at both 45 and 120 minutes at 1120°C followed by standard heat treatment for IN738LC. Compared to the base metal, joints exhibited an average reduction in yield strength and elongation of approximately 10 % and 53 % respectively, but these differences lessened at the highest temperature of 850°C. The reduction in these properties was attributed to coarsening of γ' precipitates in the joint region. Hartmann and Marsilius [102] performed tensile testing at high temperatures on 306 stainless steel joined with BNi-2 and high-Cr filler metals with both B and P as MPD. In all cases, UTS of joints was close to that of the 306 steel base metal, and again the differences decreased with increasing test temperature. The sharpest decrease in UTS for all joints and for the steel occurred at temperatures above 500^{o}C. In the aforementioned work by Zhang *et al*. [91], tensile tests on IC10 – GH3039 joints were conducted as high as 900^{o}C on joints brazed for 2 hours at temperatures between 1050^{o}C and 1200^{o}C. All joints achieved approximately 200 MPa, close to the base metal tensile strength at that temperature. Furthermore, it was noted that boride concentration had less of an effect on the high temperature tensile strength than for the room temperature strength. For dissimilar joints of Co-based superalloy X-50 and IN738 brazed with BNi-9, Henhoeffer *et al*. [49] conducted tensile testing at 950^{o}C, achieving slightly higher yield strength than for X-50 base metal, but worse tensile strength and much worse ductility. Post-brazing heat treatments improved these joint properties somewhat, but only after lengthy treatments of 120 hours at 950^{o}C, and even after 840 hours not all detrimental eutectic phases were removed.

While in many cases it has been seen that brazed joints can achieve a higher percentage of the base metal tensile strength as temperature increases, but exceptions exist. Ye *et al*. [95], conducted braze repair of artificial wide cracks in IN738LC using a Ni-Cr-Co-Al-Ta-B filler metal at 1150^{o}C for 18 hours (achieving isothermal solidification), and followed by various heat treatments. While heat treatments resulted in a greater percentage of base metal tensile strength being achieved at temperatures of 25^{o}C, 600^{o}C and 800^{o}C, in each case it was the tests performed at 800^{o}C which showed the greater disparity between brazed joint tensile strength and base metal tensile strength, while tests performed at 25^{o}C showed the lowest disparity. While insufficient detail is given of the test pieces in this study to give a full assessment, this result could be due to the greater width of the joints, meaning the brazed joint made up a larger portion of the test piece.

Other easy-to-perform tests of mechanical properties of brazed joints include microhardness measurement (details of which are given in Chapter 8). Microhardness can be used as an indicator of joint properties such as ductility (or brittleness) and yield strength. With relative ease and speed, microhardness profiles across brazed joints from base metal to base metal can be obtained, showing the variance in hardness in different microstructural zones of the joint, and hence differences in mechanical properties may be inferred. This is illustrated in Fig. 2.6. Common trends in the variance are observed across brazed joints, and for joint with similar base materials these are approximately symmetrical about the joint, as observed by numerous authors [44, 53, 55, 58, 79, 104]. In the case of dissimilar joints, the different chemistries either side of the joint can affect this symmetry, but similar trends may still be observed with regard to the distinct microstructural zones. Microstructural zones with a high concentration of intermetallic phases such as the ASZ and the DAZ, predictably display increased microhardness, whereas the zones formed of FCC solid solution (the ISZ, and the base metal sufficiently far from the DAZ) exhibit low microhardness. The difference in microhardness can be rather extreme, for instance in cases where regions of highly concentrated boride or other intermetallic phases form, which tends to be the case for insufficient brazing hold times. The ISZ is usually softer than the base metal, and as it is a γ-Ni solid solution, this is largely dependent upon solid solution strengthening from filler metals and base metal elements in solution, as well as by grain boundary strengthening. For example, Pouranvari [104] observed significantly greater ISZ hardness for joints of IN718 using BNi-9 than for joints using BNi-2 and BNi-3. Considering Gypen and Depruyttere’s model for solid solution strengthening [105] and strengthening coefficients for elements in Ni alloys proposed by Roth *et al*. [106], Pouranvari suggests this is due to the higher initial Cr content of BNi-9 filler metal, and the higher B content leading to a greater degree of base metal dissolution, and so greater quantities of strengthening elements Nb, Mo and Ti concentrated in the ISZ. Homogenisation treatment of the joint will tend to flatten the variation in microhardness over time, as represented in fig 2.6.

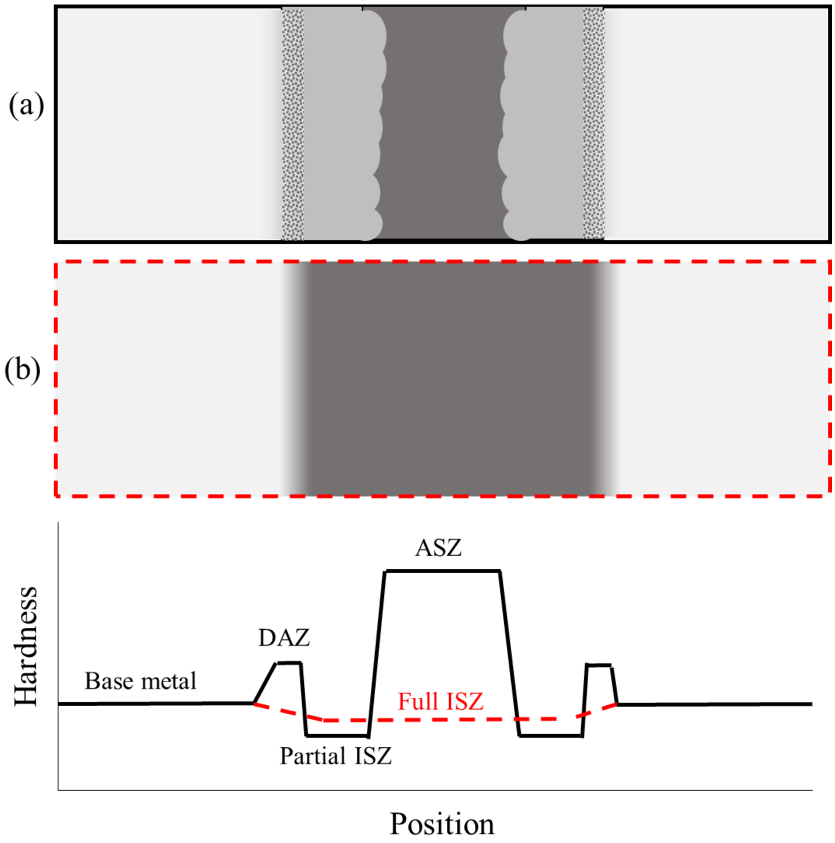

Figure 2.6: Schematic illustrating the variation of measured hardness across different regions of (a) a joint exhibitng a DAZ, ISZ and ASZ, and (b) a joint in which isothermal soldification is completed.

There are multiple other properties of brazed joints that are critical for their performance, but are not the focus of this thesis. The corrosion properties of brazed joints are often a consideration, especially in automotive exhaust applications [36, 107] along with the effects of composition and brazing parameters impacting this. As discussed above, Cr is considered a crucial alloying additions in Ni-based filler metals as well as in superalloys, yet even in filler metals containing well over 10 wt. % Cr, corrosion can occur as a result of incomplete isothermal solidification, whereby Cr forms borides and is thus relatively depleted in the surrounding regions [83, 97, 108]. This is similarly the case for base metal elements such as Nb, Mo and Ti which tend to form borides is insufficient brazing parameters are used, and so regions of local depletion in these elements can be sources of corrosion weakness [104, 109].

2.6 Role of Base Metal

The role of the base metal in the final properties of a brazed joint must also be considered. This is especially important in applications where there is a choice in component material, though this is often not the case. Variables such as composition, oxide layers, and surface preparation all have an effect on the performance of the brazing process.

The impact of filler metal composition on its ability to wet superalloy surfaces was briefly mentioned in Section 2.2, but the surface condition and chemistry of the base metal also impacts this. There is a general notion that smoother surfaces are preferred to allow for good wetting, which is beneficial for joint shear strength [6, 38]. Though, as Way *et al*. [38] point out, other studies have found that some roughness (up to a point) was noted to aid joint shear strength due to increased bonding area and infiltration paths of molten filler metal. Way *et al*. remark that, given the sparse investigative coverage of such a large number of base metal – filler metal combinations, it is hard to draw clear conclusions on this, and that the ideal surface condition likely differs from system to system [38]. Another major consideration is surface oxides of base metals such as Ni-based superalloys (as is discussed in [6]). In Ni-based filler metals, wetting and breakdown of surface oxides is aided by elements such as Si and Cr. However, the process is often aided in practice by direct mechanical removal, or partial removal, of oxide layers by simply grinding and polishing surfaces to be brazed prior to brazing.

Once brazing has occurred, the composition of the base metal can also impact the properties of the brazed region, depending on the extent to which base metal elements have made their way into the joint. Much of this, as discussed earlier, is achieved in the base metal dissolution stage of the process. A slower process for this is solid state diffusion either while still held at the brazing temperature after isothermal solidification is achieved, or during subsequent heat treatments. As shown by Pouranvari [104] and others [53, 90], this can have a significant impact on solid solution strengthening of the ISZ of a brazed joint.

2.7 Chapter Summary

This chapter has discussed the development of Ni-based superalloys and the filler metals used to braze them, as well as the underlying mechanisms in the brazing of Ni-based superalloys. This chapter has also detailed the role that elements have in the filler metal, and the mechanical properties that are achievable in brazed joints. Despite there being numerous Ni-based filler metals available commercially, their composition tends to be based around the inclusion of Cr to aid corrosion resistance and solid solution strengthening, and the inclusion of MPD elements which are almost universally one or more of B, Si and P. It has been discussed how, aside from lowering the melting and thus brazing temperature for such filler metals, these elements, through the phenomenon of diffusion, can greatly impact the properties of brazed joints. Their tendency to form brittle intermetallics, both inside the joint region (especially where insufficient diffusion has occurred) and in the base metal adjacent to the joint region, can be detrimental to the mechanical properties of joints, acting as crack propagation sites and even compromising the corrosion resistance in joints. Particularly in the case of the commonly used, and fast diffusing B, dissolution of the base metal can occur as it diffuses outwards from the joint during brazing, allowing elements found only in the base metal to act as solid solution strengthening elements in the isothermally solidified γ-FCC matrix of the final joint. Despite this positive effect, this effective widening of the joint can increase the time taken to achieve full isothermal solidification across the joint. As seen in the literature, the mechanical properties such as shear strength of a joint tend to correlate strongly with the degree to which isothermal solidification is completed, and so ensuring its completion is often of technological importance in the practical use of the method. This is achieved primarily through careful selection of filler metal, as well as brazing parameters such as temperature and hold time (not to mention initial joint width).

3. Developments in Ni-Based Brazing Alloys

While it is true that many of the current commercially available Ni-based filler metals have seen little alteration in recent times, there have been attempts in the literature to progress from these alloys, either in the physical form of the alloy or in its composition, to meet certain needs encountered in industry. Some needs have required the avoidance of certain elements, such as B in filler metals for the nuclear industry, or P when brazing steels. Other needs encountered have required new physical forms of filler metal (such as those discussed in Section 1.2). These have tended to be based around existing filler metal compositions, with additions or alterations that either way result in a final joint chemistry similar to that achievable with the conventional alloys. Another way in which Ni-based filler metals have seen development in research, however, is through compositional changes and the use of alternative MPDs to B, Si and P, for reasons of avoiding the detrimental effects their intermetallic compounds may have. Compositional changes such as these, despite having seen some attention in literature, have seemingly not made their way into industry as of yet. Here, the attempts at developing novel Ni-based filler metals in the literature are reviewed.

3.1 Alternative Melting Point Depressants

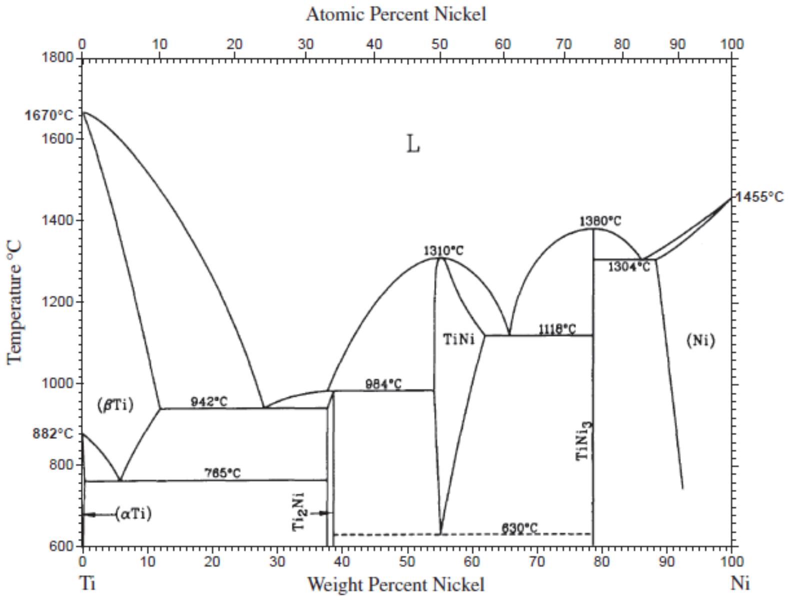

Figure 3.1: Ni-Ti binary phase diagram. From ASM Handbook [18], and based on [111].

Of particular interest for the work in this thesis, is compositional developments in the form of alternative MPDs to those used currently. As already discussed, the current fillers using elements B, Si or P have the downside of forming brittle intermetallic phases, and so any alloying additions that could take the role of these MPDs but without forming detrimental phases would be of enormous technological interest. At the same time, these elements require relatively little concentration in order to achieve a large drop in liquidus temperature. This means the vast majority of the alloy is Ni, thus largely matching the FCC matrix of the superalloy being joined. Therefore, when searching for alternative MPDs, it must be remembered that just lowering the liquidus could result in other microstructural features that would render the element unsuitable, especially in cases where comparatively large quantities are required to achieve the lower liquidus in the first place. As an example, consider the Ni-Ti binary phase diagram, shown in Fig. 3.1 (as found in [18], and based on [111]). Ti has a solubility limit of up to approximately 13 at. %, this Ti concentration would only depress the liquidus temperature to slightly above 1300^{o}C. At a composition of approximately 39 at. % Ti, a eutectic transformation occurs at 1118^{o}C, a much lower and more attractive melting temperature, but an undesirable NiTi + Ni$_3$Ti intermetallic microstructure would result.

Most studies investigating alternative MPDs have involved the addition of a single element to Ni, with this alloy then being used in a brazing trial. The Ni-Mn system (Fig. 3.2, as seen in [18] and based on [112]), having mutual FCC-solubility narrow melting range across the full compositional range, was suggested as a B replacement to achieve fast single-phase joint solidification by Laux *et al*. [113]. In this study, the binary Ni-Mn compositions contained significant Mn concentrations, of 36.7 wt.% and 58.4 wt.% (the azeotropic composition, that is, the point where liquid solidifies into a single phase solid of the same composition). Noting the high Mn content required, small Si additions were added to produce three further compositions with reduced Mn; Ni-20Mn-2Si; Ni-20Mn-3Si; and Ni-25M-2Si. The azeotropic composition had a measured liquidus of 1048^{o}C, the lowest of the alloys, whereas all other alloys had liquidus temperatures of 1150^{o}C (Ni-36.7Mn) or above. The joints in this study were wide (300 µm), yet epitaxial solidification was achieved relatively quickly with brazing times of 30 minutes (except for the azeotropic composition, demonstrating the need to limit the content of the MPD). This is suggested as a key advantage for wide-gap repairs when compared to commercial filler metals using B or Si, such as the D-15 alloy used in the study, as diffusion of Mn need not be rate-limiting on to achieve a single phase joint. However, as pointed out by the authors, further diffusion holds would not be expected to significantly increase the re-braze temperature as it would for B-containing fillers (though the high solidus temperatures of alloys other than the azeotropic composition means that the joints may already be suitable for high temperature applications).

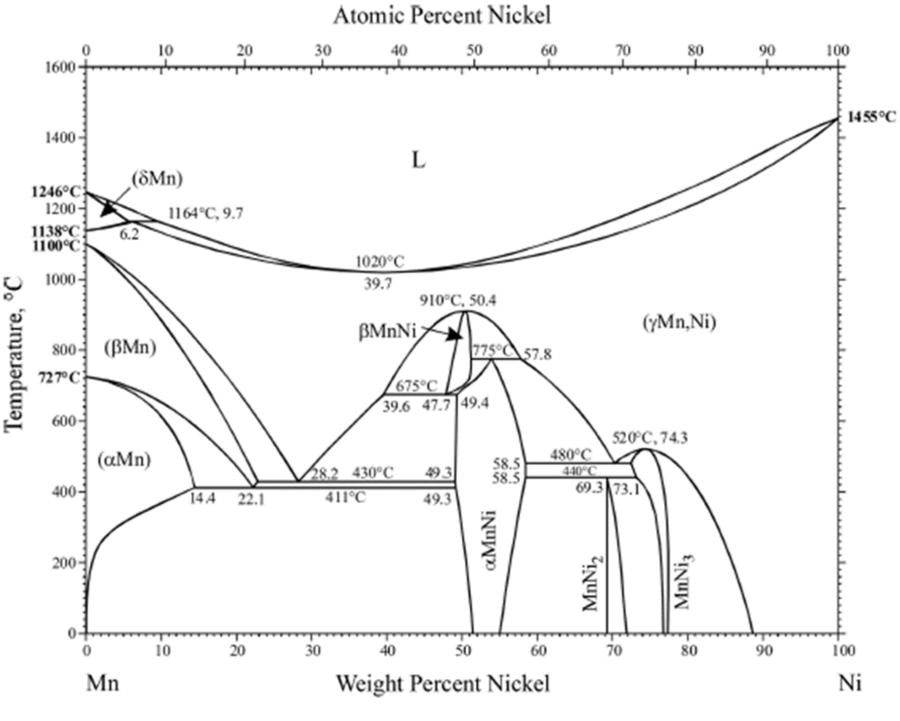

Figure 3.2: Ni-Mn binary phase diagram. From ASM Handbook [18], and based on [112].

The authors followed up with another study with a wider range of Ni-Mn binary alloys and Ni-Mn-Si ternary alloys, along with CALPHAD modelling of the liquidus projection (reproduced in Fig. 3.3) and modelling of the joints using Thermo-Calc DICTRA simulations [114]. As in the first study, the more promising final joint microstructures were obtained for the moderate Mn content (Ni-38.2Mn in at.%) and moderate Mn plus low Si content (Ni-20.6Mn-4Si, Ni-20.4Mn-6Si, Ni-25.7Mn-4Si in at.%) alloys, with wide-gap epitaxial solidification achieved. A eutectic composition of Ni-60Mn in at.% possessed the lowest liquidus of 1022^{o}C, but this was deemed too low to be of interest for the proposed application.

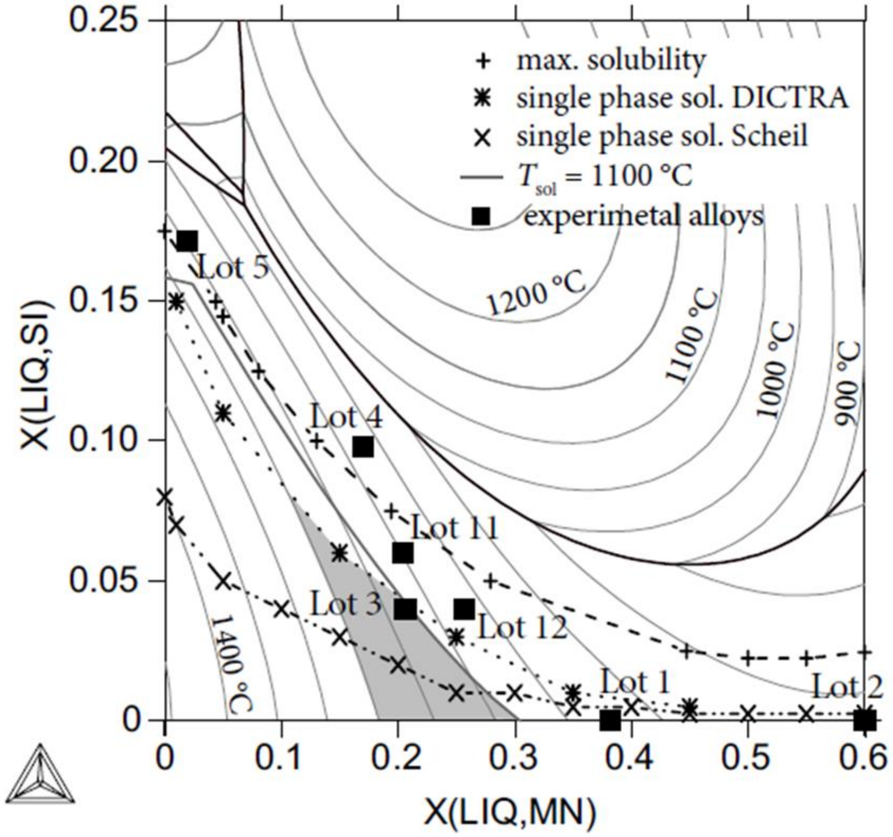

Figure 3.3: Ni-Mn-Si CALPHAD predicted liquidus projection, with Ni composition as balance. From [114].

Ge was investigated by Dinkel *et al*. [115] as a prospective sole MPD element replacing B and Si for the braze repair of single-crystal turbine components. In this study, the aim was to not only identify a suitable MPD, but too also promote beneficial microstructural features such as a γ' phase, exhibited in the Ni-Ge system for Ge concentrations between 27.1-29.9 wt. % (the Ni-Ge binary phase diagram is reproduced in Fig. 3.4 [18]). Alloys of Ni-20Ge and Ni-23Ge (in wt. %) were produced, both exhibiting dual γ-γ' microstructures, and used in the braze repair of 200 µm wide slits in 1st generation René-N5 and 2nd generation PWA-1483 respectively. Despite these moderately high concentrations of the MPD Ge, however, the liquidus temperatures of the alloys according to the Ni-Ge phase diagram meant that brazing temperatures investigated in this study were rather high at between 1160^{o}C and 1230^{o}C (indeed, 1160^{o}C was not adequate for sufficient melting of the NI-20Ge alloy). Furthermore, the hold times investigated ranged from 30 minutes to 48 hours, with the full 48 hours (at 1160^{o}C) being the only hold time achieving complete isothermal grain growth for the PWA-1483/Ni-23Ge sample, and 24 hours and 48 hours required for the René-N5/Ni-20Ge sample. In both cases this is substantially longer than required for B-containing fillers. At higher brazing temperatures, complete isothermal solidification was not completed even after 48 hours, attributed to excessive melt-back of the base metal in the case of the higher brazing temperatures, which effectively widened the initial gap. Nonetheless, promising mechanical results were achieved, with the René-N5/Ni-20Ge joint achieving 92% the strength of a reference René-N5 sample, and 97% reference-strength achieved for the PWA-1483/Ni-23Ge sample.

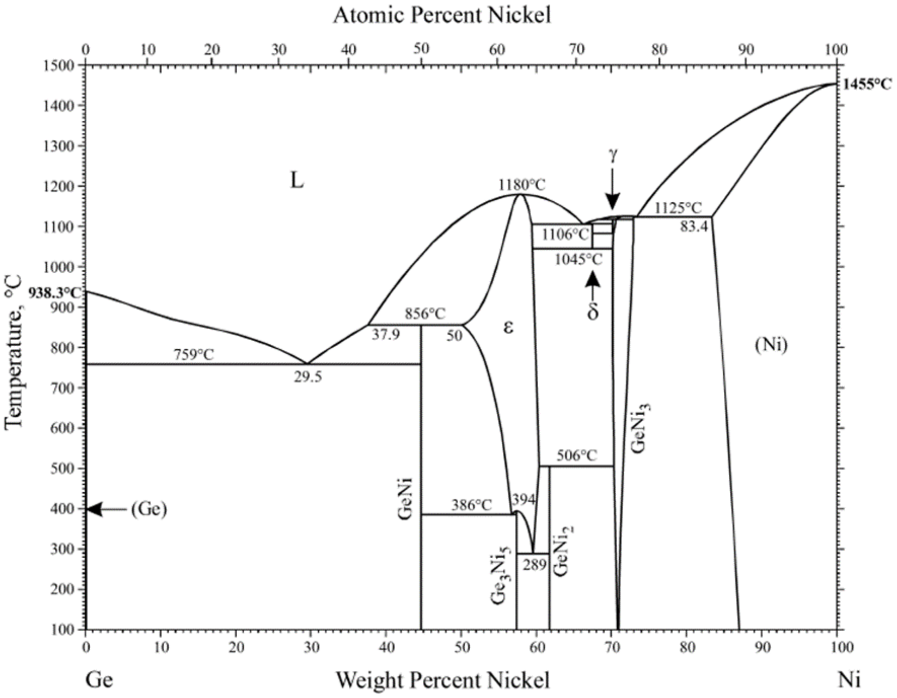

Figure 3.4: Ni-Ge binary phase diagram. From ASM Handbook [18].

There has been a reasonably high amount of attention paid to the use of Hf as a replacement MPD element as demonstrated by numerous studies, either as the sole MPD or in combination with other elements common in Ni-based superalloys. The Ni-Hf binary phase diagram (as seen in [18], and based on [116], reproduced in Fig. 3.5) exhibits a eutectic point at 1190°C and approximately 29 wt. % Hf, but at the same time Hf has apparently little solubility in Ni, approximately 3.5 wt.% at 1190°C. Hence most studies using Hf as an MPD observe Ni-Hf intermetallic phases, particularly the Ni$_5$Hf structure. Zheng and Ruan [117] produced a Ni-18.6Co-4.5Cr-4.7W-25.6Hf (wt. %) alloy for the brazing of K3 superalloy (Hf-containing), at 1220°C for 25 minutes. The Ni$_5$Hf intermetallic phase was observed, though further heat treatment was used to reduce this through allowing Hf diffusion into the base metal. It has been pointed out, however, that the Ni$_5$Hf intermetallic is substantially more ductile than for example Ni-boride phases. Lugscheider and Humm [118] suggested a Ni$_5$Hf microhardness of 400 $HV_{0.05}$, versus 2000-2600 HV0.05 for boride phases. In evaluating a series of Ni-Cr-Hf alloys as potential filler metals for joining stainless steels and Ni-base superalloys, the authors recorded good corrosion resistance, and a maximum joint tensile strength when brazing both 304 stainless steel and Inconel-600 with Ni-15Hf-13Cr (in wt. %) of 587 MPa and 517 MPa respectively. However, in both cases the brazing temperature used was rather high by necessity, at 1235°C, significantly higher than required for, for example, AWS BNi-2 (generally up to approximately 1100°C), and still much higher than for other high Cr filler metals such as AWS BNi-5 (based on Ni-Cr-Si, brazed generally between 1150°C – 1200°C).

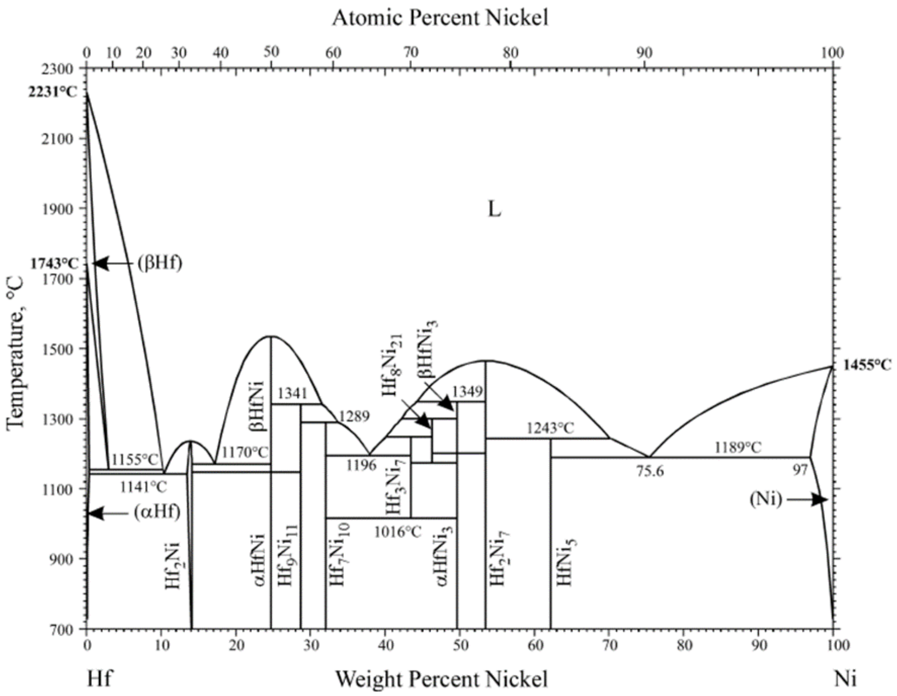

Figure 3.5: Ni-Hf binary phase diagram. From ASM Handbook [18], and based on [116].

This supposed greater ductility afforded by Ni-Hf intermetallics also made its use in brazing repair of turbine blades and vanes attractive, as repairs using B-containing filler metals reported by Miglietti *et al*. [119] only achieved 25-51% the ductility of the base material being repaired (despite apparently equivalent yield strengths). In addition, the use of Hf with another d-block transition metal, Zr, has been investigated, and at least two patents exist for the use of such [120, 121]. The first such focuses on a repair process that uses Hf, Zr, both or (less preferably) both in combination with other MPDs such as B. The second patent more clearly specifies a compositional range of a Ni-Cr-Co-Hf-Zr filler metal with solidus temperature of 1175ºC (or 1120ºC with composition refinement and the addition of Ti and Al). Hypereutectic Ni-Cr-Hf and Ni-Cr-Zr alloys were used in the braze repair of Inconel-738 by Miglietti and Du Toit [122, 123], as well as tensile testing of MarM247 brazed joints. Intermetallic phases including Ni_5Hf, Ni_7Hf_2 and Ni_5Zr were reported as having microhardness in the range 250-400 HV, in comparison to 800-1000 HV for Cr-boride phases. Tensile results at all temperatures from room to 980ºC for joints brazed at 1238ºC were greatest for the Ni-Cr-Zr joints, achieving 52-62% MarM247 strength for 40 minutes hold time, and 55-70 % for 4 hours hold time.

In cases where current MPD elements are used in conjunction with a novel MPD, there has been some preference shown for replacing the B content and retaining Si as an MPD, likely due to the greater tendency of borides to form and their high brittleness. However, as B is a stronger MPD in most systems in terms of liquidus depression, generally a corresponding increase in Si content is required so that the brazing temperature required is still sufficiently low. Nb was considered in the development of a B-free filler metal for brazing of heat-resistant steels used in liquid rocket engine nozzles by Ivannikov *et al*. [124]. A Ni-8Si-5Nb filler metal in the form of a 50 µm thickness melt-spun foil with a narrow melting range of 1103ºC – 1120ºC was trialled, achieving a tensile strength of 450 ± 30 MPa when a brazing temperature of 1150ºC was applied for 30 minutes.

Be was also considered as a novel MPD element in combination with Si rather than as a sole addition [125]. In this study, a range of alloys with varying Be and Si content around the predicted ternary eutectic, ranging from 2 – 5 wt. % and 4 – 8 wt. % respectively, were produced. Again in this study, it was found that a compromise must be struck between alloy melting temperature and brittleness, especially when in the melt-spun ribbon form which may affect its practical application. The alloys Ni-5Si-3Be and Ni-6Si-5Be were selected for brazing trials with a 12Cr21Ni5Ti steel. For a brazing temperature of 1150^{o}C and 40-minute hold time, tensile testing resulted in failure in the steel in the case of the Ni-6Si-5Be, the more brittle but lower melting temperature of the foils. Meanwhile, a tensile strength of 530 ± 50 MPa was achieved by the Ni-5Si-3Be alloy, greater than the 420 ± 30 MPa achieved by a commercially-available B-containing filler (STEMET 1301-A, Ni-3.5Fe-7.5Cr-4.5Si-2.6B). Ni with 2 wt. % Be addition was also considered in a computational study as a potential replacement of standard Be for joining of Zircaloy-4 used in components in CANDU heavy water nuclear reactors [126]. As pointed out in both studies however, Be and its oxides pose a significant health hazard.

A summary of some currently used, and prospective novel MPD elements discussed above, is shown in Table 3.1 for comparison.

Table 3.1: Summary of liquidus temperatures reported for various elements employed as MPD in Ni-based brazing alloys.

Source	MPD element(s)	Concentration (at. %)	Liquidus achieved (^{o}C)	Eutectic phase formed
[19]	B	17 (eutectic)	~ 1095	Ni_3B
[19]	Si	21 (eutectic)	1143	Ni_3Si
[20]	P	17 (eutectic)	891	Ni_3P
[113]	Mn	32 / 60	1150 / 1048	-
[115]	Ge	16.7 / 19.4	1271 / 1230	Ni_3Ge
[116]	Hf	11.8 (eutectic)	1190	Ni_5Hf
[124]	Nb + Si	3 + 15.6	1120	-
[125]	Be + Si	24.3 + 9.3	~ 915	-
[126]	Be	23.8 (eutectic)	1150	NiBe

3.2 Alternative Melting Point Depressants from Other Systems

As seen above, only a limited amount of alternative MPDs for use in Ni-based filler metals have been investigated. It may, however be beneficial to consider developments in non-Ni-based filler metals, especially those that still contain Ni or are used at similar temperatures, for example precious metal-based (or precious metal–containing) filler metals. These alloys tend to be based on Au or Pd, with usually significant Cu, Ag or Ni additions, or a combination thereof (and indeed many Pd-bearing alloys contain a majority of Ag or Cu), with the mutual FCC solubilities allowing ductile brazed joints. Others may be Ni-based, with Au or Pd additions to a conventional Ni-Cr-Si-B composition, in weight percentages in broadly in the 20 - 36 wt. % range. Lugscheider and Pelster [127] attempted to reduce the precious metal content (for economic purposes) of Ni-based filler metals Pd-36 (Ni-36.8Pd-11Cr-2.2Si-2.4B wt. %), Pd-36M (Ni-36Pd-10Cr-1Si-3B wt. %) and Au-6 (Ni-20.5Au-5.3Cr-3.4Si-2.3Fe-2.3B wt.%), possessing melting ranges of 818 – 992°C, 825 – 955°C and 943 – 960°C respectively. This was achieved with an increase in Si content, resulting in a marked decrease in precious metal content required to achieve similar results in brazing trials for two of the developed compositions (Ni-19.6Pd-8.8Cr-6.9Si-2.5B and Ni-10.7Au-5.8Cr-5.3Si-3.2Fe-2.8B). Furthermore, a reduction in both melting range and melting temperature was achieved for both of these compositions. The Ni-19.6Pd-8.8Cr-6.9Si-2.5B composition in particular displayed no brittle phases in the joint after brazing at 1000°C for 60 minutes. These appear to be rather promising results for such a low brazing temperature, and Au or Pd used as a primary MPD along with typical Si and B contents can produce ductile joints at low brazing temperatures. If the liquidus requirements are relaxed somewhat up to approximately 1050°C, further reductions in precious metal content and/or B and Si content while still allowing sub-1100°C brazing temperatures could be possible. However, it seems likely that with even such reductions in precious metal content, the raw cost of these elements means their wide use is still limited.

3.3 Other Compositional Developments

Some attempts at developing novel Ni-based filler metal compositions have focused on aims other than replacing current MPDs, instead attempting to enhance other properties of the filler metal. For example, Cu additions of 1 to 3 wt. % were added to a Ni-10Cr-3Fe-4.5Si-2.5B alloy by Zhang *et al.* [128], who reported greater solid solution volume fraction, and decreased intermetallics as Cu was increased. Isothermal solidification was possible for gap sizes up to 70 µm for this alloy, compared to 30 µm for a commercial BNi-1a filler metal, for a brazing temperature of 1120°C and a 15-minute hold time. The computer-aided design of a Ni-3Cr-4B-0.5Ce (wt. %) alloy was demonstrated by Nishimoto *et al.* [129], with the aim of using an active element, cerium, and increasing wettability on high-Al base metals, reducing the occurrence of micro-voids and increasing the creep rupture strength of the joint to comparable to the base metal. Another attempt at improving wetting on otherwise difficult-to-wet base metals was presented by Sandin [40], simply with additions of 2 – 6 wt. % of Ti to conventional Ni-based filler metals BNi-2 and BNi-5. Ceramics such as alumina and yttria-stabilised zirconia were successfully joined with various materials such as oxide-strengthened alloys, high Cr, Al and Ti alloys, and Ni-based superalloys, at temperatures higher than might be suitable for conventional precious metal fillers that would typically be used.

High Fe and Cr, and reduced Ni filler metals were developed by Shi *et al*. [130] with the motivation of reduced cost, using Si and P as MPDs. However, corrosion resistance was compromised in comparison to a Ni-29Cr-6P-4Si filler metal. High Cr compositions have also been developed for enhanced corrosion resistance in hostile applications, particularly for brazing repair of nuclear reactor components for which filler metals require approximately 30 wt. % Cr [131]. Ta additions to such alloys in small wt. % were found to be beneficial for solidification cracking resistance when used in the weld repair of nuclear reactor component materials [131]. High Cr content was also utilised by Persson and Bornegård [132], along with Mo, to develop a filler metal resistant to corrosion from coolant used in a plate heat exchanger, for which commercial options did not possess a suitable melting range. The Ni-29Cr-8Mo-XFe-YSi filler developed showed shear strengths and corrosion resistance equal to or exceeding those of filler metals BNi-5 and Ni613.

3.4 Chapter Summary

This section has reviewed the current literature on investigating novel MPD elements for use in new Ni-based brazing filler metals, used either as a complete replacement for current elements, or used in tandem with them. It can be seen that, generally, large concentrations of the prospective new MPD element are required to adequately suppress the liquidus, as is the case for Mn for example. Others, such as Hf, may still produce intermetallic phases but if these are of sufficient ductility, this can still represent an improvement compared to the more brittle boride and silicide phases. In the case of Ge, a γ′-like Ni_3Ge phase forms, taken advantage of by Dinkel *et al*. [115] to improve the mechanical properties of the joint, as well as supressing the liquidus temperature.

There are other elements that would be expected to exhibit some MPD effect according to their binary phase diagrams with Ni, that haven't been explored (or at least reported). Notably, there has also been little in the way of combining two or more novel MPD elements to further supress the liquidus temperature. This could be perhaps due to focus on specific applications where a low brazing temperature is not required, or due to the fact that this may require access to binary and ternary phase diagrams that might be unavailable or altogether unreported. Clearly though, there is much that could still be explored in terms of searching for novel MPD elements, or combinations thereof.

Some prospective basic requirements of any developed filler metals may be suggested from the discussion presented in this chapter. Firstly, it should be considered necessary for a novel MPD element to suppress the liquidus temperature to at least approximately 1200^{o}C, in order to enable brazing to be carried out comfortably below the solidus temperature of most Ni-based superalloys (and indeed, within the capability of many industrial vacuum furnaces). Furthermore, considering current commercial alloys, the upper limit of concetration of any novel MPD could be considered 25 wt. % where possible, so as to ideally allow solidification of an FCC ISZ during brazing, and reducing the propensity for brittle intermetallic phases post-braze. To further aid this, any novel MPD should exhibit ideally increased solubilty in Ni, certainly as compared to elements such as B and P. As seen later in this work, these requirements are considered further.

4. High Entropy Alloys, Multi-Principal Element Alloys, and Brazing Applications

The concept of alloying has existed for millennia, and has allowed the development of huge numbers of materials whose properties are superior to those of their base elements. Throughout this time, alloying has generally meant the small additions of one element to another element with otherwise attractive properties acting as a base, most notably the control of carbon impurities in Fe to produce steel. As discussed in Chapter 2, the development of Ni-based superalloys in the 20th century demonstrated the furthering of this concept to the point where ten or more alloying elements may be used, and some in concentrations of over 20 wt. %. Limitations of these alloys however have driven the search for materials that can operate at yet higher temperatures for future energy production and more efficient propulsion systems. High Entropy Alloys (HEAs), a relatively new class of alloys along with the broader idea of Multi-Principle Elements Alloys (MPEAs), have been touted as potentially meeting these needs. This section specifically will discuss the potential for their application to brazing. Firstly, a brief summary of their definition and background is necessary, before looking at the principles of the design and development of these alloys. Finally, this will be brought together by looking at how these concepts could be of benefit when applied to alloy development of novel brazing filler metals.

4.1 Background to High Entropy Alloys

HEAs were first reported by two separate authors in 2004 (although work on alloys of this kind existed prior to this, the definitions, as are broadly used today, were first introduced then). Yeh *et al*. [133] first defined high entropy alloys as containing five or more elements in roughly equiatomic ratios and between 5 – 35 at. % generally. In this work, Yeh *et al*. reported the solid solution formation for various HEAs. For example, the $CuCoNiCrAl_XFe$ system exhibited a single FCC phase for $0 < X < 5$, transforming to dual-BCC and eventually single BCC solid solution as X exceeds 2.8. Even for a ten-element equimolar CuCoNiCrAlFeMoTiVZr, a simple as-cast microstructure was observed, with three solid solution phases.

Meanwhile, Cantor *et al*. [134], first demonstrated the fabrication of an alloy consisting of 5 at. % of 20 different elements (Mn, Cr, Fe, Co, Ni, Cu, Ag, W, Mo, Nb, Al, Cd, Sn, Pb, Bi, Zn, Ge, Si, Sb and Mg). The aim of this was to determine which of these elements would form simple non-intermetallic phases together. This resulted in one of the more widely established HEA systems, commonly known as Cantor's alloy, consisting of transition metals Co, Cr, Fe, Mn and Ni. The 20 element alloy was found to be formed predominantly of a single FCC phase, rich in these five elements, and with substantial concentrations of solution elements. Using equimolar CrMnFeNiCo as a basis, alloys from six to nine components were investigated by additions of Nb, Ti, V, Cu and Ge. The primary FCC phase was observed to dissolve significant Nb, Ti and V quantities, whereas Cu and Ge were segregated. Cantor *et al*. concluded that the number of phases formed in these alloys was always well below that predicted by the Gibbs phase rule, given in Equation 4.1:

$$F = C - P + 2 \quad (4.1)$$

where F is the degrees of freedom (that is, independently variable parameters such as temperature, pressure and composition required to completely describe the equilibrium state of the system), C is the number of components, and P is the number of phases.

These studies, amongst others, generated significant interest in the search for similar groups of elements that, when combined in equiatomic amounts (thus maximising the configurational entropy), would promote the formation of similarly simple single phase FCC or BCC microstructures, rather than several complex intermetallic phases. The purported benefits of this discovery was that these alloys would benefit from the contribution of solid solution strengthening and high degree of lattice distortion, yet retaining sufficient ductility. This ‘lattice distortion effect’ is one of the widely used four core effects of HEAs (detailed by Murty *et al*. [135] and also discussed at length by Miracle & Senkov [136]), the other three being; the high entropy effect (proposes that high configurational entropy may encourage solid solution formation rather than intermetallic compounds); the sluggish diffusion effect (proposes that diffusion in HEAs is much slower than in conventional alloys; and the ‘cocktail’ effect (less a physical phenomena, and more (as pointed out in [136]) a decription of the unusual and unpredictable properties arising from the combination of individual component elements in HEAs). There is some dispute as to whether these effects are universal, or are reproducible, for example the purported sluggish diffusion has been questioned by Pickering and Jones [137]. However, the effect of solid solution strengthening in a highly distorted lattice, purportedly higher than in conventional alloys and arising from the different sized atoms and characterised by the δr parameter (see next section), as illustrated in Fig. 4.1, is likely to be of importance. More needs to be done to quantify this, however, and to distinguish such effects from other causes [136].

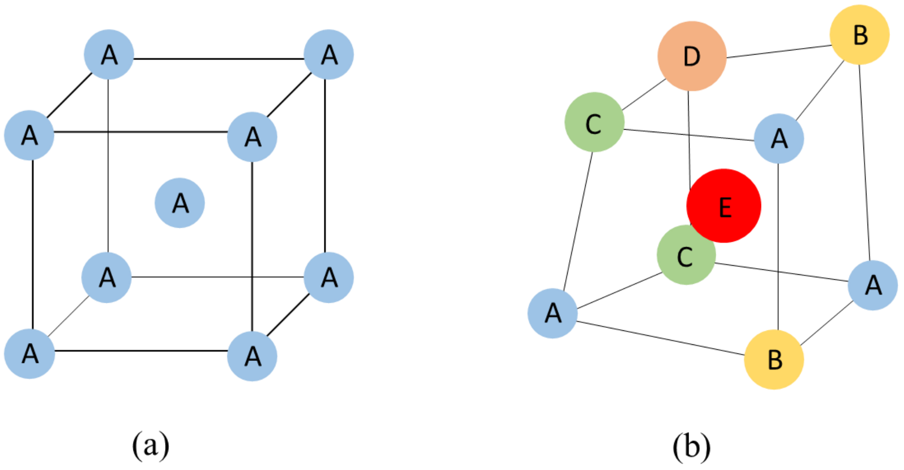

Figure 4.1: Illustration of (a) single component BCC unit cell, as compared to (b) distorted lattice as a result of varying atomic sizes of components.

4.2 Empirical Thermodynamic Parameters for HEAs

As the interest and study of HEAs developed, so did the importance of their design. As more data on many various fabricated and characterised HEAs has been catalogued from the literature, trends between composition and microstructure could be discerned and used to predict various properties of yet more novel HEA compositions, as attempted by various authors including [136, 138 - 140].

There are several empirical thermodynamic parameters that have been used to describe some fundamental properties of HEAs, and these have emerged as useful tools for the prediction and design of HEAs. Some of these are based on the Hume-Rothery rules for solid solution formation [141], which suggests that solid solution formation is favoured when elements possess similar atomic size, crystal structure, electronegativity and valence electron concentration (VEC). The atomic size mismatch is one such factor considered in the design of HEAs, and a parameter δ describes the average atomic size mismatch in an n-element system (Equation 4.2):

$$\delta = \sqrt{\sum_{i=1}^{n} c_i \, (1 - \frac{r_i}{\bar{r}})^2} \qquad (4.2)$$

where $\bar{r}$ is the average atomic radii of all elements in the system, r_i is the atomic radius of the i^{th} element, and c_i is the atomic concentration of the i^{th} element. According to the Hume-Rothery rules for conventional alloys, the difference in atomic size between solute and solvent should be less than 15% [141, 142], and so systems with small δ are predicted to favour solid solution microstructures.

The Pauling electronegativity difference, ΔχP, which describes an atoms tendency to attract a shared pair of electrons, has been considered to address the second Hume-Rothery rule. It is given by Equation 4.3:

$$\Delta\chi P = \sqrt{\sum_{i=1}^{N} c_i (\chi P_i - \overline{\chi P})^2} \qquad (4.3)$$

where χP_i is the Pauling electronegativity of the i^{th} element and $\overline{\chi P}$ is the average Pauling electronegativity of all components. According to the Hume-Rothery rules, ΔχP should be minimised between all components in order to promote solid solution. The VEC has also been considered an important parameter in predicting the stability of solid solutions, with a particular crystal structure, or intermetallics. The average VEC of all components in a system is thought to indicate the crystal structure of the formed solid solution (this is discussed in greater detail below). This parameter is given by Equation 4.4:

$$VEC = \sum_{i=1}^{n} c_i VEC_i \quad (4.4)$$

Other approaches to the prediction of stable phases in HEAs use thermodynamic parameters, namely the average enthalpy of mixing of binary pairs (ΔH_{mix}) and the entropy of mixing (ΔS_{mix}). ΔH_{mix} represents the compatibility of elements in forming solid solutions. A perfect solid solution has $\Delta H_{mix} = 0$, whereas a negative value indicates tendency to form intermetallic compounds, and a positive value indicates tendency to segregate. The ΔH_{mix} is given by Equation 4.5:

$$\Delta H_{mix} = \sum_{i=1}^{n} \sum_{j>i}^{n} \Omega_{ij} c_i c_j = \sum_{i=1}^{n} \sum_{j>i}^{n} 4 H_{mix}^{ij} c_i c_j \qquad (4.5)$$

where H_{mix}^{ij} is the mixing enthalpy of the ij binary pair, and c_i and c_j are the atomic concentrations of elements i and j respectively. ΔS_{mix} represents the configurational entropy - or the degree to which atoms in a lattice arrange themselves randomly - which is maximum for equiatomic systems, and is given by Equation 4.6:

$$\Delta S_{mix} = -R\sum_{i=1}^{N} c_i Ln(c_i) \quad (4.6)$$

where R is the gas constant. Both parameters are related by the Gibbs free-energy of mixing equation (Equation 4.7):

$$\Delta G_{mix} = \Delta H_{mix} - T\Delta S_{mix} \quad (4.7)$$

No single parameter for a given HEA system gives a complete picture of the resulting microstructure. Rather, general correlations between parameters and observed microstructures are used for predictive purposes. Guo & Liu [139] suggested that δ is the critical factor determining the formation of solid solution or bulk metallic glasses (BMGs). The widely studied equiatomic CoCrFeMnNi alloy exhibits a single-phase FCC microstructure, and has a calculated δ of just 1.18 % [143], and additions of Al up to a molar ratio of 0.2, and Al and Cu up to molar ratios of 0.3 each retained this, while increasing δ to 2.77 % and 3.65 % respectively [143]. Recently, Kube *et al.* [144] analysed some 2478 quinary as-sputtered HEAs, noting a preference for BCC formation over FCC at higher atomic size differences which was attributed to the BCC lattice being able to accommodate greater atomic size differences with less strain energy increase. However, it is noted that this preference is likely only realised for the extremely fast cooling rates experienced by the sputtering technique, and may not be observed under more equilibrium conditions [144]. Zhang *et al.* [145] plotted δ against ΔH_{mix} for reported HEAs, defining zones where only solid solutions, or solid solutions plus second phases, form. Simple solid solution HEAs had ΔH_{mix} close to zero (approximately in the range $-15 \leq \Delta H_{mix} \leq 5$ kJ mol^{-1}) and small δ (approximately in the range $0.5 \leq \delta \leq 6$) in comparison to BMGs (it should be noted that in this study, and many others, δ is multiplied by 100 to express as a percentage). However, while obeying such rules may be necessary for solid solution formation, it may not always be sufficient [146]. This can easily be seen when considering cases where a binary pair in a prospective alloy may have $\Delta H_{mix} << 0$ (favouring ordering), while another pair has $\Delta H_{mix} >> 1$ (favouring segregation). The two may largely cancel each other out in the expression for calculating ΔH_{mix}, and so give rise to an overall value close to zero, indicating solid solution formation may not form despite a ΔH_{mix} that suggests it would. But despite this close to zero value, extreme values of ΔH_{mix} between specific pairs is likely to mean that a single solid solution microstructure would not be attained with that combination of elements.

As can be seen from Equation 4.6, maximising ΔS_{mix} minimises the Gibbs free energy for a given temperature. ΔS_{mix} increases with the number of elements, and is maximised for a given number of elements when they are present in equiatomic ratios. Thus, in this way the early HEA research introduced the idea that equiatomic solid solutions may be thermodynamically favoured over intermetallics by minimising the Gibbs free energy due to the entropy contribution. Adding a third axis for ΔS_{mix}, Zhang *et al.* [145] reported solid solution forming HEAs possessed higher ΔS_{mix} values than reported BMGs, in the range 12 – 17.5 J K^{-1} mol^{-1}. Zhang & Fu [147] created a similar plot for various transition metal and Al containing HEAs, proposing rules for single solid solution formation of $\Delta S_{mix} \leq 13.38$ J K^{-1} mol^{-1}, $-10 \leq \Delta H_{mix} \leq 5$ kJ mol^{-1} and $\delta \leq 4$. However, the value of ΔS_{mix} here represents the theoretical maximum configurational entropy with perfect mixing i.e. no short-range ordering, which in reality is most often not the case. As has been discussed, when considering ΔH_{mix} of a binary pair, ordered intermetallic phases may form even for a 1:1 ratio of the elements, representing maximum ΔS_{mix} for the composition, but with ordered formation in the lattice rather than random distribution. Therefore, the use of just ΔS_{mix} in HEA design is not common beyond keeping compositions close to equiatomic and within the range proposed by Yeh *et al.* [133].

The Pauling electronegativity, χP, of elements in an alloy is another Hume-Rothery requirement for solid solution formation, and so it has been considered that this may be of similar relevance in HEAs. Guo & Liu [139], however, found little correlation between $\Delta\chi P$ (Equation 4.3) and tendency for solid solution formation across a wide array of reported HEAs. There are alternative electronegativity values defined since Pauling, for instance the Allen electronegativity, $\Delta\chi A$ (relates electronegativity to the average s and p valence shell electrons). Poletti and Battezzati [138] plotted $\Delta\chi A$ against δ and observing that for $1 < \delta < 6$ %, and $3 < \Delta\chi A < 6$, only solid solutions (BCC, FCC and both) were formed for a large catalogue of reported HEAs. Leong *et al*. [148] also discussed alternative electronegativity scales plotted against ΔH_{mix}, concluding that while $\Delta\chi A$ was better in distinguishing microstructures of HEAs compared to $\Delta\chi P$, a third scale, the Mulliken electronegativity, $\Delta\chi M$ (often termed an absolute scale, derived from the ionisation energy and electron affinity) was potentially better than both. Nevertheless, the incomplete datasets on HEAs (and possible bias towards reporting elements that do alloy) renders a clear answer to such questions difficult to obtain [148].

The average VEC has received substantial attention for being a predictor of the structure of HEA solid solutions, with the solid solution crystal structure (BCC, FCC or both) being distinguished by different average VECs. This tends to be separated from parameters like ΔH_{mix} that indicate whether solid solution will form or not in the first place. For example, Guo *et al*. [149] conducted analysis on a number of $Al_xCrCuFeNi$ and $Al_xCoCrCuFeNi$ HEAs, suggesting that while ΔH_{mix} was the important parameter for predicting solid solution or intermetallic formation, VEC was useful for distinguishing between BCC ($VEC \leq 6.7$), FCC ($VEC \geq 8$), or mixed ($6.7 \leq VEC \leq 8$) microstructures. Through this concept, VEC has been used to optimise compositions of HEAs where σ-phase formers are present in order to avoid or reduce its formation. Tsai *et al*. [150] proposed a σ-prone VEC range of 6.88 to 7.84 for Cr- and V-containing HEAs (for the set of elements Al, Co, Cr, Cu, Fe, Mn, Ni, Ti and V), meanwhile noting the overlap with the dual BCC+FCC VEC range of Guo *et al*. [149]. Similarly, Fang *et al*. [151] observed a transition to grain boundary σ formation when VEC increased from 7.9 to 8.0 due to Cr enrichment at the expense of Fe in CoCrFeNi alloys. Recently Yang *et al*. [152] conducted a high throughput CALPHAD investigation of the VEC criteria in the AlCoCrFeNi system, finding that over 90% of compositions were BCC for $5.7 \leq VEC \leq 7.2$, and 100% were FCC for $VEC \geq 8.4$. The limitations of such VEC criteria, however, are that they lose validity over a large number of elements and possible systems, and so are most useful for a specific set of elements such as in the studies described above. Put another way, the VEC criteria for BCC or FCC formation for one alloy system may not be the same for another alloy system. Even within a set of elements, the VEC criterion alone is not completely accurate as the alloy density and temperature can play a role in determining BCC or FCC formation, as shown by Yang *et al*. [152]. Nonetheless, most studies demonstrate that higher VECs increase the propensity for FCC formation over BCC formation.

It is also worth noting that for some HEAs, the criteria may only be relevant for the as-cast state in which they have been studied. Rapid cooling during fabrication may supress formation of lower temperature equilibrium phases precipitating from an otherwise simple solid solution phase, which have sometimes only been realised after further processing, heat treatment or alternative fabrication techniques. This has been pointed out by Pickering and Jones [137] for the CoCrFeMnNi HEA, which has been found to exhibit precipitation of σ-phase after exposure below 800°C [153]. Phase stability may also be impacted by irradiation [154, 155]. In all, the above correlations and criteria have limitations but can be useful tools for optimising compositions towards solid solution formation over intermetallic or glass formation (by looking at δ and ΔH_{mix}), and then for a limited system optimising for greater tendency for BCC or FCC formation as desired (by looking at VEC).

4.3 Multi-Principal Element Alloys

As well as the compositional definition put forward by Yeh *et al*. [133], other early definitions of HEAs were based on the calculated ΔS_{mix} value, arising from the ratios of element concentration in a system. From this idea, an alloy might be termed 'low' entropy ($\Delta S_{mix} < 0.69$ R) or 'medium' entropy ($0.69 < \Delta S_{mix} < 1.61$), with only those with $\Delta S_{mix} > 1.61$ technically termed as 'high' entropy [136]. This definition, however, would categorise even an equiatomic quaternary alloy possessing a single solid solution phase microstructure as a medium entropy alloy (MEA), as it would for many non-equiatomic quinary alloys. These rather restrictive definitions have over time broadened, such that alloys with only three or four elements, or HEAs with small dopant additions (< 5 at. %) may be considered as HEAs, or MEAs, or more generally multi-principal element alloys (MPEAs). The importance is on the resulting simple microstructures containing one (or more) solid solution phase, with no (or at least only those deliberately introduced for mechanical purposes) intermetallic phases while using multiple main alloying elements, rather than on the strict adherence to maximum configurational entropy that might result in a less favourable microstructure.

As it has been noted in, a single FCC phase microstructure may be insufficiently strong, while a single BCC phase may be insufficiently ductile [156-158]. Therefore, numerous attempts to address such trade-offs by encouraging dual-phase microstructures or additional strengthening phases have been made. In some instances, these attempts have been realised by moving compositions of HEA systems (either novel or previously studied) away from traditional equiatomic compositions. For example, Li *et al*. [159] demonstrated a strategy to create transformation-induced plasticity assisted, dual phase HEAs (TRIP-DP HEAs) by shifting from equiatomic CoCrFeMnNi to a $Co_{10}Cr_{10}Fe_{80-X}Mn_X$ (at. %) system. For X = 30, a TRIP-DP HEA was achieved, whereby a partial martensitic transformation from single phase FCC to FCC + HCP was observed. Compared to single phase FCC $Co_{10}Cr_{10}Fe_{80-X}Mn_X$ (observed for X = 40 and 45), the TRIP-DP HEA substantially outperformed it mechanically both before and after grain refinement. Li *et al*. [160] also furthered this strategy to demonstrate a quinary TRIP-DP HEA, $Co_{20}Cr_{20}Fe_{40-X}Mn_{20}Ni_X$ (at. %, $0 \leq X \leq 20$), which exhibited greater UTS and strain hardenability than the equiatomic composition for X = 6. Some equiatomic HEAs may possess dual-phases, such as the equiatomic composition of the widely studied AlCoCrFeNi system, possessing both ordered B2 (primitive cubic CsCl structure) and disordered A2 (BCC) solid solutions, which Lim *et al*. [161] observed as having favourable specific yield strength at intermediate temperatures compared to Ti alloy IMI834. However, a long-term transformation to FCC + σ above 500°C resulted in a notable drop in performance. In addition, Ghassemali *et al*. [162] heat-treated equiatomic AlCoCrFeNi resulting in a transition to BCC + FCC solid solutions. Studying the effect of crack propagation, the distribution of FCC precipitates acted as obstacles to propagation, either stopping cracks or redirecting them.

Eutectic HEAs and MPEAs further this idea by attempting to achieve a dual solid solution microstructure, commonly a stronger, less deformable BCC solid solution or B2 phase and a softer, more deformable FCC phase, where fine lamellae of the two phases provide balanced mechanical properties. With pearlitic steels, high temperature yield strengths can increase with decreasing lamellar spacing, λ, proportional to $\lambda^{-0.5} - \lambda^{-1}$, and a similar relationship was found for the first eutectic MPEA reported, $Al_{15}Fe_{30}Mn_{35}Ni_{20}$, consisting of FCC and B2 lamellae, which exhibited yield strength of 740 ± 30 MPa and 8 % elongation under tension [163]. The stronger phase is not always necessarily of BCC structure, and can be an intermetallic. Investigating CoFeMnNiTi eutectic HEAs, Jain *et al*. [164] found the $Co_{25}Fe_{25}Mn_5Ni_{25}Ti_{20}$ composition consisted of FCC and Laves (Ti_2(Ni,Co)) lamellae, and exhibited good high temperature strength of 560 MPa at 800°C. Chanda and Das [140] fabricated $CoCrFeNiNb_X$ ($0.45 < X < 0.65$) and $CoCrFeNiTa_Y$ ($0.2 < Y < 0.5$) HEAs, consisting of

FCC solid solution and Fe_2Nb and Co_2Ta Laves phase lamellae respectively. Meanwhile, the BCC phase was instead retained by Gao *et al*. [165] who fabricated an $AlCoCrFeNi_{2.1}$ alloy, exhibiting a dual $L1_2$ and B2 microstructure. An excellent combination of mechanical properties was reported, with a UTS of 1351 MPa and elongation of 15.4 %. The stability of eutectic microstructures is generally found to be dependent on solidification rates, for example [166]. Chanda and Das [140] also suggested that eutectic phases (in the FCC + Fe_2Nb/Co_2Ta eutectic microstructure in their CoCrFeNiNb and CoCrFeNiTa HEAs, as well as for others reported in literature) become stable for $-18 \leq \Delta H_{mix} \leq -6$, $6 \leq VEC \leq 8.5$, and $\delta > 3$ %.

The introduction of elements in small quantities that may encourage the formation of secondary precipitate phases, particularly nano-precipitates, is another strategy. Wu *et al*. [167] added 0.5 at. % C to the extensively studied equiatomic CoCrFeMnNi, as an interstitial element to advance the properties for cryogenic applications. The single phase FCC microstructure was retained, while improving strain hardening rate, yield strength and UTS. Li *et al*. [168] also studied C addition of up to 3 at. % to CoCrFeMnNi. At 1 at. % C addition, the nano-carbide volume fraction increased to 2.9 % and caused an increase in yield strength from 371 MPa to 634 MPa. Also for this HEA, Rogal *et al*. [169] investigated adding spherical SiC nanoparticles, through mechanical alloying followed by hot isostatic pressing (HIP). The resulting microstructure consisted of FCC solid solution, $M_{23}C_6$ and σ-phase. An addition of 5 wt. % of the SiC nanoparticles improved compressive yield strength significantly, from 1180 MPa to 1480 and 1940MPa (for milling speeds during mechanical alloying of 100 and 200 RPM respectively), meanwhile reducing plasticity. Oxide dispersions, such as Y_2O_3, have also been shown to significantly improve the mechanical properties of single FCC phase CoCrFeNi [170].

The above examples demonstrate a trend towards optimising the design of HEAs and MPEAs in order to enhance the properties, often requiring deviations from the traditional compositional definition of HEAs. In encouraging dual-phase and eutectic microstructures, as well as employing small concentrations (less than the usual 5 at. % lower limit for HEAs) of alloying additions in order to provide strengthening precipitates, authors have been able to balance the mechanical properties offered by single phase BCC or FCC microstructures.

4.4 Application as Brazing Filler Metals

Despite the aforementioned significant interest in recent years in HEAs and MPEAs, scant literature exists for the application of these concepts to brazing. This is perhaps surprising, as this technology could stand to benefit from the potentially attractive properties exhibited by some developed HEAs and MPEAs, such as high yield and ultimate tensile strengths (at both room and elevated temperatures), resistance to crack propagation, and high cycle fatigue strength. One reason for this lack of literature could be the still relative immaturity of the HEA field. Much in the way of fabrication and processing of HEAs, and the effect on microstructure, is not fully understood. This knowledge would be important for use in brazing where materials experience high temperature and interacting chemistries. However, a further reason could be that, of the HEAs/MPCAs that have been developed for (or applied to) brazing, the liquidus temperature (and hence required brazing temperature) is often prohibitively high for practical limitations in industry. Many industrial furnaces used for current brazing applications have operating temperatures no higher than 1200°C, and using higher temperatures can be costly. Despite this, ternary phase diagrams frequently show that liquidus decreases towards more equiatomic compositions, away from the corners of the phase diagram.

Therefore, it is possibly the case that the application of HEAs/MPEAs as brazing filler metals has been limited more by the lack of attempts at lowering the liquidus, as many of the proposed application for HEAs are in high temperature applications.

There may be a further issue when considering the limited frequency with which some elements are used in HEAs and MPEAs. Fig. 4.2 (courtesy of [136]) shows this frequency as of 2017, and it can be seen how few elements are used in a substantial proportion of studies. Elements that may have the effect if lowering liquidus in a filler metal are rarely used, but again this is not wholly surprising as if elements such as B or P were used in large or even equiatomic quantities, the microstructure may be comprised mostly of brittle intermetallics. Si has seen more use, in both small [171] and equiatomic [172] quantities, but for purposes of mechanical properties [171] or solid solution formation [172].

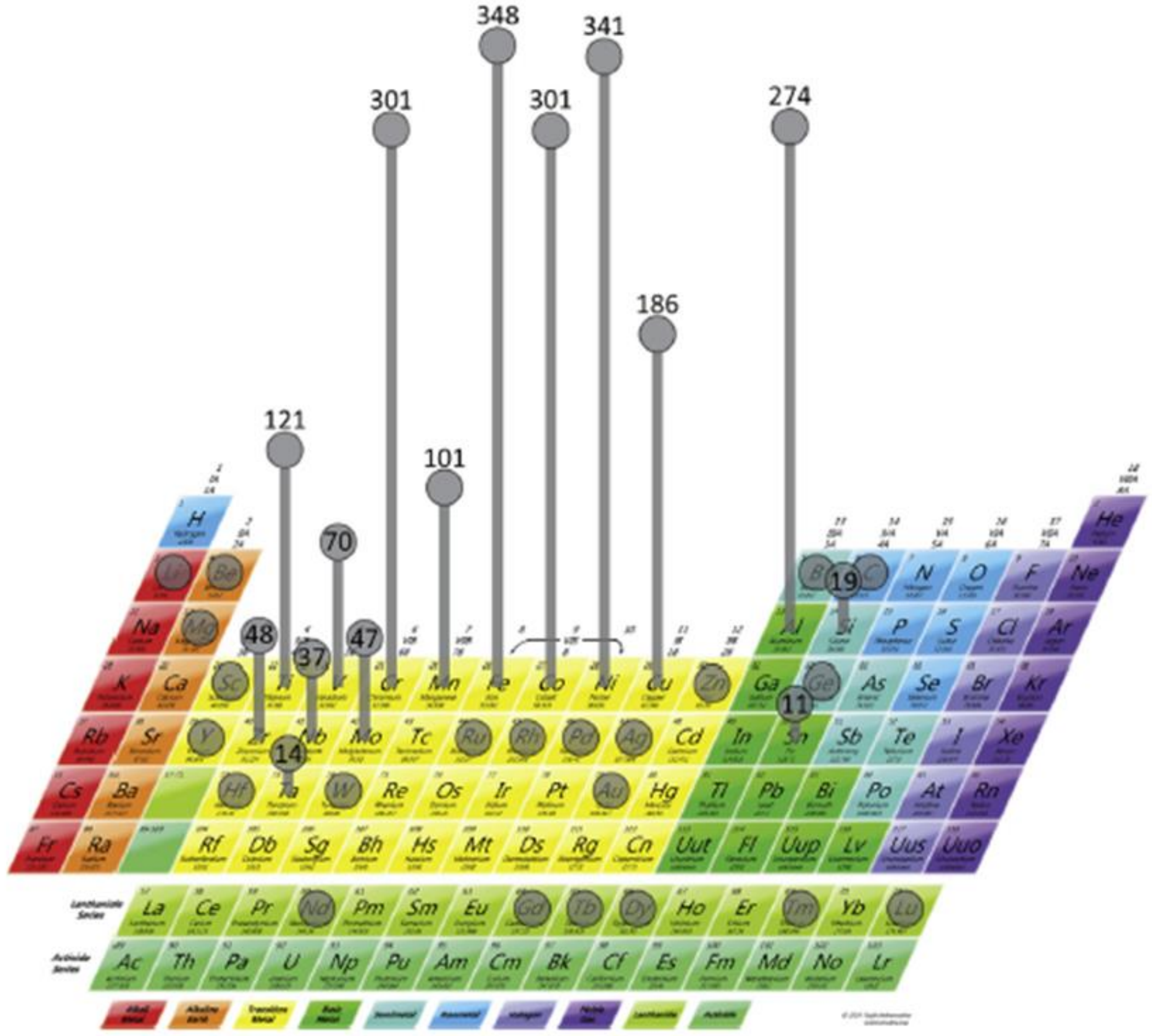

Figure 4.2: Frequency with which elements have been found in HEA studies as of 2017. Image reproduced with permission from [136].

Of the studies demonstrating the use of HEA or MPEA filler metals, the base materials being brazed have generally been either Ni-based superalloys or ceramics. For the former, the group of Tillmann and co-workers in Dortmund has been active in addressing the use of MPDs to allow use of HEAs/MPEAs as filler metals. The use of Ge and Sn as MPDs in equiatomic CoCrCuFeNi(Ge or Sn) alloys was reported by the group [171], with the HEA filler metals being used to braze Ni-based superalloy Mar M-247. While the alloy melting ranges were not verified by DSC, CALPHAD predictions gave the melting ranges of the Ge- and Sn-containing alloys as 918 – 1171ºC and 969 – 1257ºC, respectively, and so brazing was conducted at 1200ºC and 1275ºC respectively. Compared to joints brazed with commercial AWS BNi-5 filler metal, which achieved 963.6 ± 63.7 MPa (brazed at 1200ºC), the Ge- and Sn-containing HEA filler metals achieved strengths of 407.3 ± 81.0 and 306.8 ± 56.2 MPa, respectively. The Sn-containing HEA filler metal reportedly suffered from brittle low-temperature eutectics, impacting the strength, whereas the Ge-containing filler metal showed evidence of ductile behaviour in failure. Conceivably, accurate melting ranges from DSC measurements could allow optimisation of the brazing temperatures used for these alloys, potentially resulting in stronger joints. Tillmann *et al*. [172] also investigated the use of Ga in an equiatomic CoCrCuFeNi HEA. The equiatomic CoCrCuFeNiGa composition (16.66 at. % each) achieved the lowest liquidus, but this was still as high as 1259ºC. The as-cast microstructure was found to have three phases, an extra phase compared to the 10 at. % Ga composition. When brazing Mar-M 247 Ni-based superalloy with the equiatomic CoCrCuFeNiGa filler metal at 1275ºC for 30 minutes, a shear strength of 388 ± 73 MPa was recorded, where the filler thickness was 200 µm. The joint microstructure post-brazing also consisted of just two FCC phases. It is conceivable that a yet lower liquidus could be achieved through optimising the composition of the CoCrCuFeNi component for liquidus as well as using Ga as MPD, but this was not discussed by the authors.

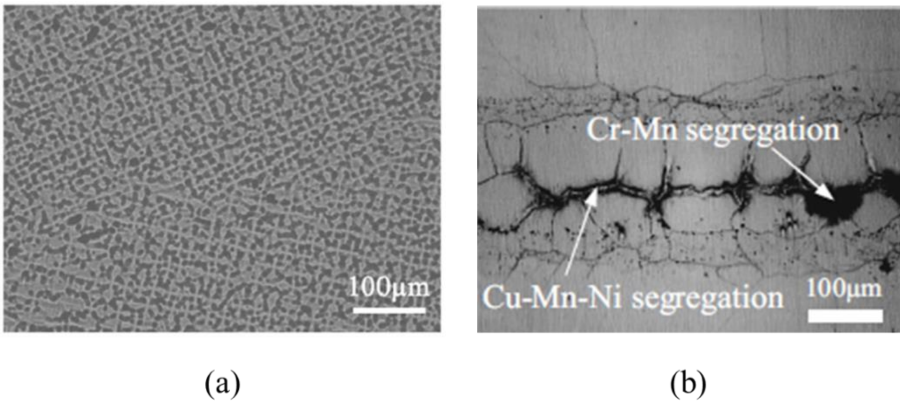

Figure 4.3: (a) As-cast microstructure of fabricated $Co_{0.25}FeNiMn_{1.75}Cu$ MPCA filler metal. (b) Section of IN600-$Co_{0.25}FeNiMn_{1.75}Cu$ brazed joint. Images reproduced with permission from [176]

Elsewhere, the first published study into using a HEA as a brazing filler metal was by Bridges *et al*. [173]. Laser brazing of IN718 superalloy with a FCC $NiMnFeCo_{0.25}Cu_{1.75}$ HEA was demonstrated, at a brazing temperature of 1165ºC (15ºC above the reported alloy liquidus temperature) and achieving a 220 MPa maximum shear strength. The HEA used in this study was cold-rolled to a 400 µm thickness, however, which would be considered overly thick for an insert such as a foil. Given the gap size here, therefore, it might be more appropriately considered a wide-gap braze, for which longer brazing times would likely be required for optimum results. Gao *et al*. [174] demonstrated joining of IN600 superalloy with a $Co_{0.25}FeNiMn_{1.75}Cu$ MPEA. The as-cast MPEA exhibited a dendritic microstructure, but with both phases possessing an FCC structure (Fig. 4.3(a)) of similar lattice parameters. Again, the MPEA filler metal in this study was rolled only to a thickness of 300 µm, which would be likely considered a gap sized more appropriate for braze repair techniques.

Nonetheless, joint shear strength increased with brazing hold time up to a maximum of 530 ± 20 MPa after 90 minutes. Beyond 90 minutes hold time, the formation of brittle Cr-Mn intermetallics occurred, which decreased the strength. Fig. 4.3(b) shows the microstructure of the IN600 - $Co_{0.25}FeNiMn_{1.75}Cu$ brazed joint following 120 minutes at 1200°C.

The brazing of ceramics (either to ceramics or to alloys) using HEA/MPEA filler metals has seen perhaps equal attention in the literature as for brazing of metallic materials. Wang *et al*. [175] used a (presumably equiatomic) CoFeCrCuNi HEA to produce joints of SiC ceramic, with the goal of achieving intermetallic free joints due to the single-phase microstructure of the HEA. In this study, a joint shear strength of 60 MPa was achieved when brazing at 1180°C for 1 hour, with both higher and lower temperatures resulting in reduced strength. This strength compared favourably in this application to reported maximum strength of 15.9 MPa using a typically used AgTiCu filler metal [176]. Again, it should be pointed out the thickness of filler used by Wang, at 600 µm, which would be considered wider than typical and is indeed six times thicker than the filler used in the study being compared to, rendering that comparison more complex. A dissimilar brazed joint was shown by Tillmann *et al*. [177], who joined Hf-metallised YSZ ceramic to Crofer 22 APU steel using a $CoCrFeNb_{0.73}Ni_{2.1}$ HEA. Using this filler metal, almost double the shear strength was achieved compared to when using a typical AgCuTi3 filler metal, albeit at a brazing temperature of 1200°C, some 280°C higher than that for AgCuTi3. Zhang *et al*. [178] brazed a ZrB_2-SiC-C ceramic to Ni-based superalloy GH99, using a composite Ti/CoCrCuFeNi filler metal. A brazing temperature of 1220°C and 60 minutes hold time was used, with a shear strength of 70 MPa achieved. This high temperature needed for brazing, however, caused a reaction between Ni and the ceramic, forming brittle intermetallics that limited the strength.

4.5 Chapter summary

This section has introduced and discussed the concepts of HEAs and MPEAs, their properties, and how these properties may make them attractive for use as brazing filler metals. Since the mid-2000s, the massive interest in HEAs and MPEAs has led to much research on certain HEA families, particularly those based around the Cantor alloy (Cr, Co, Fe, Mn, Ni), other transition metal and refractory elements (Cu, Mo, Nb, Ta, Ti, V), as well as the post-transition metal Al. Initially, much focus was placed on compositions using these elements that would possess a single phase, solid solution microstructure, usually either BCC or FCC. However, in the pursuit of more balanced mechanical properties, compositions that could promote dual-phase microstructures, eutectic microstructures, or secondary strengthening phases were studied, moving further away from the earlier, stricter equiatomic definition of HEAs. Promising combinations of high strength and ductility have been reported for several systems, and would clearly be attractive for many applications, including as brazing filler metals. However, as shown, only a limited amount of literature exists on the use of HEAs and MPEAs as brazing filler metals, perhaps due to greater interest in their promise in higher temperature applications, for example as structural materials for nuclear reactors. Of the literature that does exist, little has been attempted to suppress the typically high melting temperatures, which might otherwise limit their use as filler metals, for example when brazing lower melting point superalloys, or due to vacuum furnace temperature capabilities. Some use of MPDs as part of a HEA filler metal composition has been reported, but still the melting temperatures reported are high compared to conventional Ni-based filler metals used in industry. There exists room for development, therefore, in exploring compositions of HEAs and MPEAs with yet lower melting temperatures which could provide the mechanical benefits associated with these alloys, yet be employed within the temperature range most relevant for brazing of Ni-based superalloys in industry.

5. CALPHAD & Thermo-Calc

As metallic materials become ever more complex, so does the task of predicting their properties. With modern alloys such as the superalloys containing numerous elements, the phase equilibria calculations become dauntingly large even when established equations exist. Thankfully, many computing tools allow the modelling and prediction of properties of metallic systems, particularly those relevant to this thesis such as transformation temperatures, phase constitution and crystal structure. The CALPHAD method (CALculation of PHAse Diagrams) is one such, and allows the modelling of thermodynamic properties of materials. It greatly benefitted the development of novel alloys through allowing screening and mapping of compositions meeting the requirements of the new material, whereas previously phase equilibria and diagrams would have to be physically investigated requiring enormous time and costs.

5.1 Brief Overview of Development

Development of the CALPHAD modelling method was initially started by Kaufman in the late 1950s [181], and this continued through the 1960s and 1970s through Kaufman and various other research groups, including those of Hillert and Ansara [181]. More complete histories of the development timeline can be found elsewhere [181, 182]. By the 1970s, several databanks of calculated phase equilibria had been and were being established at various institutions, and the forming of a European-wide common databank was realised with the formation of the Scientific Group Thermodata Europe (SGTE) in 1979 [181]. These databases and the advent of more powerful computing later allowed the development of software which could undertake the burdensome calculations that previously had to be used, such as calculating tangential planes contacting minima of Gibbs energy surfaces for ternary systems. Today, numerous databases are in use for CALPHAD modelling of systems.

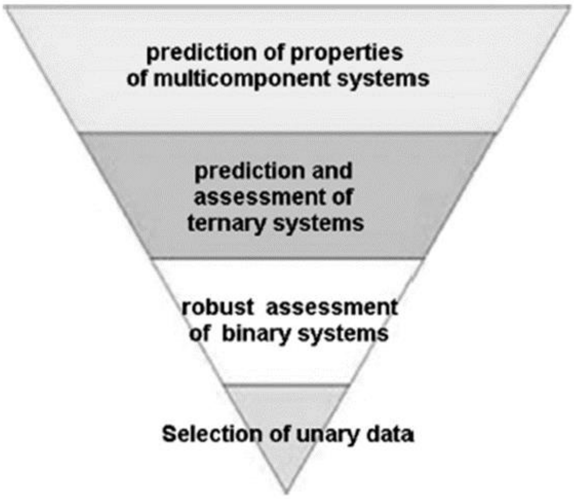

Figure 5.1: Sequential modelling stages used in CALPHAD. Image reproduced with permission from [183].

The calculations carried out by the CALPHAD method, in order to predict phase information about binary, ternary and even on to high order systems, all essentially start with the minimisation of total Gibbs energy. Thorough and extensive descriptions of this can be found in elsewhere, in particular the work of Saunders and Miodownik [182]. For individual elements, this is expressed in polynomial form, and the term coefficients are stored in databases [183]. These data are then used in the next step which is to consider binary systems, for determining the Gibbs energy of both elements in each phase. Due to the complexities of also considering intermediate phases, solubility in phases and interactions between elements, it is important to have supporting experimental data on phase equilibria and phase thermodynamic properties [183]. With rigorous binary modelling it is then possible to build up to ternary system modelling, using only the binary parameters (i.e. constructing the ternary system from the three separate binary systems covering possible combinations of three elements). Again, supporting experimental data, particularly for ternary phases existing only in the ternary system, is required for a complete picture [182, 183]. Continuing to build in this way, the method eventually extends to multi-component systems reflecting real-life alloys, with the amount of supporting experimental data influencing the overall accuracy (Fig. 5.1, courtesy of [183]).

The total Gibbs energy of a system is a sum of the Gibbs energies of the phases in the system, and the Gibbs energy of each phase has multiple contributing Gibbs energies, depending on the phase. For metallic systems, for instance, important contributing Gibbs energies are G_{ref} (weighted sum of molar Gibbs energies of each individual element), G_{ideal} (contribution from ideal random mixing of elements), and G_E (contribution from excess energies not covered by other terms, including non-ideal mixing). Therefore, the Gibbs energy of a phase can be expressed as:

$$G = G_{ref} + G_{ideal} + G_E \dots \qquad (5.1)$$

Other terms can be included for a complete accounting of contributions, such as G_{mag} (contribution from magnetic behaviour), which is important for magnetic materials, but for others the contribution in metallic systems is much less than the terms in Equation 5.1 (though some like G_{surf} (contribution from surface energy) become more important for nanomaterials [183]). In an n-component case, for a phase A, these terms can be calculated as in Equations (5.2) – (5.5):

$$G_{ref}^{A} = \sum_{i}^{n} x_i \cdot G_i^A \qquad (5.2)$$

where x_i is the molar fraction of element i and G_i^A is the Gibbs energy of element i, given by the temperature-dependent polynomial expression:

$$G_i^A = a + bT + cT\ln(T) + \sum_{i} d_i\, T \qquad (5.3)$$

where a, b, c and d_i are adjustable parameters that are stored in the database, and T is temperature.

$$G_{ideal}^{A} = R\,T \sum_{i}^{n} x_i \cdot \ln x_i \qquad (5.4)$$

where R is the gas constant.

$$G_E^A = \sum_{i}\sum_{j>i} x_i x_j \Omega_{ij} \qquad (5.5)$$

where Ω_{ij} is a temperature-dependent interaction parameter between elements i and j, derived from Redlich-Kisler formalism [184] as described in [182, 183]. Equation 5.1 now becomes, generally:

$$G_{ref}^{A} = \sum_{i}^{n} x_i \cdot G_i^A + R\,T \sum_{i}^{n} x_i \cdot \ln x_i + \sum_{i} \sum_{j>i} x_i x_j \Omega_{ij} \qquad (5.6)$$

Where ternary interactions are a consideration, extra interaction terms such as Ω_{ijk} can be added to extend Equation 5.6, but for even higher order systems it has been proposed that contributions from higher order terms have a negligible effect, yet would drastically increase the computing demands [182].

Equation 5.6 is the general case for simple substitutional phases such as liquids, FCCs and BCCs, but as described in [182], more complex computational methods have been proposed for interstitial solutions and ordered intermetallic. When the Gibbs energy for each phase in a system is calculated in this way, the total Gibbs energy of the system can be determined and the minimisation of this (for a given composition, temperature and pressure) gives the thermodynamic equilibrium state. The construction of accurate and complete databases used in CALPHAD software such as Thermo-Calc (TC) relies on rigorous theoretical assessment of available experimental data available in the literature, judging the accuracy and reliability of such data. This includes not only phase equilibria and boundaries, but other properties including enthalpies of mixing, enthalpies of formation, and heat capacities [182, 183]. All this data feeds into the Gibbs energy model in Equation 5.6, allowing its optimisation to increase agreement with existing experimental data. Kroupa summarises three conditions that constructed databases must fulfil for prediction of properties in multi-component (i.e. greater than three components) systems [183]:

- The polynomials used in the calculation of the composition-, temperature- and pressure-dependent Gibbs energy of components must be mutually compatible (i.e. parameters used in one series must be applicable to a different series).

- Within a database, the same model used for the Gibbs energy determination for a particular phase, must be used for other phases of the same or similar crystal structure.

- Identical sets of parameters must be used to describe the Gibbs energy of pure element constituents, across all systems in the database.

In this work, the CALPHAD software used was Thermo-Calc (TC), which contains various databases containing assessed data for a variety of alloy types. Two in particular were of importance in this project: (1) TCNI8, a Ni-based superalloy database containing experimentally verified binary and ternary data for most elements found in Ni-based superalloys, and (2) SSOL4, a more general purpose database used for alloy design, containing a much wider range of elements available for selection, with most of the binary combinations assessed experimentally. Both have seen wide use across literature, though the most up-to-date SSOL database is now the SSOL6 version, containing an increased number of assessed binary and ternary systems. Newer databases have included TCHEA4, a database for BCC, FCC and HCP HEAs and MPEAs. Table 5.1 summarises some of the relevant and recent databases in terms of the elements, phases, binary systems and ternary systems available for modelling in TC. The following sections will look at the application of these databases in the literature on brazing (and related), more general alloy design (focusing on Ni and its alloys), and finally HEAs and MPEAs.

Table 5.1: Summary of numbers of elements, phases, and assessed binary and ternary and higher order systems included in various TC databases.

	Elements	Phases	Binary systems	Ternary & higher order systems
TCNI8.2 (Ni-superalloys)	27	490	280	272
TCFE10.1 (Steels/Fe-alloys)	29	435	308	346
TCMG5 (Mg-alloys)	31	478	195	91
SSOL4 (Alloy solutions)	78	716	N/A*	N/A*
SSOL6 (Alloy solutions)	79	1331	575	153
TCHEA4	26	500	307	493**

**while the exact number is not stated on available data sheets, it is likely to be somewhere between that of SSOL2 (106 binary and 61 ternary & higher order systems) and SSOL6 (575 binary and 153 ternary & higher order systems).*

***192 of which are assessed to the full range of composition and temperature.*

5.2 Application to Brazing Filler Metals

Despite the absence of a dedicated brazing and soldering database, many studies modelling equilibrium phases and diffusion processes for brazing applications have employed TC (along with the DICTRA module for diffusion), using databases such as the TCNI and SSOL databases instead. The majority of brazing studies using TC have done so for reasons of comparison, however, rather than as a tool for initial predictions or optimisation. The TCNI databases in particular have seen wide use due to the assessed binary and ternary systems including common elements in Ni-based filler metals, Ni, Cr, Fe, B and Si.

Riggs *et al*. [108] modelled diffusion phenomena and equilibrium phases for comparison with experimental results, when brazing CMSX-4 superalloy with AWS BNi-2 (B and Si containing) & BNi-9 (B containing), using the TCNI7 superalloys database. Reasonable agreement between DICTRA simulations and experiments was found when predicting the maximum gap size permitted for complete isothermal solidification when brazing with BNi-2 at 1170ºC for various hold times, though agreement was better for shorter hold times. It was also noted that the filler metal was modelled only as Ni-B, the other elements not included due to the orders of magnitude faster diffusion of B comparatively. Predictions of equilibrium phases for both BNi-2 and BNi-9 were also made, and were found to correlate well to the phases observed in the joint post-brazing, with agreement on the intermetallics formed and the presence of γ-FCC matrix. It should be pointed out, however, that predictions made in this way through TC do not take into account compositional changes in the joint due to base metal dissolution and diffusion, and so fully accurate predictions would not be expected.

Ruiz-Vargas *et al*. [185] previously conducted similar analysis for BNi-2/pure Ni joints brazed as DSC couples. Phases predicted by TC were in broad agreement with observations, and in comparable proportions. However, when the compositions of the predicted phases were interrogated, discrepancies were observed, in particular a notably reduced Cr content in most phases predicted. Furthermore, TC predicted that 76.8 wt. % solid phase remained at 1050ºC, contrary to results in this study and others, not to mention the widely used industrial standards. Ruiz-Vargas *et al*. conclude that *quantitative* TC predictions should be used with caution [185].

TC has also seen use in the design of simple binary and ternary brazing filler metals, including some of those already discussed in Chapter 3. In the design of a Ni-Mn-Si filler metal, Piegert *et al*. [186] used DICTRA to model the epitaxial temperature-driven solidification, and also used TC to predict the equilibrium phases and liquidus surface over a compositional range. Again, the inability to take into account base-metal dissolution was noted as a possible source of inaccuracy, and DICTRA simulations of diffusion in the joint showed discrepancies in the final elemental distribution in the joint.

As discussed in Chapter 3, use of the concepts of HEAs and MPEAs for novel filler metals has seen some recent attention, and indeed some existing filler metal families already possess compositions falling within the wider HEA/MPEA definition, such as Ag-based filler metals. Tillmann *et al*. used TC predictions to screen for compositions giving a suitable melting range in the development of equiatomic CoCrCuFeNi+Ga HEA filler metals [173] as well as for equiatomic CoCrCuFeNi+(Sn/Ge) filler metals [174]. In the former case, TC predicted narrower melting ranges than were measured, with larger discrepancies in the predicted liquidus temperatures, though the overall effect on melting temperature measured was generally mirrored by the TC predictions. In the latter study, the opposite occurred, with TC predicting a wider melting range than was measured, and greater discrepancies in solidus temperature observed, for both the Sn and Ge containing compositions. The former study (Ga-containing filler metal) used the SSOL6 database, while the latter study used SSOL6 and TCHEA2 for predictions of the Ge- and Sn-containing filler metals respectively. The discrepancies may show the inaccuracies that may arise when attempting to predict properties of higher order (six components in this case) systems, in cases where not all binary and ternary systems are assessed (for example, unassessed systems in the SSOL6 database include the Cu-Ga, Fe-Ga, Fe-Ge and Ge-Ni binaries).

Snell [187] compared TC-predicted melting ranges of various four-component Ag-based filler metals to the quoted and measured melting ranges. Predicted melting range was consistently wider than quoted and measured, though agreement increased for the higher melting temperature alloys (which have wider quoted melting ranges than lower temperature alloys), though consistently TC overestimated the liquidus. Surprisingly, however, TC predictions actually tended to agree more with *measured* melting ranges (determined by DTA), which had also shown higher liquidus temperatures than those quoted for all alloys. This raises and important consideration – quoted values for a commercial alloy may show differences to measurements made in the lab, which could be due to wide elemental content ranges quoted for the alloy compositions, or the quoted melting range being based more on industrial experience rather than on specific laboratory-confirmed values. Despite these differences, however, it was seen that broad trends in solidus, liquidus and melting range predicted by TC are in agreement with quoted and measured values, even though these compositions are more similar (in terms of proportions of components) to HEAs/MPEAs rather than conventional alloys. Snell also fabricated a range of novel Ag-based (same elements used but in different proportions) brazing filler metals, again comparing predicted and measured melting ranges. Generally, wider melting ranges were again predicted than were measured, and liquidus was generally predicted as higher than measured. Again, broad agreement in the overall trends in solidus and liquidus due to compositional changes was seen.

Differences between the TC predictions made here, and the observations reported, raises an important consideration when using TC in alloy design, aside from the information on elements for which assessed binary and ternary data is available. The CALPHAD method used by TC is provided predictions for the equilibrium condition of a system, which is unlikely to be representative of alloys produced conventionally that do not solidify under equilibrium conditions. Laboratory-scale production of novel filler metals via arc-melting such as those reported by Snell [187] are a clear example of this, given the likely high cooling rate experienced (the arc-melting method is discussed in greater detail in Chapter 7). For industrially-produced brazing filler metals, particularly those used in amorphous foil form which requires rapid-quench melt-spinning, this is even more so the case. The result of this is that observed properties such as phase constitution and abundance are generally likely to show discrepancies from TC predictions.

5.3 Application to Design of HEAs and MPEAs

CALPHAD-aided design of HEAs and MPEAs has seen a significant amount of attention since the start of the interest in HEAs and MPEAs over the last two decades. As mentioned above, the CALPHAD approach relies upon datasets of experimentally assessed binary and ternary systems, and so for predictions of higher order systems such as HEAs and MPEAs, extrapolation is required, which is the main cause of inaccuracies for this application. Motivation to improve the accuracy of extrapolation by including more complete assessed binary and ternary systems for the more common elements in HEAs and MPEAs led to the development of a dedicated HEA database (TCHEA1) by Chen *et al*. [188], now in its fourth version (TCHEA4). But even without this, several previously existing databases contained assessed binary and ternary systems for elements that are commonly employed in HEAs and MPEAs. For example, TCNI8 contains all assessed binary and the majority of ternary systems covering the vast majority, if not all, elements used in the CoCrFeMnNi Cantor alloy and similar transition metal HEAs. However, these more specific databases, while having fairly complete assessments across compositional ranges of possible systems within the database, nonetheless have limited element coverage in respect to the full periodic table of elements. On the other hand, databases such as the SSOL (currently SSOL6) databases have much wider coverage of elements, but the proportion of all possible ternary systems in the database that are fully assessed is lower than for the specialised databases, and some atypical binary systems that can be assessed in TC also lack experimental verification. The number of assessed binary and ternary systems required for a full thermodynamic description of selection of N elements or components is illustrated in Fig. 5.2, for up to N = 79 components, as in SSOL4. It is easy to see from this that for databases containing more than 20 components, such as all those in Table 5.1, vastly greater numbers of assessed systems would be required for complete accuracy. For SSOL4, in fact, the number of binary and ternaries required would be 3081 and 79079 respectively.

It could therefore be expected that properties of HEAs and MPEAs with more common and typical compositions such as those based around the Cantor alloy and similar, and which have established phase diagrams for binary and most ternary combinations of constituent elements, may be easier to predict than for those containing atypical combinations of elements. Miracle and Senkov [136] discuss this elemental ‘bias’ across databases, and point out examples such as Fe, Mo, Si, Ti and Zr being included in all but one databases, and Ni included in all but two databases. This could go much of the way in explaining discrepancies observed between predictions and observations for the HEA filler metals developed by Tillmann *et al*. [174] and by Snell [187] as described in the previous section. But at the same time it should not be considered that more widely studied HEAs and MPEAs are fully captured by the CALPHAD modelling, nor that specialist databases such as the TCHEA databases automatically provide the most accurate predictions when compared to observations. In addition, the aforementioned issue of CALPHAD equilibrium predictions not being directly comparable to observations of conventionally fabricated alloys also apply here.

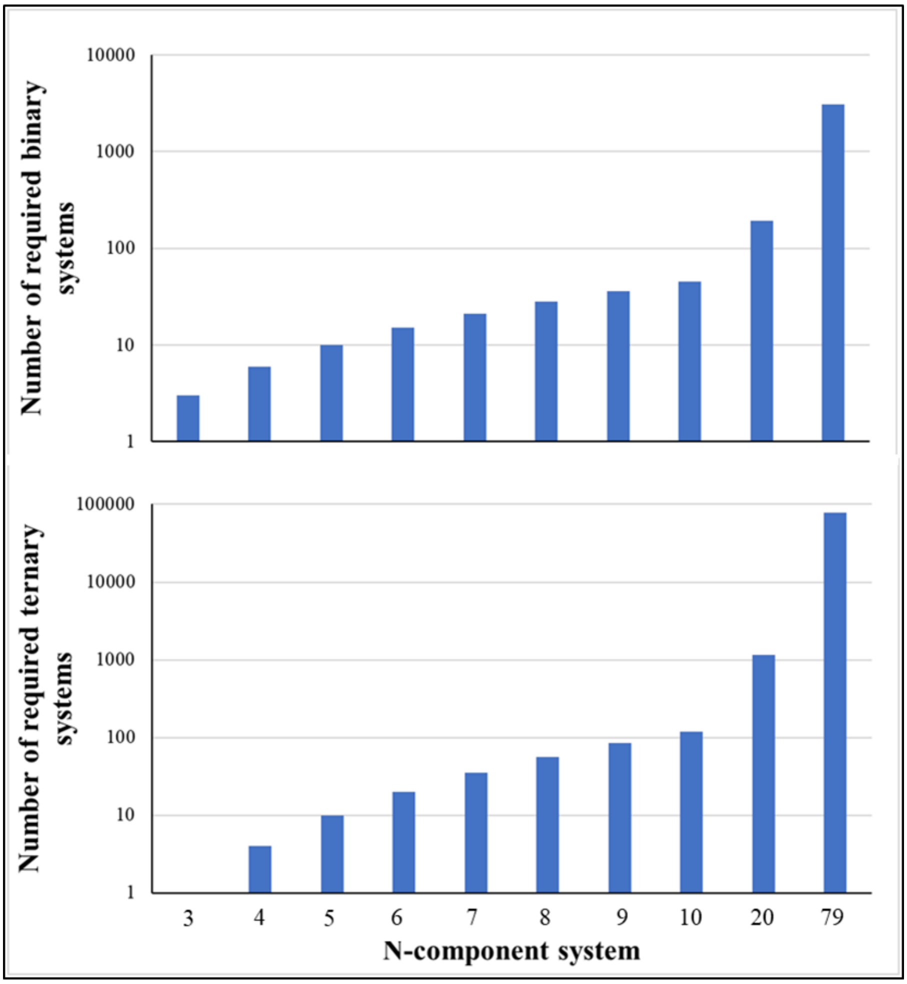

Figure 5.2: Number of assessed binary and ternary systems required for a complete thermodynamic description of an N-component database. Image reproduced with permission from [189].

Nonetheless, there are numerous examples of agreement between predictions and observations in the CALPHAD-aided design of HEAs and MPEAs observations, for example in systems including AlCoCrNi [190], AlCoCrFeNi [191], MoNbTaTiVW [192]. It has been observed that non-equiatomic compositions possess a great solid solution-forming potential, and the CALPHAD-aided refinement of compositions away from equiatomic has also been reported, for example in systems CoCrFeMnNi [193], CoCrFeMnNiV [194], CrMoNbTaVW [195] and (Co)CrMoVW [154]. In contrast to the three former examples, which used different versions of the TCHEA databases, in this latter example Patel *et al*. [154] used the SSOL4 database for the prediction of solid solution formation of the HEA, demonstrating the applicability of databases not necessarily designed with HEAs and MPEAs in mind. Limitations of using CALPHAD for such systems, however, include predictions of lower temperature phases that were not observed in the final microstructure, for example σ-phase and Ni_3Ti ($D0_{24}$) in equiatomic CoCrMnNiTi [164] (though attributed to the non-equilibrium cooling of the ingot). Furthermore, Miracle and Senkov [136] reported significant differences in experimental results and CALPHAD predictions, noting the much higher preference for solid solution formation experimentally than in CALPHAD predictions, whereas solid solution plus intermetallic microstructures were predicted by CALPHAD at a higher frequency than was observed experimentally.

5.4 Chapter summary

This chapter has provided a brief introduction to the development of the CALPHAD method, and its uses for alloy design, particularly for brazing filler metals and on to higher order systems such as HEAs and MPEAs. The nature of CALPHAD is such that the accuracy of extrapolations for high order systems is dependent on the availability and inclusion in databases of experimentally validated information on binary and ternary systems. For many databases, there are already large amounts of such assessed data, and in many cases, such as in the dedicated databases for Ni-based superalloys or steels (TCNI and TCFE respectively), all binary systems of included elements are assessed across the full compositional range. However, gaps exist in the coverage especially where less commonly seen binary systems are concerned, and this in turn means even less coverage of ternary systems that include elements not often used together in alloys. More general databases that include a much wider range of elements, such as the SSOL databases, give the possibility of modelling some of these atypical systems, and while in many cases at least some experimentally validated data exist for these, caution must be used when using CALPHAD for such systems, and where possible database information sheets detailing the systems that have been assessed should be consulted. Another point of consideration leading to discrepancies between CALPHAD predictions and what is observed, is the fact that CALPHAD predictions represent the equilibrium condition, unlikely to be directly comparable to phase abundance and constitution observed in conventionally fabricated alloys, in particular fast-cooling methods such as arc-melting, often used to produce small-scale quantities of experimental alloys, and melt-spinning, used in the production of amorphous filler metal foils.

Nonetheless, the usefulness of the CALPHAD method, as well as software such as TC, has been demonstrated across a wide variety of applications. In alloy design for brazing filler metals, TC can be used to predict the microstructure, phase abundance, phase composition, solidus temperature and liquidus temperatures of both existing filler metals and novel compositions of filler metal. In the case of novel compositions where one or more of the involved binary systems is not assessed, TC predictions may be taken as an indication of the effect that composition has on properties such as melting temperature, rather than as a precise measure, and in this way TC may be used to show expected trends in properties as a function of composition. When applied to the design or otherwise prediction of HEAs and MPEAs, CALPHAD and TC are again considered useful tools, particularly when identifying initial regions of composition space that have predicted single solid solution phase microstructures, for instance. Development of the more specialised TCHEA databases have aided the application of CALPHAD to these higher order systems, by the inclusion of wide coverage of common ternary systems assessed across full compositional ranges. In order to improve CALPHAD across all applications, ever increasing coverage of binary and ternary systems is required, particularly for those that are less common but still of technological interest, which could greatly expand the possibilities for alloy design for future materials.

6. Literature Review Summary & Statement of Problem

The preceding chapters have reviewed the current state of the art as reported in the literature. It is clear that brazing, and in particular vacuum furnace brazing (detailed in Chapter 1), is a crucial technology for joining a wide range of materials, some of which are unsuitable for other techniques such as welding. As discussed in Chapter 2, Ni-based brazing filler metals are generally the preferred filler metal for joining Ni-based superalloys, and their use for joining dissimilar materials, steels, Co-based superalloys and even certain ceramics has been demonstrated. While excellent joint mechanical performance is achievable with these alloys, the need for MPD elements, in particular B, Si and P, can potentially have a detrimental effect on the joint, due to the formation of brittle intermetallic phases. These phases can be avoided (or at least reduced over time) with appropriate selection of parameters, including brazing time, brazing temperature, selection of suitable filler metal, and filler metal thickness (or overall joint width). The effect of these parameters has been extensively investigated, and for a wide range of filler metals (though mostly the commercially available AWS BNi- series alloys) and base metals, as reported in Chapter 2. It can be seen in the literature that increased time at temperature is often required for best results, and in some cases lengthy post-brazing heat treatments. At the same time, relatively little has been attempted to address this, in the decades since many of the current commercially used Ni-based filler metals first saw use, by developing novel compositions. Development in this area could allow improved joint mechanical properties, and also potentially reduce the time required to achieve such properties. Of the attempts to develop new compositions in the literature, detailed in Chapter 3, several have focused on the use of alternative MPD elements, with the aim of replacing the currently used B, Si and P. In some cases, the proposed new MPD has been used alongside Si or B in reduced concentrations. Another development that has seen more recent attention in the literature is application of the concepts of HEAs and MPEAs to the development of novel brazing filler metals, which was discussed in Chapter 4. However, of the few reported studies, most such attempts have focused on applying the more widely studied HEAs and MPEAs, such as the CoCrFeMnNi and related alloys, which have liquidus temperatures significantly higher than most commonly used Ni-based filler metals. Only one or two have taken the further step to produce a HEA or MPEA filler metal containing an MPD element, and even there the compositional range studied was limited to equiatomic.

There is scope, therefore, to explore both the substitution of an alternative, novel MPD for the traditionally used B, Si and P, and the use of a novel MPD as part of a HEA or MPEA brazing filler metal. Part of this study will also assess the ability of CALPHAD-based software such as Thermo-Calc to predict trends in melting temperature and phase abundance, especially in cases where experimentally verified data may not be available for atypical alloying additions, or compositions (such as for Ni binary systems with novel MPD elements, and for HEAs/MPEAs). In this way, the usefulness of Thermo-Calc as a design tool for brazing filler metals, and HEAs/MPEAs in general can be assessed. There is also room to explore the applicability of the design rules used in the development of HEAs and MPEAs, discussed in Chapter 4, to compositions outside the ‘norm’ for such alloys (both in the elements used, and in the concentration of each element).

7. Experimental Methods

This chapter details the various experimental techniques used during the research for fabrication, characterisation and mechanical testing. The parameters and steps detailed in each section were used throughout the research, except for where others are detailed.

7.1 Arc-Melting

Arc-melting is a process carried out at various scales for the fabrication and casting of alloys from raw element feed material. Arc-melting on the laboratory-scale was used extensively during this project, primarily on two different arc-melting systems: Edmund Buehler MAM1, and Arcast Arc 200. The former was used initially, and was suitable for the preparation of up to 6 x 5g ingots at a time. This arc-melting system had limited capacity, and was not suitable for preparing samples containing elements with melting points above approximately 1900ºC – 2000ºC due to limitations on power supply. On the other hand, the Arcast Arc 200 system was more suitable for larger scale alloying, able to melt a single alloy of up to approximately 200 g at a time (or an amount of alloy that does not exceed the melting crucible capacity upon melting). The maximum deliverable current of this system was greater than the MAM1, up to 600 A. This system was therefore capable of processing high-temperature elements, even up to pure W. The vacuum capability of the Arcast Arc 200 system was also greater than for the MAM1, and vacuums of the order 10^{-5} Torr (10^{-3} Pa) were easily achievable thanks to the attached diffusion pump.

Nonetheless, the principles behind the arc-melting technique are generally consistent across models. Fig. 7.1 shows a basic schematic of a typical arc-melting system. A power supply provides a high current to a normally W electrode. The electrode is housed at one end inside a Cu fixture, which itself is attached to the manipulator stick that extends out of the vacuum chamber for use by the operator. The dimensions and tip sharpness of the electrode determine the suitable operating current range (as too high a current can lead to damage or even melting of the electrode), and the shape of the arc used to melt material (a tip sharpened to a point results in a more diffuse arc that covers a larger area, whereas a blunter or flatter tip produces a more focused arc beam). Material to be melted is held in a Cu hearth or crucible, the size and shape of which can differ considerable and is often tailored to the operators need. For instance, specific shapes or depths may be provided if the final ingot is to be formed into such a shape. Cu is chosen as the material due to its extremely high thermal conductivity properties (in fact second only to those of Ag), and this ability to conduct away the intense heat from the arc is augmented by a network of water-cooling pipes inside and underneath the base of the crucible. For this reason, most arc-melting systems need a constant and steady supply of water during operation.

The crucible and electrode assemblies are all encased in the vacuum chamber in which the arc-melting is to be performed. To prevent significant contamination and oxidation of the resulting ingot, the general procedure is to draw a vacuum in the chamber before melting, ranging from 10^{-2} to 10^{-5} Torr (10 to 10^{-3} Pa), depending on the system and the requirements (some elements more readily oxidise than others and so a higher vacuum will be required). Often, to aid in protecting the ingot from oxidation, a small amount of an element with a high affinity for O (typically Ti or Zr) may be melted nearby (but separately) to the material to be melted. These act as a sacrificial ‘getter’, and are used to soak up the majority of residual O that may infiltrate the vacuum chamber due to small leaks etc. After an adequate vacuum is reached, some medium needs to be introduced to a high enough pressure in order to be ionised, producing the arc of plasma. This is most commonly high-purity Ar gas, which may be introduced up to a pressure of -10 and -2 inHg (-34 and -6.7 kPa), depending on the system. Under-pressuring of this ‘back-fill’ gas can prevent the arc from striking, whereas over-pressuring the chamber can exert excessive force on the chamber door or other ports, which may then break the vacuum and introduce leaks. It should be noted that the heat from the arc in operation will also result in a slight increase in chamber pressure, which must be taken into account.

When a suitable back-filled pressure is attained, the current can be delivered safely to the electrode in order to strike the arc for melting. It is usually necessary to strike the arc by positioning the electrode tip quite close (1-3 mm) from, or even touching, either the getter, a separate W striking pin, or even the crucible itself. Using a strike pin in this way can have a slight chance of inadvertently introducing molten W as a contaminant to the sample, but at the same time using the crucible to strike arc can over time mark, scratch and damage the crucible surface. Once arc is struck and is stable (no more than 1 or 2 seconds), the manipulator can be used to raise the electrode tip and apply the arc to the material to be melted, generally at a distance of at least 25 mm from the material, otherwise molten material may splash or otherwise contaminate the W electrode and result in melting. Once the material has been sufficiently melted, it is usually necessary to wait generally 5 - 10 minutes for the electrode and crucible to cool. The melting should generally not be sustained for periods more than 60 seconds at a time to avoid damage to the equipment. Ingots produced may be turned over and re-melted to improve homogeneity as required. Some systems, such as the Arc 200, can also employ magnetic stirring of the molten material (again, this can also increase the internal pressure of the chamber and so should be monitored).

Except where otherwise stated, arc-melting carried out with the Arcast Arc 200 was performed with a maximum operating current of 400 A, the amount delivered controlled by a foot pedal. The arc was struck on a W striking pin embedded in the side of the Cu crucible, and material was then melted for a period of 5 – 10 seconds at a time, for 5 melts. During the final melt, magnetic stirring was employed for at least 5 seconds.

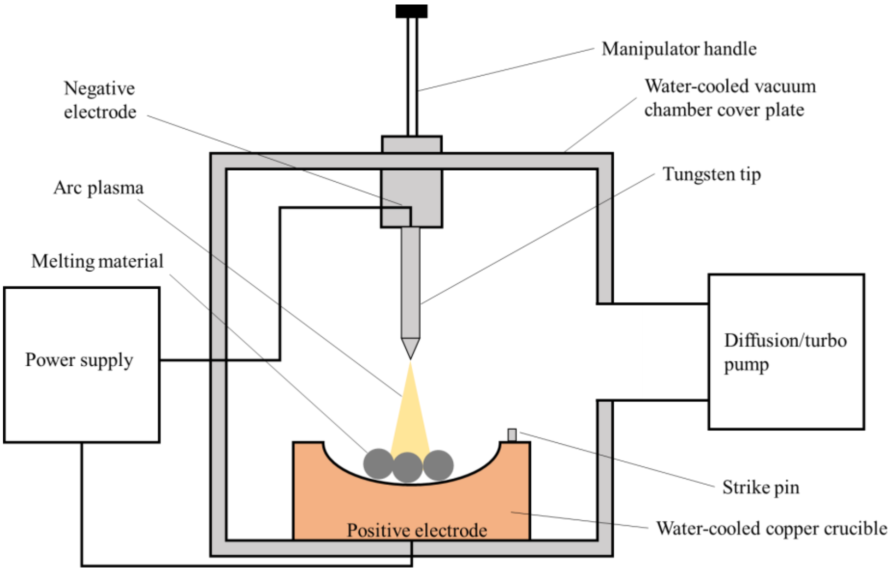

Figure 7.1: Schematic of basic arc-melting system used for fabrication of alloys and casting.

7.2 Vacuum Furnace and Belt Furnace Brazing

The principles of brazing in general, and vacuum furnace and belt furnace brazing in particular, are covered in Chapter 1 of this work. However, two different vacuum furnaces and one belt furnace was used for the research presented here. The majority of trials for vacuum furnace brazing of IN718, detailed in Chapters 10 and 11, were conducted at Kepston Ltd. (Walsall, UK). The second vacuum furnace, used for further trials in chapter 11, was the furnace installed at the Royce Translational Centre, and operated by the National Metals Technology Centre (NAMTEC). The brazing parameters used for these trials are detailed where relevant in the proceeding chapters. The belt furnace used in this research was operated by Armeg Ltd. (Dronfield, UK), and was used for work detailed in Chapter 10 (Sections 10.5 and 10.7), with exact parameters detailed there.

Regardless of which furnaces were used, appropriate preparation of materials was critical. Base material to be brazed was in each case ground with p1200 SiC grit papers to remove contaminants and oxide layer from the surface prior to brazing (within 24 hours prior). Both base metals and filler metals (in foil form) were then also ultrasonically bathed for at least 5 minutes, except where otherwise stated. Where the filler metal used was in the form of paste (containing powdered filler metal, see next section for details of production), the paste was stored in a plunger syringe used for applying the paste. Paste kept this way, where an organic binder is used, is suitable for storage for approximately 6 months, preferably refrigerated. As paste used in the present work was used within one week of its preparation, refrigeration was not necessary. Paste was added to filler metal powder and stirred manually, with a weight ratio of binder to filler metal powder of 12:1, and for this research 30 g of filler metal paste was produced.

7.3 Gas-Atomisation

Gas atomisation is a technique for producing metal powders, where the metal is first melted before introducing a jet of gas to separate the melt into droplets, which then solidify in powder particles of varying sizes, but generally below 150 μm. The solidified droplets then collect at the bottom of the chamber, which is typically filled with inert gas. Gas atomisation has been found to produce particles of greater sphericity than those produced by water atomisation. The distribution and range of droplet, and hence particle size, is dependent on the material, the gas jet velocity and application, and the temperature of the melt. The rate of solidification is then also a function of particle diameter, and this then has an effect on the microstructure of the metal powder produced. Some atomisation chambers may be partially filled with water to increase the cooling rate. Fig. 7.2 shows a basic schematic of a gas atomisation set-up.

The gas to metal ratio is a primary controlling factor in the resulting particle size distribution. The ratio itself is a result of the volume of gas delivered to a volume of molten metal in a given period of time, and so controlling the gas flow and metal flow is required. The median particle diameter, D_m, can be given as a function of gas flow, G, and metal flow, M, as in Equation 7.1:

$$D_m = \frac{k}{\sqrt{G/M}} \qquad (7.1)$$

where k is a constant median particle size, in μm, for a gas flow of 1 m^3 per 1 kg of molten metal.

There is a demand, in certain applications (e.g. metal injection moulding), for fine powders of average size below 20 µm. Average particle size this low are not typically required for use as brazing filler metal powders, and indeed may be undesirable. Filler metal foils generally have a thickness of 50 µm for a suitable gap width, and filler metal powders should have a size distribution accordingly. A typical size range used in a filler metal paste might have a D90 (that is, the diameter under which 90 % of the powder particles possess) of 120 µm, a D50 of 60 µm, and a D10 of 20µm. Sieving can then be used to further reduce the range of particle size as necessary. As long as a majority of the powder is of adequate size (approximately 50 µm), separating out smaller sizes is generally not necessary, and the smaller particles can in fact fill in gaps between larger particles. For these reasons, advanced gas atomisation techniques that ensure small particles sizes were not required for the filler metal powder used in this work. Gas atomisation to produce the powder required for a brazing filler metal paste for this work was carried out externally, by Arcast Inc.

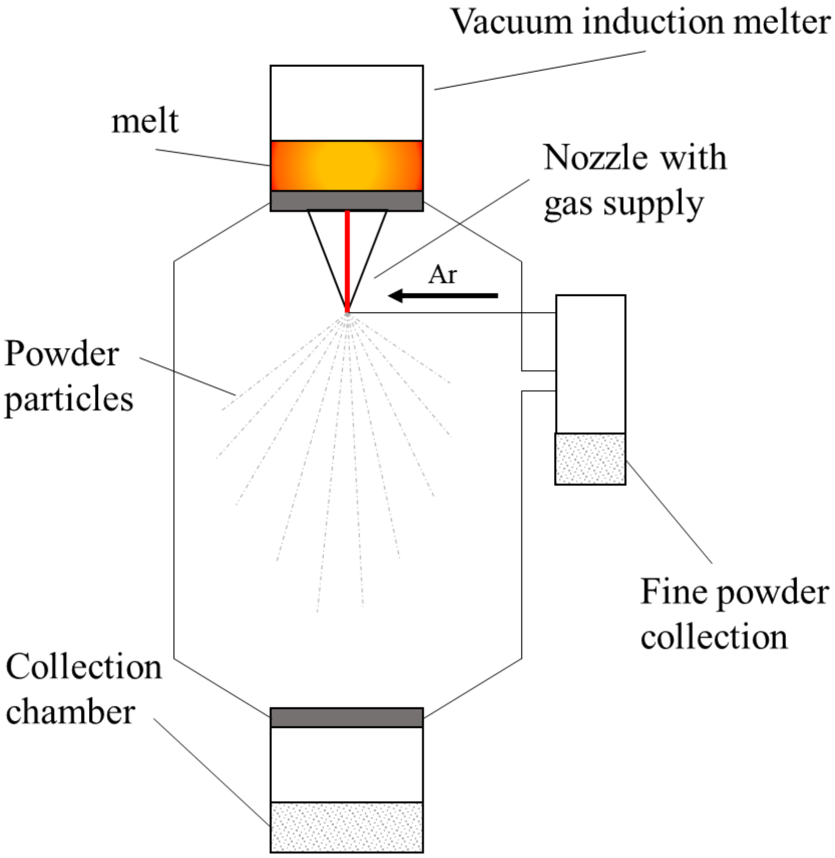

Figure 7.2: Schematic of typical gas atomisation set-up for production of metal powders.

7.4 Scanning Electron Microscopy

Electron microscopy, as the name suggests, uses a beam of electrons in vacuum aimed at a sample under investigation in order to analyse the structure of a wide range of biological and non-biological materials. Normal 'optical' microscopes are limited in their resolution by the wavelength of visible light used to illuminate the surface of the sample (approximately 400 – 700 nm). The best resolution possible is limited to approximately half of the wavelength used, thus optical microscopy has a theoretical maximum resolution of around 200 nm. However, since the wave-like properties of particles were posited, wavelengths much shorter than that of visible light could be used to break this limit. The de Broglie wavelength of electrons in the beam, given by Equation 7.2, can be shown to depend on the electron velocity, in turn determined by the accelerating voltage as in Equation 7.3. It can therefore be determined that the theoretical maximum resolution is less than 4 pm at a 100 keV accelerating voltage.

$$\lambda = \frac{h}{\rho} = \frac{h}{mv} \qquad (7.2)$$

$$eV = \frac{1}{2}mv^2 \qquad (7.3)$$

where λ is the wavelength, h is the Planck constant (= $6.63 \text{x} 10^{-34}$ J·s), m is the electron mass, v is the electron velocity, e is the electron charge, and V is the voltage. Therefore, the electron microscope offers the capability to achieve far greater resolutions than traditional optical microscopy.

Scanning electron microscopy (SEM) is a type of electron microscopy where the image is formed by scanning a beam of electron over the sample. Fig. 7.3 shows a schematic representation of a typical scanning electron microscope and its components. The electrons interact differently with different atoms, and these interactions contain information needed to form an image or determine composition. In the normal imaging mode, secondary electrons (that is, electrons that have been emitted from an atom as a result of the energy from the incident electron beam) are detected, with the number detected determining the signal intensity in the image. As the incidence angle of beam differs across an uneven surface, the amount of secondary electrons emitted varies, creating the contrast seen in SEM images and allowing the topography of the sample to be observed. Other types of electron detected are known as backscattered electrons. These are higher energy electrons originating in the beam, which are reflected back from a sample due to elastic scattering when interacting with an atom. The amount of scattering is greater for heavy elements and less for light elements, and so this creates a contrast in the backscattered electron image between regions of different chemistry. This is particularly useful in studying microstructure in metals, allowing the elemental distribution between phases to be observed.

In most standard SEMs, the electron beam is produced thermionically (released through increasing temperature) from an electron gun which has a (typically) W filament. The beam is sequentially focused electromagnetically by two condenser lenses. The scanning raster is then implemented by deflector coils, allowing the beam to scan lines over the sample. Sample preparation is critical for obtaining quality images. While compared to biological samples, preparation for metallic samples is simpler, there is still a need to grind and polish samples and to mount in an electrically conductive material to fit the sample holder. Unless otherwise stated, samples in the present work were ground, sequentially, using p800, p1200, p2500 and p4000 SiC grit papers, before polishing with diamond suspensions with particle size 6, 3, 1 and 0.25 μm. Samples were mounted in conductive Bakelite using a Buehler Simplimet mounting press. The SEM used in this work was an FEI Inspect F50, and unless otherwise stated the accelerating voltage used was 20 keV, the spot size was 4, and a working distance of approximately 10 mm was used.

Another key technique used in the present work was Energy Dispersive X-ray Spectroscopy (EDS). EDS is a technique allowing the composition of materials to be examined. The electrons from the beam incident on an atom within the sample may excite an electron from an inner, low energy orbital shell. A higher energy electron from an outer shell may then fill in the hole left by the escaped electron, but as shells can only accommodate discrete electron energy levels, the excess from this outer shell is released as an X-ray. As the X-ray energy has a characteristic energy for that atom, the atom can be identified. At the same time, the amount of these characteristic X-ray detections gives information on the abundance of that element in the sample. The EDS software used in this project was Aztec (Oxford Instruments).

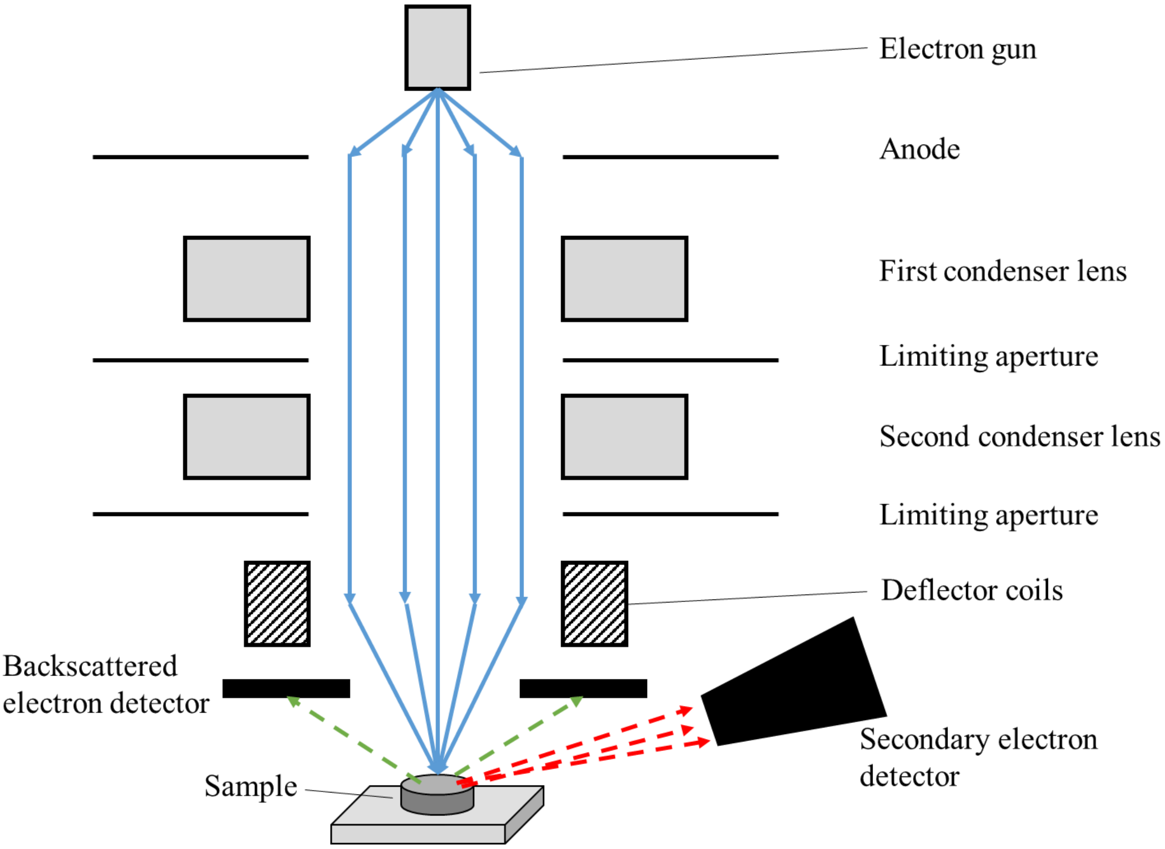

Figure 7.3: Basic schematic of standard Scanning Electron Microscope (SEM) and major components.

7.5 X-Ray Diffraction & X-Ray Fluorescence

X-ray diffraction (XRD) is a useful tool for determining numerous physical properties of a crystalline material by exploiting the diffraction of incident X-rays by crystal planes in a material. As X-ray wavelengths are in the range 0.01 – 10 nm, this is roughly of the order of separation of crystal planes, allowing diffraction to occur. The properties that can be determined through X-ray diffraction include phase, crystal structure, orientation, lattice parameter, crystallite size, lattice strain and dislocation density, among others.

The diffraction behaviour between the incident X-rays is described by the Bragg equation in Equation 7.4:

$$n\lambda = 2\,d\,\sin\theta \qquad (7.4)$$

where n is the order of reflection (typically only the n = 1 reflection is used in crystallography), λ is the wavelength of the incident X-ray, d is the distance between crystal planes, and θ is the angle between incident X-ray and the diffracting plane.

Incident X-rays are either scattered by atoms on a crystal plane or they transmit through unimpeded. When an incident beam is diffracted by the first plane, whereas a parallel beam is diffracted by the second plane having transmitted through the first, we may get constructive or destructive interference (or in practice, something in between). Complete constructive interference, that is, two in-phase beams combining their amplitudes, occurs when the second beam travels an integer number of wavelengths more than the first beam. Complete destructive interference, that is, out-of-phase beams cancelling out each other's amplitudes, when the second beam travels a half-integer number of wavelengths further than the first. In practice, there is often varying degrees of constructive and destructive interference occurring, though the occurrence of constructive interference is what produces the characteristic peaks in the X-ray signal. For a single angle of incidence, we see that we may not satisfy the Bragg condition for constructive interference which would give us a characteristic peak. However, by varying the angle of incidence through a range of θ, we can achieve constructive interference at the angle which satisfies the Bragg condition. Therefore, information collected by an X-ray diffractometer is generally plotted as a spectra of peak intensity versus 2θ (2θ is used as this is the difference in angle between the original incident beam and the diffracted beam detected).

For simple crystal structures such as FCC and BCC, there are different planar spacings, d, and so for any plane (h,k,l), the inter-planar spacing is often denoted d_{hkl}. As the spacings change, so does the θ that satisfies the Bragg condition. This means that a certain crystallographic plane will have a characteristic peak at a certain 2θ. These peaks can therefore be used to identify crystal structure. For multiphase samples, or intermetallic and non-cubic phases, databases XRD spectra exist containing patterns for a vast number of phases and compounds, which can be match to the pattern of a sample. The XRD in this work was conducted using a Bruker D2 Phaser diffractometer, with a Cu Kα1+2 anode. An air scatter screen module was used with 3 mm setting, and two Ni Kβ filters were fitted. The primary divergence slit was 1 mm. Sample were rotated at 15 revolutions per minute in order to maximise the area scanned of irregular shaped samples. Software used for X-ray pattern indexing was International Centre for Diffraction Data's (ICDD) Sieve+. This was used to search Powder Diffraction Files (PDF) cards of indexed phases, from the -4+ database.

X-ray fluorescence (XRF), in contrast to X-ray diffraction, gives information on the composition of a material, and has similar principles to EDS. Incident X-rays of sufficient energy on a material may ionise the material, causing the excitation and loss of an electron from the lower energy inner orbitals. The now unstable atom replaces this electron with one from a high energy outer shell, to regain stability. The difference in energies between the electrons is released in the form of photons (hence fluorescence) which are characteristic of the particular orbital shell in the particular atom being irradiated. In this way, the type of atom can be identified, and so the bulk composition of a metallic sample can be determined. XRF conducted throughout this research was performed with a PANalytical Zetium spectrometer, and the sample cup spot size used was 6 mm.

7.6 Differential Scanning Calorimetry

Differential Scanning Calorimetry (DSC) is a technique for determining the temperature at which thermally-induced phenomena occur in a sample, and the energy released by such phenomena. This is done by heating a sample and measuring the amount of heat applied required to heat the sample. A reference sample, usually an empty crucible of the same material as the crucible holding the sample, is heated and maintained at the same temperature of the sample, and the different heat required to maintain the same temperature provides the DSC signal, generally displayed as heat flow as a function of temperature. When a phase transformation, crystallisation or melting occurs, the heat flow will need to decrease (for an exothermic reaction) for the sample being analysed compared to the reference crucible, or increased (for an endothermic reaction). In this way, the DSC signal can be used to determine such properties as solidus, liquidus, and temperatures at which phase transformations occur in a metallic material.

In this work, samples in Chapter 8 were analysed using a TA Instruments SDT Q600 DSC calorimeter, whereas samples in Chapters 10 and 11 were analysed in a Netzsch 404 F1 Pegasus calorimeter. For all samples, an alumina crucible was used, and ramp rates used were 20°C min^{-1} except where else stated. An inert gas supply of Ar was maintained throughout. Typical sample mass used was between 20 and 60 mg, and of sufficient size to fit in the 6 mm diameter alumina crucible, covering as much of the base as possible.

7.7 Mechanical Testing

Of the wide range of mechanical testing available for materials, there are some that are particularly relevant for testing the mechanical properties of brazed joints. As the brazed joints produced throughout this project were single lap joints or sandwich joints, shear strength of the brazed joint was used as a key measure of mechanical integrity, as is commonly used in the literature. Shear can be applied to such joints using standard universal testing machines in either tensile or compressive mode. For such testing in this work, a Zwick Roell 0.5 tester was used, with 50 kN load cell connected. All such testing was performed at room temperature, and the loading rate for shear testing was maintained at $2\text{x}10^{-3}$ mm s^{-1} for all tests.

Other methods used for determining mechanical properties of both materials and brazed joints included hardness measurements via microindentation. Hardness, while not in itself an inherent property of a material, provides insight as to other properties. These rely on optical measurement of the dimensions of the indent left on the material by a diamond-tipped indentor after some constant compressive load applied for some dwell time. Microhardness can also give an approximate indication as to the ductility or brittleness of a material, both in the value itself and by optically examining the region of the indent (cracks or deformation may be visible). This can be particularly valuable in multi-phase materials, as the relative ductility between phases may be examined. In brazed joints, the difference in properties between the base material and the filler material, as well as between different phases in the filler material post-braze, can be investigated. In this research, microhardness was performed using a Struers Durascan microindentor. Except where otherwise stated, the compressive load used was HV0.05 (equivalent to 0.05 kg of compressive load), and the dwell time applied was 15 s.

8. Selection of Alternative Melting Point Depressants

This chapter details the early experimental stages of this project, involving the consideration, and then evaluation, of potential alternative MPDs that may be useful in the development of novel Ni-based filler metal compositions. Using binary phase diagrams of Ni with the prospective MPDs, as well as Thermo-Calc (TC) software, potential MPDs were judged on their effect on liquidus temperature in a binary Ni alloy, considering both the liquidus achievable and the amount of MPD required for this, and also their solubility in an FCC Ni matrix (or low likelihood of forming brittle intermetallics, but this is less easy to ascertain).

Initially, focus was placed on identifying novel, yet 'conventional', alloy compositions. That is, being similar to current Ni-based filler metals in their majority Ni composition (above approximately 75 wt. %), and limiting the content of MPD accordingly. The MPDs were also evaluated for their potential to completely negate the need for currently used MPDs such as B and Si where possible, in order to avoid possibility of very brittle boride or silicides forming in the joint. However, MPDs that still form other intermetallics are not necessarily ruled out unless they are known to be particularly detrimental, or more-so than borides or silicides. Thus, potential MPDs were first considered for further investigation if they satisfied:

- A reduction in liquidus to at least below approximately 1200°C, requiring no more than approximately 25 wt. % of the MPD in the alloy, according to the binary phase diagram.
- Solubility in FCC γ-Ni matrix to some degree, greater than that of B and at least comparable to that of Si, such that intermetallics might be avoided up to a certain amount of MPD used necessary for adequate liquidus suppression.
- No other incompatibilities for practical (for example, particularly expensive elements or elements in a form unsuitable alloy fabrication via arc-melting) or health reasons.

8.1 Ni-In System

8.1.1 Phase Diagram Consideration

In, meeting the broad initial requirements detailed above, was selected for further study as a novel MPD element to use in a Ni-based brazing alloy. The Ni-In binary phase diagram is shown in Fig. 8.1. A eutectic exists at 910°C for a composition of 24 at. % (39.5 wt. %), where liquid freezes to form a two-phase ζ (non-stoichiometric) + Ni solid solution. Therefore, between the eutectic and pure-Ni compositions, In reduces the liquidus by approximately 13.8°C per 1 wt. %, and so a 1200°C liquidus can be obtained with an approximately 18.5 wt. % alloying addition. For comparison, this figure for B would be approximately 100.6°C per 1 wt. %. In also exhibits solubility in the FCC γ-Ni of up to approximately 7.5 at. % (14.5 wt. %) at 910°C, though this decreases to negligible solubility at temperatures below 200°C.

As an alloying addition, In is not generally used in Ni or its alloys. Several intermetallic phases are formed exhibiting various crystal structures: Ni_3In (hexagonal, $P6_3/mmc$), Ni_2In (hexagonal, $P6_3/mmc$), $Ni_{13}In_9$ (monoclinic, C_2/m), NiIn (hexagonal, $P6/mmm$), NiIn (hexagonal, $P6/mmm$), Ni_2In_3 (trigonal, $P\bar{3}m1$), Ni_3In_7 (cubic, $Im\bar{3}m$), δ (cubic, $Pm\bar{3}m$) and ζ (undocumented crystal structure). For microstructural and mechanical reasons, therefore, it was deemed perhaps necessary to limit the In content further than just the 25 wt. % upper limit mentioned above.

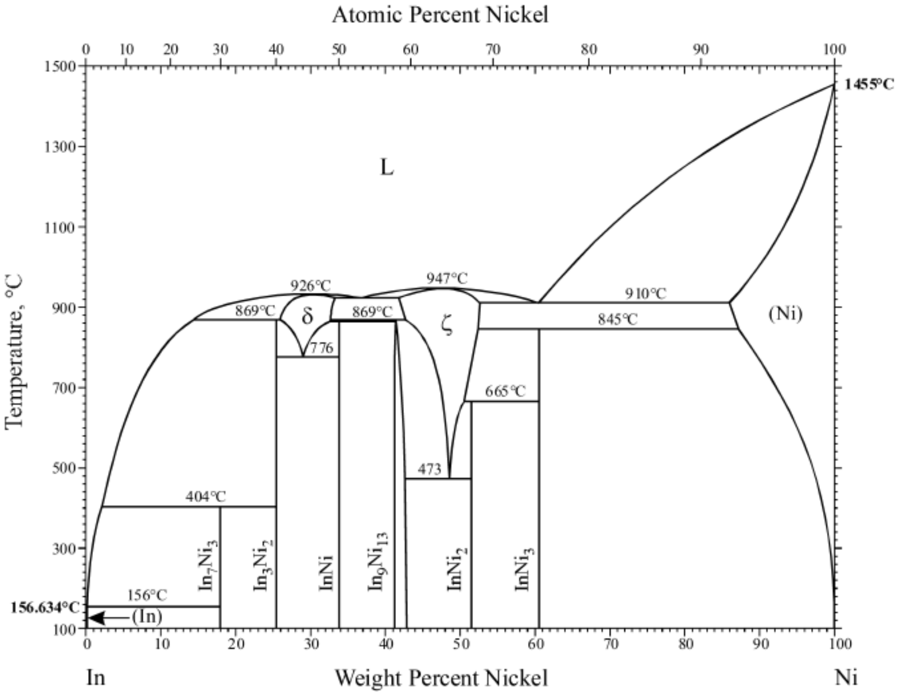

Figure 8.1: Ni-In binary phase diagram, in ASM Handbook [18], and based on [196]).

8.1.2 Thermo-Calc Analysis

The Ni-In system was also modelled using TC software for comparative purposes, and to assess the accuracy of TC when predicting properties of In as an alloying addition to Ni. This second point is important, given that, despite the existence of established phase diagrams for the Ni-In system, no database versions (of those available for the duration of the project) within TC contained experimentally verified data for the CALPHAD modelling. Therefore, comparisons drawn between the established phase diagrams and the predictions of TC may inform the accuracy of further alloy development, especially for cases where TC lacks the experimental data. The database used was the SSOL4 database, which contains the most elements available for modelling (and the only one available to allow modelling of In with Ni). SSOL4 contains experimental data for many binary combinations, but not for the Ni-In system. It should be noted that the more recent SSOL6 database does contain assessed data for the Ni-In system, but was not available in this project.

Fig. 8.2 shows the TC Ni-In phase diagram, for In compositions up to 50 wt.%, demonstrating the lack of information predicted for the system. Only a Liquid + FCC A1 region is predicted, corresponding seemingly only to the upper right corner of Fig. 8.1. Meanwhile, plotting phase abundance versus temperature for specific Ni-In compositions (in steps of 5 wt.% In from 0 to 50 wt. %) shows that only FCC_A1 solid solution is predicted to exist across all temperatures, and even at compositions above where, according to Fig. 1, solid solution would not form. Fig. 8.3 shows the TC predicted solidus and liquidus lines for this phase superimposed on the Ni-In phase diagram for comparison.

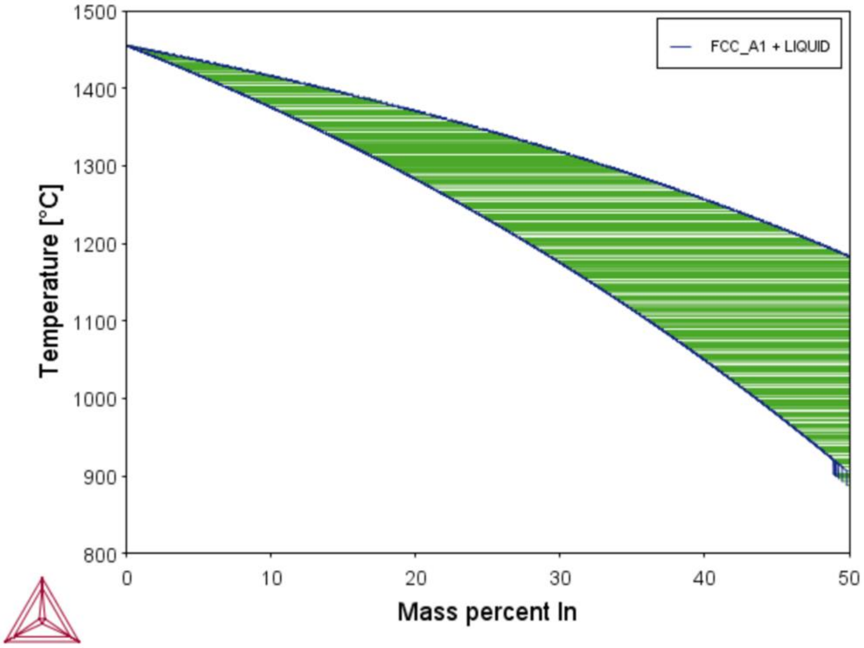

Figure 8.2: TC predicted phase diagram for the Ni-In system, for In compositions of up to 50 wt. %.

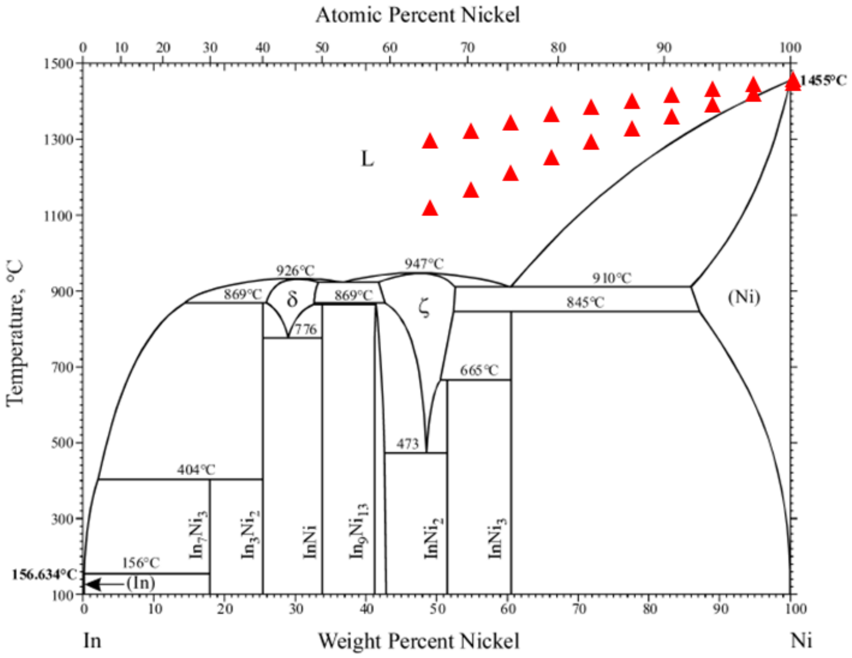

Figure 8.3: TC predicted solidus and liquidus lines for the FCC_A1 phase superimposed on the Ni-In binary phase diagram from Fig. 1.

8.1.3 Fabricated Binary Ni-In Alloys

To further investigate the Ni-In system for prospective application as a filler metal, a series of three binary alloys were fabricated via vacuum arc melting. These were made with the aim of comparing the as-cast microstructures and solidus and liquidus temperatures with both the phase diagram in Fig. 8.1 and the TC predicted phase diagram in Fig. 8.2, and also informing on the feasibility and suitability of fabricating such alloys through the arc-melting method in general. It should be noted, however, that both the phase diagram and TC predictions represent the equilibrium case, which is unlikely to be achieved from the arc-melting process due to the rapid cooling rate. Therefore, differences may well be expected between observations and what would be expected considering both the phase diagram and TC predictions. However, Ni-based filler metals are often supplied in the form of foils or powders, the production of which also involve rapid cooling, and so are also unlikely to be in their equilibrium state, so investigating the as-cast state of the Ni-In alloys is still informative. Furthermore, given the large difference in melting points and vapour pressures between Ni and In, it was not inconceivable that some difficulty in achieving desired alloy chemistry may have been encountered, and so the suitability of this fabrication method can be demonstrated.

Raw materials of Ni foil (0.5 mm thickness) and In shot (4mm size and down) were sourced from Alfa Aesar, both with purities above 99 %. Nominal compositions selected for fabrication were 5, 10 and 15 wt. %, with 5 g of each alloy prepared. The MAM1 arc-melter was used for melting, with the current set to 3 on the operating current dial. The chamber was evacuated to achieve a vacuum of below $6x10^{-5}$ torr ($8x10^{-3}$ Pa), before backfilling with Ar gas to a partial pressure of -0.7 Bar (-70 kPa). A Ti getter was placed in the melting crucible, which was melted before each alloy in order to trap any residual impurities. Due to the small quantity and difference in melting temperatures, the current was applied for no more than 5 seconds at a time, and the formed buttons were flipped and re-melted 5 times to improve homogeneity.

Table 8.1 displays XRF-measured bulk composition of the samples, and Fig. 8.4 shows SEM BSE micrographs for the as-cast (a) Ni-5In, (b) Ni-10In and (c) Ni-15In alloys, with EDS maps also shown in Fig. 8.5. Table 8.2 shows the EDS point scan measurements for the phases in each alloy (averages of five measurements). The microstructure of each alloy is characterised by three distinct phases; a dark contrast Ni-In solid solution, a grey phase richer in In, possibly an In-saturated solid solution according to the phase diagram, and a light contrast phase richer in In but punctuated by small islands of Ni-rich phase (~ 1 µm or less but with some larger islands). This latter phase is likely a the Ni_3In phase according to the phase diagram. The grey phase surrounds the light phase, giving the appearance of a somewhat cored microstructure, arising presumably from the solidification sequence Ni-In solid solution → In-saturated solid solution → Ni_3In phase. The apparent fraction of the light contrast Ni_3In increased with increasing In content, as in Fig. 8.4(c), whereas the grey contrast phase appears to be equally prevalent across compositions. For the Ni-10In and Ni-15In alloys, there was a noticeable region exhibiting a different microstructure towards the lower portion of each ingot (i.e. the portion in closest contact with the Cu hearth in the arc-melter), with lower concentration of the Ni_3In phase, but with longer dendrites.

Table 8.1: Bulk composition in wt.% (at.%) of Ni-5In, Ni-10In and Ni-15In alloys as measured by XRF.

Alloy	Ni – wt.% (at.%)	In – wt.% (at.%)
Ni-5In	95.4 (97.6)	4.6 (2.4)
Ni-10In	90.7 (94.8)	9.3 (5.2)
Ni-15In	87.0 (92.9)	13.0 (7.1)

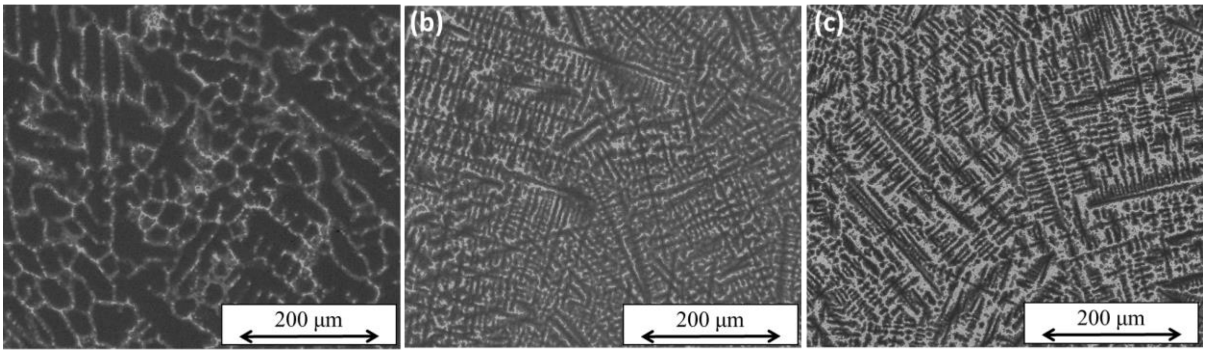

Figure 8.4: SEM BSE micrographs of as-cast (a) Ni-5In, (b) Ni-10In and (c) Ni-15In, in wt. %.

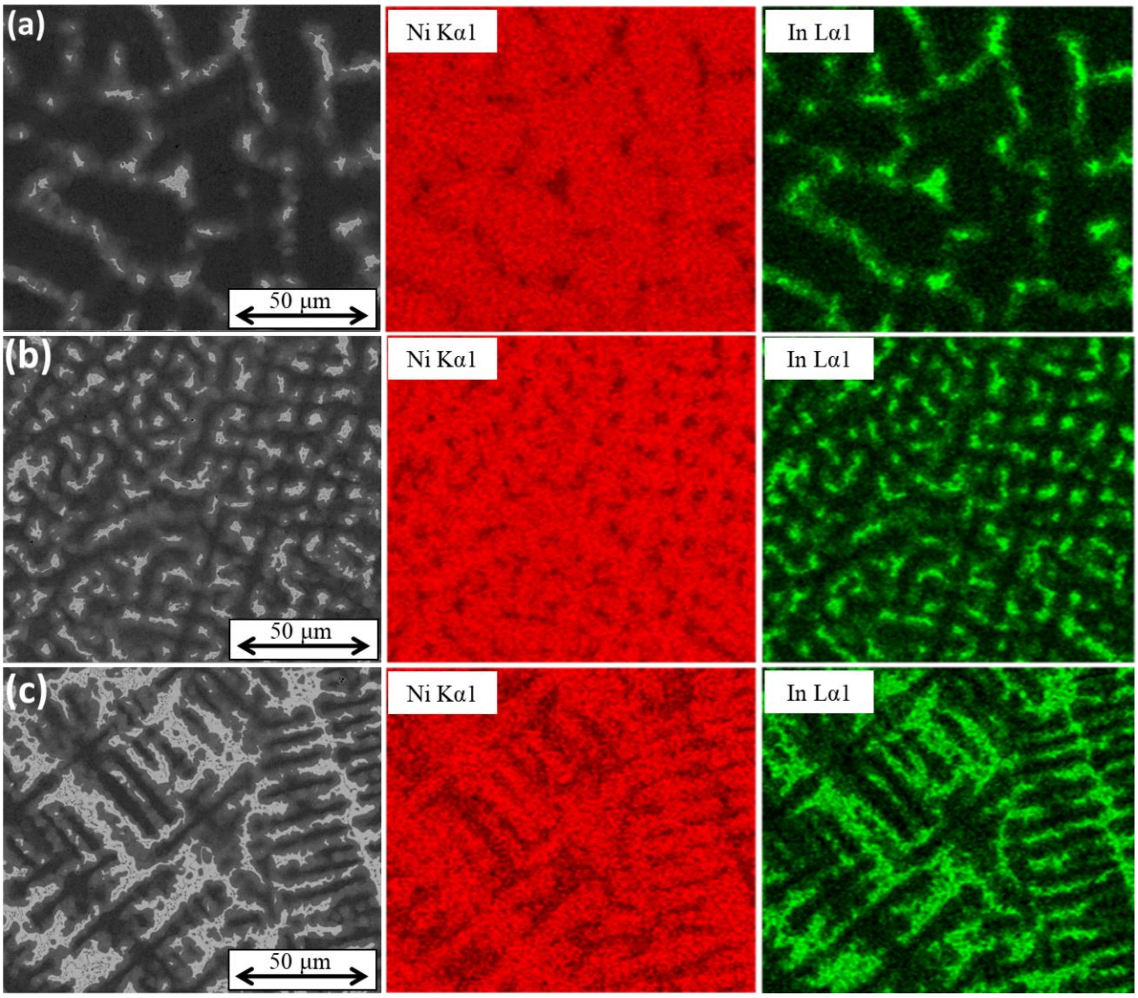

Figure 8.5: SEM BSE micrographs (at increased magnification compared to Fig. 8.4) of as-cast Ni-5In, Ni-10In and Ni-15In alloys, with EDS mapping showing distribution of Ni and In in phases observed.

Table 8.2: EDS point scan measurements for as-cast Ni-5In, Ni-10In and Ni-15In alloys (average of 5 measurements, errors derived from standard deviation).

Alloy	Phase	Ni (atomic %)	In (atomic %)
Ni-5In	Light contrast	75.9 ± 2.3	24.3 ± 2.0
	Grey contrast	92.3 ± 0.84	7.7 ± 0.84
	Dark contrast	99.3 ± 0.05	0.7 ± 0.05
Ni-10In	Light contrast	74.7 ± 2.9	25.3 ± 2.9
	Grey contrast	92.2 ± 0.52	7.8 ± 0.52
	Dark contrast	98.2 ± 0.19	1.8 ± 0.19
Ni-15In	Light contrast	71.3 ± 1.4	28.7 ± 1.4
	Grey contrast	91.5 ± 0.35	8.5 ± 0.35
	Dark contrast	98.3 ± 0.09	1.7 ± 0.09

Fig. 8.6 shows the XRD spectra for the as-cast Ni-5In, Ni-10In and Ni-15In alloys. For the Ni-5In composition, despite two phases being apparent from the SEM BSE micrograph in Fig. 8.4(a), only one phase was resolved by XRD, corresponding to the primary Ni-rich FCC phase. For the Ni-10In and Ni-15In compositions, which exhibited greater fractions of the light contrast In-rich phase, peaks for an Ni0.92-In0.08 solid solution phase were indexed, with a cubic NaCl-type crystal structure (space group $Fm\bar{3}m$), that can be described as two inter-penetrating FCC lattices. In addition peak positioned matched those of Ni_3In, of hexagonal crystal structure.

To give some idea of the mechanical properties of these compositions, Vickers microhardness measurements were taken. The average value from 5 measurements for each alloy is shown in Fig. 8.7, with the standard deviation given as the margin of error. The microhardness was found to increase with In content, from a minimum of 160 ± 11 HV for the Ni-5In composition, to 302 ± 3 HV for the Ni-15In composition. This correlates with the apparent increase in fraction of the Ni_3In compound observed in the SEM micrographs (Fig. 8.4), indicating possible embrittlement due to the phase, but also somewhat due to solid solution strengthening of the Ni.

Fig. 8.8 shows DSC curves for the as-cast Ni-5In, Ni-10In and Ni-15In alloys, from which solidus and liquidus temperatures may be read off. The main probable melting events observed in the DSC curves are rather wide as expected from the phase diagram, and clearly much wider than predicted by TC. This made the reading off of solidus and liquidus values somewhat inaccurate, and for the Ni-10In and Ni-15In alloys smaller events were also recorded (possibly corresponding to melting of Ni_3In phase), highlighted in Fig. 8.8. As a general observation, however, the onset and completion of melting appears to occur at lower temperatures with increasing In content. Comparison between phase diagram and TC predicted values of solidus and liquidus are summarised in Table 8.3.

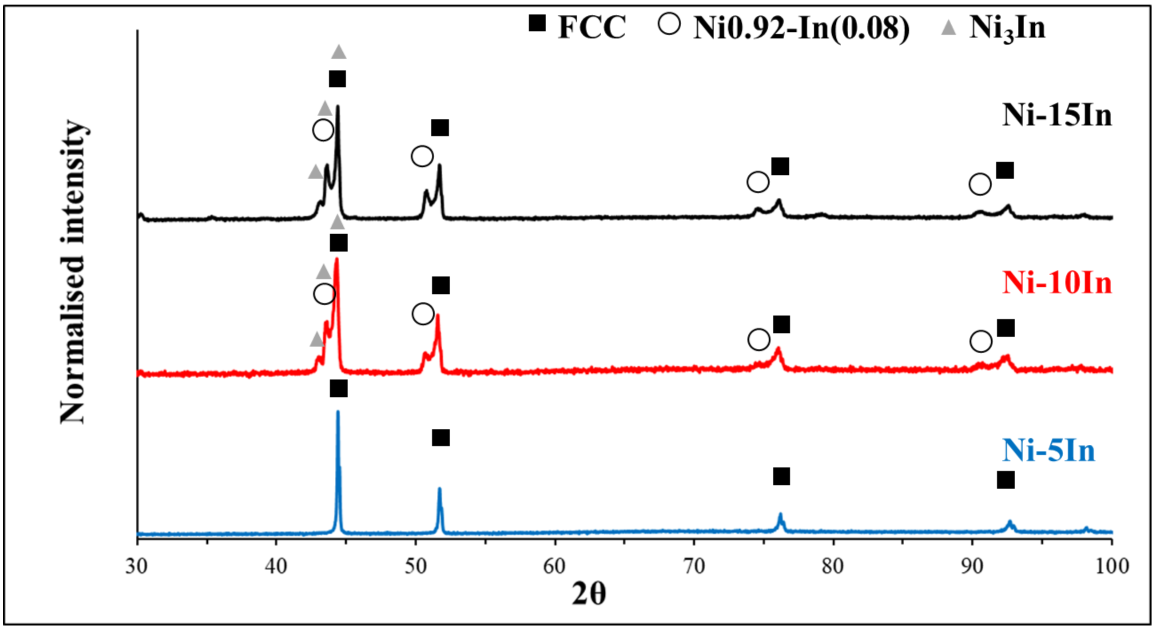

Figure 8.6: XRD patterns for as-cast Ni-5In, Ni-10In and Ni-15In, with peaks indexed as FCC and Ni0.92-In0.08 phase.

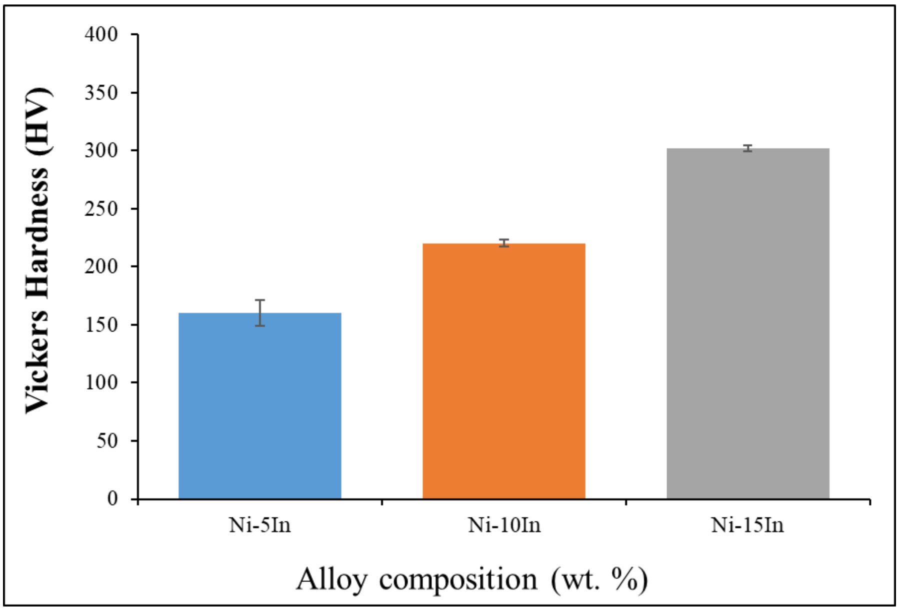

Figure 8.7: Average microhardness (HV1) of as-cast Ni-5In, Ni-10In and Ni-15In alloys (average of five measurements). Error derived from standard deviation.

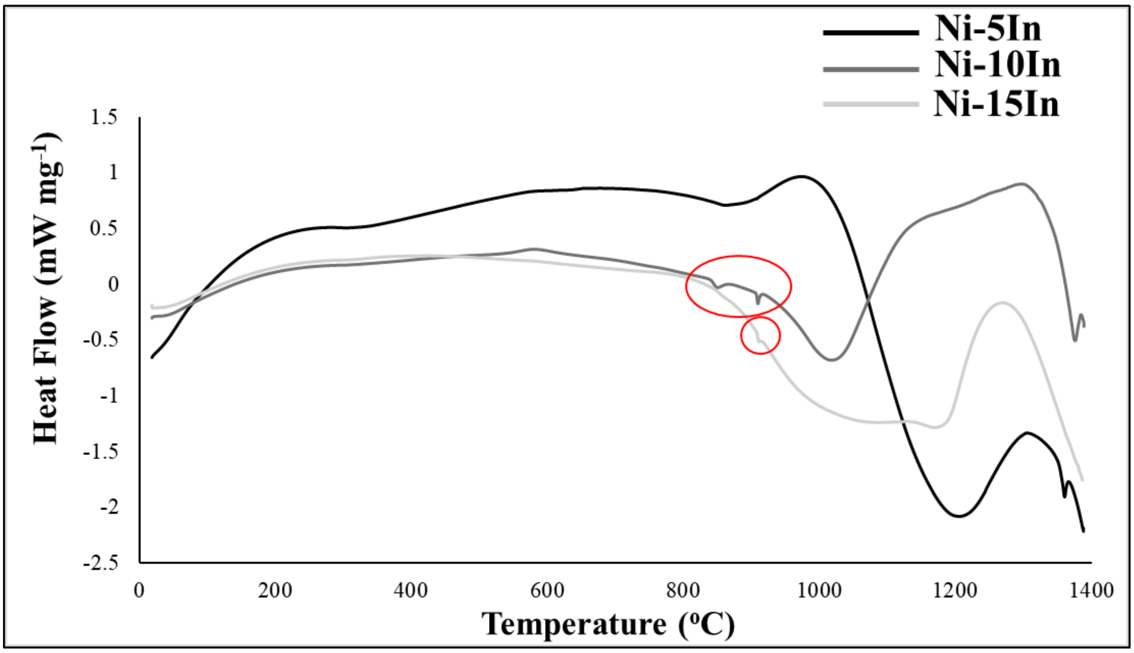

Figure 8.83: DSC Heating curves for as-cast Ni-5In, Ni-10In and Ni-15In.

Table 8.3: Comparison between phase diagram and TC-predicted solidus and liquidus, for as-cast Ni-5In, Ni-10In and Ni-15In alloys.

		Phase diagram	**TC predictions**
Ni-5In	**Solidus (°C)**	1120	1417
	Liquidus (°C)	1386	1436
Ni-10In	**Solidus (°C)**	950	1375
	Liquidus (°C)	1317	1416
Ni-15In	**Solidus (°C)**	910	1331
	Liquidus (°C)	1248	1394

8.2 Ni-In-B System

Considering the main findings detailed in Section 8.1, the use of In as a sole MPD in Ni for use as a brazing filler metal would not be feasible, as high weight percentages (particularly when compared to B content in current Ni-based brazing alloys) would be required to allow for a comparable brazing temperature to current commercial Ni-based filler metals. This is undesirable on both an economic and mechanical basis, as the apparent volume fraction of the intermetallic component of the as-cast alloys increases with In composition, and the microhardness measurements, in Fig. 8.7, show increasing hardness with increased In content, indicating possibly increased brittleness. It is likely that if used during brazing, at a suitably high temperature, this initial as-cast microstructure may be changed such that the volume fraction of intermetallics may be reduced by cross-diffusion of elements. However, In diffusion is most likely slow in Ni and Ni-based superalloys, certainly orders of magnitude slower than for B, and so homogenisation may require excessive (by typical industrial standards) hold times at high temperature.

With this in mind, the addition of B was considered to allow a lower liquidus temperature using a lower concentration of In than would otherwise be required. This could be attractive for several reasons. Firstly, the use of both In and B may mean that, compared to most current B-bearing Ni-based filler metals, a lower B content (hence potential for boride formation) may be used. With lower B concentrations, sufficient diffusion away from the joint may be achieved quicker, thus quicker completion of isothermal solidification. Furthermore, the use of elements such as Si (used as a further MPD in many Ni-based filler metals) may be avoided, or eventually limited to quantities sufficient to improve wettability if required. In, while forming intermetallics with Ni, does not form intermetallics with B. If a low combined In and B content can be realised, an optimised brazing cycle could result in an intermetallic-free brazed joint consisting only of Ni-In solid solution, in times potentially quicker than for current Ni-based brazing alloys. Therefore, a series of Ni-In-B alloys were considered. In content was chosen to be kept at 10 wt. % (5.4 at. %) to strike a balance between lower liquidus and solubility in Ni.

8.2.1 TC Predictions

No ternary phase diagram for the Ni-In-B system was known to be established at the time of this work. Nonetheless, TC was used in a similar manner to predict the effect of B addition on the liquidus of a Ni-In alloy. As in the case of the Ni-In binary alloys, the SSOL4 database was used, and while Ni-In and In-B experimental data is not included in the database, the Ni-B binary system is experimentally verified. Fig. 8.9 shows the TC predicted phase diagrams for B addition of up to 10 wt. % in a binary Ni-10In alloy. TC predicts a very limited solubility range, as might be expected from knowledge of the Ni-B binary system (for which TC has experimentally verified data). A eutectic point is predicted at approximately 3 wt. % B and approximately 1070°C, forming binary FCC solid solution and Ni_3B eutectic, with remaining liquid. Below approximately 1050°C for compositions up to approximately 4 wt. % B, a two-phase microstructure is predicted consisting of FCC solid solution and Ni_3B intermetallics. From these predictions, liquidus temperature decreases with B content until the eutectic composition, at which point the liquidus temperature could be comparable to some currently used commercial Ni-based brazing filler metals. Compositions at 1 and 2 wt. % B would represent sizeable reductions in the B content compared to many, if not most, commercially available B-containing Ni-based filler metals, though the liquidus, as it is predicted, would still be likely too high to merit use. Meanwhile, the 3 wt. % B composition, while not offering a substantial reduction in B content, is predicted to achieve a sub 1100°C liquidus without the use of additional intermetallic-forming MPDs such as Si or P.

Another consideration aside from the solidus/liquidus values predicted for these B-containing compositions, is the predicted boride content. If such alloys were to be used in brazing, then some diffusion of B would be expected to occur, and so boride content post-brazing might be expected to be somewhat diminished compared to any present in an as-cast state (which is what TC predictions of boride content would represent). Nonetheless, compositions with a predicted higher boride concentration could be expected to retain a higher concentration post-brazing, for a given brazing hold-time, while the opposite would be true for compositions with lower predicted boride content. Therefore, this would still warrant some consideration. Fig. 8.10 shows the room temperature boride content predicted by TC for the Ni-10In-(1,2,3)B compositions. The only boride phase predicted is Ni_3B, and the molar percentage of this phase at room temperature predictably increases with B content, and it approaches 60 mol. % for the Ni-10In-3B composition, making it the majority phase. The only other phase predicted is an FCC solid solution, but as with the Ni-In binary alloys, TC does not capture the presence of Ni_3In phase that was observed via SEM, and so this phase might be again expected here.

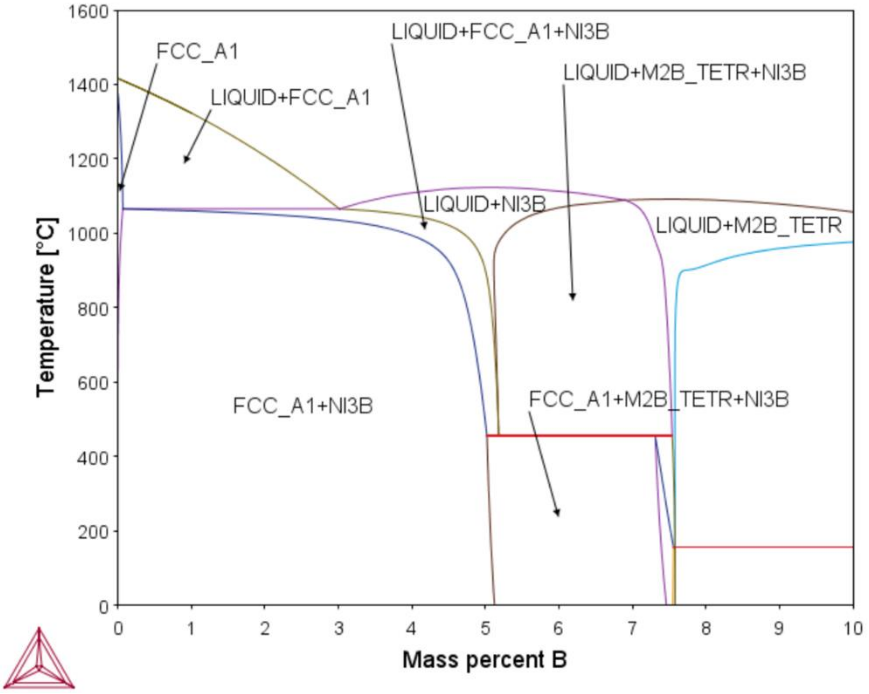

Figure 8.9: TC predicted phase diagram for Ni-10In with B addition of between 0 and 10 wt. %.

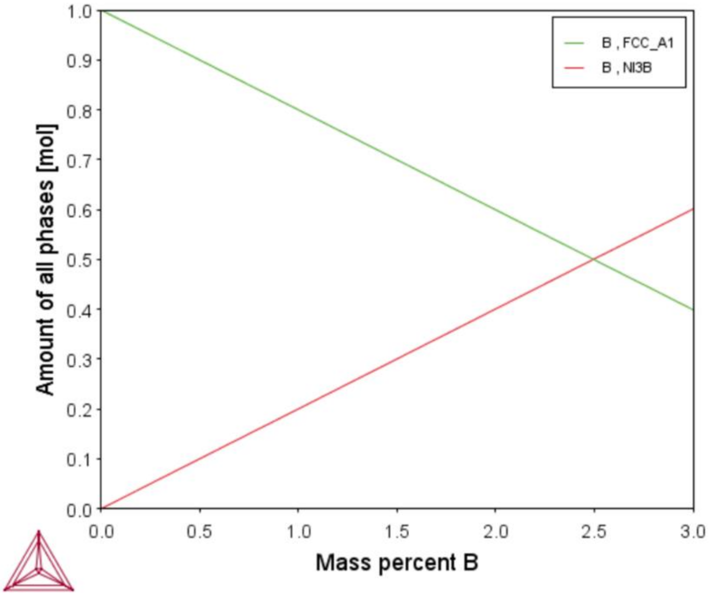

Figure 8.10: TC predictions of Ni_3B phase molar fraction (at room temperature) versus B content in Ni-10In-(1,2,3)B compositions.

8.2.2 Fabricated Ternary Ni-In-B alloys

To investigate the accuracy of predictions made by TC in Section 8.2.1, B content of 1, 2 and 3 wt. % was added to a Ni-10In composition. 5 g alloys of nominal composition Ni-10In-1B, Ni-10In-2B and Ni-10In-3B (in wt. %) were fabricated via arc-melting. Pure B (99.5% purity, Alfa Aesar) was added to pre-alloyed Ni-10In, using the same parameters described in Section 9.1.3. Due to the aggressive arc-melting procedure and the brittleness of B, on several occasions cracked B pieces were ejected from the melt, requiring opening of the melting chamber to place the B back in the crucible. Therefore, the number of re-melts was not constant for each alloy, but was in each case at least three times. Due to the difficulty in detecting light elements such as B, quantification of B content of the as-cast alloys was conducted via Inductively Coupled Plasma – Optical Emission Spectroscopy (ICP-OES) (AMG Superalloys, Rotherham).

Table 8.4 shows results of compositional analysis, using XRF (for Ni and In) and ICP-OES (for B). Intended compositions were largely achieved except for the B content of the nominal Ni-10In-1B alloy, which was found to be 1.655 wt. %. Fig. 8.11(a-c) shows the SEM BSE micrographs for the as-cast Ni-10In-1B, Ni-10In-2B and Ni-10In-3B alloys, with Table 8.5 summarising the composition of each phase, from the average of five EDS point scans. EDS maps at a higher magnification are also displayed, in Fig. 8.12(a-c). For the as-cast Ni-10In-1B and Ni-10In-3B alloys (Fig. 8.10(a) and Fig. 8.10(c) respectively), three distinct phases are apparent; a dark contrast Ni-rich phase, a light contrast In-rich phase, and a grey matrix phase. In the case of the Ni-10In-3B sample, the dark contrast phase takes on a more structured dendritic morphology, whereas for the Ni-10In-1B sample, this phase is more globular with broken up rather than continuous dendrites. In both cases, this dark contrast phase is lean in In, and the dark contrast of the backscattered electron image suggests the presence of lighter elements, and so this phase is likely a Ni-boride phase (the lack of B detection by EDS, as shown in Table 3, in this case is due to the known limitation of the method in detecting elements with atomic mass below that of F). The light contrast phase is also interdendritic and its morphology suggests it was formed from the freezing of the last remaining liquid phase upon solidification. This phase is likely to be the same Ni_3In as seen in the case of the Ni-In binary alloys in Fig. 4. The grey matrix phase is believed to be an In-saturated solid solution, similar to that seen in the Ni-In binary alloys.

Table 8.4: Comparison between phase diagram, TC-predicted, and DSC-measured solidus and liquidus, for as-cast Ni-5In, Ni-10In and Ni-15In alloys.

Nominal (intended) composition	Measured composition (XRF + ICP)	Comments
Ni-10In-1B	Ni-8In-1.655B	Decreased In, increased B
Ni-10In-2B	Ni-8In-2.096	Decreased In
Ni-10In-3B	Ni-8In-3.068	Decreased In

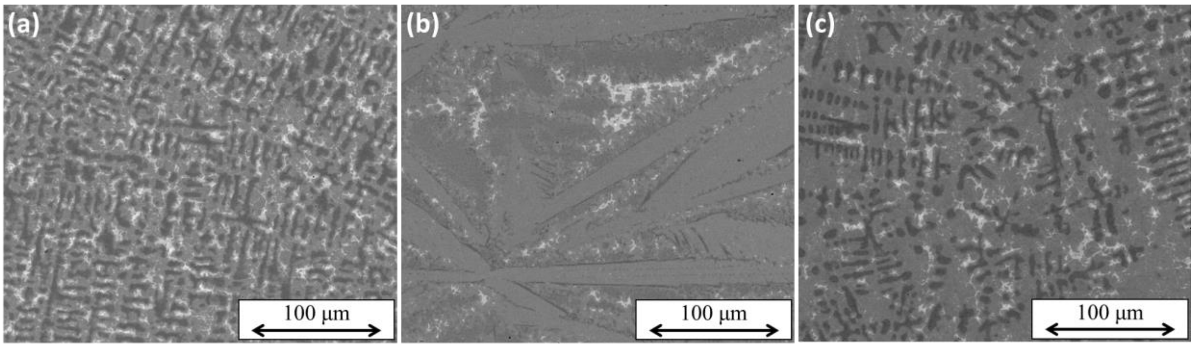

Figure 8.11: SEM BSE micrographs of the (a) Ni-10In-1B, (b) Ni-10In-2B, and (c) Ni-10In-3B alloys.

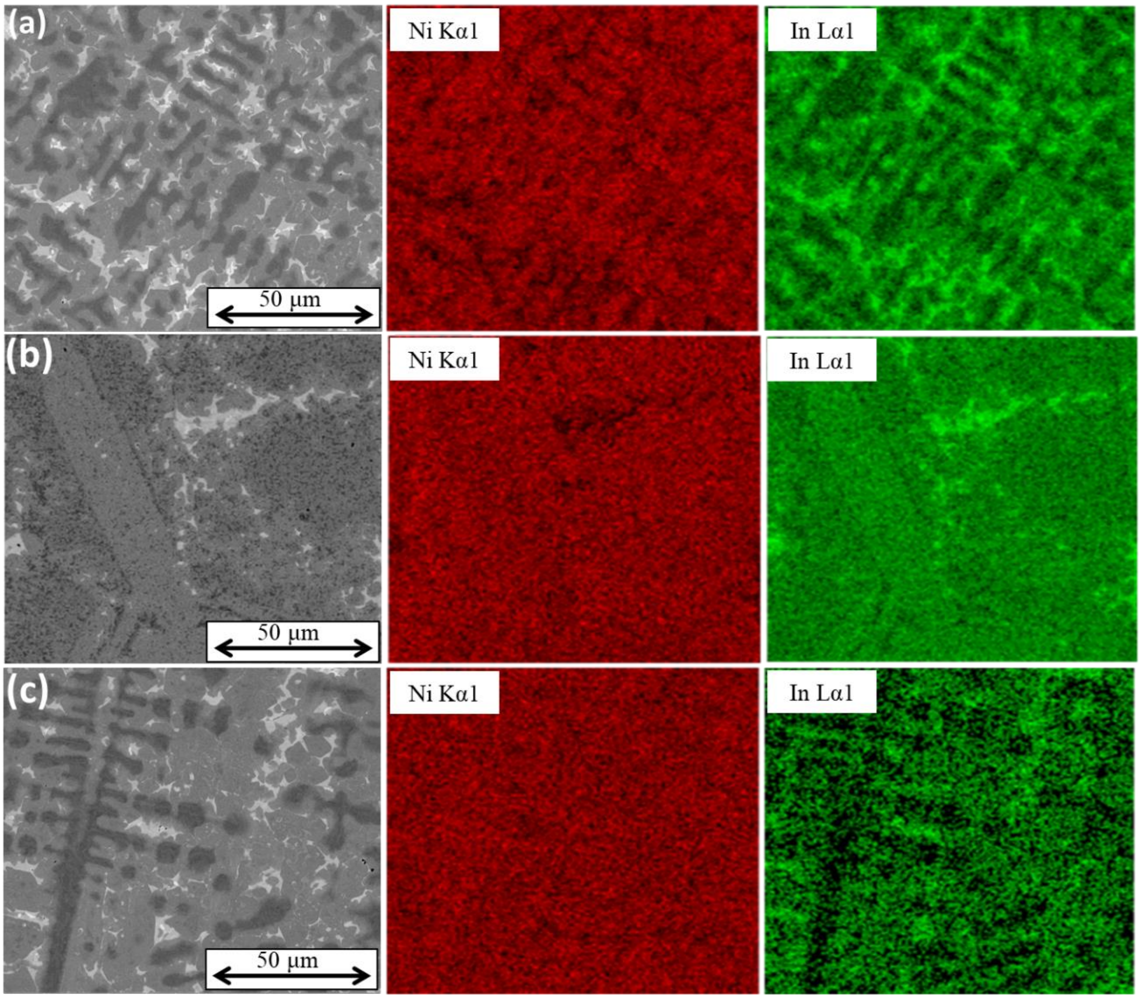

Figure 8.12: SEM BSE micrographs (at increased magnification compared to Fig.) of as-cast Ni-10In-1B, Ni-10In-2B and Ni-10In-3B alloys, with EDS mapping showing distribution of Ni and In between phases (B could not be sufficiently detected by EDS).

Table 8.5: EDS point scan measurements of the phases observed in the SEM BSE micrographs of as-cast Ni-10In-(1,2,3)B alloys (average of 5 measurements, errors derived from standard deviation).

Alloy	Phase	Ni (atomic %)	In (atomic %)
Ni-10In-1B	Light contrast	75.0 ± 0.4	25.0 ± 0.4
	Grey contrast	91.0 ± 0.4	9.0 ± 0.4
	Dark contrast	98.4 ± 0.1	1.6 ± 0.1
Ni-10In-2B	Light contrast	75.4 ± 1.4	25.4 ± 1.4
	Grey contrast	91.8 ± 0.8	8.2 ± 0.8
	Grey contrast (petals)	91.7 ± 0.1	8.3 ± 0.1
	Dark contrast (bordering petals)	97.4 ± 0.6	2.6 ± 0.6
	Eutectic region	94.3 ± 0.6	5.7 ± 0.6
Ni-10In-3B	Light contrast	74.9 ± 0.3	25.1 ± 0.3
	Grey contrast	92.6 ± 0.2	7.4 ± 0.2
	Dark contrast	98.5 ± 0.1	1.5 ± 0.1

In the case of the as-cast Ni-10In-2B sample, the microstructure exhibits some notable differences. Large (> 100 μm) grey contrast petal-like dendrites were observed, as in Fig. 8.11(b), which EDS measurements show are likely the Ni-In solid solution. Light, grey and dark contrast phases were also observed in between the large petal-like dendrites, with similar compositions to those observed in the Ni-10In-1B and Ni-10In-3B alloys. However, the dark contrast (probable boride) phase appears as fine (< 5 μm) globules or eutectic lamellae, as well as bordering the large petal-like grey phase, which may that some of the remaining liquid during solidification underwent a eutectic transformation. While regions of microstructure more similar to the other compositions were observed towards the bottom of this ingot, which likely cooled faster, this different microstructure was the dominant one, though it is not clear what caused this.

Fig. 8.13 shows the XRD spectra of the as-cast Ni-10In-1B, Ni-10In-2B and Ni-10In-3B alloys. As in the XRD spectra for the Ni-In binary alloys (Fig. 8.6), a Ni0.92-In0.08 phase is identified for the Ni-10In-1B spectra, corresponding to the grey contrast phase in Fig. 8.11(a), and matching the EDS measurements. However, this phase apparently dissipates with increasing B according to Fig. 8.13, with no peak observed for the Ni-10In-3B alloy. While a grey contrast phase is observed in Figs. 8.11(b) and 8.11(c), it can be seen in Table 8.5 that the In at. % measured decreases, and this decrease may take the composition across a phase boundary into the Ni-In solid solution region, hence leaving the FCC peaks. Meanwhile, peaks in Fig. 8.13 appear to match those for a $Ni_{21}In_2B_6$ phase with similar crystal structure, possibly corresponding the dark contrast, In-lean, possible Ni-boride phase observed in Fig. 8.11. Fig. 8.14 shows the microhardness values for the as-cast Ni-10In-1B, Ni-10In-2B and Ni-10In-3B alloys (average of five measurements for each alloy). A clear increase in average hardness with increasing B content is observed, with an average of 365 HV1 for the sample with 1 wt. % B, and 685 HV1 for the sample with 3 wt. %. This trend would point to a predictable increase in brittleness with increasing B content. Fig. 8.15 shows the DSC curves for each of the three alloys. The read-off solidus and liquidus values are compared to the TC predictions in Table 8.6. Predicted solidus temperatures are in each case relatively close to measured, but predicted liquidus temperatures, except for the Ni-10In-3B alloy, were significantly different to that measured. XRF had confirmed In content to be close to nominal, and wet chemical analysis had confirmed B wt. % to be close to nominal except for the Ni-10In-1B sample (1.6 wt.% B). The apparent similarity of measured solidus and liquidus between B content values is somewhat surprising, as it would be expected that the B content would have a significant influence.

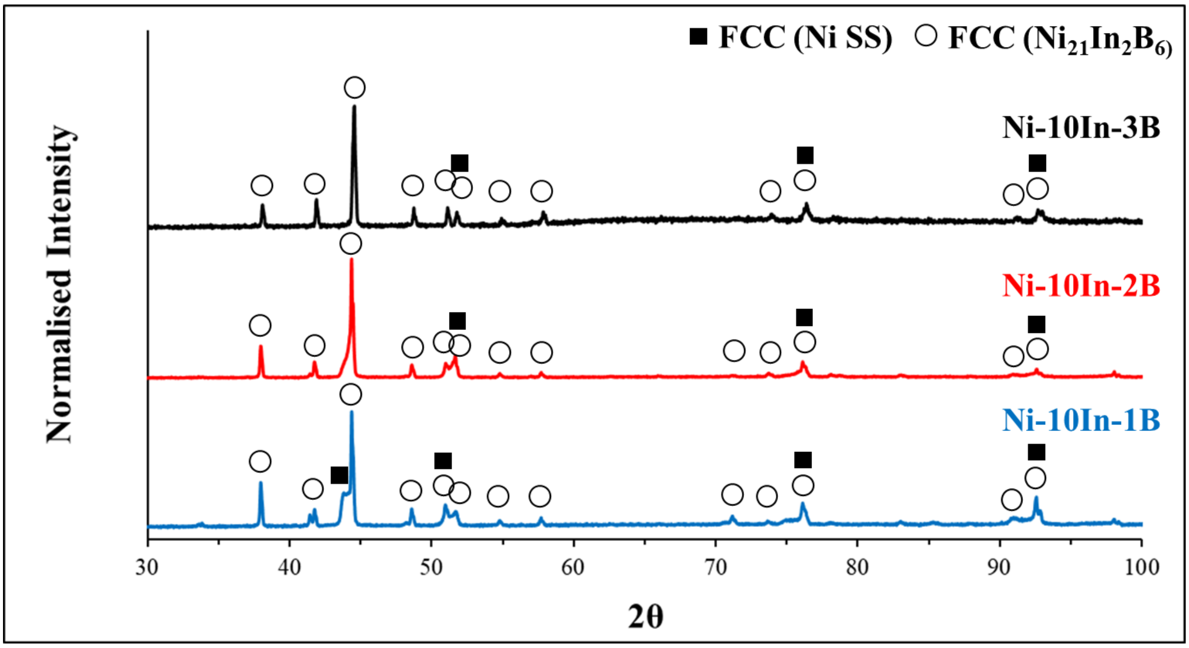

Figure 8.13: XRD patterns for the as-cast Ni-10In-1B, Ni-10In-2B and Ni-10In-3B (in wt. %), with peaks matching FCC Ni solid solution and a FCC-type $Ni_{21}In_2B_6$ phase.

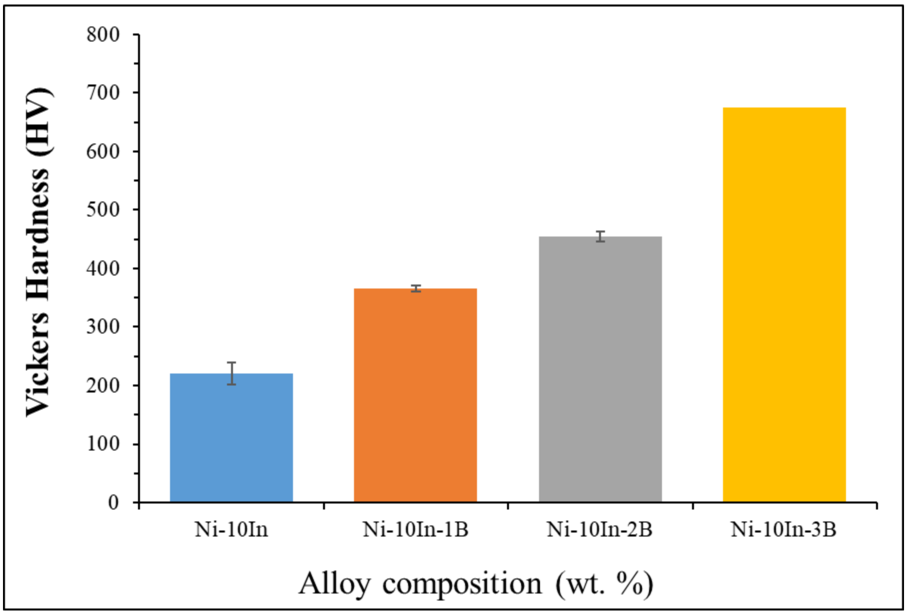

Figure 8.14: Average Vickers microhardness values (HV1) of as-cast Ni-10In-1B, Ni-10In-2B and Ni-10In-3B alloys. Also plotted for comparison is the value for Ni-10In without B addition, from Fig. 8.6

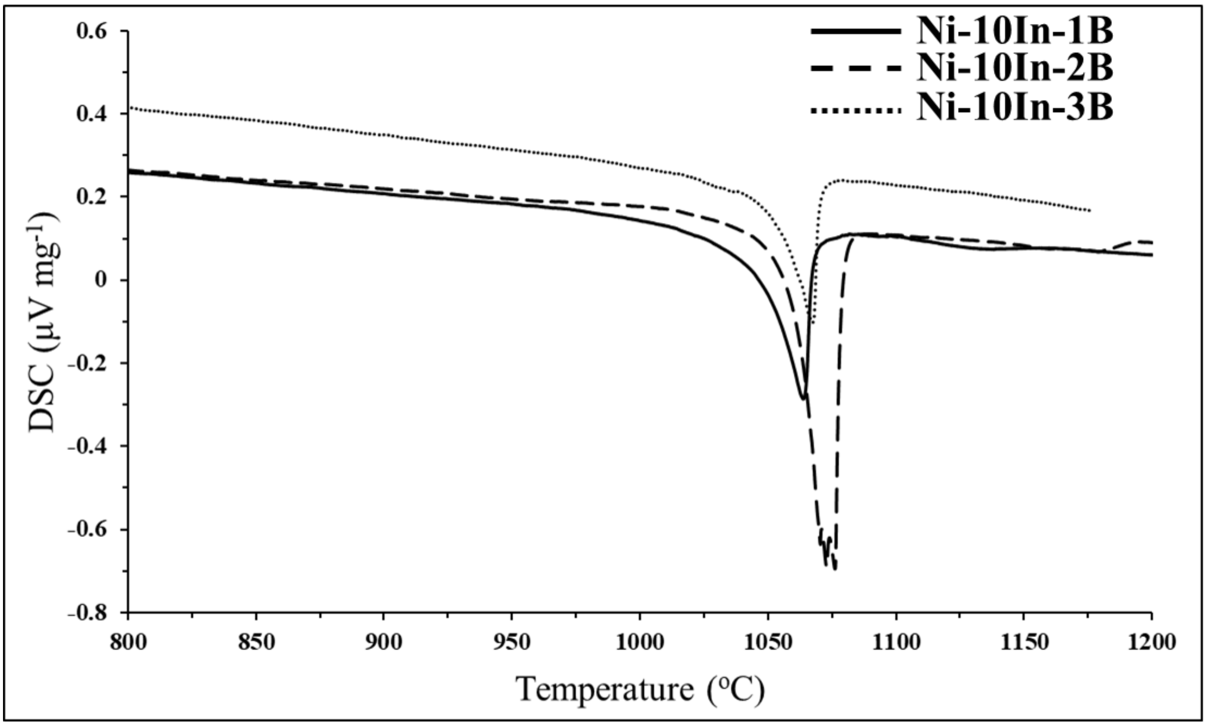

Figure 8.15: DSC Heating curves for as-cast Ni-10In-1B, Ni-10In-2B and Ni-10In-3B alloys.

Table 8.6: Comparison between TC predicted solidus and liquidus temperature and DSC measured solidus and liquidus, for as-cast Ni-10In-1B, Ni-10In-2B and Ni-10In-3B alloys.

Alloy		DSC	TC Predictions
Ni-10In-1B	**Solidus (ºC)**	1035	1060
	Liquidus (ºC)	1070	1323
Ni-10In-2B	**Solidus (ºC)**	1046	1051
	Liquidus (ºC)	1088	1208
Ni-10In-3B	**Solidus (ºC)**	1048	1035
	Liquidus (ºC)	1075	1068

8.3 Ni-In & Ni-In-B Systems - Summary

Section 8.1 shows the fabrication and characterisation of Ni-In binary alloys (Ni alloyed with 5, 10 and 15 wt. % of In), in order to evaluate the potential for In as a novel MPD element, replacing elements such as B and Si. According to the Ni-In binary phase diagram, between the pure Ni composition and eutectic composition (24 at. %, 39.5 wt. %), the liquidus of binary Ni-In can be reduced by approximately 13.8ºC per wt. % of In. While a sub-1200ºC liquidus is achievable with 18.5 wt. % In (or even sub-1100ºC for In content above approximately 29 wt. %), these compositions are clearly far richer in the MPD than for current commercially available Ni-based filler metals. This may prove undesirable for economic reasons (given the raw cost of In) as well as due to mechanical performance. By comparison, the TC predictions made for the Ni-In binary alloys was found to differ significantly from the phase diagram, although it did at least predict a decrease in liquidus with increasing In content. DSC measurements, while not wholly conclusive, appeared to suggest primary melting at lower temperatures as In content increased. As-cast binary Ni-In alloys exhibited three-phase microstructure including Ni solid solution with low In content, a phase richer in In (possibly a saturated solid solution), and a phase much richer in In, likely the Ni_3In intermetallic phase. While the mechanical properties of the intermetallic phase is not known to be documented, microhardness measurements indicate a possible increase in brittleness associated with the increasing content of this phase. Furthermore, the large atomic size of In suggests that outward diffusion during brazing, which allows for the dissolution of brittle boride phases in B-bearing filler metals, would be slow, and hence these phases may remain heavily concentrated within the joint, acting as a potential region of weakness and crack propagation.

In order to address these limitations, the use of In in conjunction with B as MPDs was investigated, with the idea that a balance may be struck whereby In content is in solution, while the B content required to achieve a liquidus comparable to current B-bearing filler metals is reduced. In the series of Ni-10In-(1,2,3)B alloys fabricated, DSC measurements actually showed slight increase in solidus with increasing B, and the sample with 2 wt.% B actually had the highest liquidus, contrary to expectation. While chemical analysis via XRF and wet chemical analysis is taken into account, it is possible that inhomogeneity in samples may have altered the composition that was measured. Regardless, TC predictions showed some significant discrepancy with DSC results, possibly more than would be expected even accounting for different compositions than were nominally expected. At the same time, TC solidus predictions were similar to measure across all compositions, and so it is possible that the TC predictions were aided by the presence of assessed binary Ni-B data, even though the Ni-In, In-B and Ni-In-B ternary data was not available in the database used. While the use of both In and B as MPD elements had the desired effect, it may be inferred from the average microhardness measurements that the brittleness increases with B content, and indeed the molar fraction of Ni boride phase (in Fig. 8.11) increased with B content. Other Ni-In intermetallic phases were again observed, however, in addition to the Ni-boride phases, and these also likely contributed to this.

8.4 Ni-Ge System

Ge was another element selected as a potential alternative MPD element meriting consideration, meeting the broad requirements described at the beginning of this chapter. Fig. 8.16 shows the binary Ni-Ge phase diagram. There is a eutectic point at approximately 22 at. % (26 wt. %) Ge, at 1125ºC, below which liquid transforms to Ni solid solution plus Ni_3Ge phase. Interestingly, this Ni_3Ge phase (23.1 to 25.6 at. %) has the $L1_2$ crystal structure similar to the γ′ phase in Ni-based superalloys ($Ni_3(Al,Ti)$). This was exploited by Dinkel *et al*. [115] who produced a joint with γ′ precipitates using Ni-Ge filler metal. Between the pure Ni composition and the eutectic point, the average reduction in liquidus is 12.7ºC per 1 wt. % Ge, slightly less than for In.

As with In, Ge is not a common alloying element in Ni, and is not used in Ni-based superalloys or brazing alloys generally. However, it exhibits greater solubility in Ni as compared to In, up to approximately 13.9 at. % (16.6 wt. %) at 1125ºC, comparable to that of Si which is used in several Ni-based brazing filler metals. Beyond this, the Ni-Ge system exhibits several intermetallic phases: Ni_3Ge (FCC ($L1_2$), $Pm\bar{3}m$), γ (cubic, $Fd\bar{3}m$), δ (hexagonal, $P6_3/mmc$), $GeNi_2$ (orthorhombic, *Pnma*), Ge_3Ni_5 (monoclinic, *C*121), ε (hexagonal, $P6_3/mmc$) and GeNi (orthorhombic, *Pnma*). Beyond approximately 29 at. % (33 wt. %) Ge, the liquidus temperature increases again. As per [115], of these phases the $L1_2$ Ni_3Ge phase could be of mechanical benefit to a brazed joint. With this in mind, it was deemed that a higher Ge content compared to that of In might be allowed for in a prospective Ni-Ge brazing alloy, up to approximately 25 wt. %.

It can be inferred from Fig. 8.16, however, that the lowest liquidus achievable using Ge as the sole MPD is still higher than for In, and factoring in the higher raw cost of Ge compared to In, it is unlikely to represent an attractive option as a sole MPD except for situations where the higher brazing temperature is acceptable in order to achieve γ′ precipitation in the joint as in [115]. Fig. 8.17 shows TC predictions of solidus and liquidus projected on the Ni-Ge phase diagram from Fig. 8.16. Immediately these TC predictions appear to more closely match the phase diagram than was the case for the Ni-In system. While divergence from the phase diagram increases with wt. % Ge, within the 0 – 10 wt. % Ge range the agreement is good. Therefore, while perhaps not suitable as sole MPD, TC predictions of systems containing Ni and Ge may have reasonable accuracy.

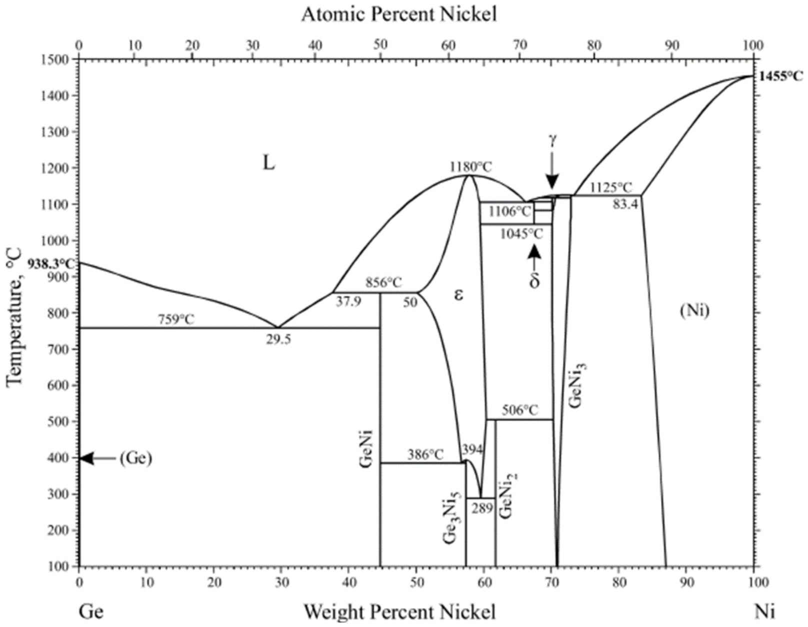

Figure 8.16: Ni-Ge binary phase diagram. From ASM Handbook [18], and based on [197].

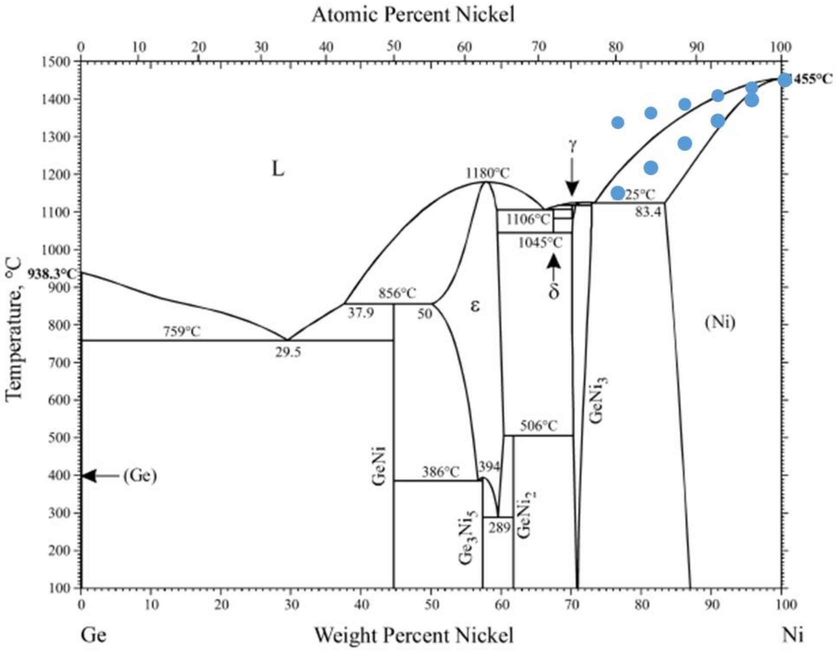

Figure 8.17: TC predictions of solidus and liquidus temperatures projected on Ni-Ge binary phase diagram.

As with the Ni-In system, it was considered that introduction of a secondary MPD in the form of B might allow for a desirably low melting temperature, while requiring lower Ge content and lower B content (than in commercial filler metals). Table 8.7 shows TC predictions for Ni-10Ge-(1,2,3)B compositions, in weight percent, as a comparison with the Ni-10In-(1,2,3)B alloys in Table 4. These predictions are comparable to those for the Ni-10In-(1,2,3)B alloys, and in fact for the Ni-10Ge-3B composition the achievable liquidus is lower, though there is a wider melting range as compared to the Ni-10In-3B composition. Again, as with the Ni-10In-(1,2,3)B compositions, the fraction of intermetallics predicted is likely an important consideration in addition to the solidus and liquidus temperatures. Fig. 8.17 shows TC predictions of boride molar fraction at room temperature for the Ni-10Ge-(1,2,3)B compositions. As with the Ni-10In-(1,2,3)B predictions, the sole boride phase predicted is the Ni_3B phase, with a molar fraction approaching 60% for the Ni-10Ge-3B composition. It is also notable here that, aside from an FCC solid solution, a pure Ge phase is predicted (denoted 'DIAMOND_A4'), suggesting Ge segregation is preferred to forming any Ni-Ge intermetallic phases.

Table 8.7: TC predicted solidus and liquidus for Ni-10Ge-1B, Ni-10Ge-2B and Ni-10Ge-3B alloys.

	TC Predictions	
Alloy	**Solidus (ºC)**	**Liquidus (ºC)**
Ni-10Ge-1B	1018	1287
Ni-10Ge-2B	996	1170
Ni-10Ge-3B	950	1054

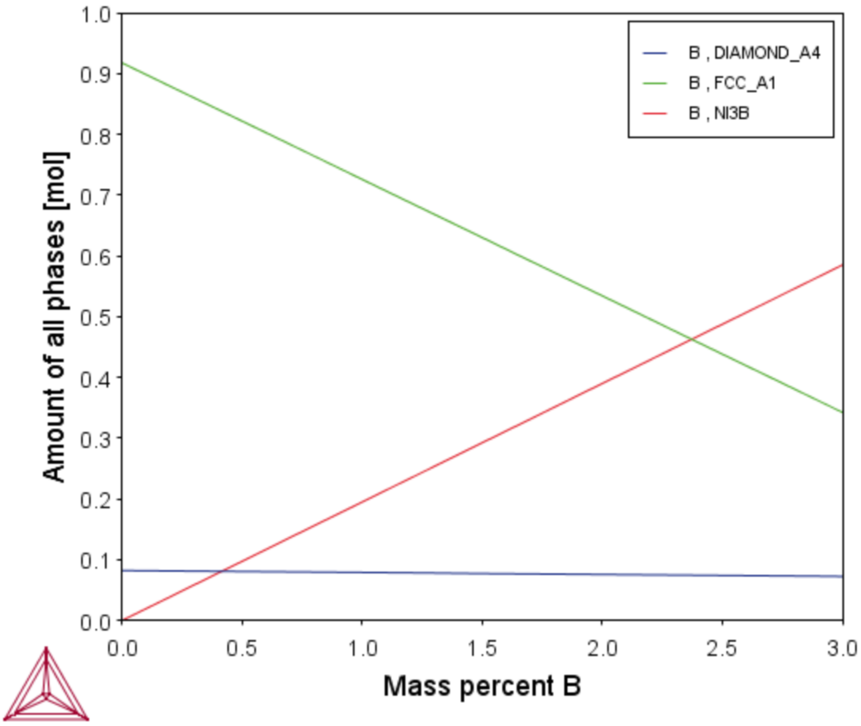

Figure 8.17: TC predictions of phase molar fraction (at room temperature) versus B content for the Ni-10Ge-(1,2,3)B compositions.

8.5 Chapter Summary & Implications

This chapter has detailed investigations into potential alternative MPD elements for use in a Ni-based brazing filler metal, namely In and Ge. Both of these elements, while not typical alloying additions to Ni or its alloys, nonetheless exhibit a suppressing effect on the liquidus in their respective binary phase diagrams with Ni. The first considered element, In, according to the phase diagram could suppress the liquidus temperature down to 910ºC but would require almost 40 wt. % (24 at. %) of In, whereas to achieve a liquidus comparable to current commercial Ni-based filler metals (sub-1100ºC), almost 30 wt. % (17 at. %) In would be needed. At the same time, while the solubility limit of In in Ni solid solution of approximately 7.5 at. % compares very favourably to such common MPDs as B and P, confining the In content to within the solubility limit according to the phase diagram would give a liquidus of no lower than 1300ºC. When this system was modelled using TC software, the effect of the lack of experimentally verified Ni-In data was clear, as predictions of solidus and liquidus temperature differed significantly from what was observed via DSC and the existing Ni-In phase diagram.

Clearly, the MPD effect of In is not as potent as for B or even Si (which exhibits greater solubility in Ni solid solution in any case, at both the limit and at low temperatures). When a series of Ni-In alloys was fabricated via arc-melting (in wt. %, Ni-5In, Ni-10In and Ni-15In), in all cases a three-phase microstructure of Ni solid solution, an In-saturated solid solution, and Ni_3In intermetallic was observed. While this represents only the as-cast state from the rapid cooling following arc-melting, given the decreasing solubility of In in Ni at lower temperatures, it would be expected to retain the Ni_3In intermetallic phase, although it remains to be seen if homogenisation treatment could result in a finer dispersion of this phase. In the as-cast state, this phase resulted in increasing microhardness with increasing In content, pointing towards a tendency for embrittlement. But in either case, all indications of solidus and liquidus temperatures from both the phase diagram and DSC measurements of the alloys suggest that these compositions do not possess a sufficiently low liquidus as compared to commercial Ni-based filler metals such as BNi-2.

Despite this, an investigation of using In as MPD along with a more potent element (B in this case), allowing for a reduced content of both, while possibly achieving a more desirable liquidus temperature, was warranted. When Ni-10In-(1,2,3)B, in wt. %, alloys were fabricated, similar phases to the Ni-In binary alloys were observed, including the Ni solid solution phase and the probable Ni_3In intermetallic phase. A starkly different microstructure was observed for the Ni-10In-2B alloy, however, with evidence of fine eutectic lamellae between Ni solid solution and a probable Ni-boride phase. Large petal-like grains of In-saturated solid solution were observed, as opposed to in the Ni-10In-1B and Ni-10In-3B alloys, which exhibited this phase only in dendritic morphology. Predictions made using TC software (no Ni-In-B ternary phase diagram was known to exist) suggest a liquidus as low as 1068ºC for the Ni-10In-3B composition, making it comparable to that of commercially available Ni-based filler metals, but at 3 wt.% B this hardly represents an improvement in reducing B content. Indeed, the combination of probable borides and the Ni_3In phase resulted in a high microhardness of 685 HV, indicating a probably brittle composition. If such a composition were to be used as a filler metal, it is likely that similarly long diffusion times as for commercial B-containing filler metals would be required to avoid deleterious boride phases remaining in the joint post-braze. The DSC measurements also seemed to indicate that increasing B content from 1 wt. % to 3 wt. % did not decrease liquidus further, with all solidus and liquidus temperatures similar amongst alloys with measured B content of 1.6, 2 and 3 wt. %, contrary to expectations.

The second element considered as an alternative MPD element was Ge. When compared to the In, Ge appears to have a slightly less potent MPD effect, with a low liquidus achievable of 1125°C with an approximate 26 wt. % (22 at. %) addition required. However, Ge exhibits greater solubility in Ni, with the solubility limit of approximately 13.9 at. % at 1125°C being more comparable to that of Si. Furthermore, this solid solubility extends down to lower temperatures, in contrast to In. Also of note, is the much better agreement between the Ni-Ge phase diagram and the predictions made by TC. While the solidus and liquidus lines predicted by TC diverge increasingly from the phase diagram as Ge content increases, there is good agreement within at least the first 10 – 15 wt. % Ge.

Another consideration for the use of Ge is the Ni_3Ge intermetallic phase, which possesses the same $L1_2$ structure as the strengthening γ′ $Ni_3(Al,Ti)$ intermetallics found in many Ni-based superalloys. As mentioned, this has been exploited in the literature [115]. However, while this phase may be beneficial mechanically, the liquidus temperature achievable using Ge, at least as a sole MPD element, is still considerably higher than for most commercially available Ni-based filler metals. Combined with the high raw cost of Ge (exceeding that of In and B), Ge is unlikely to be feasible as a sole MPD element. The addition of B was considered for the Ni-Ge system, as it was for the Ni-In system. Again, TC predictions showed the Ni-10Ge-3B (in wt. %) composition, for example, could have a liquidus of approximately 1054°C, comparable to the commercially available filler metals and below that predicted for Ni-10In-3B, but with a much wider predicted melting range which could pose problems for usage. In addition, as already mentioned for the Ni-10In-3B composition, 3 wt. % B would not constitute a significant reduction as compared to such filler metals as BNi-2 for example, and a high hardness and thus possible brittleness would be expected for a Ni-10Ge-3B composition, without any potential benefit from Ni_3Ge phase. If the Ge content of a prospective Ni-Ge-B composition was increased such as to encourage the formation of γ′ Ni_3Ge, it is not known how B content would affect this. It may be possible, inferring from the Ni-Ge phase diagram and from TC predictions, that a γ′-forming Ni-23Ge (wt. %) composition with a small B content may achieve a desirably low liquidus temperature while forming the γ′ Ni_3Ge phase, but even so heat treatment would likely be required to obtain a sufficiently fine dispersion of the phase, as seen in [115].

In all, while the considered elements In and Ge are unlikely to be attractive as like-for-like switches with currently used MPD elements in Ni-based filler metals such as B, Si and P, the potential for combining them with elements such as B is likely to permit a temperature suitable to be used in standard brazing cycles for filler metals such as BNi-2, for which a sub-1100°C liquidus would be required. However, balance must be struck between striving for a low enough liquidus temperature, raw element cost, and ensuring a mechanically desirable microstructure without excessive concentration of intermetallic compounds. At least for the Ni-In-B and Ni-Ge-B systems, striking this balance is apparently not readily feasible. However, this does not rule out the concept, rather, it only speaks to the feasibility when such MPDs are added to Ni. If the concept of using novel MPDs such as In and Ge, as well as using them in conjunction with a more potent MPD element (for Ni and its alloys) such as B, is extended to other systems other than just pure Ni, it is conceivable that a suitably low liquidus is achievable while restricting the MPD content to levels that will not encourage excessive formation of brittle intermetallics. For example, the Ni-Cr-Fe system (which forms the basis for many Ni-based superalloys and Ni-based filler metals) exhibits lower liquidus temperatures than pure Ni, particularly toward more superalloy-like and equiatomic compositions. The following chapters in this work aim to investigate and test this concept further.

9. MPEA Filler Metal Design Approach

Considering the conclusions of Chapter 8, in which In and Ge were deemed insufficient as sole additions to Ni as novel MPD elements for use as brazing filler metals, another strategy was attempted, based on what was discussed in Chapter 4 of this work. This strategy involves the design of a MPEA filler metal, yet one which also contains a suitable element as part of the composition that acts as both MPD and solute in an ideally FCC solid solution.

For this strategy to be feasible, there were several points to consider initially. Firstly, as is the case for any brazing filler metal, the elements used should be compatible with the base metal being joined. For this reason, it was considered that Ni should be a major component of the alloy, such that it would be present in concentrations at least equal to, or greater than, other elements in the alloy. These other elements could feasibly be selected from the elements common in transition metal FCC HEAs and MPEAs, namely Al, Co, Cr, Cu, Fe and Mn, and a wider selection may even include other elements found in Ni-based superalloys such as Nb, Ta and Ti. Cr is almost universally used as an alloying addition in Ni-based superalloys, and so was selected for use in the proposed MPEA filler metal. Fe is also used in certain Ni-Fe superalloys, including Inconel 718, and is furthermore an inexpensive element and exhibits full solubility in an FCC solid solution according to the Ni-Fe phase diagram [198]. The Ni-Cr-Fe ternary liquidus projection is established, as seen in Fig. 9.1 [199], and it shows the liquidus temperature decreases somewhat towards the equiatomic region. The Cr-Fe-Ni ternary phase diagram also shows the γ-FCC formation region for Ni-rich compositions, for example see Fig. 9.2 [199]. For these reasons, the prospective MPEA filler metal was chosen to be based around a Ni-Cr-Fe system, providing an inexpensive basis with anticipated good compatibility with most Ni-based superalloy base metals, as well as potentially allowing the formation of FCC solid solution.

As was the case for the binary and ternary alloys described in Chapter 8, some conditions were considered necessary to narrow the potential alloy combinations of interest:

- Liquidus below 1100°C, such that the developed MPEA filler metal can be used under similar conditions to many commercial Ni-based brazing filler metals.
- To retain good chemical compatibility with the base metal, and to increase likelihood of FCC formation, no element should be present in concentration greater than Ni. The minimum Ni content, and maximum MPD content, would be 25 at. % (i.e. the equiatomic composition).
- In keeping with the empirical thermodynamic parameters, based on the classical Hume-Rothery rules and used for the design of HEAs and MPEAs as discussed in Chapter 4, compositions that minimise $|\Delta H_{mix}|$ and δr, and maximise VEC, such that FCC solid solution is promoted (but not at the expense of a low liquidus temperature).

These conditions prioritise achieving a low liquidus of the prospective MPEA filler metal, as the aim is to develop a novel filler metal operating in the same temperature range as commercially available Ni-based brazing filler metals. In addition, consideration was given to the very likely compositional and microstructural changes to the MPEA filler metal during the brazing process, due to diffusion and relatively slow heating and cooling rate (compared to that experienced during the arc-melting fabrication process). Essentially, achieving a MPEA-like solid solution microstructure *post*-brazing may likely be of more importance than achieving it in the as-cast MPEA filler metal *pre*-brazing (though interaction with base metals and cross-diffusion during brazing could make this harder to achieve). This chapter details the development of MPEA filler metals, employing phase diagrams, the CALPHAD method implemented via Thermo-Calc (TC) software, and empirical thermodynamic parameters described in Chapter 4.

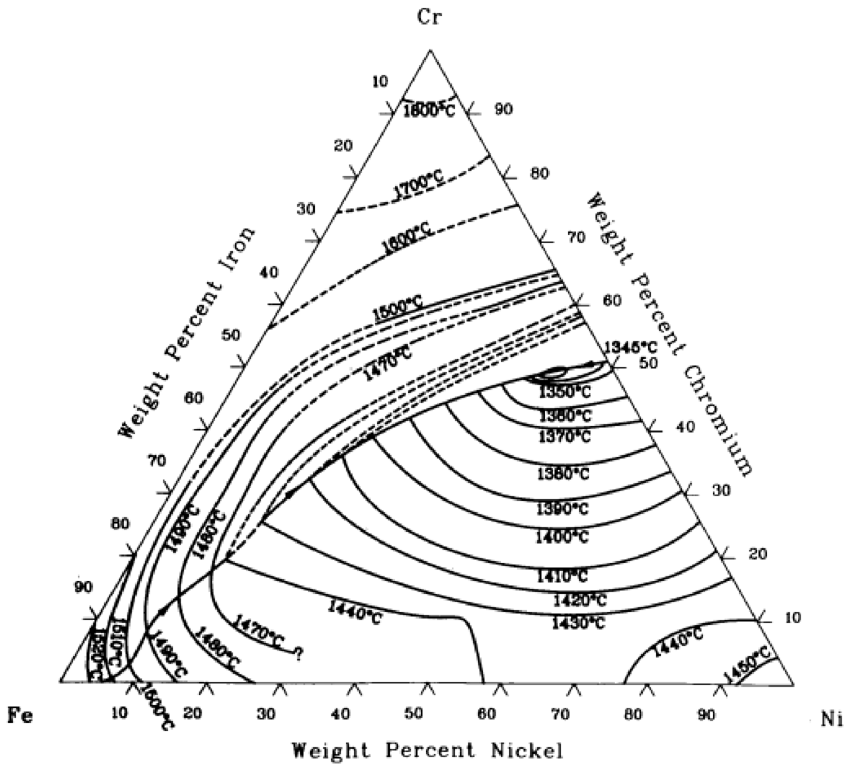

Figure 9.1: Cr-Fe-Ni ternary liquidus projection. From ASM Handbook [18], and based on [199].

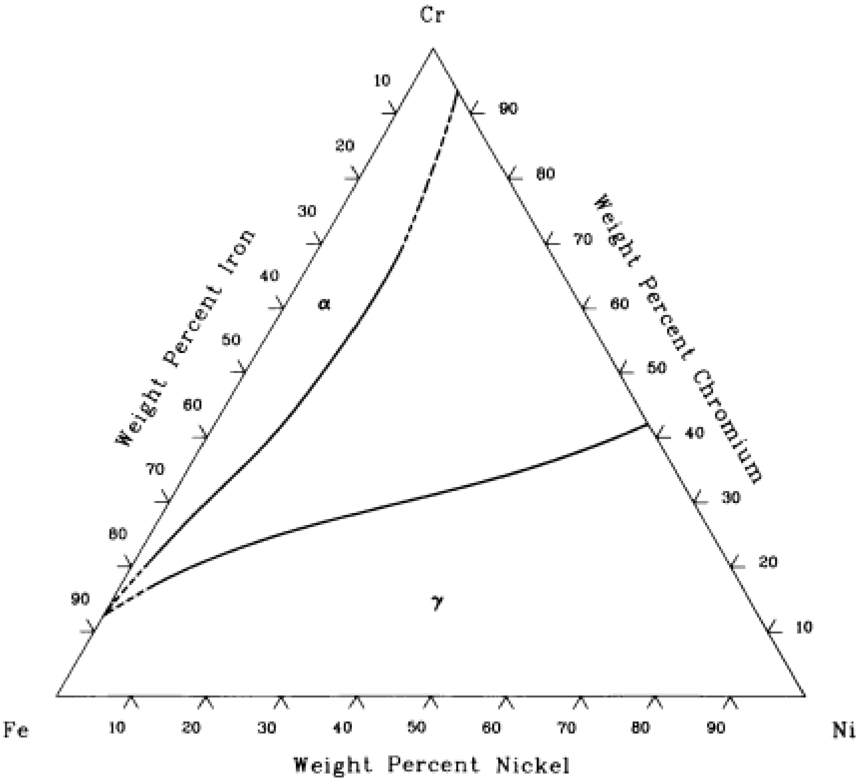

Figure 9.24: Cr-Fe-Ni ternary isothermal section at 1000ºC. From ASM Handbook [18], and based on [199].

10. MPEA Filler Metal Incorporating In as Melting Point Depressant

Having set out the basis for the MPEA filler metal design strategy in the previous chapter, this chapter will document the development of such, using In as the primary novel MPD element. This work began considering the equiatomic NiCrFeIn system.

10.1 NiCrFeIn System

Using the strategy described in the previous chapter, and considering what was discussed in Chapter 8, In was selected as a MPD alloying addition to a Ni-Cr-Fe basis. As a starting point, the simple equiatomic composition was considered. This system was modelled in TC software, with Fig. 10.1 showing the predicted phase abundance as a function of temperature. For this system, TC predicts a liquidus temperature of approximately 1152ºC, with solidification of FCC A1 then BCC A2 solid solutions, and a solidus temperature of approximately 953ºC. The compositions of the FCC and BCC solid solutions at solidus are predicted, in atomic percent, as Ni(27.9)-Cr(22.2)-Fe(26.0)-In(23.8) and Ni(11.9)-Cr(37.4)-Fe(20.4)-In(30.3) respectively. However, upon cooling to room temperature, the BCC A2 phase becomes the majority, with an almost 50 % molar fraction, with a Cr(50.0)-In(50.0) composition, with no Ni or Fe. Rather, the Ni and Fe have segregated completely, as the initial FCC A1 phase gives way to a second FCC A1 phase of approximate composition Ni(59.0)-Fe(41.0), and a minor (~ 8 mol. %) second Fe-rich BCC A2 phase, of approximate composition Fe(96.0)-In(4.0). At first glance, such a (largely) dual phase equilibrium microstructure may be desirable, if it proved possible to achieve an adequate dispersion of a BCC phase in a FCC phase, possibly imparting increased strength while retaining ductility. However, maintaining this post-braze would be a further challenge, and the predicted liquidus temperature would be considered too high to be of interest for use as a filler metal in this study.

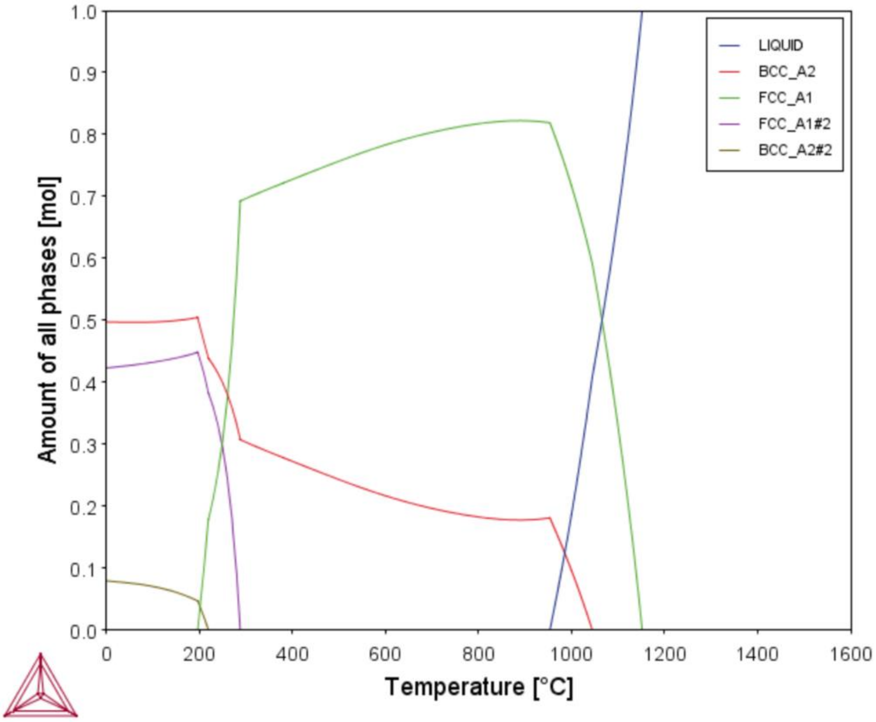

Figure 10.1: TC predictions of phase abundance versus temperature for the equiatomic NiCrFeIn system.

Aside from the TC predictions, the empirical thermodynamic parameters discussed in Chapter 4 were used as a design tool. For the equiatomic NiCrFeIn composition, these parameters were calculated as shown in Table 10.1. Values used in calculations of ΔH_{mix} were obtained from [200], based on the Miedema model [201], atomic radii were obtained data compiled in [37].

Table 10.1: Calculated values of ΔH_{mix}, δr and VEC for the equiatomic NiCrFeIn.

	ΔH_{mix} (kJ mol^{-1})	**δr (%)**	**VEC**
NiCrFeIn (equiatomic)	7.75	3.86	6.75

To establish comparisons between these predictions and observations of a fabricated MPEA filler metal, fabrication of the equiatomic NiCrFeIn system was attempted by arc-melting. However, it was found that this system did not adequately mix and form an alloy, with pools of molten segregated material sat on top of an already solidified portion of the material. Potential technical issues aside (if indeed there were any), no abnormal occurrences were noted during the melting (which was attempted three times), and so this could have been a result of the chemistry of the equiatomic composition. According to calculations by Takeuchi and Inoue [200] based on the Miedema model [201], the mixing enthalpies of both Cr and Fe with In are high, at 20 and 19 kJ mol^{-1} respectively, meaning that segregation between these elements is likely and this potentially led to the issues with alloy formation observed. This contributed to the positive average ΔH_{mix} value of 7.75 kJ mol^{-1}, which would likely be considered high compared to the vast majority of indexed solid solution-forming HEAs and MPEAs. This observation is also apparently somewhat in disagreement with the TC predictions; whereas In segregation from Fe was predicted, TC also predicted In preferentially forming a BCC phase with Cr, even though this binary pair has the highest mixing enthalpy. Another consideration is the apparent lack of a reported phase diagram for the Cr-In system, which may otherwise have informed this attempted fabrication, and may also go some way to explaining the TC predictions.

10.2 NiCrMnIn System

To reduce the overall impact of the high mixing enthalpies, replacement elements for Cr or Fe were considered, prior to optimisation of the composition. The replacement element must equally satisfy the conditions set out above, and in particular retain a good chemical compatibility with Ni-based superalloy base metal. Co, a common alloying addition in Ni-based superalloys, was considered; it has a lower mixing enthalpy with In than either Cr or Fe (7 kJ mol^{-1}). Co does however have potential for greater costs, and future geopolitical issues. Mn, which has a yet lower mixing enthalpy with In (3 kJ mol^{-1}), was also considered. Mn is not a common addition in Ni-based superalloys; it may be discouraged due to factors including the potential for forming σ-phase intermetallics with Cr. However, Mn does exhibit complete solid solubility in FCC Ni and Fe, and according to the binary Ni-Mn, Cr-Mn and Fe-Mn phase diagrams, is likely to further reduce the liquidus temperature (indeed, Mn was used as MPD in [113]). Therefore, Mn was considered a suitable replacement element for Cr or Fe in the prospective MPEA filler metal. Retaining both Cr and Fe in a Mn-containing alloy was considered undesirable, as it could both increase the likelihood of σ-phase formation (considering the Cr-Fe-Mn ternary phase diagram [199]), and also retain the problem of high mixing enthalpy between the Cr-In and Fe-In pairs. Fe was selected to be replaced by Mn in the alloy; this had the positive effect of retaining Cr for corrosion properties of the MPEA filler metal, but perhaps reduced the tendency for FCC solid solution formation.

The equiatomic NiCrMnIn system was taken as a starting point, and TC software was used to predict the phases formed and melting range. Fig. 10.2 shows the phase abundance against temperature, along with the solidus and liquidus temperatures, for the equiatomic NiCrMnIn system. TC predicts a liquidus temperature of approximately 1156°C, and solidification of a BCC A2 then FCC A1 phase takes place. At the solidus (923°C), the compositions of these, in atomic percent, are Ni(15.1)-Cr(34.2)-Mn(19.6)-In(31.1) and Ni(35.4)-Cr(15.4)-Mn(30.6)-In(18.6) respectively. This dual-phase microstructure remains down to room temperature, though the abundance varies throughout cooling, with the molar fraction of the BCC and FCC phases predicted as approximately 52 % and 48 % respectively. The room temperature composition of the BCC and FCC phases is predicted as Cr(47.4)-Mn(4.5)-In(48.0) and Ni(51.9)-Cr(1.0)-Mn(47.0) respectively. Only at very low temperatures are two other phases predicted in small molar fractions, a Cr_3Mn_5 and then a cubic A13 phase (denoted CUB_A13 in Fig. 10.2), with composition Ni(42.4)-Mn(57.5). As with the equiatomic NiCrFeIn system, this mostly dual-phase microstructure could be desirable, though the predicted liquidus temperature is considered too high to be of interest for use. The preference of In to form a BCC phase with Cr is again predicted despite what might be otherwise expected considering the large mixing enthalpy, with the Ni and Mn content forming the FCC solid solution, which is feasible.

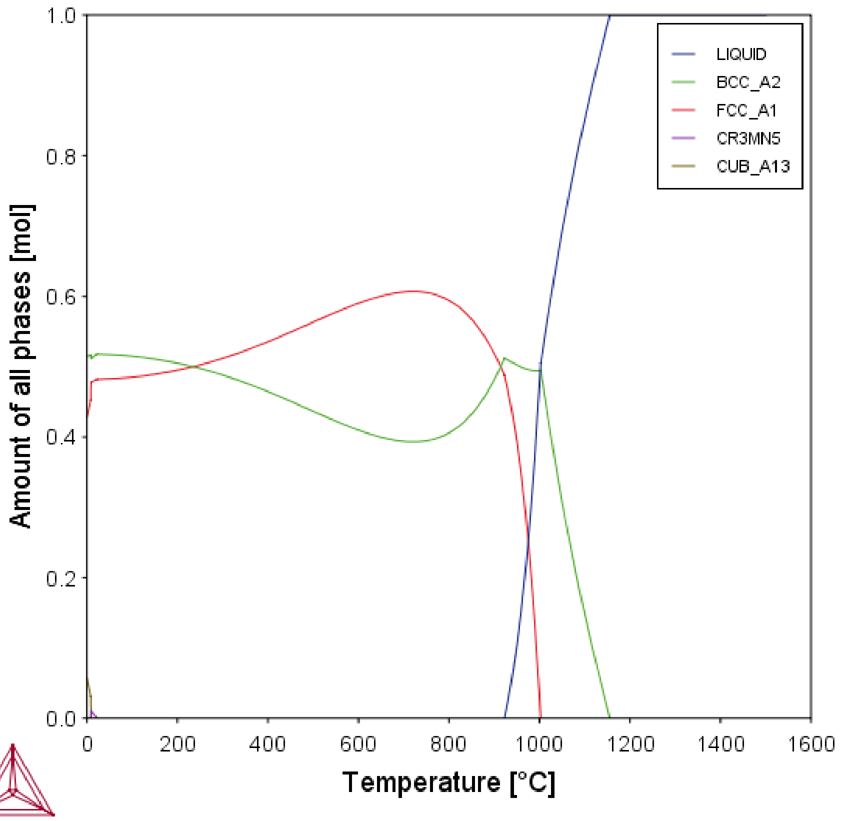

Figure 10.2: TC predictions of phase abundance versus temperature for the equiatomic NiCrMnIn system.

Table 10.2: Calculated values of ΔH_{mix}, δr and VEC for the equiatomic NiCrMnIn.

	ΔH_{mix} (kJ mol^{-1})	δr (%)	VEC
NiCrMnIn (equiatomic)	3.00	3.98	6.50

Table 10.2 shows calculated thermodynamic parameters for the equiatomic NiCrMnIn system. Compared to the equiatomic NiCrFeIn system, the ΔH_{mix} values is reduced, with a slight increase in δr. This could indicate a slightly greater tendency to solid solution formation, but, meanwhile, the VEC is reduced, indicating a greater preference for BCC crystal structure over FCC. From these values, clearly the high positive mixing enthalpy of Cr-In again shifts the average ΔH_{mix} to slightly positive. Conceivable changes to the equiatomic NiCrMnIn compositions, therefore, may be in reducing the In content to a level that may be soluble in a Ni-Cr-Mn matrix. Reducing to too low a level, however, would be expected to increase the liquidus temperature. At the same time, Cr content may be considered for reduction, which may allow solution in a Ni, Mn-rich FCC phase and reduce BCC content. These changes were investigated systematically using TC software. Fig. 10.3 shows a 'heat-map' indicating abundance of liquid at 1100^{o}C as Cr and In content varies (keeping Mn content at 25 at. % and Ni as balance). TC predicts that a maximum liquid phase content, hence liquidus, of 1100^{o}C (i.e. the darkest red regions on Fig. 10.3) is achieved for In contents above 14 at. %, but only up to Cr contents of approximately 22 at. %. The In content appears to have a greater influence on the liquidus temperatures predicted. Fig. 10.3 does show, however, that both Cr and In content can be suitably decreased to promote FCC solid solution formation, while still achieving a liquidus of no higher than 1100^{o}C.

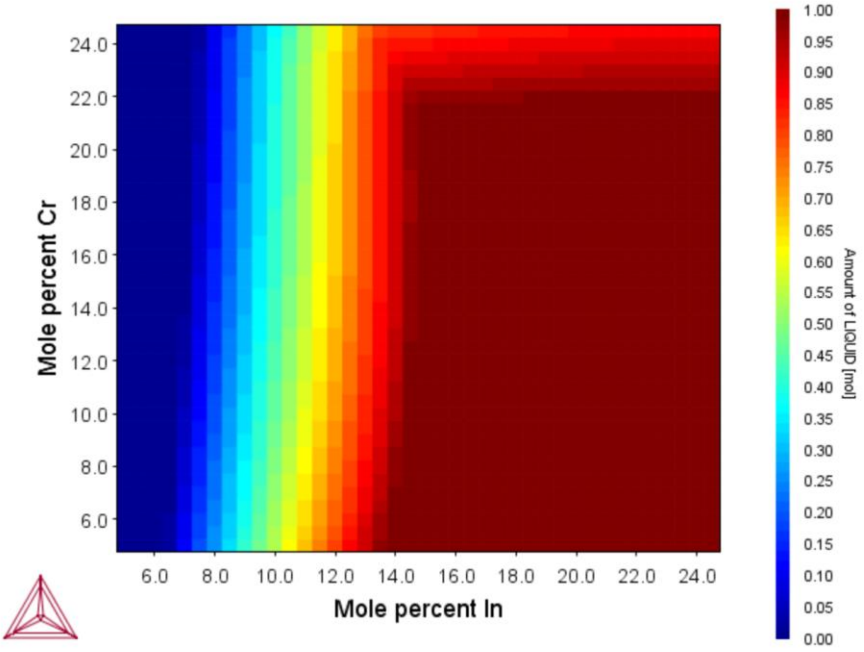

Figure 10.3: TC 'heat map' showing Cr and In contents required for a predicted maximum liquidus of 1100^{o}C.

Meanwhile, the effect of altering element abundance on the abundance of phases in the resulting alloy can be predicted. Fig. 10.4 shows the room temperature phase abundance versus element abundance, for varying amounts of Cr, Mn and In (in each case, the element is varied from 0 to 25 at. %, while Ni is kept as balance and the other two elements are kept at 25 at. %). Increasing Cr, Mn and In content, is predicted to decrease the room temperature FCC A1 abundance and increase the BCC A2 abundance in the NiCrMnIn system. However, The BCC A2 promotion is reduced when increasing Mn concurrently with a reduction in both Cr and In, as shown in Fig. 10.5. At the same time, as shown in Fig. 10.3, reducing In content below approximately 14 at. % will likely increase the liquidus temperature even at low Cr content. While this could perhaps be offset by increasing Mn content, this might be deemed undesirable to avoid increasing the potential for σ-phase formation due to interaction with the base metal during brazing, and to keep Ni as the majority element for good compatibility with a Ni-based superalloy base metal. Meanwhile, some Cr is deemed necessary to provide corrosion resistance in any potential MPEA filler metal, and to reduce the potential for the predicted tertragonal phase (labelled TETRAGONAL_A6 in Fig. 10.4).

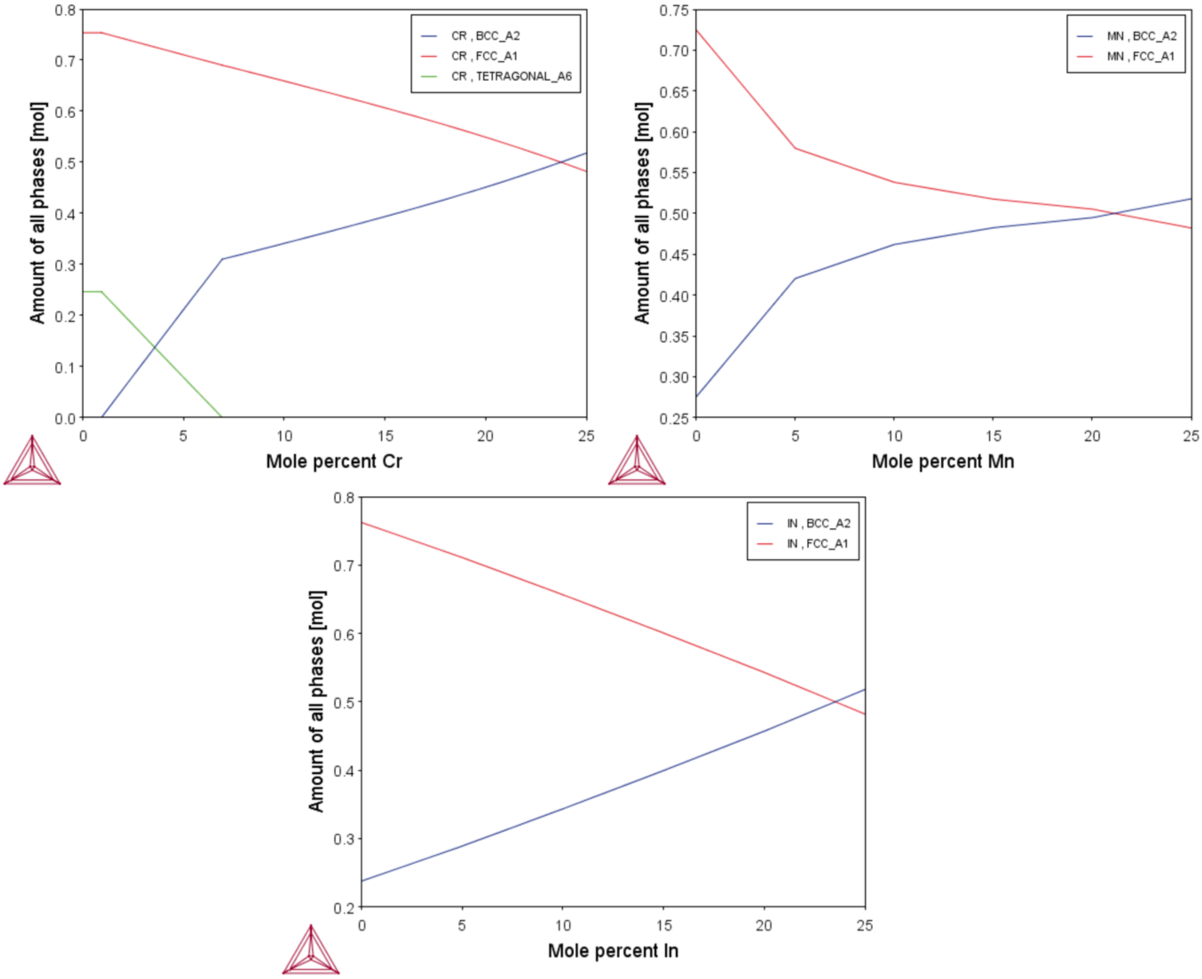

Figure 10.4: TC predictions for room temperature phase abundance (at room temperature) versus concentration of (a) Cr, (b) Mn and (c) In. For each case, Ni was the balance and the other two elements were maintained at a constant 25 at. %.

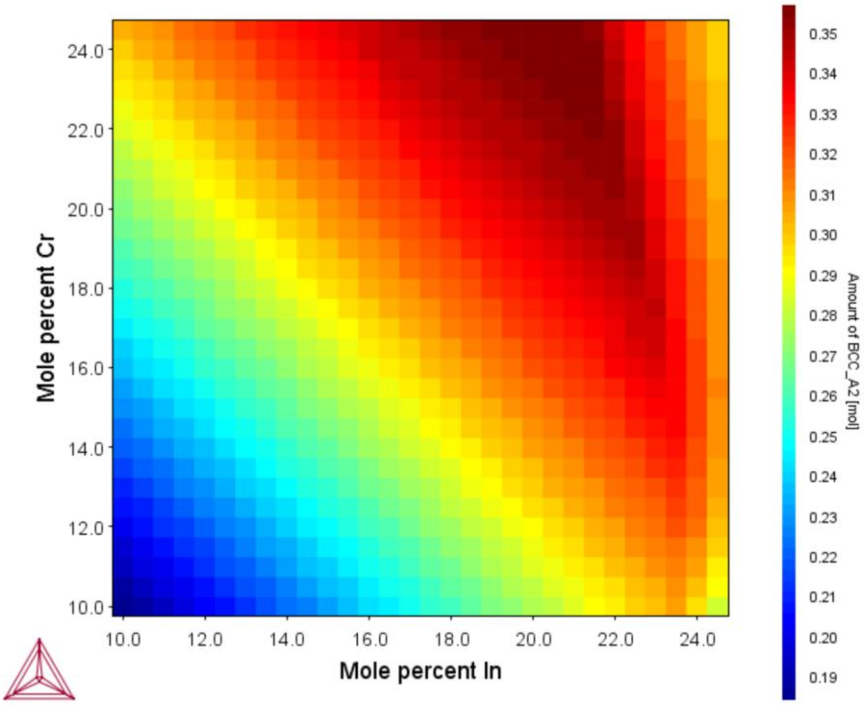

Figure 10.5: Room temperature abundance of BCC A2 phase for varying Cr and In at. %. Ni content is maintained at 50 at. %, while Mn is maintained as balance (such that Mn content varies from 0 - 30 at. %).

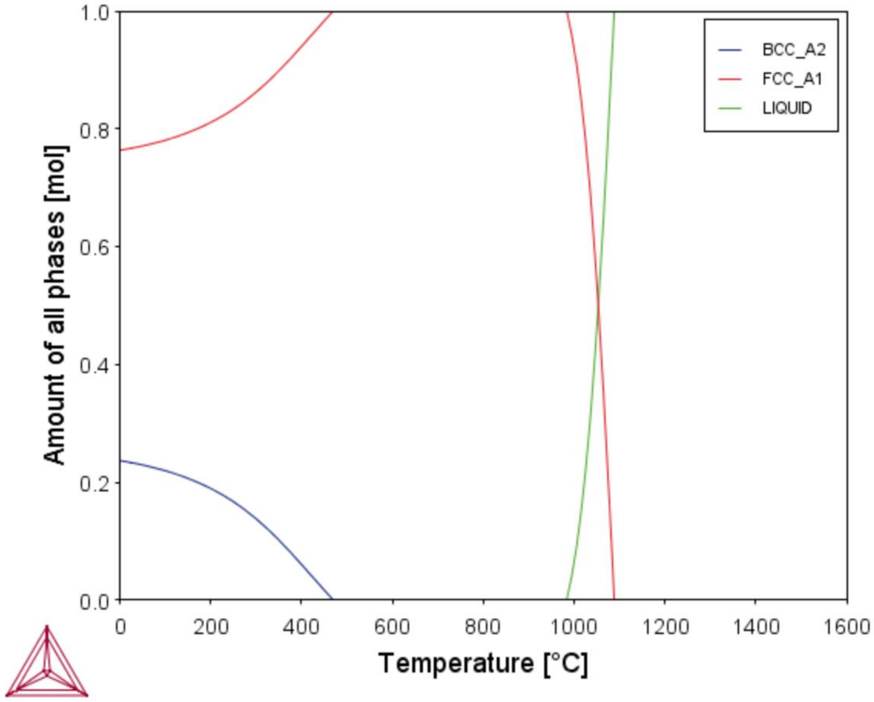

Figure 10.6: TC predictions of phase abundance versus temperature for the Ni(50)-Cr(9)-Mn(25)-In(16) composition.

Considering these predictions, a Ni(bal.)-Cr(9)-Mn(25)-In(16) (in at. %) was deemed of interest. Fig. 10.6 shows the TC-predicted phases against temperature, along with solidus and liquidus temperatures for this composition. The liquidus temperature is predicted as approximately 1088ºC, below which an FCC A1 phase solidifies, with solidus at 985ºC. This composition is predicted to remain single phase to below 500ºC, where a BCC A2 phase precipitates. At room temperature, the predicted compositions of the FCC and BCC phases, in atomic percent, is Ni(65.2)-Cr(2.0)-Mn(32.6) and Cr(32.7)-In(67.3), respectively. At room temperature, the FCC solid solution phase molar fraction is predicted as approximately 76 %, comparing favourably to the 48 % predicted for the equiatomic composition as in Fig. 10.2.

Aside from the TC predictions for this optimised composition, thermodynamic parameters were also calculated, as shown in Table 10.3. This optimisation for both liquidus and FCC solid solution abundance is reflected in the calculated parameters, with a small ΔH_{mix} and δr. Due to the high Ni content, the VEC is predictably greater and likely favours FCC solid solution over BCC. Considering these values and the TC predictions, solid solution formation, either single or dual phase, could be seen as more likely. However, it is still noted that the TC predictions have In and Cr preferentially forming BCC phase, despite the large mixing enthalpy of this pair. How this manifests in the fabricated alloy will be explored in the next section.

Table 10.3: Calculated values of ΔH_{mix}, δr and VEC for the optimised Ni(50)-Cr(9)-Mn(25)-In(16).

	ΔH_{mix} (kJ mol^{-1})	**δr (%)**	**VEC**
NiCrMnIn (optimised)	2.62	3.18	7.77

10.3 Fabrication of Optimised NiCrMnIn MPEA Filler Metal

A 20 g ingot of the optimised NiCrMnIn alloy (of nominal composition bal.-9-25-16 in at. %) was arc-melted from Ni foil (0.5 mm thickness), Cr pieces (irregular), Mn pieces (12 mm and down) and In shot (4 mm and down), all of at least 99.5 % purity (Alfa Aesar). The Arcast Arc-200 system with water-cooled Cu melting crucible was used for melting, with an operating current of 400 A. The chamber was evacuated down to below 4x10^{-5} Torr (5.3x10^{-3} Pa), before backfilling with Ar to a partial pressure of between -10 and -2 inHg (-34 and -6.7 kPa). The ingot was flipped and re-melted 5 times to improve homogeneity, with magnetic stirring also employed.

The as-cast microstructure was analysed by SEM in BSE mode, with two distinct regions in terms of phase morphology observed. Figs. 10.7 and 10.8 show SEM micrographs and EDS maps of typical sections of the upper, majority microstructure and the lower, minority microstructure, respectively. Table 10.4 shows EDS point scan measurements confirming the composition of these phases (averages of five measurements). These differences in microstructure are believed to be a result of the rapid cooling experienced by the lower portion of the ingot in contact with the water-cooled Cu crucible. The majority microstructure as shown in Fig. 10.7 is typified by regions of Cr-rich phase of irregular morphology (marked *1*), which in some cases are surrounded by a phase (marked *2*) with the same dark contrast, but which the EDS maps indicate are somewhat Ni-rich as well as containing significant Cr content. Both such phases are devoid of In. Other regions consist of fine eutectic lamellae (marked *3*), separated by regions of light contrast phase (marked *4*) which also surround the phases marked *1* and *2*, though EDS maps do not appear to distinguish between these regions compositionally, suggesting the only the dark contrast lamellae are distinct from the light contrast phase (the dark contrast lamellae were too fine to obtain point scan measurements in this case, and so are not included in Table 10.4). In Fig. 10.8, again EDS maps indicate the presence of the Ni- and Cr-rich phase (marked *5*), this time of dendritic morphology, with only few regions of the predominantly Cr-rich phase (marked *6*). Both the fine eutectic lamellar and light contrast phases as observed in Fig. 10.7 are observed here (marked *7* and *8* respectively). In both Figs. 10.7 and 10.8, the Mn content appears to be more homogenously distributed, with somewhat decreased content only in the Cr-rich cores. Meanwhile, In and Cr segregation is apparent in both figs. EDS revealed compositions of these phases to closely resemble those reported for phases in Fig. 10.7, and are not reported again in Table 10.4.

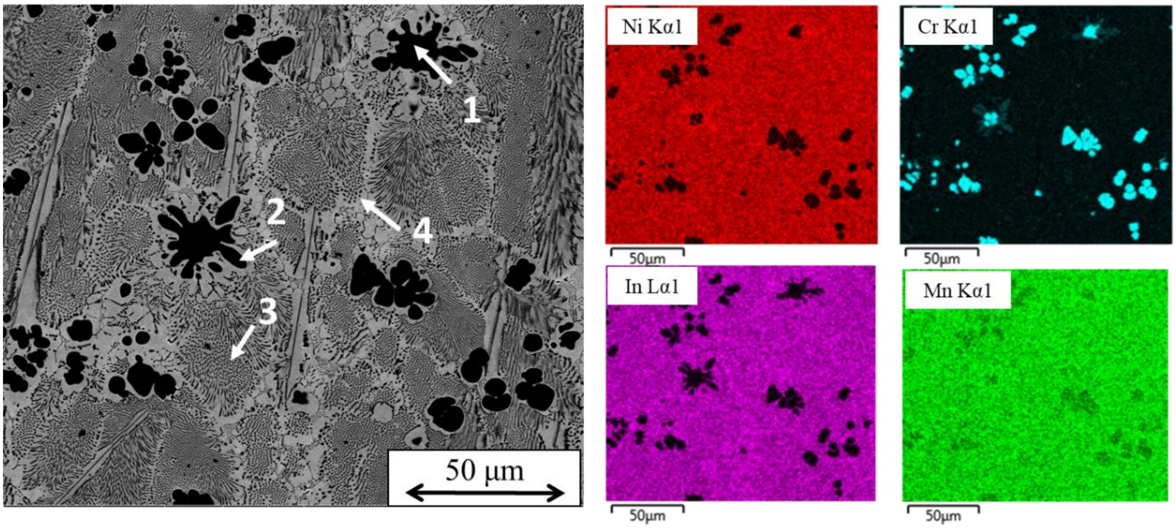

Figure 10.7: SEM BSE micrograph of typical portion of majority microstructure observed for as-cast Ni(bal)-Cr(9)-Mn(25)-In(16) filler metal. EDS Maps (right) indicate elemental distribution between phases.

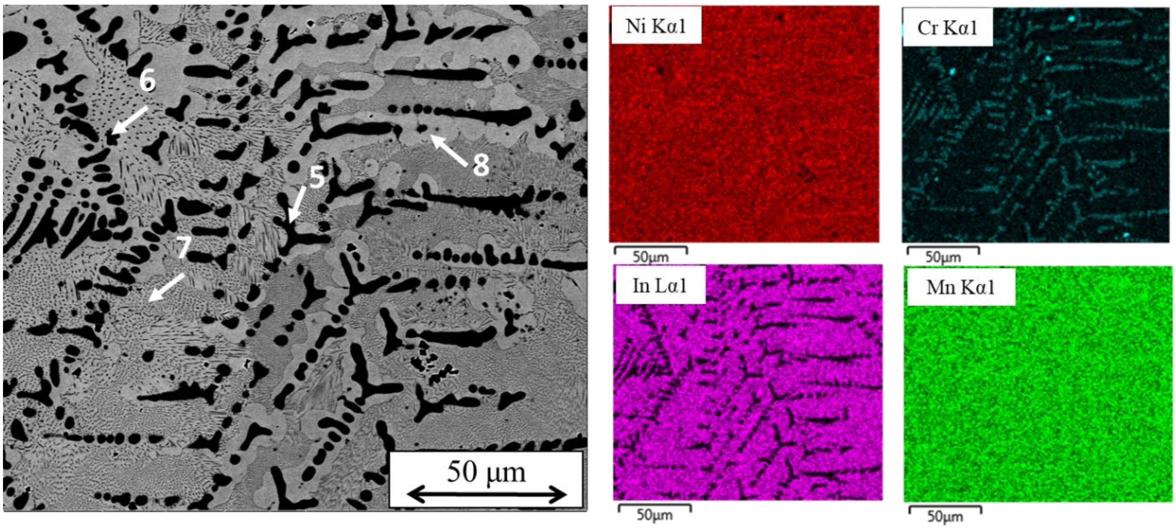

Figure 10.8: SEM BSE micrograph of typical portion of minority microstructure observed for as-cast Ni(bal)-Cr(9)-Mn(25)-In(16) filler metal. EDS Maps (right) indicate elemental distribution between phases.

Table 10.4: EDS point scan measurements (average of five) of various phases observed in the majority microstructure of the as-cast optimised Ni(bal.)-Cr(9)-Mn(25)-In(16) filler metal.

Region	Phase	Ni (at. %)	Cr (at. %)	Mn (at. %)	In (at. %)
Upper majority microstructure (Fig. 10.7)	1	7.5 ± 1.0	87.1 ± 1.3	5.3 ± 0.35	0.2 ± 0.05
	2	52.7 ± 1.2	24.3 ± 2.3	22.0 ± 1.6	1.1 ± 0.1
	4	48.8 ± 0.4	3.7 ± 0.5	28.7 ± 0.4	18.9 ± 0.3

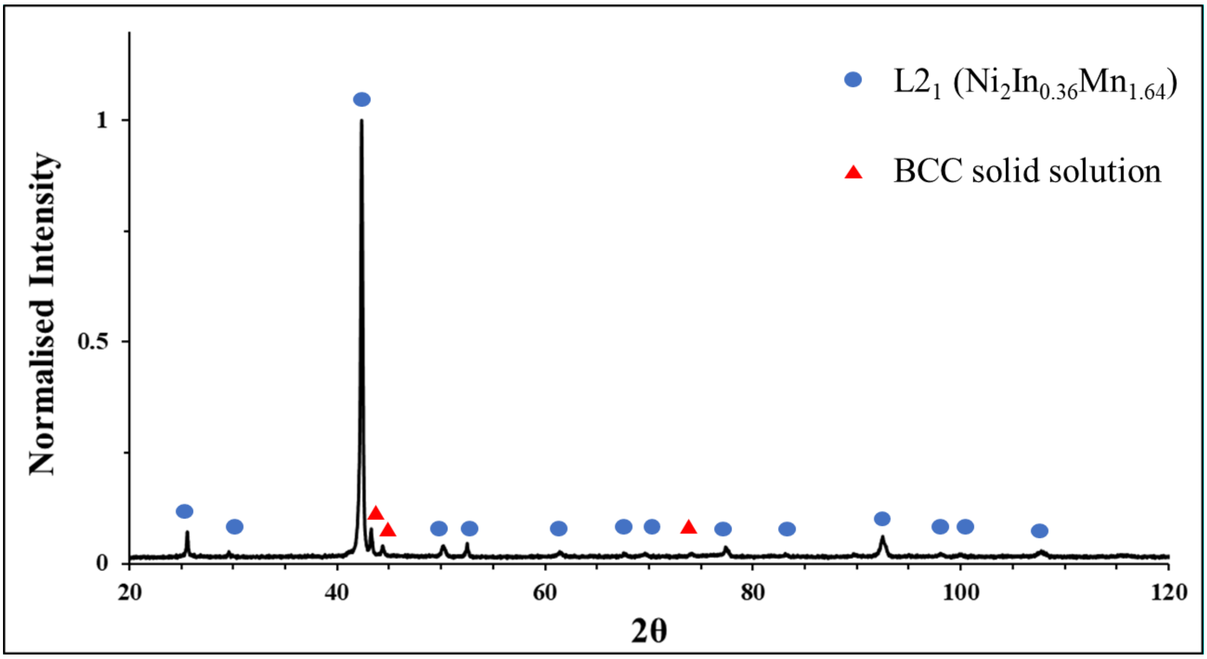

Figure 10.9: XRD Pattern for as-cast optimised Ni(50)-Cr(9)-Mn(25)-In(16) filler metal, with peaks matching Ni2In0.36Mn2 phase, and BCC solid solution.

SEM and EDS analysis of the as-cast optimised NiCrMnIn alloy was complemented by XRD analysis, with the XRD patterns shown in Fig. 10.9. As with the SEM observations, at least two phases are captured in the analysis. From PDF card matching, the majority of the alloy appears to be analogous to a cubic L2$_1$ Ni$_2$Mn$_{1.36}$In$_{0.64}$ phase (of space group Fm-3m), corresponding most likely to the light contrast matrix phase (marked *4* in Fig. 10.7). The particularly prominent peak at 2θ = 42° is likely due to favourable orientation for this reflection. Other peaks of smaller magnitude were less easily identified, with peaks matching BCC Cr solid solution possible, which may well correspond to the dark contrast Cr-rich phase (marked *1* in Fig. 10.7). As these other phases were somewhat less prevalent, this likely contributed to the low magnitude peaks in Fig. 10.9.

Fig. 10.10 shows a DSC curve for the as-cast optimised NiCrMnIn alloy. The main endothermic peak was taken to be the primary melting of the eutectic component of the as-cast optimised NiCrMnIn alloy, with solidus and liquidus temperatures of 943°C and 966°C read off. A minor lower temperature endothermic peak was observed at approximately 800°C, though given the other two phases observed in the as-cast state were rich in Ni and Cr and lean in In, it was deemed unlikely that these peaks correspond to any melting as they likely have a higher melting point than the matrix Ni-Mn-In eutectic. TC predictions of solidus and liquidus temperatures were 985ºC and 1088ºC respectively, for the alloy as a whole, or for a more direct comparison for the DSC-derived values that likely correspond to the eutectic matrix, the TC solidus and liquidus predictions for the composition reported under phase *4* in Table 10.4 would be 903ºC and 1035ºC respectively. While these values more closely agree with the DSC measured values, this actually represents a widening of the predicted melting range, suggesting TC does not predict this accurately. Finally, microhardness indentation was performed on the as-cast optimised NiCrMnIn alloy to assess the hardness as a basic indicator of the mechanical properties. Five measurements were taken of both microstructural regions identified in figs. 10.7 and 10.8, but it was found that the difference in phase morphologies had little impact on the values. The average microhardness values for the majority microstructure and minority microstructure were 408 ± 8 HV1 and 398 ± 8 HV1 respectively (with error derived from the standard deviation).

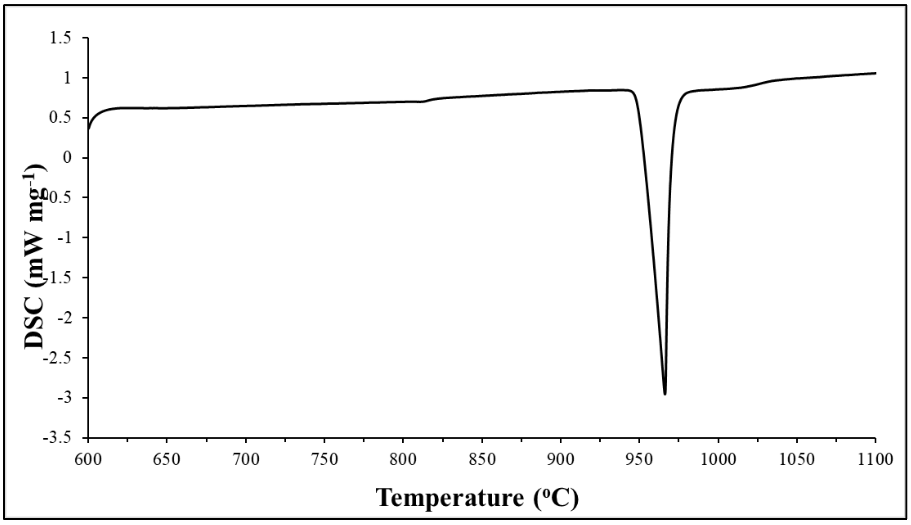

Figure 10.10: Example DSC heating curve for as-cast Ni(bal.)-Cr(9)-Mn(25)-In(16) filler metal, with read-off solidus and liquidus values of 943ºC and 966ºC respectively.

10.4 Vacuum Brazing of IN718

The optimised NiCrMnIn filler metal was trialled in the vacuum brazing of IN718, using vacuum furnace facilities at Kepston Ltd. (Wednesbury, UK). A 3 mm diameter cylinder was extracted from the as-cast optimised NiCrMnIn ingot via EDM. This was then sectioned so as to obtain thin discs of 3 mm diameter. A disc was then manually ground using a steel holding jig with p800 grit paper, until a foil thickness of approximately 55 μm was achieved. This was placed between two tokens of IN718, each with dimensions of 25 x 25 x 1 mm, forming a sandwich joint. Prior to brazing, IN718 tokens were ground with p1200 grit papers to remove surface oxides, before treatment in an ultrasonic bath along with the optimised NiCrMnIn foil in acetone for 10 minutes. The brazing cycle consisted of heating at 15ºC min^{-1} up to 900ºC, where the temperature was held for 5 minutes to equalise the temperature, before again ramping up to the brazing temperature of 1060ºC. The brazing temperature was held for 10 minutes, before furnace cooling down to 900ºC commenced, followed by N gas quenching.

Upon inspecting the joint following the brazing cycle, it was found that the foil was unsuccessful in joining the IN718 tokens, with the foil bonding somewhat to the lower token of the assembly, while the upper token remained loose. Fig. 10.11 shows an SEM BSE micrograph of a typical section of the foil-IN718 bond for the lower token. Some infiltration along grain boundaries of the IN718 base metal is apparent (light contrast phase, marked 1), extending some 350 – 400 μm into the IN718. EDS point scan measurements (summarised in Table 10.5) revealed this phase to be rich in In and Ni, but lean in Mn compared to the expected composition of the filler metal, and also very little Cr content. Meanwhile, EDS analysis also revealed some Mn content in the IN718 grains infiltrated by the filler metal (dark contrast, marked 2), much above what would be expected, suggesting diffusion of Mn into the IN718 base metal.

To explain this phenomenon, it appears that Mn depletion from the matrix phase seen in the as-cast state of the optimised NiCrMnIn alloy has resulted in liquation, that is, the separation of low melting temperature constituents from the bulk alloy. The Mn separation seems to have occurred either due to significant diffusion into the base metal, which EDS measurements seem to suggest, but also possibly due to the known high vapour pressure of Mn, causing volatilisation in the vacuum furnace. While some diffusion of Mn is evident, Mn is not expected to diffuse quickly into the IN718 filler metal, and so in order to be observed at distances of the order of hundreds of μm from the interface with the filler metal, the diffusion may have occurred after infiltration of the IN718 grains from the liquated In- and Ni-rich phase. However, due to initial dissolution of the IN718 base metal during heating, some diffusion of Ni and Mn away from the matrix Ni-Mn-In eutectic may have occurred, resulting in a phase comparatively richer in In, as indicated by Table 10.5. TC predictions for the composition of this phase suggest the onset of melting at temperatures below 300°C, which, even allowing for a substantial margin of error due to aforementioned TC inaccuracies, suggests that this phase is likely to melt and begin to flow due to capillary action, with this occurring on the lower IN718 token simply due to gravity. Given the heating rate of 15°C used in the brazing cycle, the assembly will have spent a significant amount of time at the intermediate temperatures allowing melting of this phase with no melting of the other higher temperature phases.

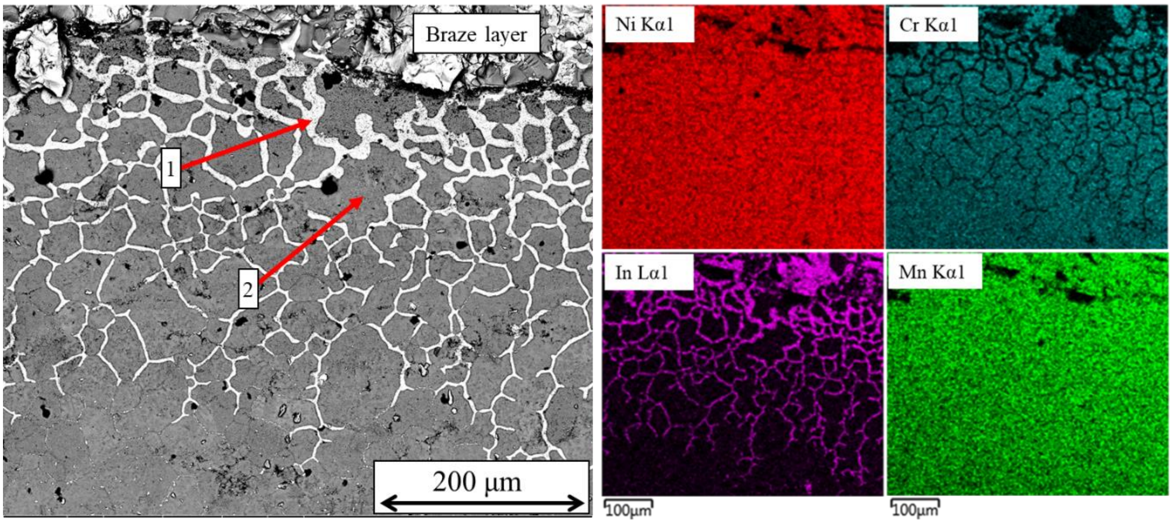

Figure 10.11: SEM (BSE) micrograph of section of lower portion of failed vacuum brazed NiCrMnIn-IN718 joint. EDS maps (right) indicate elemental distribution.

Table 10.5: EDS point scan measurements (average of five) of phases observed in the failed vacuum furnace brazed optimised NiCrMnIn-IN718 joints, based on Fig. 10.10. Errors derived from standard deviation.

	EDS point scan measurement (average of 5) (at. %)				
	Ni	**Cr**	**Mn**	**In**	**Fe**
1	32.2 ± 0.2	<1 ± 0.1	12.0 ± 0.1	33.5 ± 0.2	1.3 ± 0.1
2	45.5 ± 0.2	15.0 ± 0.1	8.2 ± 0.1	<1 ± 0.1	10 ± 0.2

10.5 Belt Furnace Brazing of IN718

Taking into account what was learnt in the preceding section, it was considered that the developed optimised NiCrMnIn filler metal may be better suited for belt furnace brazing using a protective inert atmosphere. This is expected to aid the brazing process by introducing the assembly to the brazing temperature faster, while the atmosphere will help to prevent Mn volatilisation and hence avoid liquation. Downsides may include less time at temperature, which may result in incomplete isothermal solidification. However, this alloy composition does not contain any fast diffusing elements such as B regardless, and so its use as a brazing filler metal is less dependent upon diffusion processes.

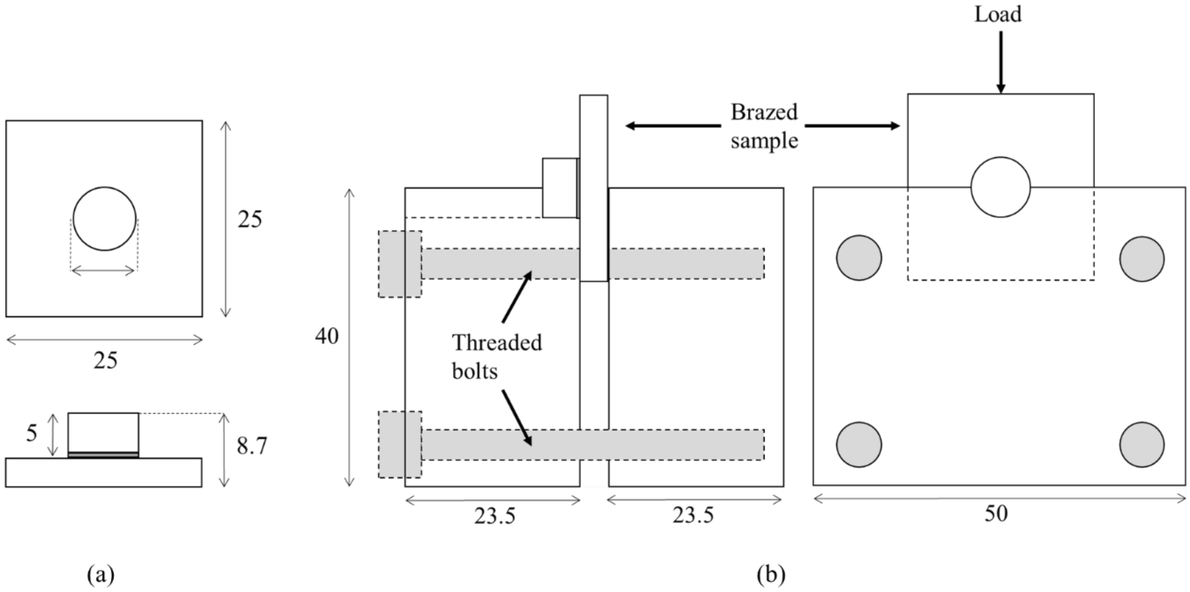

Figure 10.12: Schematic showing (a) brazed joint to be shear tested, and (b) side and front view of steel rig used to seat sample for shear testing by applying compressive load.

The belt furnace trial was conducted at Armeg Ltd (Dronfield, UK). For this trial, fabrication took an essentially similar route, with the differences being in the dimensions. In order to facilitate mechanical testing of any produced joint, the optimised NiCrMnIn filler metal disc was 8 mm in diameter, and was ground to an approximate thickness of 60 µm. This foil was placed in between an IN718 cylinder of 5 mm height and 8 mm diameter, and an IN718 token with dimensions 25 x 25 x 3.7 mm. Such an assembly was produced in order to sit in a steel testing rig, whereby a compressive load is applied in order to provide shear on the joint (see Fig. 10.12). The brazing cycle conducted by the belt furnace involved approximately 16 minutes moving through three consecutive heating chambers at 1070ºC, 1090ºC and 1100ºC, followed by gas quenching. It should be noted that this cycle was not optimised specifically for the brazing of IN718 with the optimised NiCrMnIn filler metal, rather it was the normal operation cycle employed by Armeg Ltd for their usual business.

Fig. 10.13 shows an SEM BSE micrograph of a typical section of the optimised NiCrMnIn-IN718 joint, with EDS point scan measurements for various regions and phases summarised in Table 10.6 (averages of five measurements). Supplementary EDS mapping at higher magnification is displayed in Fig. 10.14. A distinctive non-planar interface is observed on both sides of the joint, with an apparently abrupt change in composition judging by the contrast change from light to dark. Compared with the as-cast state, post-braze it is immediately obvious that the initial microstructure of the optimised NiCrInMn alloy has altered due to interaction with the base metal. The light contrast phase in the joint region (marked *a* in Fig. 10.13) is rich in Ni, Mn and In, consistent with the primary matrix phase in the as-cast optimised NiCrMnIn filler metal, but slightly richer in In and slightly less rich in Mn. However, compared with the as-cast state, the eutectic lamellae were not observed post-brazing, indicating the composition may have moved away from eutectic due to the inclusion of base metal elements such as Fe, Nb, Mo and Ti. Regions of a darker irregular morphology phase were observed (marked *b* in Fig. 10.13), which possibly mark the grain boundaries of the primary light contrast Ni-In-Mn phase. This phase was found to be Ni, Cr and Mn-rich, and so seemingly corresponds to the phase marked *2* in Fig. 10.7 for the as-cast optimised NiCrMnIn filler metal. However, the presence of Fe is due to the dissolution of the base metal and diffusion of Fe. Notably, in contrast to the as-cast state, none of the Cr-rich phase (marked *1* in Fig. 10.7) was observed.

Table 10.6: EDS point scan measurements (average of five) of various phases observed in the belt furnace brazed optimised NiCrMnIn-IN718 joints, based on Fig. 10.12.

Phase	Ni	Cr	Mn	In	Fe	Nb	Mo	Ti
a	48.5 ± 0.1	2.7 ± 0.3	24.4 ± 0.2	21.8 ± 0.2	1.2 ± 0.1	0.7 ± 0.04	0.1 ± 0.1	0.4 ± 0.0
b	51.3 ± 0.5	21.7 ± 0.8	16.4 ± 0.2	1.2 ± 0.4	7.6 ± 0.2	1.2 ± 0.1	0.5 ± 0.2	0.1 ± 0.2
c	49.4 ± 0.2	25.2 ± 0.2	13.4 ± 0.3	0.6 ± 0.1	9.5 ± 0.1	0.8 ± 0.1	1.1 ± 0.04	0.1 ± 0.1
d	52.3 ± 0.1	21.5 ± 0.1	0.3 ± 0.04	0.0 ± 0.0	18.7 ± 0.1	3.0 ± 0.1	1.7 ± 0.1	1.2 ± 0.04

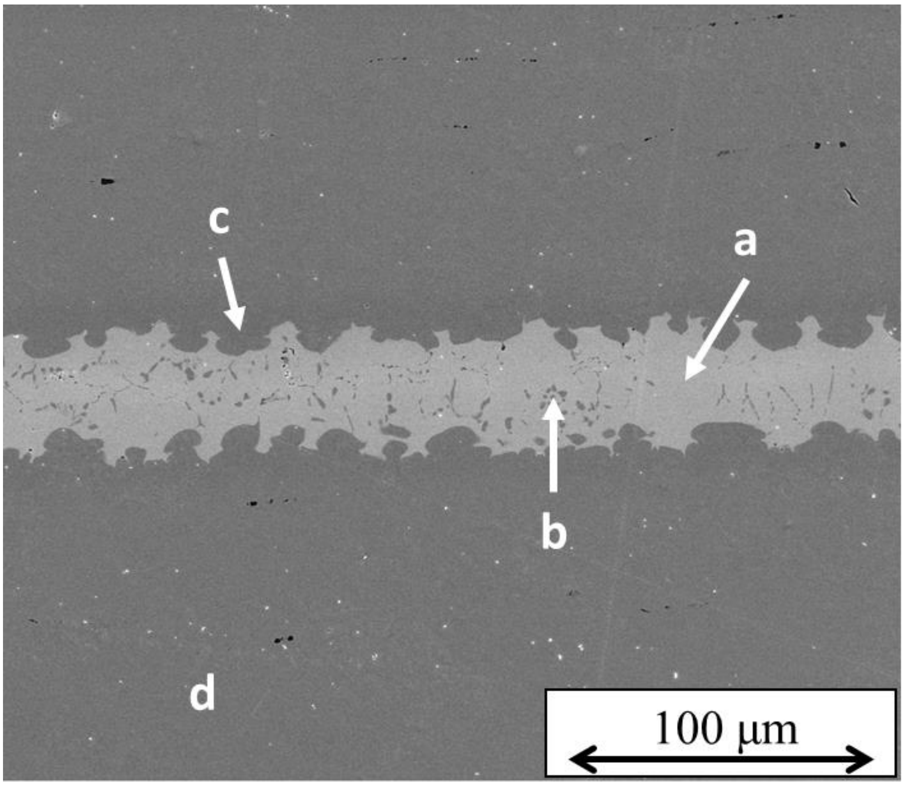

Figure 10.13: SEM (BSE) micrograph of typical section of optimised NiCrMnIn-IN718 belt furnace brazed joint. Distinct microstructural features are labelled, with the wavy interface between base metal (d) and joint region (a) also of note.

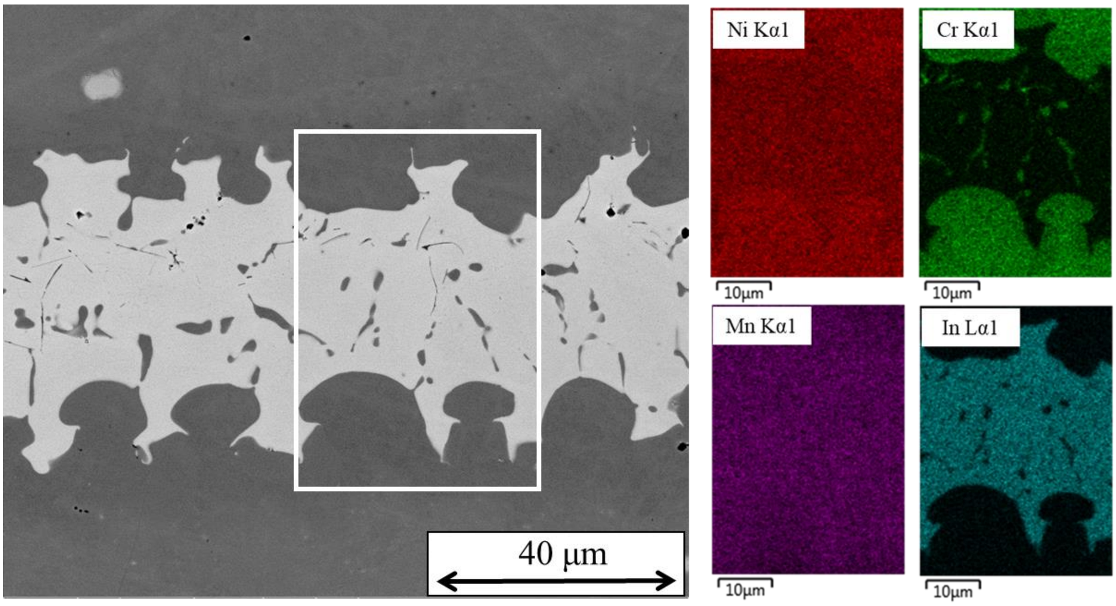

Figure 10.14: EDS maps of highlighted region of belt furnace brazed NiCrMnIn-IN718 joint.

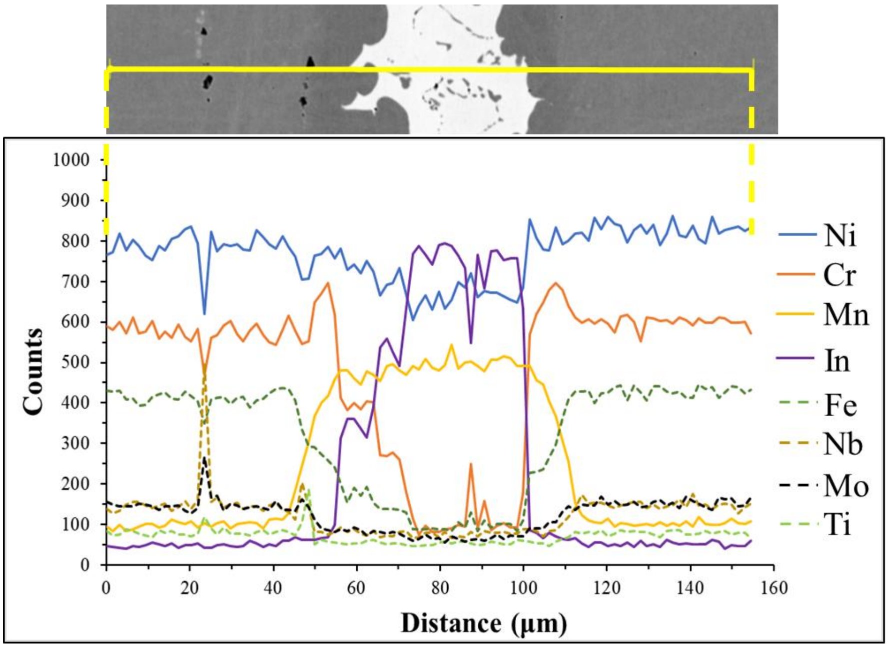

Figure 10.15: EDS Linescan of section of NiCrMnIn-IN718 belt furnace brazed joint, highlighting elemental ditribution across joint, and the extent of cross-diffusion between base and filler metal elements.

The EDS line scan (Fig. 10.15) showed the In content was largely confined to the light contrast joint phase, with little evidence of diffusion into the IN718 base metal. However, some inter-diffusion particularly between Mn and Fe evidently took place, resulting in the zone marked *c* in Fig. 10.13. This region is also slightly richer in Cr than even the IN718 base metal (marked *d*), possibly explaining the absence of the Cr-rich phase (seen in the as-cast state) in Fig. 10.13. Immediately beyond the region marked *c*, no appreciable Mn content beyond the nominal IN718 content was measured, indicating Mn diffusion confined only to within approximately 40 µm of the joint centreline. In all observed phases, in similarity with the as-cast state, the Cr and In content remain very much segregated.

Taking into account partition coefficients, segregation and melting temperatures of phases, the resulting microstructure of the brazed joint can be explained as follows. As the joint assembly reaches temperature during the brazing cycle, the primary eutectic component of the as-cast optimised NiCrInMn filler metal proceeds to melt. Dissolution of the IN718 base metal occurs at the interface with the filler material primarily due to Mn diffusion, introducing base metal elements into the melt and hence the Fe, Nb, Mo and Ti content of phases *a* and *b* in Fig. 10.13. Segregation and diffusion of Cr away from the In-rich melt results in isothermal solidification of a Ni, Cr-rich phase, also containing Mn and Fe (marked *c* in Fig. 10.13). As the isothermally solidified front advances, In is rejected, enriching the already Ni, In-rich melt further with In. Meanwhile, the Ni, Cr-rich dark phase within the joint region, marked *b* in Fig. 10.13, may not have experienced melting, or was initially dissolved during brazing before solidifying due to Cr-In segregation upon cooling. As the time spent at temperature during this belt furnace brazing cycle is not long, and due to the lack of presence of fast-diffusing elements such as B, the isothermal completion was not completed. As the joint reaches the cooling zone of the belt furnace, the remaining light contrast Ni, In-rich melt finally solidifies, pushing the dark contrast phase to grain boundaries. In comparison to elements such as B, solid-state diffusion of the elements involved in this scenario is expected to be much slower. Mn has been suggested to diffuse at a rate similar to other alloying additions to Ni, but much slower than B [176].

This, combined with the relatively short time at high temperature, means further homogenisation of the joint did not occur, and also the region of the base metal immediately outside region marked *c* remained undisturbed, with no apparent evidence of intermetallic phases either intra-or inter-granular.

Typically, in brazing, isothermal solidification results in an approximately planar growth of the solid from the joint interface inwards. Clearly, in the resulting joint microstructure observed in Fig. 10.13, this is not achieved, with cellular protrusions instead evident. Such phenomena may be explained by the presence of an atypically high constitutional undercooling, that is, the constitution-dependant presence of liquid below the freezing point. While under ideal conditions of no undercooling, any protrusions from a planar solid-liquid interface are energetically unfavourable due to the need for increased heat flow through a larger interfacial area. In reality however, impurities can lead to constitutional undercooling, and a protrusion would then encounter undercooled liquid ahead of it able to freeze, thus furthering the protrusion into the features observed in Fig. 10.13.

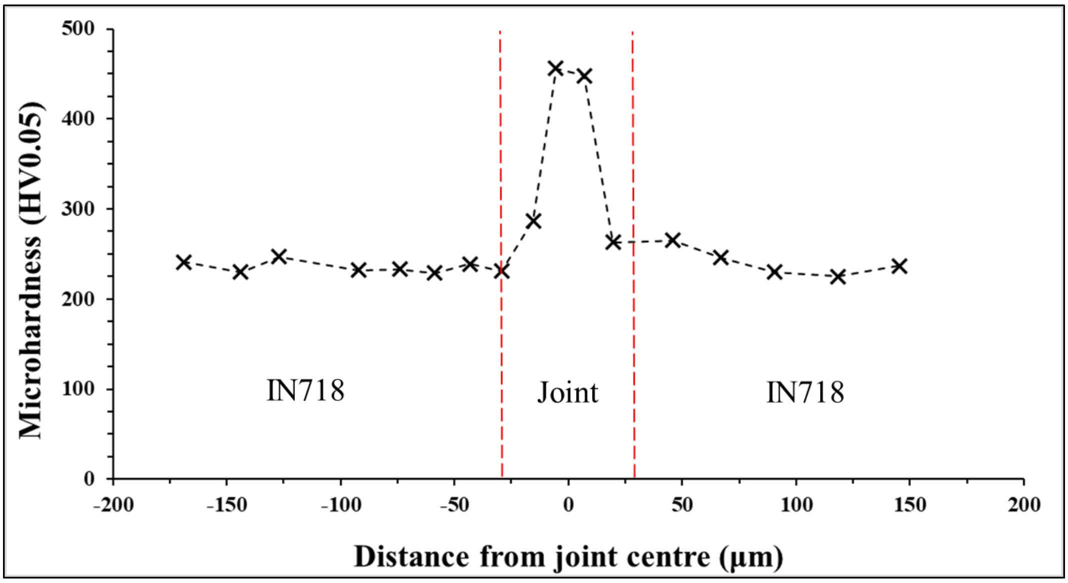

Figure 10.16: Microhardness profile taken across the optimised NiCrMnIn-IN718 brazed joint.

A profile of the microhardness of the joint was obtained to give some indication as to the mechanical properties of the resulting joint, as shown in Fig. 10.16. While the limited diffusion from the filler metal and lack of intermetallic formation in the vicinity of the joint interface resulted in a mostly flat profile until within the joint region, the measured microhardness within the joint region almost doubled to approximately 450 HV(0.05). This is slightly higher than the measured microhardness for the as-cast optimised NiCrMnIn alloy (approximately 400 HV1 on average), possibly due to the presence of base metal elements in solution. The region immediately outside the joint region (*c* in Fig. 10.13), exhibited a slight increase in hardness as compared to the base metal, perhaps due to increased Cr and Mn content. While this increase in hardness between the base metal and joint is significant, it is also less than is commonly observed for joints using commercial filler metals which exhibit a brittle eutectic centreline, for example in [109], though it is higher than for joints exhibiting completed isothermal solidification across the joint, for example in [79]. Despite this, as the primary joint phase is likely to be of the same cubic crystal structure as the primary matrix phase in the as-cast state (according to the EDS measurements in Tables 10.4 and 10.6), it is not believed to be of particular brittleness, and the increased hardness could be due to solid solution strengthening. When tested in shear, however, the joint achieved only approximately 40 MPa. This is an order of magnitude lower than can be achieved for IN718 brazed joints, and so in its current form this filler metal is unlikely to be attractive for applications where joint strength is important.

10.6 Use in Other Brazing Applications

With the knowledge that the developed optimised NiCrMnIn filler metal is unsuitable for vacuum brazing applications, but has been successfully used for brazing in a belt furnace with an inert or reducing atmosphere, opens up the possibility of using this alloy for the joining of other materials that are often brazed in this manner. In addition, the composition of the alloy may lend its applicability to materials outside Ni-based superalloys. Mn in particular is a useful alloying addition as an active element, increasing the ability to wet ceramics such as carbides [202]. Meanwhile, In has previously seen use as a MPD in some Cu and Cu-Ag filler metals to improve ductility.

Another application that this filler metal might be expected to be suitable for, therefore, is the brazing of W-carbide drill tips to steel drill bits. Such carbide-tipped drill bits are a widely used tool for the most demanding drilling applications, and yet are relatively cheap and easy to make. They are generally produced quickly in batch brazing using a belt furnace with reducing atmosphere. The geometry of these parts, specifically the small amount of brazed surface between the steel drill bit and carbide tip, means that only small amounts of filler metal are required, but is more suited for flow of molten filler metal as opposed to direct placement of a foil, due to multiple surfaces with various orientations. As such, filler metal in the form of powder or paste is more commonly used. In terms of joint mechanical properties, the forces applied to the joint while in operation are complex and not unidirectional, and so shear or tensile strength in any specific direction is not a major consideration (indeed, the carbide tips are generally expected to wear out during use before the joint itself fails). Instead, a bigger concern might be (as for all instances of metal-to-ceramic joints) differences in thermal expansion coefficients, sufficient ductility, and ability to adequately wet both metal and ceramic.

To investigate the applicability of the optimised NiCrMnIn filler metal to the brazing of W-carbide tips to steel drill bits, brazing trials were conducted at Armeg Ltd., using a production line belt furnace currently used for the production of carbide-tipped drill bits.

10.7 Brazing of W-carbide to EN24T steel drill bit

W-carbide drill tips were joined to EN24T steel drill bits (Cr, Ni and Mo-containing) via belt furnace brazing at Armeg Ltd. (Dronfield, UK), using both the optimised Ni(bal.)-Cr(9)-Mn(25)-In(16) (in at. %) filler metal and currently commercially used Cu(bal.)-Mn(12.5)-Ni(2.3) filler metal, known commercially as C-Bronze (Table 10.7 shows the two compositions in at. %, and melting ranges, for comparison). Although the nature of the two materials is different, and the application is rather different than what had been envisaged with designing the alloy, it was felt that the similarity of melting temperatures and constituents in the alloy might allow successful brazing in this application. The brazing cycle used was the same as for the belt furnace brazing of IN718 with optimised NiCrMnIn as described in Section 10.5, involving approximately 16 minutes at temperature moving through three consecutive heating chambers at 1070°C, 1090°C and 1100°C, followed by gas quenching. This is the same cycle Armeg Ltd use for commercial production of the drill bits using the C-Bronze filler metal.

The geometry of the joint makes the use of foil form of the optimised NiCrMnIn filler metal likely to be unsuitable. For this reason, a 20 g ingot was fabricated via arc-melting in the same manner as described in Section 10.3. This ingot was then crushed manually into a coarse powder using a steel billet and cup, with sieving used to remove particles larger than approximately 300 µm. Due to the low amount of alloy needed, other powder production routes such as attrition milling, which require substantially more feed material, were deemed unsuitable for this study. The C-Bronze filler metal was provided in powder form by Armeg Ltd. The method of application of both filler metals to the surfaces to be joined involved application of a binder paste to the pre-assembled drill bit, before dipping into a container of the filler metal powder. When assembled, the drill bits were placed on the conveyor belt and experienced the same brazing conditions in the belt furnace as for the commercially-produced drill bits.

Table 10.7: Nominal compositions, in at. %, and solidus and liquidus, values of commercial C-Bronze filler metal and optimised NiCrInMn filler metal.

	Composition (at. %)					Solidus (ºC)	Liquidus (ºC)
Filler metal	**Ni**	**Cr**	**Mn**	**In**	**Cu**		
C-Bronze	2.3	-	12.5	-	85.2	965	995
Optimised NiCrMnIn	50	9	25	16	-	943	966

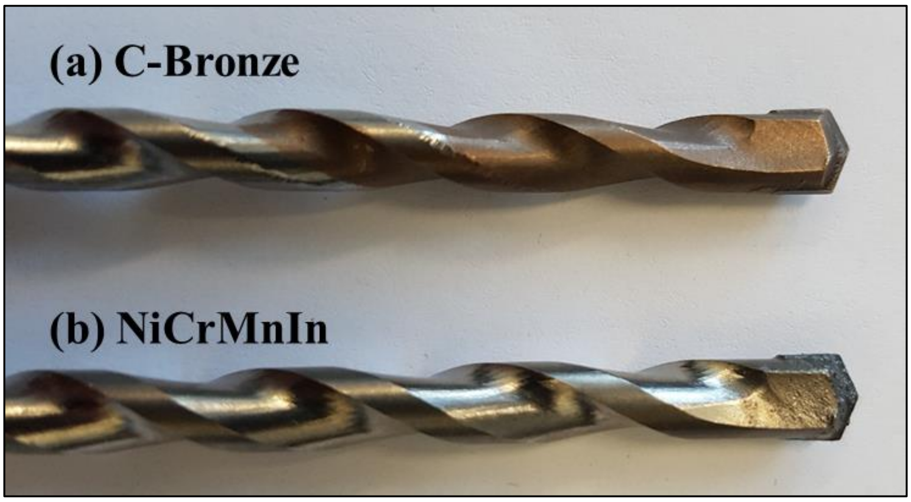

Figure 10.17: Photograph taken of example drill bits brazed using (a) commercial C-Bronze filler metal and (b) optimised NiCrMnIn filler metal.

Fig. 10.17 shows a photograph illustrating the differences in drill bits brazed using the C-Bronze and optimised NiCrMnIn filler metals. Figs. 10.18 and 10.19 show SEM BSE micrographs of typical sections of brazed drill bits using the commercial C-Bronze filler metal and optimised NiCrMnIn filler metal, respectively. It should be noted here that due to the extremely hard W-carbide tip, sectioning of the joint in order to observe the internal microstructure of the joint was not possible, and so the micrographs in Fig. 10.18 and 10.19 show the microstructure closer to the outer region of the joint where grinding with SiC papers was possible. In Fig. 10.18, it can be seen that substantially more interaction with the EN24 steel has occurred than with the W-carbide drill tip (marked *i*), as evidenced by the apparently largely intact interface with the drill tip. Meanwhile, penetration of the EN24 steel grains appears to have occurred, and EDS point scans (Table 10.8), average of five measurements) shows diffusion of Cu and Mn into the steel (marked *i*). According to the Cu-Fe phase diagram, this Cu concentration is above the solubility limit in Fe, though the presence of Mn, Ni and Cr may extend this limit. The joint region itself (marked *ii*), spanning approximately 100 – 150 μm, is slightly reduced in Mn content and the presence of a small Fe content was detected, presumably due to dissolution and diffusion processes. No appreciable W content was detected in this region. The arrow on Fig. 10.18 points to a region within approximately 25 μm of the interface with the W-carbide tip, where an apparently Fe-rich phase was observed, which may have formed due to rejection from the Cu, Mn-rich melt during solidification. With little or no diffusion, or other interaction, with the W-carbide tip, this phase appears to have built up along the interface. Referring to the Cu-Fe phase diagram and the EDS measured composition of the primary Cu, Mn-rich phase of the joint region, this region likely consisted of γ-Fe solid solution + liquid at the highest brazing temperature. Upon quenching, the Cu-rich liquid solidified, and so it is possible that while before this occurred, the Fe-rich phase, un-melted, simply built up at the W-carbide interface due to gravity. Another possibility is due to some kind of reaction layer at the W-carbide interface, but without further study, the origin of this Fe-rich phase is difficult to determine.

In comparison, when using the optimised NiCrMnIn filler metal (the microstructure for which is shown in Fig. 10.19), the joint was observed to be much narrower, with a joint width below approximately 50 μm. EDS point scan measurements are recorded in Table 10.9 (average of five measurements). The microstructure somewhat bears resemblance to that observed when belt furnace brazing IN718 with the optimised NiCrMnIn filler metal (see Fig. 10.13), with a central In, Ni-rich phase (marked *I*), outside which is a darker contrast phase (marked *II*) rich in Ni, Fe and Mn, evidencing some probable dissolution and cross-diffusion of particularly Fe, which is not present in the filler metal. However, EDS measurements revealed a Cu contamination in this phase, which is most likely to have occurred just prior to brazing where some contact with the C-Bronze filler metal powder may have occurred. The interface between these two regions is again notably wavy rather than planar, though not to the extent as was observed in Fig. 10.13. Another noticeable difference as compared to the joint produced using the C-Bronze filler metal in Fig. 10.18, was the apparently much more limited interaction with the EN24 steel (marked *III*) in this case. No grain boundary penetration of the filler metal melt was observed. When also considering qualitative observations of the drill bits shown in Fig. 10.17, in which the C-Bronze filler metal could be seen to have flowed some distance along the steel drill bit, the reason for the differing interactions with the steel by the two filler metals may be due to differences in wetting. The better-wetting C-Bronze filler metal was apparently able to penetrate the grain boundaries of the EN24 steel whereas the optimised NiCrMnIn filler metal was not.

Due to the geometry of these joints and the materials used in the drill bits, there was limited capability to perform quantitative mechanical testing, such as shear or tensile testing. However, measurements of microhardness of different regions of the joints were performed, to give an indication as to the difference in mechanical properties across different regions. The ability to join such materials as W-carbide to tool steels, in a way that can accommodate the different thermal responses of the materials, is of particular importance in the tool production industry. As such, a filler metal used to join such materials should be sufficiently ductile, thus preferably of FCC crystal structure, in order to effectively deform and relieve stresses built up during the brazing process, and for this reason Cu-based filler metals such as the C-Bronze used here are often selected. Microhardness measurements may offer some indication of how the C-Bronze and optimised NiCrMnIn filler metals compare in this regard. Fig. 10.20 shows plots showing the average microhardness (HV0.05, five measurements) for the EN24 steel and W-carbide base materials, as well as for the primary joint region microstructure in both of the above joints. The lowest hardness, and hence likely highest ductility, was obtained for the joint using the C-Bronze filler metal, at 215 ± 31 HV0.05, which was less than half that of the joint using the NiCrMnIn filler metal, at 447 ± 57 HV0.05.

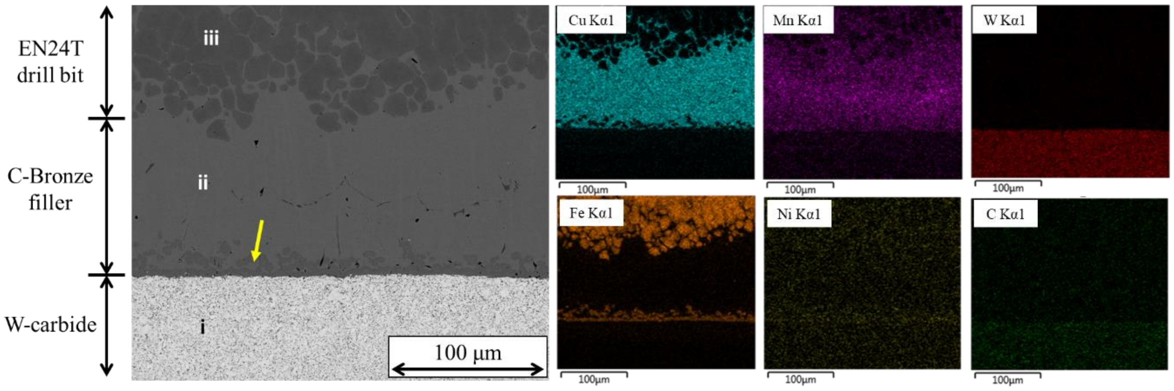

Figure 10.18: SEM (BSE) micrograph of typical section of drill bit brazed using commercial C-Bronze filler metal. EDS maps (right) highlight the elemental distribution between phases.

Table 10.8: EDS point scans (average of five) showing elemental concentration of various phases observed in Fig. 10.18

	Cu	**Mn**	**Ni**	**Fe**	**W**	**Cr**	**Mo**
i	0.3 ± 0.4	0.2 ± 0.1	-	0.2 ± 0.2	82.4 ± 1.1	0.3 ± 0.1	-
ii	86.3 ± 0.7	9.2 ± 0.3	2.2 ± 0.3	1.9 ± 0.2	0.2 ± 0.3	0.1± 0.1	0.1 ± 0.2
iii	4.0 ± 2.6	3.5 ± 2.1	3.4 ± 1.4	86.8 ± 5.9	0.5 ± 0.3	1.6 ± 0.2	0.4 ± 0.2

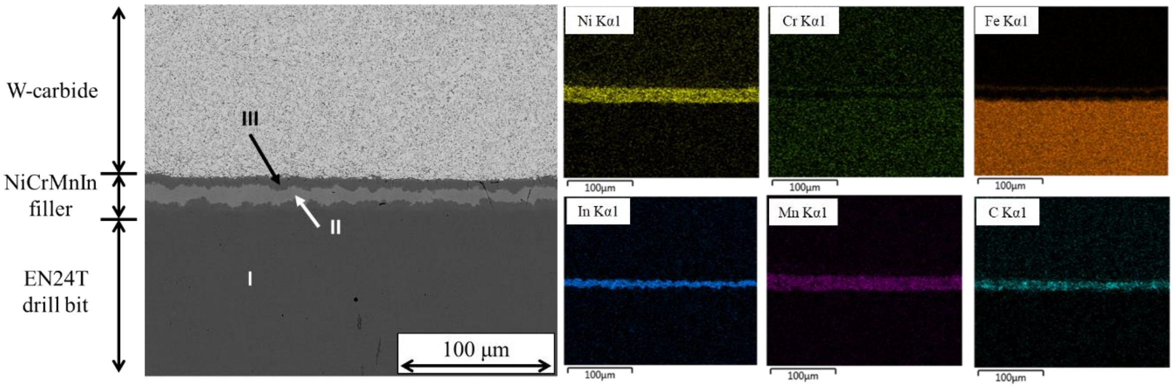

Figure 10.19: SEM (BSE) micrograph of typical section of drill bit brazed using optimised NiCrMnIn filler metal. EDS maps (right) highlight the elemental distribution between phases.

Table 10.9: EDS point scans (average of five) showing elemental concentration of various phases observed in Fig. 10.19

	Ni	**Cr**	**Mn**	**In**	**Fe**	**Cu**	**Mo**
I	1.9 ± 0.3	1.9 ± 0.2	0.9 ± 0.2	0.1 ± 0.1	95.2 ± 0.8	-	0.3 ± 0.3
II	25.5 ± 4.6	-	16.4 ± 3.0	32.9 ± 0.4	1.6 ± 0.2	23.4 ± 7.8	0.1 ± 0.1
III	38.4 ± 1.4	3.1 ± 0.3	18.7 ± 1.2	1.5 ± 0.3	28.9 ± 2.3	8.3 ± 0.5	0.2 ± 0.2

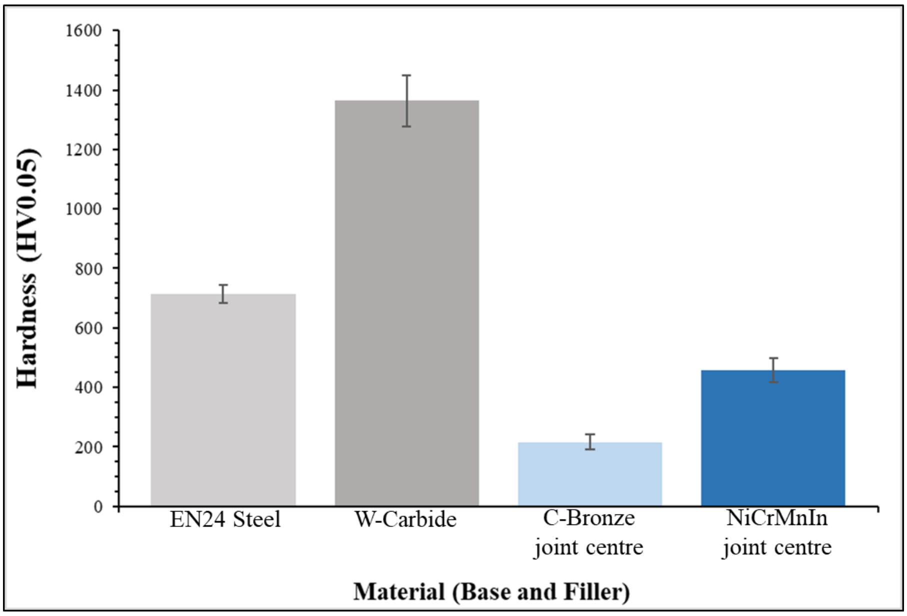

Figure 10.20: Average microhardness measurements of different regions of brazed drill bits, including EN24 steel and W-carbide base materials, and the joint regions using both commercial C-Bronze and optimised NiCrMnIn filler metals, as in indication as to the variation of mechanical properties across the joints.

10.8 Chapter Summary and Implications

This chapter, building upon the investigations into using In as a novel MPD element as detailed in Chapter 8, reports the design, development and trialling of a novel NiCrMnIn MPEA filler metal, with composition, in at. %, of Ni(50)-Cr(9)-Mn(25)-In(16). Design began by considering equiatomic NiCrFeIn, only to find that due to excessive elemental segregation, this composition was unable to be satisfactorily fabricated via arc melting. This led to the consideration of Mn as a substitution for Fe, which was predicted to have a better alloy forming ability with In due to the lower mixing enthalpy of the Mn-In binary as compared to the Fe-In binary. Furthermore, Mn was also predicted to further help reduce the liquidus according to the Ni-Cr-Mn ternary phase diagram, and so essentially acting as a secondary MPD element. Cr, while also expected to segregate from In (even though TC actually predicted the formation of a Cr-In BCC phase, likely due to the lack of assessed data for the Cr-In system), was deemed a necessary inclusion in order to provide corrosion resistance to the alloy. Therefore, a reduced Cr content was included.

By comparing observations of the as-cast state of the fabricated optimised NiCrMnIn filler metal with TC predictions, an assessment was made as to the suitability and usefulness of TC as an alloy design tool for such applications and alloys. As noted in this chapter, and in Chapter 8, experimentally assessed data for the binary In systems was not included in the databases available for the duration of this project. Phase diagrams for both Ni-In and Mn-In do, however, exist. Considering the mixing enthalpies, ΔH_{mix}, of all binary pairs in the NiCrMnIn system, Ni-In and Mn-In have $\Delta H_{mix} = 2$ kJ mol^{-1} and $\Delta H_{mix} = 3$ kJ mol^{-1} respectively, whereas Cr-In has $\Delta H_{mix} = 20$ kJ mol^{-1}, which would suggest likely segregation of the two elements. Indeed, this was seen to be the case in the as-cast microstructure, but TC instead had predicted the opposite, with Ni-Mn forming an FCC A1 phase and Cr-In forming a BCC phase (it should be noted that these are equilibrium predictions). Therefore, for specific phase information such as crystal structure and composition, TC should be used with caution, particularly in cases where assessed binary information is not available for certain elements in a composition. Rather, the use of established phase diagrams and empirical thermodynamic parameters used in the design of MPEAs and HEAs can be used in conjunction in order to help predict the formation of solid solutions or other phases. At the same time, TC proved more useful as a tool for optimising solidus and liquidus temperatures for this system. While comparisons between DSC measurements and TC predictions for solidus and liquidus showed discrepancy in the specific values, the process of finding local minima in liquidus temperatures in TC proved useful in optimising the composition for liquidus, which was of importance in this work, in the aim to develop filler metals with sub-1100°C liquidus temperature so as to be comparable with current commercially used Ni-based filler metals.

When used in the vacuum brazing of IN718, the optimised NiCrMnIn filler metal was found to be unsuitable, as it was observed that it had failed to adequately join the IN718 due a combination of high vapour pressure particularly of Mn, as well as liquation of the low temperature matrix phase of the filler metal. However, when used to join IN718 in a belt furnace with a reducing atmosphere, the optimised NiCrMnIn filler metal successfully joined the IN718. Post-braze, the microstructure exhibited a primary Ni, In, Mn-rich phase, from which Cr was largely segregated. Meanwhile, cross-diffusion of Fe and Mn resulted in the formation of a Ni, Mn, Fe and Cr-rich phase immediately outside the primary In-containing phase. The transition between these two phases was abrupt, with only Mn and Fe showing gradual concentration gradients whereas Cr and In were largely confined to their respective phases. The interface morphology was also observed to exhibit more cellular protrusions into the In-containing phase, attributed to a high degree of constituent undercooling. Beyond the Ni, Mn, Fe and Cr containing phase, little diffusion of filler metal elements into the IN718 base metal was observed, leaving its microstructure largely intact. Mechanically, however, when tested in shear the joint only achieved a low strength of approximately 40 MPa. Overall, this filler metal is unlikely to be useful in the brazing of Ni-based superalloys in its current form, in applications where joint strength is important.

Finally, due to the cubic FCC-type crystal structure of the primary Ni-In-Mn matrix phase of the as-cast optimised NiCrMnIn filler alloy, as well as the known ability of Mn to wet carbide and other ceramic surfaces, an opportunity to trial the filler metal in the brazing of W-carbide drill tips to EN24 steel drill bits was taken. While the ductility of the braze (judging from microhardness measurements) seemed to be less than that obtained for a standard joint using Cu-based C-Bronze filler metal, the microstructure of the joint appeared to show less effect on the EN24 steel as compared to the C-Bronze joint, leading to a narrower joint on average. It may be foreseen that further optimisation of the NiCrMnIn filler metal towards this application could be of merit.

11. MPEA Filler Metal Incorporating Ge as Melting Point Depressant

The previous chapter detailed the development and trialling of an MPEA filler metal utilising In as the MPD element. As was detailed, high mixing enthalpies between In and Cr and Fe contributed to the inability to form an alloy, leading to the selection of Mn to replace Fe. While this allowed an alloy to be fabricated, the high volatility of Mn (even exceeding that of In) meant it was unsuitable for vacuum brazing. This chapter will detail research on using the other investigated MPD element, Ge, in a similar manner.

11.1 NiCrFeGe System

As discussed in Chapter 9, for reasons of compatibility with a Ni-based superalloy base metal and for promoting an FCC solid solution, a Ni-Cr-Fe basis was considered to which Ge would be the MPD element, and the equiatomic NiCrFeGe composition was first considered. Fig. 11.1 shows the TC predictions of phase abundance versus temperature for this system. The liquidus temperature predicted is approximately 1110^{o}C, with the first solidified phase an FCC A1 solid solution, followed by BCC A2 solid solution. The composition of these phases, at the solidus of approximately 897^{o}C, is Ni(35.3)-Cr(19.0)-Fe(27.9)-Ge(17.8) and Ni(15.4)-Cr(30.6)-Fe(22.3)-Ge(31.8) respectively, in atomic percent. Of note, is the predicted precipitation of a phase denoted 'DIAMOND_A4' at approximately 740^{o}C, composed entirely of Ge, and so a prediction of complete segregation of the Ge content from the BCC solid solution, which decreases in abundance. At approximately 350^{o}C and down to room temperature, the first FCC A1 phase is predicted to give way to a second FCC A1 phase and a second BCC A2 phase. The final room temperature microstructure is predicted as comprising a Ni-Fe FCC solid solution, with completely segregated Cr, Fe and Ge (denoted as the two BCC A2 phases and the 'DIAMOND_A4' phase). These predictions seem spurious; Ge might be expected to form intermetallic phases with Ni, Cr and Fe rather than segregate (according to phase diagrams and mixing enthalpy of binary pairs), and there is apparently little reason to expect segregation of Fe and Cr from each other, let alone from Ni. It is possible that the lack of accurate, experimentally assessed ternary, and perhaps even binary, systems including Ge with Ni, Cr and Fe led to these unexpected predictions.

As with the previous chapter, empirical thermodynamic parameters (detailed in Chapter 4) were also used as a design tool, for assessing likelihood of solid solution formation and the crystal structure of the NiCrFeGe system. Table 11.1 shows the calculated values of ΔH_{mix}, δr and VEC for the equiatomic composition. The ΔH_{mix} and δr values are both rather extreme compared to what would be expected for solid solution formation. When looking at individual binary pairs, it is clear that the ΔH_{mix} for Ge with Ni, Cr and Fe is highly negative, particularly for Ni which is -23.5 kJ mol^{-1}. Furthermore, Ge has a much smaller atomic radius than Ni, Cr and Fe, contributing disproportionately to the high δr value. Clearly, a single solid solution formation would not be expected for this equiatomic composition.

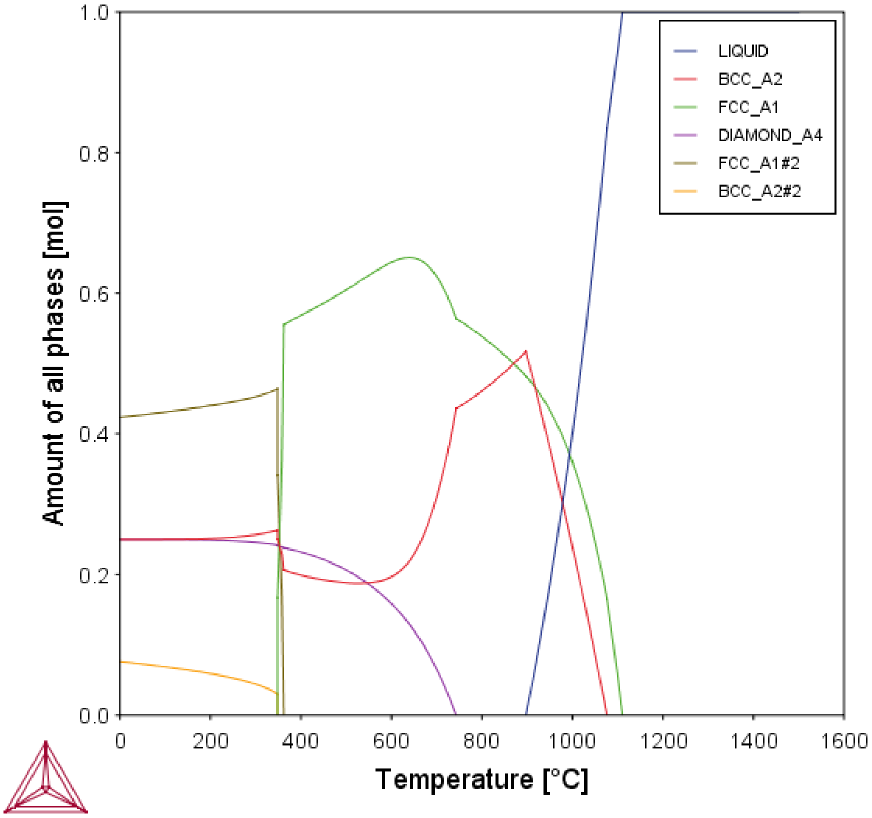

Figure 11.1: TC predictions for phase abundance versus temperature for the equiatomic NiCrFeGe system.

Table 11.1: Calculated values of ΔH_{mix}, δr and VEC for the equiatomic NiCrFeGe system.

	ΔH_{mix} (kJ mol^{-1})	**δr (%)**	**VEC**
NiCrFeGe (equiatomic)	-16.88	10.15	7.00

11.2 Fabrication of Equiatomic NiCrFeGe Alloy

In order to assert the extent to which such predictions offer an accurate picture, the equiatomic NiCrFeGe composition was fabricated by arc-melting. As was the case for the In-containing MPEA filler metal, the Arcast Arc-200 with water-cooled Cu melting crucible was used for melting, with an operating current of 400 A. The chamber was evacuated down to below 4×10^{-5} Torr (5.3×10^{-3} Pa), before backfilling with Ar to a partial pressure of between -10 and -2 inHg (-34 kPa and -6.7). The ingot was flipped and re-melted 5 times to improve homogeneity. Raw material of Ni foil (0.5 mm thickness), Cr plate (irregular pieces), Fe pieces (8 mm and down) and Ge pieces (12 mm and down), of at least 99.5 % purity (Alfa Aesar) was used.

Fig. 11.2 shows an SEM BSE micrograph of the as-cast microstructure of the equiatomic NiCrFeGe alloy, along with EDS maps showing elemental distribution. Three distinct phases are apparent – dark grey, medium grey and light grey contrasts in Fig. 11.2. EDS point scans were used to quantify the composition of each phase (average of five point scans), and the results are summarised in Table 11.2. The dark grey phase, marked *1*, appears to be an elongated and blocky intermetallic phase, mostly below 25 µm in length, and found to be rich in Cr and Ge, with a small Fe content and very little Ni. The medium grey phase, marked *2*, is rich in Fe, Ni and somewhat less Ge, with a minor Cr content, and is potentially a solid solution phase. The light grey phase, marked *3*, appears to be interdendritic, and is rich in Ni and Ge, with somewhat less Cr and leaner in Fe. Notably, the Ge appears to be more evenly distributed between the phases compared to the other elements, whereas it might have been expected to preferentially migrate to the Ni content due to the more negative mixing enthalpy. Each phase also contains at least some percentage of each element, meaning identification of specific phases is complex. The solidification sequence, which may be inferred from TC predicted liquidus temperatures, is likely to have been (using the phase labels in Fig. 11.2) 1 → 2 → 3.

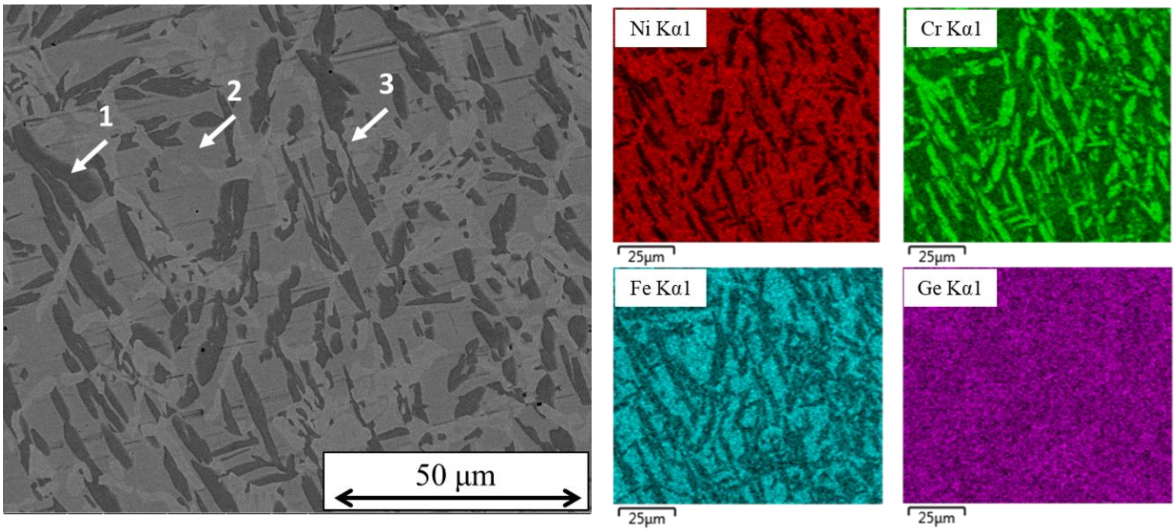

Figure 11.2: SEM BSE micrograph of the as-cast equiatomic NiCrFeGe alloy. EDS maps (right) show elemental distribution between phases.

Table 11.2: EDS measurements (average of 5) of composition of phases identified in Fig. 2, in atomic percent. Errors derived from standard deviation.

	EDS measured atomic percentage			
Phase	**Ni**	**Cr**	**Fe**	**Ge**
1	3.7 ± 0.1	59.3 ± 0.4	14.1 ± 0.4	22.9 ± 0.3
2	30.7 ± 1.2	11.4 ± 0.4	35.2 ± 1.1	22.7 ± 0.3
3	34.4 ± 1.0	20.3 ± 0.8	14.2 ± 1.1	31.1 ± 0.5

These SEM findings are complimented by XRD phase analysis, shown in Fig. 11.3. Most peaks were matched by a Cr_3Ge phase, which likely corresponds to the phase marked *1* in Fig. 11.2, though with all phases containing roughly similar Ge contents, there may be some peak overlaps, and double peaks indicating phases with similar lattice parameters. The indexed Cr_3Ge phase is of space group Pm-3n, which is a cubic system with Ge atoms at the cube corners and centre, and two Cr atoms at the face centres. Other peaks, including the prominent double peaks at approximately 2θ = 65°, appear to best match a BCC crystal structure, presumably corresponding to the solid solution phases marked *2* and *3* in Fig. 11.2, though the double peaks at approximately 2θ = 30° was not able to be identified.

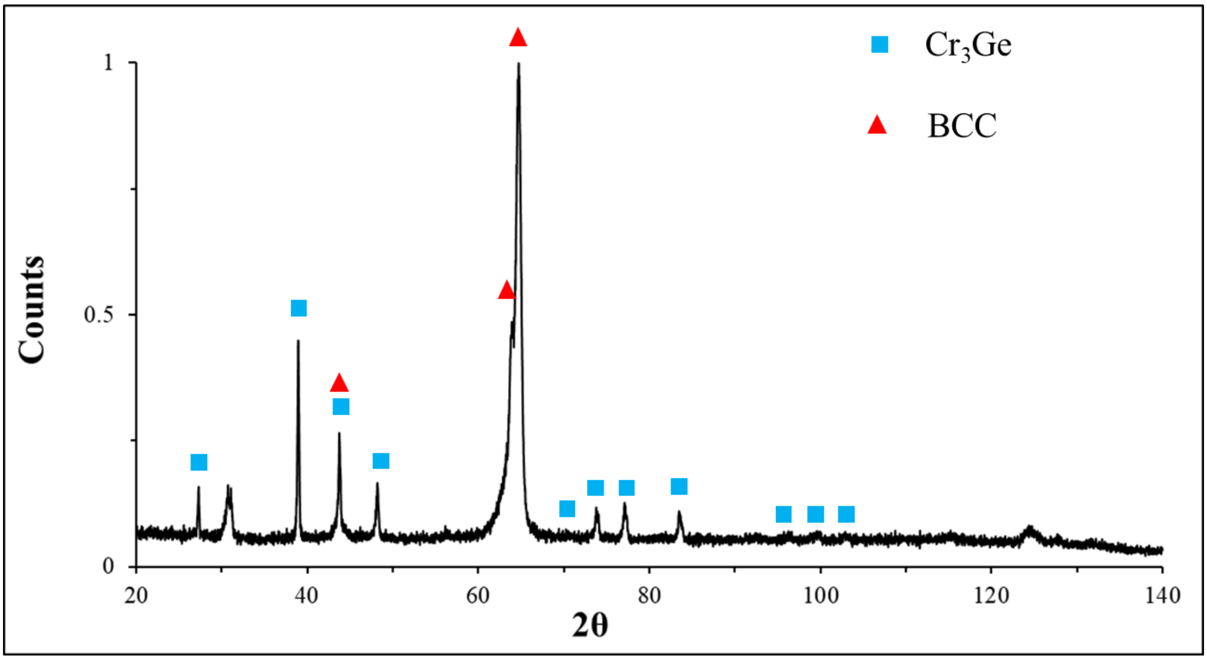

Figure 11.3: XRD spectra and identified peaks for the as-cast equiatomic NiCrFeGe alloy.

When compared to predictions from TC software, and the empirical thermodynamic parameters in Table 11.1, the as-cast equiatomic alloy exhibited some comparable features but also significant differences. As seen in Fig. 11.1, TC initially predicted the solidification of Fe and Ni-rich FCC and Cr and Ge-rich BCC phases, eventually giving way to segregated elemental Cr, Fe and Ge throughout equilibrium solidification. These may correspond to the observed phases *2* and *1* from Table 11.2 respectively (i.e. the dark contrast and medium grey contrast phases in Fig. 11.2), though whether these phases are in fact FCC and BCC in structure is perhaps disputed by XRD observations. The indexing of peaks shows that phase *1* in Fig. 11.2 is analogous to a cubic Cr_3Ge intermetallic. Meanwhile, predictions based on the calculated thermodynamic parameters are comparable to the observations, with the highly negative mixing enthalpy of Ge with Ni and Cr contributing to the formation of intermetallics rather than a solid solution phase. The average VEC of 7.00 would also suggest a mix of FCC and BCC, or a slight favouring of BCC, structures for formed solid solutions, which is reflected in the TC predictions.

11.3 NiCrFeGe System – Optimisation

Considering the above, the composition of the NiCrFeGe system was optimised for promotion of FCC solid solution, using TC software and considering thermodynamic parameters. This was attempted as a further test of the TC software for these alloys, allowing an assessment of its ability as a microstructure-optimising tool, rather than just a liquidus-optimising tool. Fig. 11.4 shows the TC predictions for room temperature FCC phase abundance as a function of (a) Cr content, (b) Fe content and (c) Ge content. In each case, Ni was maintained as balance while the other two elements were maintained at 25 at. %. TC predicts a clear decrease in FCC molar fraction with increasing Cr and Ge content, whereas increasing Fe is predicted to decrease FCC molar fraction to a lesser extent. Concurrently, total molar fraction of BCC phases is predicted to increase with increasing Cr, Fe and Ge. Looking closer, the rate of increase in FCC molar fraction, per at. % Cr removed, decreases past 15.6 at. % Cr, according to TC predictions. At the same time, simply reducing the concentration of Cr, Fe and Ge, and increasing Ni concentration, is predicted to increase the liquidus temperature (Fig. 11.5), therefore some attention was paid to balancing an increased FCC molar fraction with a lower liquidus. For this reason, Ge content was maintained at 25 at. % while the effect of Cr and Fe content on liquidus temperature was investigated. Fig. 11.6 shows a TC predicted heat-map of the fraction of liquid at 1150ºC, while maintaining Ni as balance and Ge at 25 at. %. According to these predictions, an increase in Fe content towards 29.5 at. % would allow a reduction in Cr content to the 15.6 at. % mentioned, while keeping the liquidus below 1150ºC.

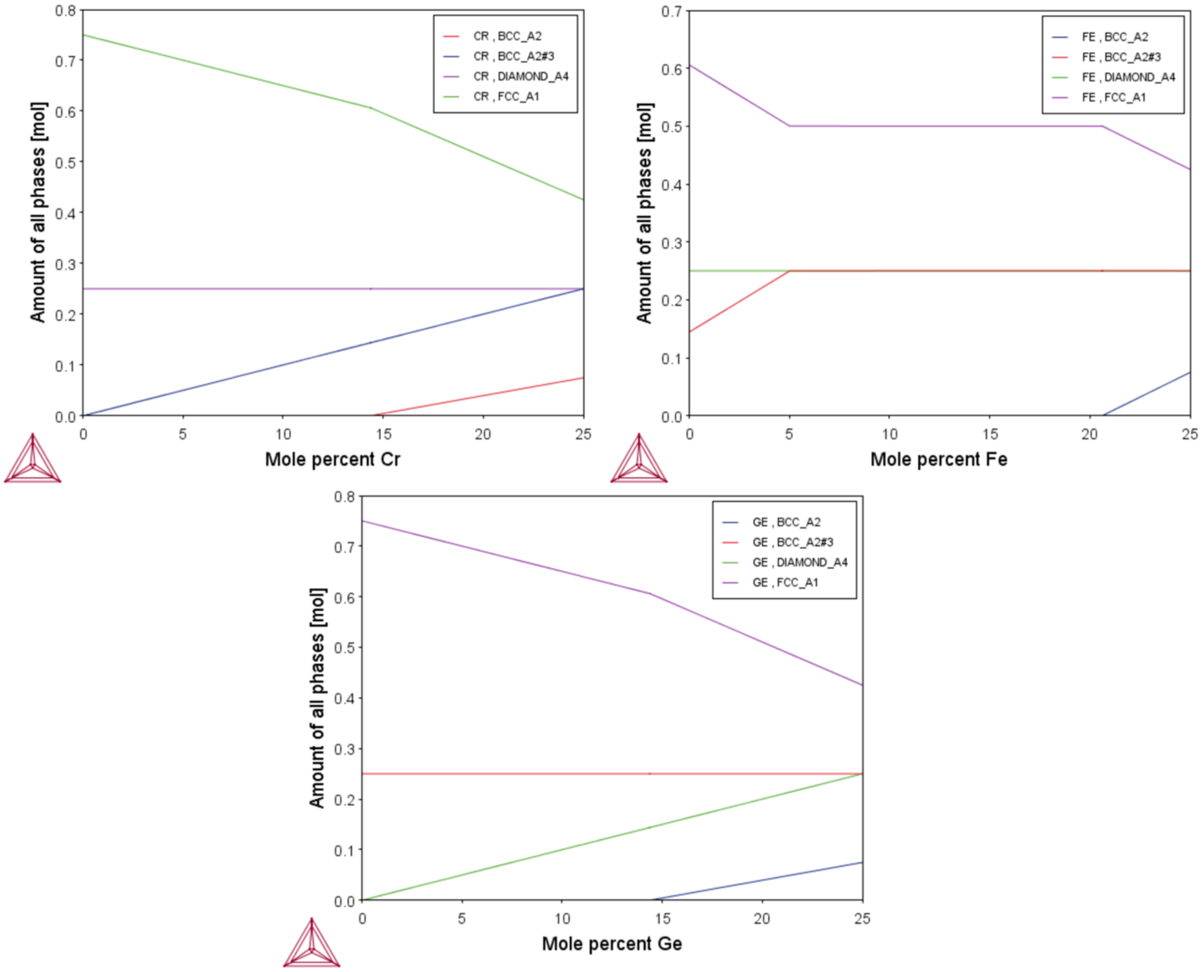

Figure 11.4: TC predictions of room temperature phase abundance versus atomic percentage of (a) Cr, (b) Fe and (c) Ge. In each case, Ni is kept as balance and the other two elements are maintained at 25 at. %.

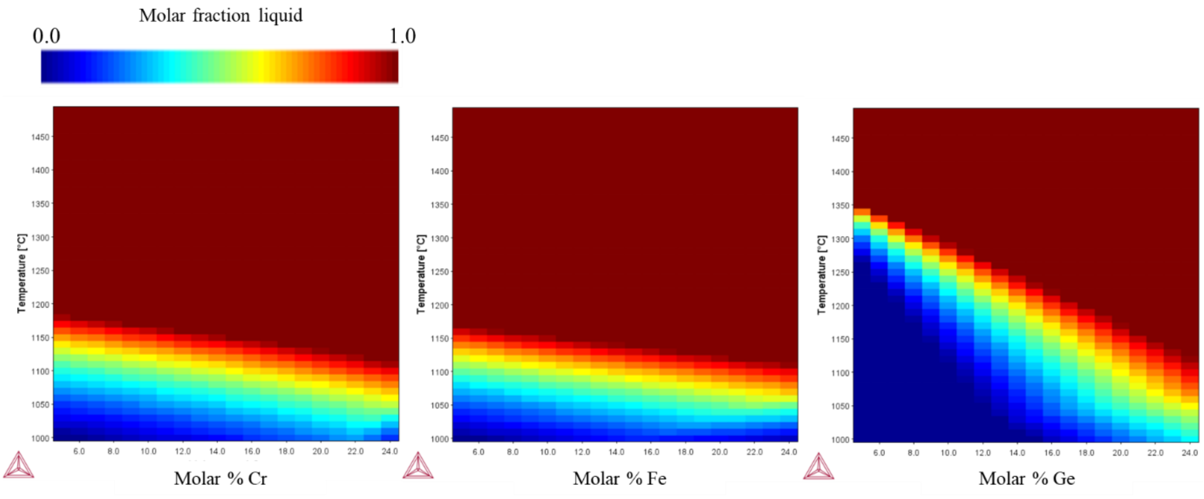

(a) (b) (c)

Figure 11.5: TC-predicted liquidus projection (at mol. fraction liquid = 1.0) for (a) NiCr(5-25 at.%)FeGe, (b) NiCrFe(5-25 at.%)Ge, and (c) NiCrFeGe(5-25 at.%).

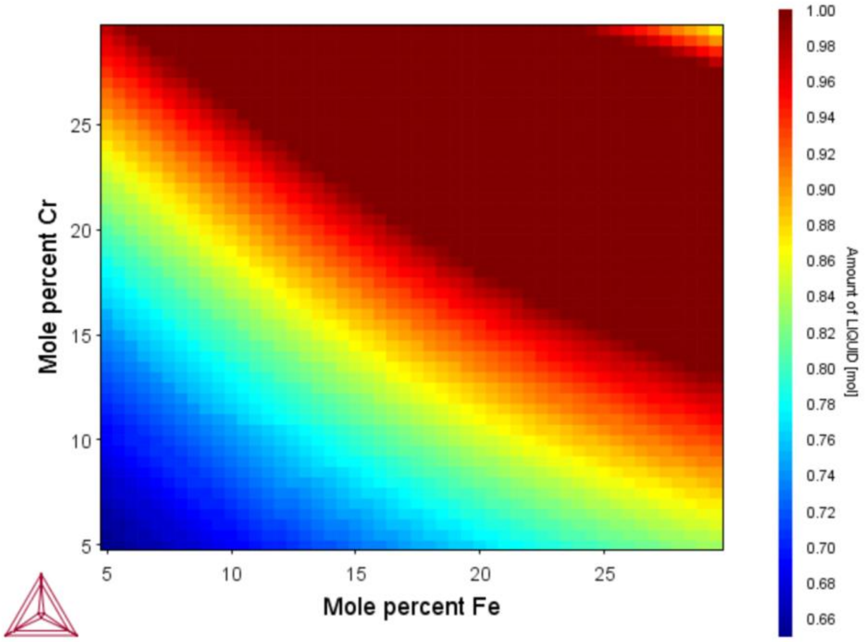

Figure 11.6: TC predictions of Cr and Fe concentration required for a maximum liquidus of 1150ºC, while maintaining Ni as balance and Ge at 25 at. %.

Based on these predictions, a Ni(bal.)-Cr(15.6)-Fe(29.5)-Ge(25) composition (hereafter referred to as ‘optimised NiCrFeGe’) was predicted as having a majority FCC solid solution microstructure. Fig. 11.7 shows the TC predictions of phase abundance versus temperature, and Table 11.3 shows the calculated thermodynamic parameters for this composition. A liquidus of approximately 1141ºC is predicted, with solidification of an FCC A1 solid solution commencing. At approximately 850ºC, a BCC A2 phase forms. At the solidus (approximately 791ºC), the composition of the FCC and BCC phases, in atomic percent, is Ni(33.3)-Cr(14.1)-Fe(30.7)-Ge(21.8) and Ni(12.9)-Cr(24.2)-Fe(23.9)-

Ge(39.0). Again, just below 800°C, the Ge is predicted to completely segregate from the FCC and BCC solid solutions, and at room temperature the near complete segregation of each element has been predicted, with only an FCC Ni-Fe solid solution making up approximately 50 % molar fraction.

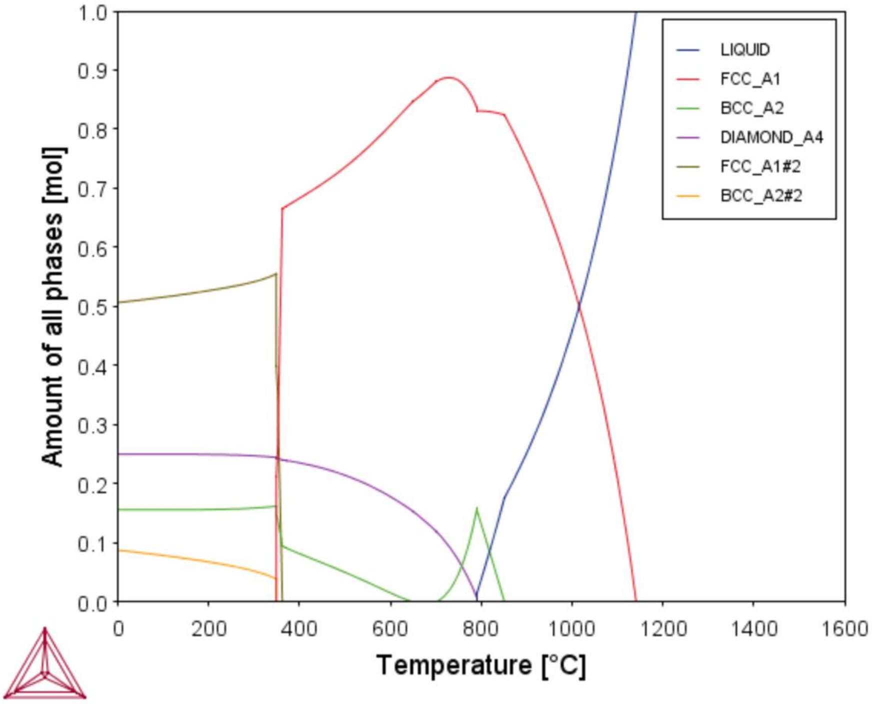

Figure 11.7: TC predictions of phase abundance versus temperature for the optimised Ni(bal.)-Cr(15.6)-Fe(29.5)-Ge(25) composition.

Table 11.3: Calculated values of ΔH_{mix}, δr and VEC for the optimised Ni(bal.)-Cr(15.6)-Fe(29.5)-Ge(25) composition.

	ΔH_{mix} (kJ mol^{-1})	δr (%)	VEC
NiCrFeGe (optimised)	-16.58	9.67	7.29

11.4 Fabrication of Optimised NiCrFeGe Alloy

To determine the accuracy of the TC predictions for the optimised Ni(bal.)-Cr(15.6)-Fe(29.5)-Ge(25) composition, this alloy was fabricated, in the same manner as the equiatomic alloy. Fig. 11.8 shows the SEM BSE micrograph of the as-cast alloy, along with EDS maps. For this optimised composition, two main solid solution phases are apparent, a dark grey contrast phase and lighter grey interdendritic phase, marked *A* and *B* respectively in Fig. 11.8. EDS point scans were again used to determine the composition of these phases, with the findings summarised in Table 11.4 (average of 5 measurements). The phases appear to have somewhat similar compositions to the medium grey and light grey phases in Fig. 11.2 (marked *2* and *3* respectively), with phase *A* being rich in Fe and Ni, and phase *B* rich in Ni and Ge. Fe appears to be the most distinctly segregated between the two phases. Most notable is the almost complete absence of the Cr,Ge-rich intermetallic phase that was observed in Fig. 11.2 (marked *1*). Small instances only (< 5 μm) of what is likely the same phase are identified by noting the bright patches on the Cr Kα1 EDS map in Fig. 11.8 (top right), and are marked *C*, but these were not measured by EDS point scanning, being too small for accurate measurement. Inferred from TC predictions of liquidus temperature, the solidification sequence of the two majority phases was likely A → B.

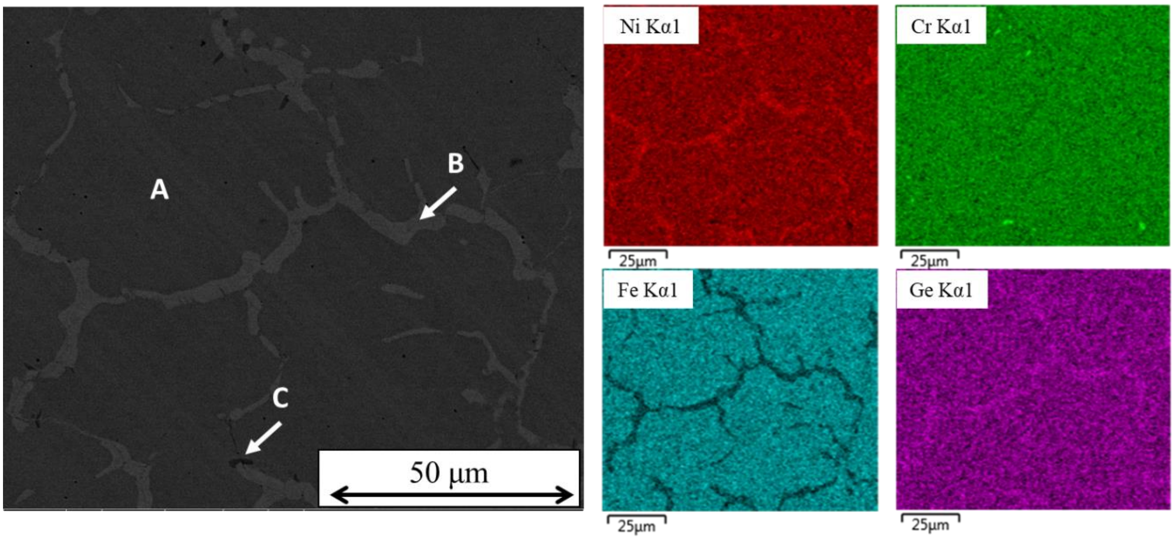

Figure 11.8: SEM BSE micrograph of as-cast optimised Ni(bal.)-Cr(15.6)-Fe(29.5)-Ge(25) alloy, with EDS maps showing elemental distribution between phases.

Table 11.4: EDS measurements (average of 5) of composition of phases identified in Fig. 4, in atomic percent. Errors derived from standard deviation.

	EDS measured atomic percentage			
Phase	**Ni**	**Cr**	**Fe**	**Ge**
A	28.4 ± 0.2	16.7 ± 0.1	31.2 ± 0.2	23.6 ± 0.1
B	37.0 ± 0.5	14.7 ± 0.1	16.9 ± 0.7	31.6 ± 0.3

Fig. 11.9 shows the XRD spectra with indexed peaks for the as-cast optimised NiCrFeGe composition (Bruker D2 phaser). Again, due to the composition of each of these phases, identification of a specific matching phase was unlikely. However, the XRD spectra indicates that both phases are BCC solid solution phases with similar lattice parameters (hence the apparent double peaks). EDS measurements (Table 11.4) showed these phases are of slightly different composition than the BCC phases in the equiatomic alloy, which may explain the peaks here being more resolvable from each other. The peak at approximately $2\theta = 30^{o}$ was again unable to be identified. This XRD analysis is in contrast to TC predictions for these phase compositions however, which indicates probable majority FCC crystal structure. However, this could be a result of the prediction of Ge segregation at temperatures below approximately 800°C, leaving only FCC Ni-Fe-Cr phases, whereas we see in the as-cast alloys the presence of Ge in the solid solution phases appears to promote the BCC crystal structure.

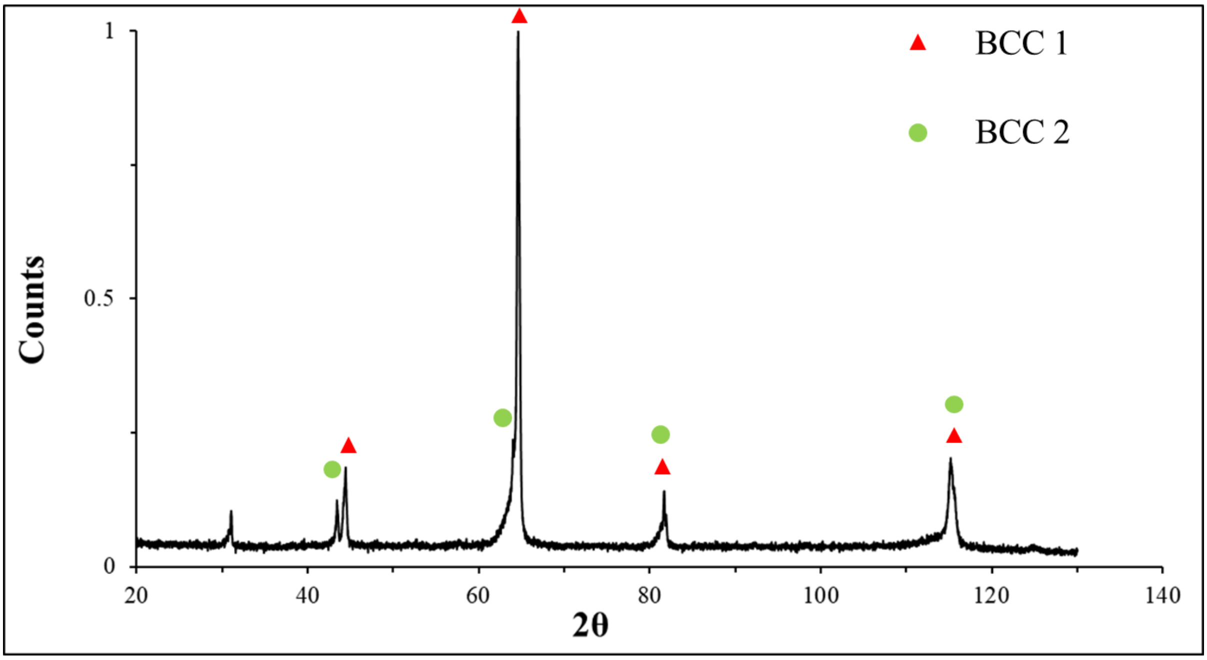

Figure 11.9: XRD pattern for as-cast optimised NiCrFeGe composition, with peaks matching two seperate BCC solid solution phases.

When compared to the TC predictions, the as-cast optimised NiCrFeGe composition again exhibits significant differences. While the primary phase, marked *A* in Fig. 11.8, may correspond to the predicted FCC phase (see Fig. 11.7), XRD indexing suggests this is in fact a BCC solid solution. The phase marked *B* is perhaps captured by the TC prediction of the BCC phase (Fig. 11.7), and the XRD peaks indicate this is indeed a BCC solid solution phase with lattice parameter similar to phase *A*. Only marginal reductions in $|\Delta H_{mix}|$ and δr were calculated for the optimised NiCrFeGe composition, due again to the contributions to these calculations from the Ge content (the second most abundant element in the optimised composition). Despite this, two solid solutions appear to have formed, though small instances of the previously observed (in Fig. 11.2) Cr,Ge-rich intermetallic were likely observed in Fig. 11.8, indicating that not all the Ge is in solution.

11.5 Differences in Mechanical Properties Following Optimisation

As a simple indication of the change in mechanical properties between the equiatomic and optimised NiCrFeGe compositions, microhardness measurements of both as-cast alloys were taken (Fig. 11.10). The average of 5 measurements for each showed values of 720 ± 15 HV1 for the as-cast equiatomic alloy, and 550 ± 11 HV1 for the as-cast optimised alloy. This might be tentatively linked with an expectation for decreased brittleness following the composition optimisation, mainly as a result of the avoidance of the Cr,Ge-intermetallic phase in the optimised case. Therefore, despite differences between TC predictions and findings, this approach to composition refinement could be a useful tool. Despite this anticipated beneficial increase in ductility, however, TC predictions show that the objective of a sub-1100°C liquidus would not be met by these compositions. Indeed, TC predicted that, for the NiCrFeGe system, only a higher Ge content, towards 30 at. %, would meet this objective.

As detailed in the requirements proposed in Chapter 9, however, this would be deemed undesirable for the microstructure of the MPEA filler metal, as it would presumably promote intermetallic formation and discourage solid solution formation. For this reason, the introduction of a minor addition of a further MPD element was considered.

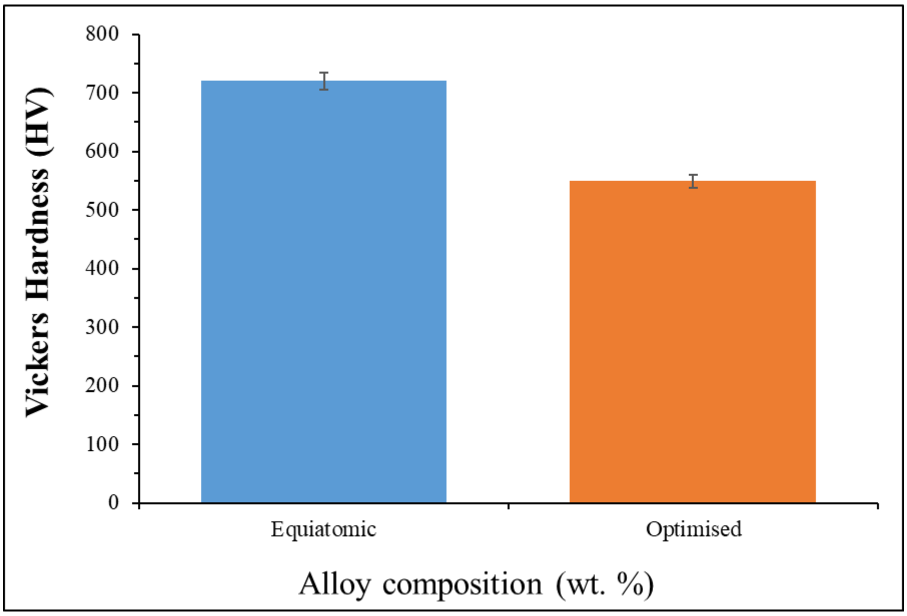

Figure 11.10: Average microhardness values for as-cast equiatomic NiCrFeGe and TC-optimised NiCrFeGe, with erros derived from standard deviation.

11.6 NiCrFeGeB System

Preliminary TC investigations as to what element might be selected as a minor MPD addition to the NiCrFeGe system revealed that elements including In, Mn, or others that according to their binary phase diagrams with Ni, Cr and Fe might suppress liquidus temperature, would still require a significant concentration. Furthermore, TC optimisation for a quinary alloy, with two additions that have limited or no assessed data either with each other or with Ni, Cr and Fe, is likely to be yet more inaccurate than for a quaternary alloy, or for a quinary whose fifth element is more widely used.

With this in mind, currently used MPDs Si and B were considered, as it was deemed likely that a reduced concentration of these might be required as compared to those in current commercial brazing alloys (for example, AWS BNi-2 contains approximately 14 at. % B). However, as already discussed, including these elements runs the increased risk of intermetallic formation in the form of borides and silicides. B was ultimately selected, as aside from being the faster diffusing element, the ΔH_{mix} of the Ge-B pair was lower than that for Ge-Si (-0.5 kJ mol^{-1} versus -14.5 kJ mol^{-1}) [200]. In order to merit the inclusion of B, it was considered that the concentration should be limited at 5 at. % as a starting point, representing a significant reduction as compared to filler metals such as AWS BNi-2.

With a suitable small B addition, a sub-1100°C liquidus MPEA filler metal may be obtained, which following brazing, would diffuse away the B content, leaving behind an otherwise MPEA-like NiCrFeGe-based composition in the joint region. This could have potentially beneficial mechanical properties from solid solution strengthening, as well as a higher post-braze melting temperature (meaning the joint may withstand much higher temperatures). The following section of this chapter (Section 11.7) is a journal article manuscript, now published in *Metallurgical and Materials Transactions A*, detailing an investigation into developing a NiCrFeGeB composition for the brazing of IN718.

11.7 Development & trialling of NiCrFeGeB filler metal for brazing of IN718

(See journal article manuscript attached overleaf. Figures, tables, subheadings and references are self-contained)

Development of a novel Ni-based Multi-Principal Element Alloy filler metal, using an alternative melting point depressant

Liam Hardwick (**corresponding author**)[1], Pat Rodgers[2], Ed Pickering[3] & Russell Goodall[1]

[1] Department of Materials Science & Engineering, University of Sheffield, Sheffield, United Kingdom, +44

[2] VBC Group, Loughborough, United Kingdom, +44

[3] Department of Materials, University of Manchester, Manchester, United Kingdom, +44

Corresponding author email: lhardwick1@sheffield.ac.uk

Abstract

Brazing is a crucial joining technology in industries where Ni-superalloy components must be joined. Ni-based brazing filler metals are extensively employed, possessing excellent mechanical properties, corrosion resistance and retained strength at elevated temperatures. To function as a filler metal, the alloy melting point must be reduced to below that of the materials being joined, but the addition of melting point depressants (MPDs) such as B, Si, and P can, however, lead to the formation of brittle intermetallics, potentially compromising the joint performance. In the present work, a novel multi-principal element brazing alloy (in the style of a high entropy alloy), utilising Ge as an alternative MPD along with a reduced B addition, is investigated. The design process considered binary phase diagrams and predictions based on Thermo-Calc software and empirical thermodynamic parameters. The alloy was used to vacuum braze Ni-superalloy Inconel-718, and microstructural and mechanical investigations are reported. The maximum shear strength achieved was 297 MPa with a brazing temperature of 1100^{o}C and 60-minute hold time, with isothermal solidification completed. Shear strength was only slightly reduced with increased joint width. Assessments are made of the ability to accurately predict properties of multi-principle element alloys using Thermo-Calc software and empirical thermodynamic parameters.

Introduction

Brazing has become an important technology for the joining of materials unsuitable for welding, such as Ni superalloys, which could otherwise be susceptible to strain age cracking in the post-weld heat affected zone. Brazing instead employs a filler metal which melts and bonds the two materials through a diffusion-controlled process. This may be either placed directly in the joint, or applied such that capillary action will draw the molten filler metal into the joint. Current commercially available Ni-based filler metals are preferred for the brazing of Ni superalloy components in applications demanding high mechanical performance, at elevated temperatures and in corrosive envFements. The properties of such alloys are generally achieved by alloying additions including Cr for enhanced corrosion resistance [1] and Fe for increased solid solution strengthening [2]. In addition, to enable brazing at a suitably low temperature, elements acting as melting point depressants (MPDs) are added to the brazing alloy in relatively small weight percentages in order to attain a suitable liquidus. The most prevalent of these elements are B, Si and P.

It is well documented, however, that such additions encourage the formation of undesirable intermetallic phases in the form of borides, silicides and phosphides, particularly with the elements Ni, Cr and Fe [3-5] whose solubility limit of these elements is typically very low. Fig. 1 shows schematically the basic sequence of processes occurring during brazing (or transient liquid phase bonding (TLPB), discussed in detail elsewhere [6]) of a base metal with a solid filler metal containing an MPD (Fig. 1(a)). When the brazing temperature is reached, the filler metal is fully molten (Fig. 1(b)), and a widening of the liquid may occur as the composition at the solid/liquid interface is adjusted to that of the solidus/liquidus MPD concentrations (Fig. 1(c)). Diffusion of MPD elements at the brazing temperature from the molten filler into the materials being bonded (which, under the definition of brazing, remain solid at the processing temperature) gradually increases the liquidus of the melt, until an elemental concentration is reached locally where the melt begins to solidify at the brazing temperature, a process known as isothermal solidification. This occurs as two solidification fronts move inwards from the interfaces with the base material (Fig. 1(d)). When the time at the brazing temperature is not sufficient for isothermal solidification of the entire joint, and the onset of cooling follows, brittle intermetallic phases can form via eutectic transformation of the remaining melt, enriched in these elements due to their low solubility in the advancing gamma matrix phase, usually occurring along the joint centre [7,8]. A joint examined at this stage may exhibit two phenomena often referred to as the isothermally solidified zone (ISZ), and the athermally solidified zone (ASZ). Furthermore, fast diffusing elements such as B can react with the base metal elements, creating what is commonly referred to as a diffusion-affected zone (DAZ) at the interface of filler metal and into the base metal [9,10], which may remain even if isothermal solidification is complete within the joint. These phenomena are represented in Fig. 1(e). As well as providing a potentially continuous crack propagation path, reacting with base metal elements such as Cr, Nb and Mo can result in their diminished concentration within the base metal matrix, and thus reduce the corrosion resistance locally. When sufficient time at the brazing temperature is allowed, however, isothermal solidification may progress fully across the joint. Further homogenisation heat treatments following brazing may be used to remove the DAZ through further diffusion, as is typically the final stage in TLPB. In this case, a brazed joint may be largely indistinguishable from the original base metal, as in Fig. 1(f). In total, the inclusion of the current MPD elements in concentrations used in current brazing alloys, can cause increased brittleness and ultimately premature failure in the joint [11-13] without the use of either prolonged brazing cycles or post-braze heat treatments, both of which are economically undesirable, and may present practical challenges.

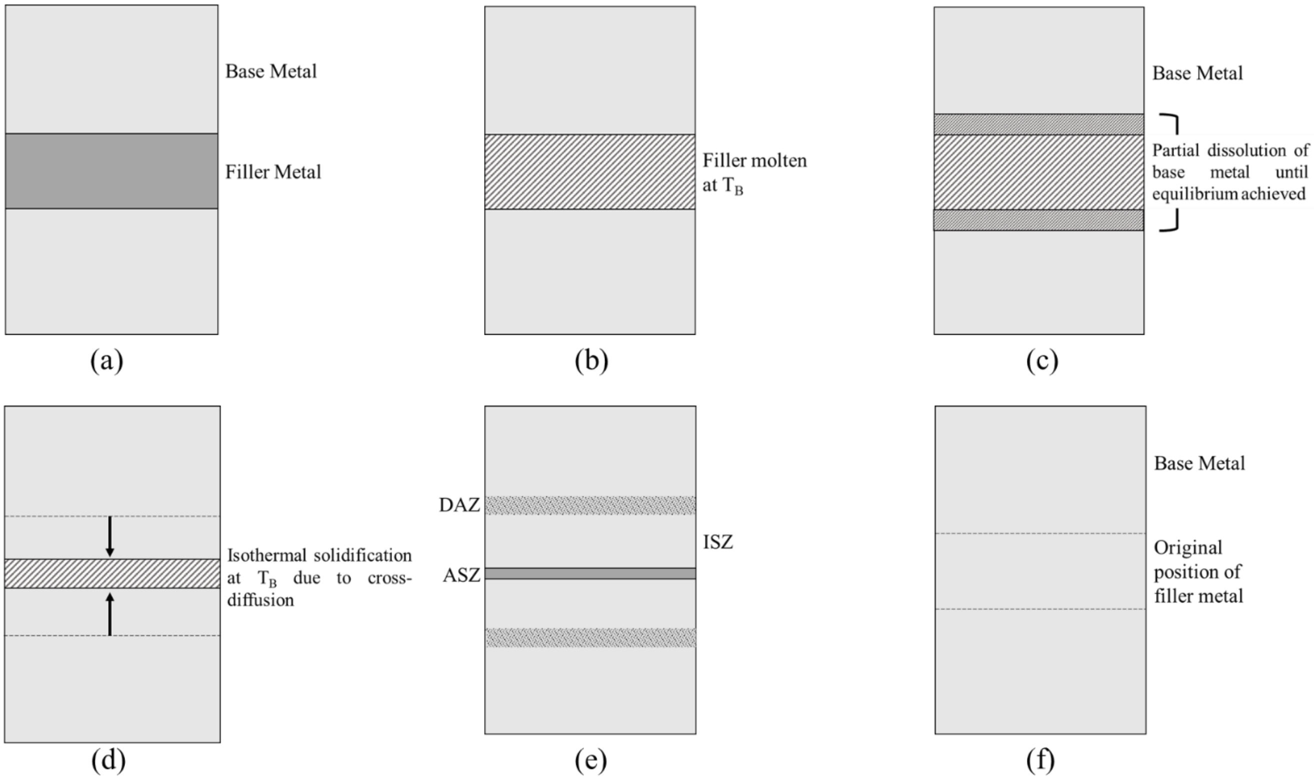

Fig.1. Typical stages in brazing; (a) Initial set-up of joint; (b) Molten filler upon reaching T_B; (c) Dissolution of base metal and widening of liquid layer; (d) Isothermal solidification stage and reduction of width of liquid layer; (e) Remaining DAZ and ASZ as a result of cooling onset before isothermal solidification; (f) Joint where isothermal solidification is allowed to complete before onset of cooling, and DAZ removed via homogenisation.

The majority of studies into viable alternative MPDs involve exploration of the addition of a single alternative MPD element to Ni. Dinkel *et al*. (2008) investigated the use of Ge as a potential MPD in binary Ni-Ge alloys, for brazing superalloys PWA 1483 and René N5 with Ni-23wt.%Ge and Ni-20wt.%Ge respectively [14]. With joint gaps reported as 200 µm, for the first alloy 48 hours at 1160°C was required for gap closure, and 24 hours at 1180°C for the second alloy. Laux *et al*. (2008) trialled a range of Ni-Mn (36.7 and 58.4 wt.%Mn) and Ni-Mn-Si (20wt%Mn-2wt.%Si, 20wt%Mn-3wt.%Si and 25wt%Mn-2wt.%Si) alloys for the wide-gap brazing of a Ni-7.5Co-7.0Cr-1.5Mo-5.0W-6.5Ta-6.2Al-3.0Re (in wt. %) superalloy [15]. For constant brazing hold times of 30 minutes, brazing temperatures ranged from 1040°C for the highest Mn content (Ni-58.4Mn in wt.%), to 1260°C for the lowest Mn content (Ni-20Mn-2Si in wt.%). Evidently, such alloys often require substantial amounts of the proposed MPD, yet the liquidus temperature is often still considerably higher than for most current

Ni-based brazing filler metals (which would typically be between 1000°C and 1150°C). There is motivation, therefore, to seek novel compositions that can achieve a strong joint, free of brittle intermetallic phases within typical industrial brazing cycles.

In recent years significant attention has been paid to high entropy alloys (HEAs), a relatively new class of materials comprising typically 5 or more elements, in roughly equiatomic proportions or concentrations originally defined as 5 – 35 at.% [16]. They are so-named due to the supposed role that their enhanced configurational entropy plays on their potentially unique properties. More recently, the definition of HEAs has undergone some broadening, extending to non-equiatomic compositions, or systems with as few as three elements [17]. Such systems are sometimes referred to generally as multi-principal element alloys (MPEAs) [18,19]. Often based on transition and/or refractory metals, HEAs and MPEAs have proved of interest due to their potentially exceptional mechanical properties [20-22] and corrosion resistance [23-25]; properties which could be of clear benefit to brazing applications. However, perhaps due to both the typically high melting point of such systems (although melting temperature often tends to decrease towards equiatomic compositions), and little or no attempts at designing for a melting temperature relevant to brazing (through refining composition or and/or use of a MPD element), relatively little has been published on employing HEAs as brazing filler metals. From those studies that do exist, the brazing temperature required is often significantly higher than typically used for current brazing filler metals. Bridges *et al*. (2017) demonstrated laser brazing of IN718 superalloy with a Ni-Mn-Fe-Co-Cu HEA, at a brazing temperature of 1165°C and achieving a 220 MPa maximum shear strength [26]. Tillmann *et al*. (2018) joined Hf-metallised YSZ ceramic to Crofer 22 APU steel using a Nb-Co-Cr-Fe-Ni HEA, achieving almost double the shear strength than when using a typical AgCuTi3 filler metal, albeit at a brazing temperature of 1200°C, some 280°C higher than that for AgCuTi3 [27]. Gao *et al*. (2019) demonstrated a maximum shear strength of 530 MPa when joining IN600 superalloy with a Fe-Co-Ni-Mn-Cu MPEA, with a brazing hold time of 90 minutes at 1200°C [28].

The present work therefore demonstrates an alloy design process, with the aim of developing a novel HEA or MPEA-derived filler metal composition able to produce superior joints when used within typical industrial brazing cycles. This process employs binary and ternary phase diagrams, empirical thermodynamic parameters, and Thermo-Calc software (SSOL4 database), which uses the CALPHAD method of extrapolating thermodynamic information of a system from experimentally verified data on binary and ternary systems.

Preliminary Alloy Design Study

It is clear from binary Ni phase diagrams and the literature [14,15] that, of numerous candidate MPD elements (transition and post-transition metals, metalloids and refractories), most would require excessive atomic percentages (compared to that of B or Si) to achieve a liquidus comparable to current B/Si-containing filler metals; in many cases 30 at.% or more of addition would be needed. In other cases, the liquidus may still be over 150ºC above that of B/Si-containing filler metals. In this study, Ge was considered as an alternative MPD. According to the Ni-Ge binary phase diagram (Fig. 2), a liquidus of 1125°C is achieved with 22 at.% Ge [29], hence a reasonable MPD effect is exhibited. Ge also exhibits a greater solubility in Ni than B or P, at approximately 13 at.% at 1125°C, which is closer to that of Si at 14.6 at.%. As reported in the phase diagram [29] a gamma-prime (γ') phase is formed at compositions between approximately 23 and 26 at. % Ge, which could enhance mechanical properties of the joint through a similar mechanism to the γ' phase in standard Ni superalloys. Fig. 3 and Fig. 4 show the binary phase diagrams for the Cr-Ge [30] and Fe-Ge [31] binary systems respectively. As is the case in the Ni-Ge binary system, at high Ge contents, numerous intermetallic phases form with Cr and Fe, though it can also be seen that Ge has a similar effect on the liquidus of the Cr-Ge (1564°C at approximately 25 at.% Ge) and Fe-Ge (1105°C at approximately 30 at.% Ge) binary systems, and exhibits somewhat similar solubility (11 and 16 at.% Ge respectively).

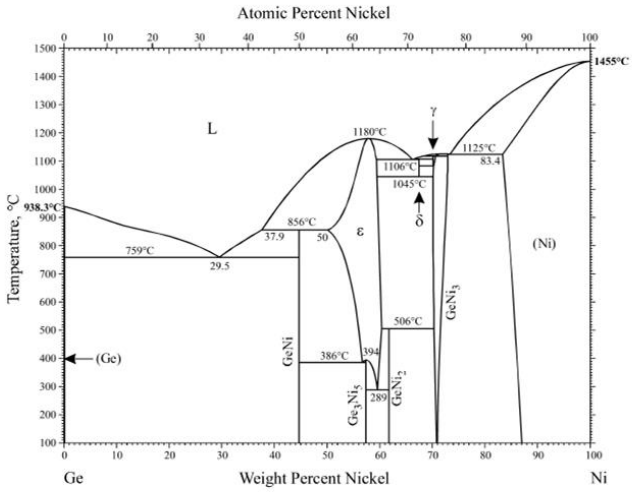

Fig. 2. Ni-Ge binary phase diagram.

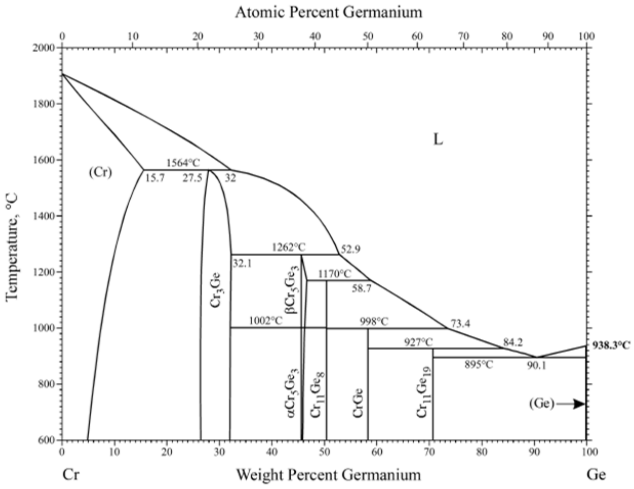

Fig. 3. Cr-Ge binary phase diagram.

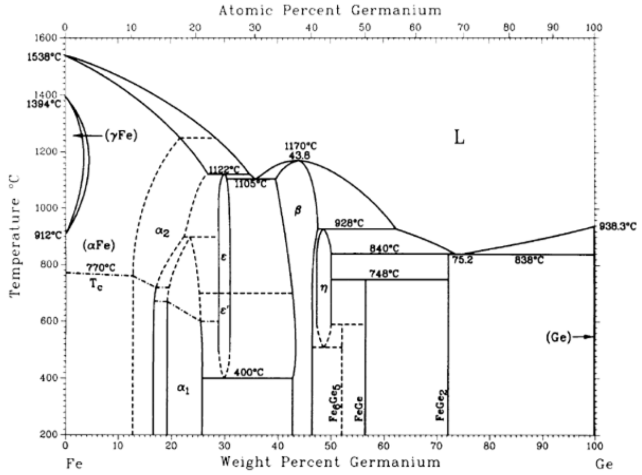

Fig. 4. Fe-Ge binary phase diagram

Clearly, however, the use of Ge as a like-for-like substitute for B or Si in a conventional Ni-based filler metal, despite any potential microstructural improvements in the form of gamma-prime precipitates, would not achieve a liquidus similar to those of many current commercial brazing alloys. While increasing the at. % of Ge in any developed alloy may well further reduce the liquidus and hence brazing temperature, this increases the risk of brittle intermetallic formation. However, according to the liquidus projection in the Cr-Fe-Ni ternary system [32], the liquidus decreases towards the equiatomic composition, reaching 1390°C at approximately equiatomic concentrations. In addition, Ni, Cr and Fe are chemically compatible with a superalloy base metal, and exhibit an extended mutual solubility range, providing an intermetallic-free, lower liquidus matrix to which less Ge may be added than may otherwise be required. An increased Fe content may also confer cost benefits. Data on the diffusivity of Ge in Ni and Ni-superalloys exists [33] and so with an appropriate brazing cycle sufficient Ge diffusion may take place such that the remaining Ge in the joint is soluble in a superalloy-like Ni-Cr-Fe joint matrix.

In light of this, the addition of Ge to an initially equiatomic NiCrFe ternary system was considered, utilising both Thermo-Calc (TC) software, as well as empirical thermodynamic parameters used in the design of HEAs; the average enthalpy of mixing of binary pairs (ΔH_{mix}); the average atomic size mismatch (δr); and the average valence electron concentration (VEC). TC software may be useful in predicting the melting temperature of a developed filler metal. Considering typical brazing cycles used in industry, it was deemed necessary to aim for a filler metal liquidus of no higher than 1100°C, and for it to ideally possess a predominantly FCC microstructure, in order to more closely match the base metal gamma-matrix. The empirical thermodynamic parameters could aid in predicting the microstructure. In keeping with classic guidelines based on the Hume-Rothery rules, it has been suggested that minimising $| \Delta H_{mix} |$ promotes the formation of solid solution, with negative or positive values promoting intermetallic formation or segregation respectively [34]. Similarly, a small δr is considered beneficial for promoting solid solution [34,35]. In other studies, it is suggested that the average VEC can be used to predict crystal structure of the solid solution, with higher VEC associated with FCC and lower with BCC (though the exact threshold values differ between systems) [36,37]. For example, it is suggested that an average VEC of over 8, or below 6.87, would favour promotion of a FCC or BCC microstructure respectively [36,37]. For $8 \geq \text{VEC} \geq 6.87$, both FCC and BCC phases would be present. Each of these parameters can be calculated using Equations (1) – (3):

$$\Delta H_{mix} = \sum_{i=1}^{n} \sum_{j>i}^{n} \Omega_{ij} c_i c_j = \sum_{i=1}^{n} \sum_{j>i}^{n} 4 H_{mix}^{ij} c_i c_j \quad (1)$$

$$\delta r = \sqrt{\sum_{i=1}^{n} c_i \, (1 - \frac{r_i}{\bar{r}})^2} \quad (2)$$

$$VEC = \sum_{i=1}^{n} c_i VEC_i \quad (3)$$

Alloy Design Results

Fig. 5 shows the TC property diagram for the equiatomic NiCrFeGe system, exhibiting solidus and liquidus temperatures of 900°C and 1110°C respectively. The TC predictions show a multi-phase microstructure upon solidification to room temperature, but with a desirable FCC majority phase. Promotion of the primary FCC phase was possible by moving away from the equiatomic composition, but this resulted in an increase in the predicted liquidus temperature. A predicted compromise between increased FCC content and decreased liquidus content could be achieved for a Ni(bal.)-Cr(15.6)-Fe(29.5)-Ge(25) at.% composition, but the predicted liquidus was still higher than in the equiatomic case, and so neither composition was deemed of interest for this study.

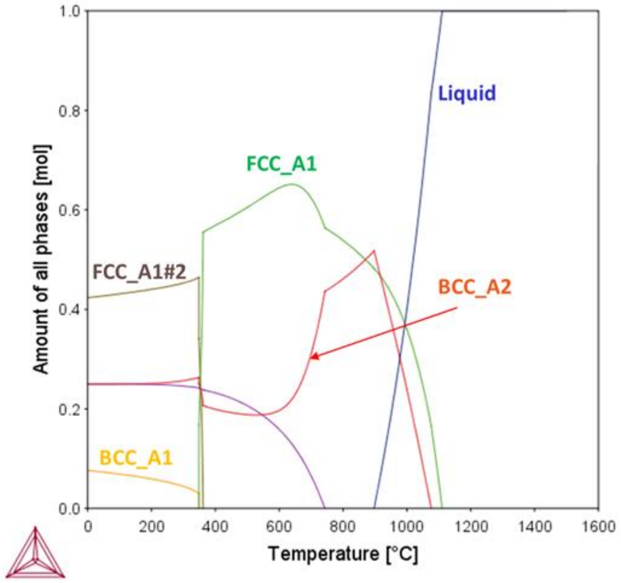

Fig. 5. Thermo-Calc diagram showing predicted proportion of phases as a function of temperature for the equiatomic Ni-Cr-Fe-Ge composition.

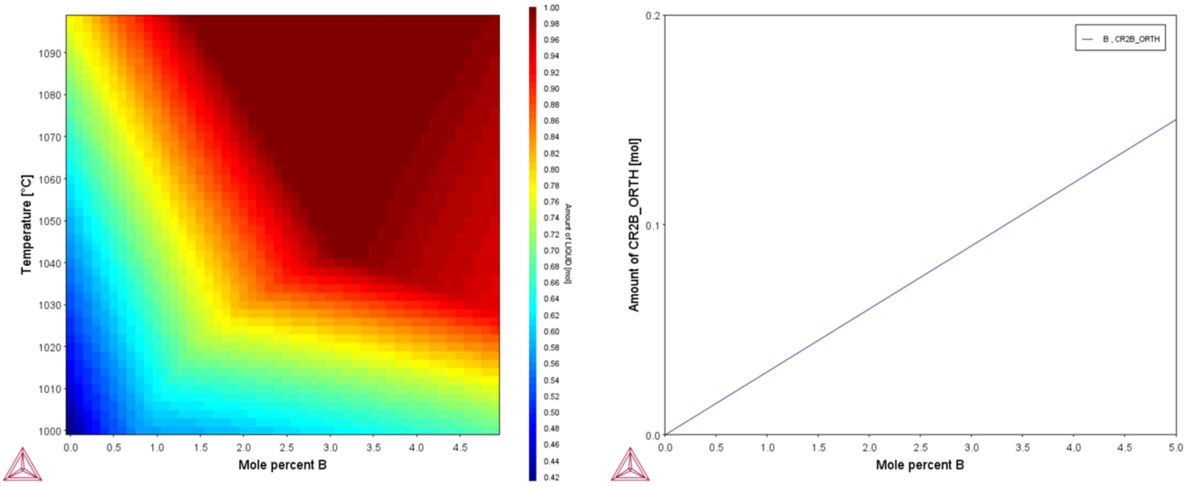

(a) (b)

Fig. 6. Thermo-Calc diagram showing (a) predicted liquidus projection for B addition (in at. %) to Ni(bal.)CrFeGe, and (b) Thermo-Calc diagram showing predicted room temperature proportion of Cr_2B phase in NiCrFeGe+B, for B concentration of 0 – 5 at. %.

Indeed, it was found that, except at Ge concentrations of approximately 30 at. % and higher, a sub-1100°C liquidus was not predicted to be achieved in the NiCrFeGe system. Given both the need for good chemical compatibility with a prospective Ni-based superalloy, and the high raw cost of Ge, it was however deemed necessary to limit the Ge content to 25 at. % and to ensure that no one element is present in a higher concentration than Ni. B, as discussed, is widely employed as an MPD in Ni-based filler metals and is well known as a fast diffusing element in Ni-based superalloys. It can therefore be conceived that an appropriately small amount of B (compared to current commercially available options that utilise B as MPD) contained by the developed filler metal may sufficiently reduce the liquidus temperature, and during brazing diffuse away from the joint over the course of an appropriate brazing cycle, leaving behind a HEA or MPEA-like central joint region. Initially, a B content of between 0 and 5 at. % was therefore considered as an addition to the equiatomic NiCrFeGe system, while noting the additional need to consider the boride content now predicted by TC. A suitable predicted liquidus temperature was achieved at 2.5 at. % B, giving solidus and liquidus temperatures of 840ºC and 1038ºC respectively, with TC predicting a low CrB content of 7.5 mol.% (in comparison, for BNi-2, TC predicts approximately 13 mol.% and 15 mol.% of Cr_2B and Ni_2B respectively). This B concentration is significantly lower than contained in, for example, BNi-2 which has approximately 14 at. % B.

Upon further optimisation of the composition (in terms of predicted liquidus temperature, predicted FCC content, and predicted boride content), this alloy design approach resulted in the development of a Ni-rich off-equiatomic MPEA with a composition (in at.%) of Ni(30.5)-Cr(25)-Fe(18)-Ge(24)-B(2.5). Predicted solidus and liquidus temperatures for this composition were 820°C and 1062°C, with a primary FCC matrix and predicted Cr-boride molar concentration of under 10%. The TC predicted phase diagram for this composition is shown in Fig. 7. The predicted properties of the above series of alloy compositions is summarised in Fig. 8.

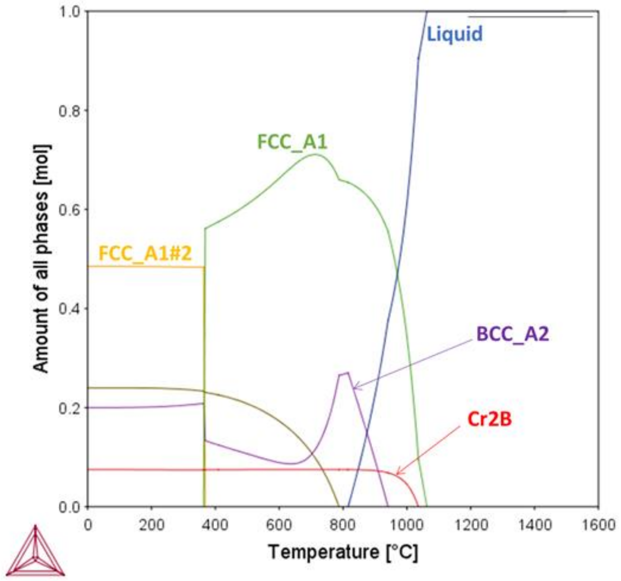

Fig. 7. Thermo-Calc diagram showing prediction proportion of phase as a function of temperature for the final Ni(30.5)-Cr(25)-Fe(18)-Ge(24)-B(2.5) composition.

Investigating the constitution of these predicted phases, the primary FCC phase was predicted to consist of only a Ni-37at.%Fe solid solution, whereas the Cr and Ge content was predicted to be completely segregated in the microstructure, showing as BCC_A2 and DIAMOND_A4 respectively in Fig. 7, which may be attributed to the lack of assessed Ge binary or ternary systems data in the SSOL4 database. At the same time, the SGTE Solutions SSOL databases, such as SSOL4, are the only current databases to include Ge along with elements Ni, Cr, Fe, and B. Rather, the previously mentioned empirical thermodynamic parameters, shown in Table 1, were also considered. For the Ni(30.5)-Cr(25)-Fe(18)-Ge(24)-B(2.5) composition, it can be seen that the average VEC tends toward favouring mixed BCC/FCC formation, but that $|\Delta H_{mix}|$ is also minimised compared to the other compositions. It must be noted here that such trends between microstructure and these parameters arises from the screening of numerous HEAs, and is mainly based only on transition and refractory metals, and very little has been established for cases of mixed transition metal – metalloid systems such as this. Table 1 summarises the development of the composition in terms of the empirical thermodynamic parameters.

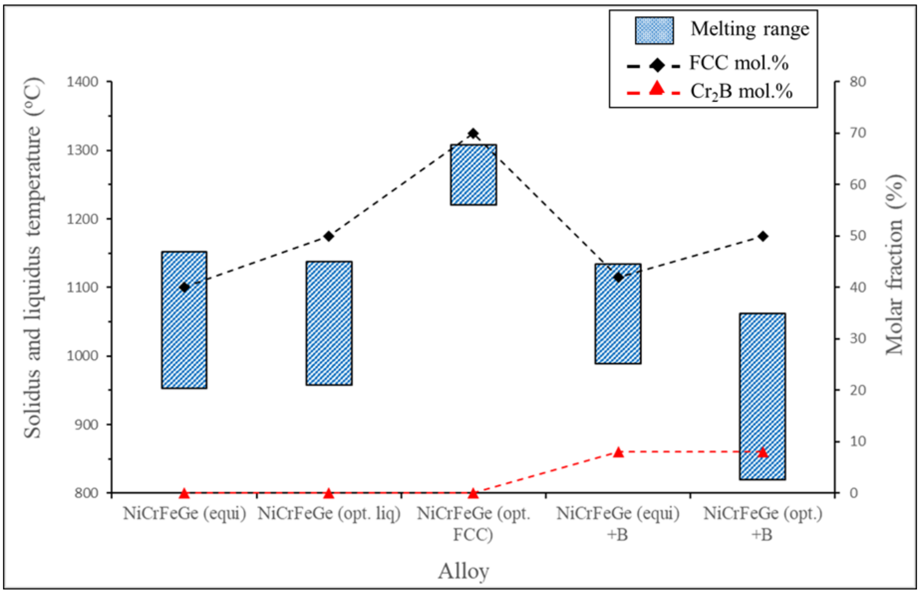

Fig. 8. Chart summarising predicted melting range, FCC mol.% and Cr_2B mol.% of each alloy composition throughout the design process

Table 1. Calculated empirical thermodynamic parameters ΔH_{mix}, δr, and VEC for each alloy composition throughout the design stage.

Parameter	**NiCrFeGe (equiatomic)**	**NiCrFeGe (optimised for FCC)**	**NiCrFeGe (equiatomic) + 2.5 at.% B**	**Ni(bal.)-Cr(25)-Fe(18)-Ge(24)-B(2.5)**
ΔH_{mix} (kJ mol^{-1})	7.75	-4.00	5.60	3.00
δr	2.85	3.98	3.60	3.98
VEC	7.00	7.3	6.8	7.0

Experimental Procedure

Pure elements (of at least 99.9% purity, Alfa Aesar) were arc-melted in an Arcast 200 Arc-melter, producing an ingot of the NiCrFeGeB alloy of approximately 20 g in a water-cooled Cu crucible. The operating current was 450 A, and the ingot was flipped and re-melted five times to improve homogeneity, with electromagnetic stirring also applied for this reason. An 8 mm Ø cylinder of length

10 mm was removed from the as-cast ingot via electron discharge machining. Thin slices (400 – 800 µm) were then sectioned from this cylinder, which were then manually ground to a thickness of approximately 65 µm using a stainless steel grinding jig and SiC grit papers. A further slice was ground to a thickness of approximately 100 µm in order to demonstrate the effect of increased gap size for the developed composition.The NiCrFeGeB foils were used to vacuum braze 8 mm Ø, 5 mm length cylinders of Inconel-718 (IN718) to 25 x 25 x 5 mm sheets of IN718. A schematic of the brazed joint is shown in (Fig. 9(a)). Brazing was performed at 1100°C for 15 (for 65 µm thickness) and 60 (for 65 µm and 100 µm thickness) minutes. In each case, a 15-minute equalisation hold was performed at 1010°C below the brazing temperature. After brazing, the joints were furnace cooled to 900°C before gas quenching. Ramp rates were 15°C min^{-1} in each trial. The same brazing cycles were repeated for AWS BNi-2 in melt-spun foil form of 50 µm thickness (VBC Group, Loughborough, UK) for mechanical comparison. Prior to brazing, all IN718 pieces were ground with P1200 papers, before ultrasonic cleaning in acetone for 10 minutes along with the NiCrFeGeB and BNi-2 foils. A load of 0.02 kg was placed on each joint during the brazing cycles. Shear testing of the brazed joints through applying compression was performed based on the method of Matsu *et al.* [38], with the aid of an EN30B steel test fixture (shown schematically in Fig. 9(b)). In addition, in order to observe any microstructural changes induced under approximate service conditions (as superalloys are normally used at elevated temperatures for extended times), a 5 mm length section of a joint brazed at 1100°C for 60 minutes was heat treated in an inert atmosphere at 700°C for 100 hours.

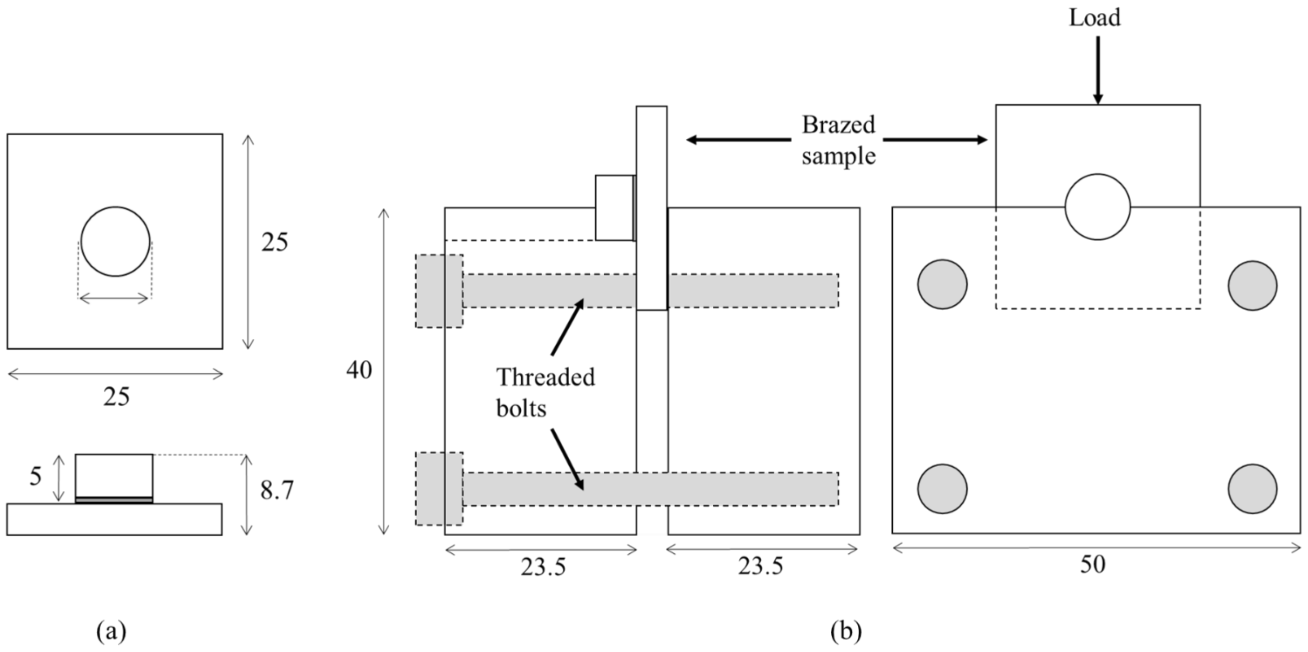

(a) (b)

Fig. 9.; (a) Schematic of brazed joint specimen; (b) Schematic of steel fixture used to seat brazed joint specimen for shear testing.

The composition of the as-cast NiCrFeGeB alloy was measured via X-ray fluorescence (XRF) (PANalytical Zetium), and phase analysis was performed by X-ray diffraction (Bruker D2 Phaser). Microstructural investigation of the as-fabricated alloys was performed via SEM (BSE) (FEI Inspect F50 operated at 20 keV) and energy dispersive spectroscopy (EDS) using Aztec software. Differential Scanning Calorimetry (DSC) of a 30 mg sample of the as-cast NiCrFeGeB alloy was performed in an Ar atmosphere with heating and cooling rate of 20°C min^{-1} (Netzsch 404 F1 Pegasus). Average peak onset of three heating curves was determined with Proteus software. The NiCrFeGeB and BNi-2 brazed joints were imaged via SEM. Further elemental distribution analysis was performed by Electron Probe Micro-Analysis equipped with Soft X-ray Emission Spectrometer (EPMA-SXES) (JEOL JXA-8530F). Micro-hardness measurements of the as-fabricated alloys and both NiCrFeGeB and BNi-2 brazed joints were performed using a Struers Durascan, with a dwell time of 15 seconds. 1

kg load was used for the as-cast sample, and 0.05 kg load was used for hardness profiles of the joints post-braze.

Results & Discussion

As-Cast NiCrFeGeB Alloy

Bulk composition of the as-cast NiCrFeGeB alloy, as measured by XRF, is shown in Table 2. The typical as-cast NiCrFeGeB microstructure SEM micrograph is shown in Fig. 10 (a), along with EDS maps showing the elemental distribution (Fig. 10 (c)). Four distinct phases were observed; a thin needle-like phase (black contrast) between 50 – 200 µm length (marked 1); an irregular-shaped phase (dark grey contrast), approximately 20 µm in size (marked 2); and upon increasing magnification (Fig. 10 (b)) two further phases (medium and light grey contrast respectively) (marked 3 and 4). The needle-like dark phase is most likely a Cr-rich boride (known difficulties in detecting light elements via EDS means B concentration may be inaccurate), containing also some amount of Fe. The more irregular dark grey phase was found to be more complex, primarily containing Cr but with significant Ge content, as well as Fe. The medium and light grey phases were found to contain all Ni, Cr, Fe and Ge, with the light grey being more Ge-rich and the medium grey more Ni-rich. The composition in atomic percent of each phase is reported in Table 2, as the average of five EDS point scan measurements. Average Vickers microhardness for the as-fabricated NiCrFeGeB alloy was found to be 773 ± 10 HV1.

Table 2. Bulk composition (converted to at. %) of NiCrFeGeB alloy as measured by XRF. This technique is not capable of quantifying B content.

	Ni (at. %)	Cr (at. %)	Fe (at. %)	Ge (at. %)
As-cast NiCrFeGeB alloy	29 ± 2	26 ± 2	20 ± 2	21 ± 2

Table 3. EDS-determined (average of 5 point measurements) composition of phases identified in Fig. 10. Errors derived from standard deviation of measurements.

	Element concentration (at. %)				
Phase	Ni	Cr	Fe	Ge	B
1	0.8	66.5	8.3	0.6	23.7
2	3.5	63.8	10.2	22.6	-
3	34.0	11.4	26.3	27.6	-
4	34.4	16.5	9.8	36.0	-

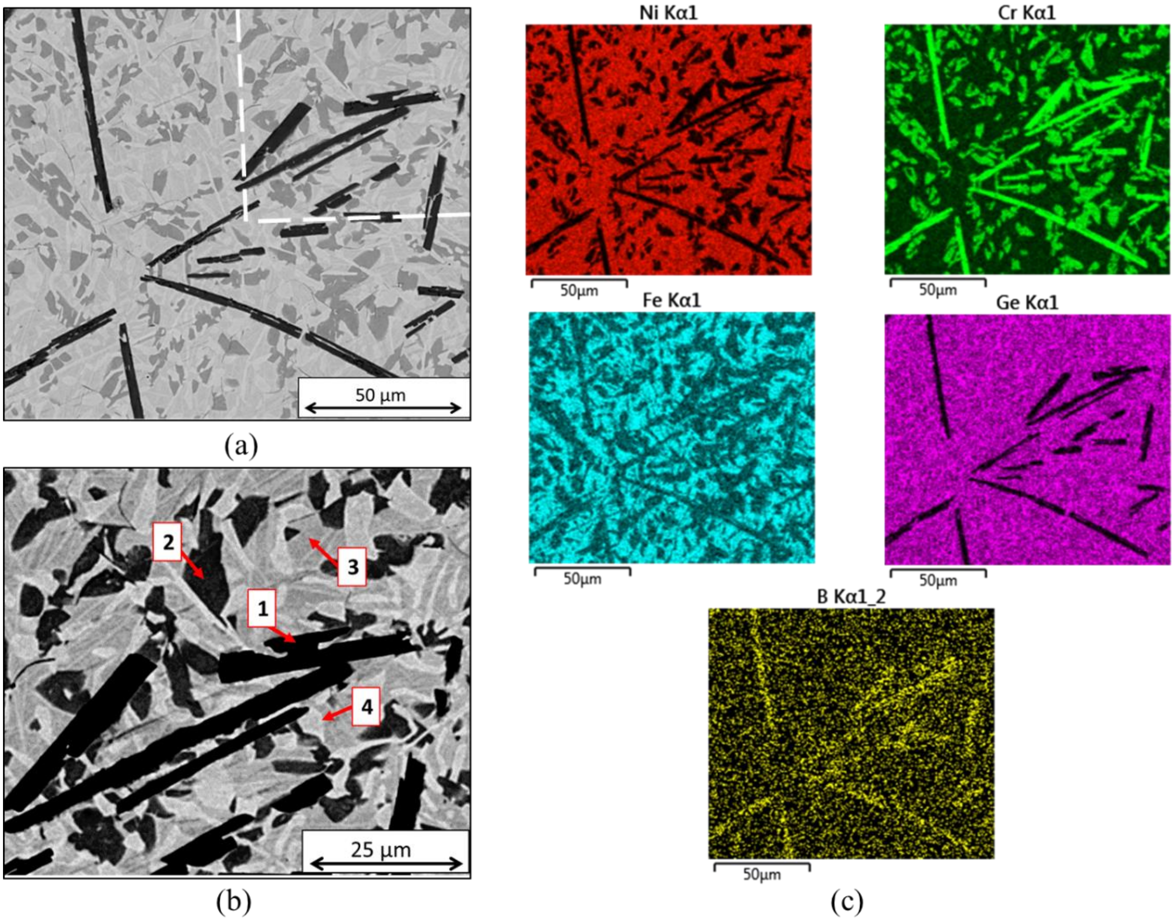

(a) (b) (c)

Fig. 10. (a) SEM micrograph of typical section of as-cast Ni(30.5)-Cr(25)-Fe(18)-Ge(24)-B(2.5) alloy with EDS mapped region highlighted, (b) Magnified micrograph of EDS-mapped region highlighted and distinct phases marked, (c) EDS maps of (a) showing elemental distribution.

Fig. 11 shows a representative DSC cooling curve for the as-cast NiCrFeGeB ingot. Solidus and liquidus temperatures of 1038°C and 1055°C were determined from this. It is possible that the two phases marked 1 and 2 in Fig. 10, both being rich in Cr, possess much higher solidus and liquidus temperatures and so no transition relating to their melting was recorded for the temperature range used in the DSC cycle.

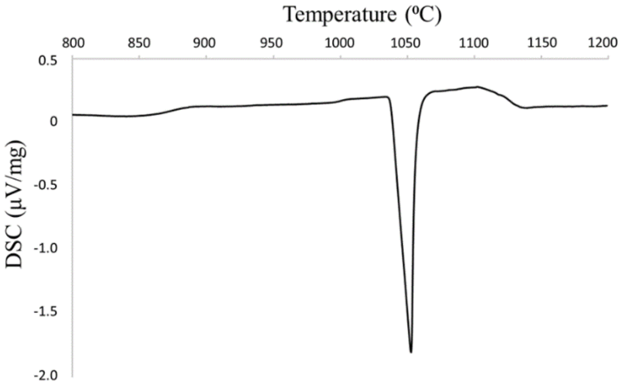

Fig. 11. Average of three DSC cooling curves for 30 mg sample of the as-cast NiCrFeGeB alloy.

Brazed Joints (Microstructure)

Typical sections of the NiCrFeGeB-IN718 joint microstructures are shown in Fig. 12, for both (a) 15- and (b) 60-minute braze cycles (65 µm foils). The primary microstructural difference immediately noticeable is the presence of boride phases, apparently retained from the as-cast microstructure, in the case of the 15-minute brazing time, which is not observed in the 60-minute case (marked A in Fig. 12). This suggests that while the 15-minute hold time did not result in significant dissolution of these boride phases, after 60 minutes at the hold time sufficient dissolution of the boride phases had occurred. Furthermore, in both cases distinct zones containing a white-contrast phase were evident, commencing at a distance of approximately 30 µm from the joint centre (marked B in Fig. 12). This irregular, globular shaped phase appears to primarily form along grain boundaries (GB) and EDS point scans revealed it to be rich in Ni, Ge and Nb, and of similar composition for both 15 and 60-minute braze cylces. The presence of Nb (not contained by the filler metal), and the location of the phase, indicates base metal dissolution was the primary cause of formation. As well as possessing a highly-negative mixing enthalpy with the filler metal elements Ni and Ge, Nb segregation is a known phenomenon in Inconel-series alloys [39], factors which encouraged the formation of this phase. Similarly, Ni-Ge-Nb phase was observed within the joint region for the 15-minute hold time sample (marked C in Fig. 12), attributed to rejection from advancing IS fronts, followed by the onset of cooling before IS could complete and the phase dissolved through diffusion processes. Given that this phase was not seen in the joint region for the 60-minute hold time sample, this lends credence to the notion that IS was completed in this case.

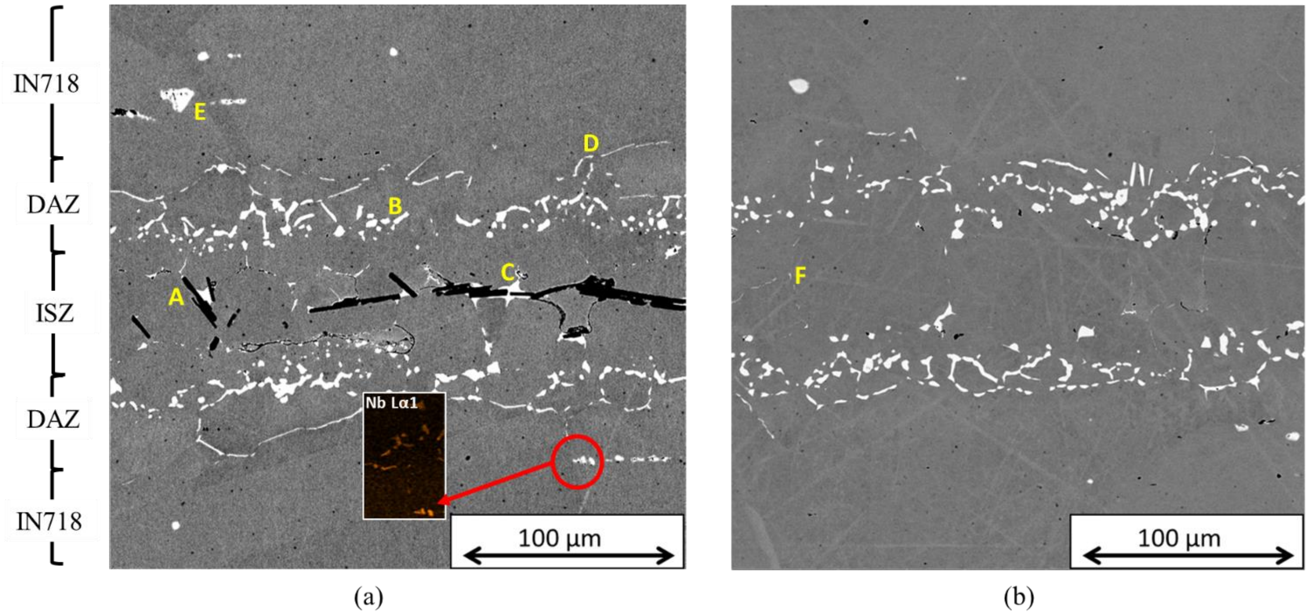

Fig. 12. SEM micrographs of brazed joint microstructures for; (a) 15-minute at hold time at 1100°C; (b) 60-minute at hold time at 1100°C. Identified phases marked A-F, and microstructural regions labelled.

Extending approximately 50 µm into the base metal from the interface are boride phases forming a relatively sparse DAZ (compared to DAZs commonly seen for B-bearing filler metals in literature). This includes GB Nb-Mo borides, and other coarser X-borides (where X represents base metal elements including Nb, Mo and Ti) (marked D and E in Fig. 12 respectively). The GB borides were observed generally out to a greater distance from the interface with the base metal, owing to faster diffusion along grain boundaries. While these were too fine to accurately measure with EDS point scans, EDS mapping indicated the presence of Nb and Mo (Fig. 12 (a)). The X-boride phases observed were generally found to be few and far between, but were typically larger than the Nb-rich DAZ phase and of differing composition from instance to instance. The abundance of these phases was also reduced compared to similar joints using B-bearing filler metals seen in the literature. Of note is the greater concentration of GB borides in the case of the 15-minute hold time (a potential cause of which is mentioned in the discussion below). Probable fine Nb-borides were again observed predominantly along GBs in the IS grains in the 60-minute hold time sample (marked F in Fig. 12), but again these were too fine for EDS analysis. For both 15-minute and 60-minute braze cycles, the grey contrast matrix phase in the joints is the isothermally solidified Ni-rich solid solution, with noticeably reduced Ge content compared to the as-cast filler metal composition. Base metal elements were also observed in solution in this phase. A summary of EDS measurements of the main observed phases (A, B, C and solid solution) is shown in Table 3.

Table 4. EDS-determined (average of 5 point measurements) composition of phases identified in Fig. 12. Errors derived from standard deviation of measurements.

	Element concentration (at. %)						
Phase	Ni	Cr	Fe	Ge	Nb	Mo	Ti
A	1.4	68.7	6.6	0.4	-	2.1	-
B	39.2	5.7	5.8	15.6	24.8	1.1	1.6
C	38.5	11.4	26.3	27.6	28.8		
Solid solution	39.9	25.3	20.8	10.2	1.2	1.4	0.4

Fig. 13 (a) shows a typical section of the NiCrFeGeB-IN718 joint brazed for 60 minutes followed by heat treatment at an approximate service temperature of 700°C for 100 hours, in an inert atmosphere. The microstructure is largely comparable to Fig. 12 (b), with the Ni-Ge-Nb phase and DAZ remaining largely undisturbed by the heat treatment process. Upon higher magnification (Fig. 13 (b)), fine GB borides are again observed in the ISZ, as marked by the arrow in Fig. 13 (b) (though these were on too fine a scale for quantification via EDS techniques).

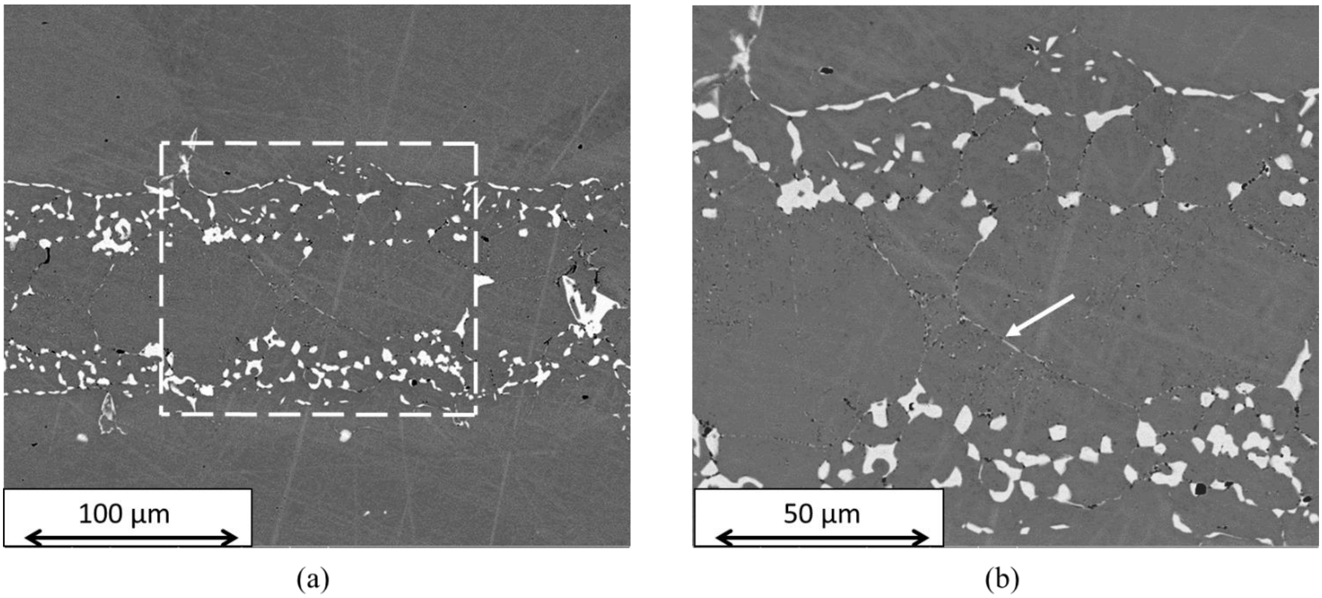

(a) (b)

Fig. 13. (a) SEM micrographs of typical section of brazed joint (60-minute hold time at 1100°C) following heat treatment at 700°C for 100 hours in inert atmosphere, with magnified region indicated. (b) Magnified region of part (a) with GB borides indicated.

Fig. 14 shows a typical section of the NiCrFeGeB-IN718 joint brazed using the 100 µm foil for 60 minutes, with EDS measurements shown in Table 4. Immediately observable is the increased joint width, due to the initial thickness of the foil. In addition, the presence of retained boride phases (marked X in Fig. 14) is apparent, despite the 60-minute hold time seemingly being adequate to dissolve these phases in the case of the 65 µm thickness foil. The borides observed in this case are typically reduced in size (under approximately 30 µm) compared to in the as-cast state of the NiCrFeGeB alloy, indicating some partial dissolution of these phases has occurred. Furthermore, there appears to be a reduced concentration of the Ni-Ge-Nb phase at the interface with the base metal (marked Y in Fig. 14), yet an increased concentration of the white contrast phase within the joint region (marked Z in Fig. 14), generally close to the joint centre presumably as a result of incomplete IS. An increased concentration of Nb-Mo borides was observed in the DAZ instead, extending out to between 50 to 100 µm into the base metal, but this phase was not quantified by EDS point scans due to its fineness.

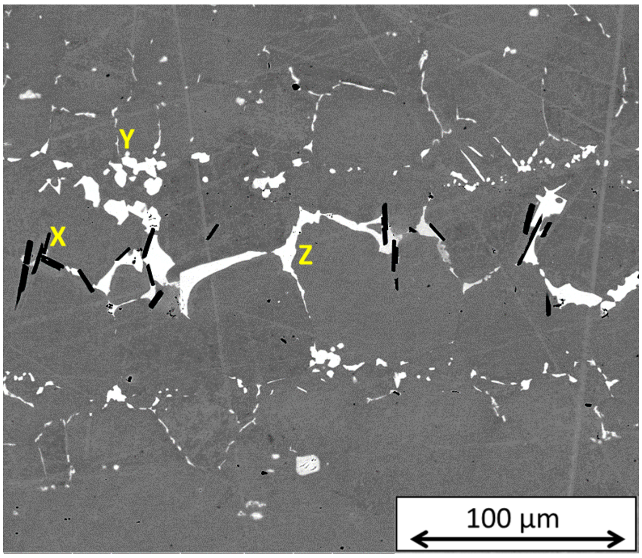

Fig. 14. SEM micrograph of brazed joint (60-minute hold time at 1100°C) using 100 µm thickness foil.

Table 5. EDS-determined (average of 5 point measurements) composition of phases identified in Fig. 14. Errors derived from standard deviation of measurements.

	Element concentration (at. %)						
Phase	Ni	Cr	Fe	Ge	Nb	Mo	Ti
X	1.4	68.7	6.6	0.4	-	2.1	-
Y	49.4	3.3	4.8	22.1	17.9	1.1	2.2
Z	49.6	2.8	4.2	27.6	17.3	-	3.1
Solid solution	39.8	24.8	20.0	10.3	0.6	0.8	0.4

Brazed Joints (mechanical properties)

Microhardness profiles taken across the brazed joints are shown in Fig. 15 for each of the brazed joints (15-minute hold, 60-minute hold, 60 minute hold with 100 µm foil). Little variation in microhardness was observed across the joints for all cases, with only localised changes in the joint centreline. Here, in the case of the 15 minute hold time, a sharp increase in microhardness was presumably caused by the presence of retained boride. On the other hand, the 60 minute hold time sample exhibited a slight reduction across the ISZ zone, owing to the dissolution of borides phases and the joint region consisting of just Ni-rich solid solution. In the case of the 100 µm foil sample, again an increase in hardness was observed, likely due to the presence of the retained boride phases near the joint centre, but also possibly due to the increased presence of the Ni-Ge-Nb phase in this region.

Fig. 16 shows the comparison of measured shear strengths for the three NiCrFeGeB-IN718 joints, and the BNi-2-IN718 joint. For the NiCrFeGeB filler metal, the highest shear strength was observed for the 60-minute hold time sample at 296 MPa, and the 60-minute hold time joint using the 100 µm foil was only marginally weaker than this at 292 MPa. For the 15-minute hold time sample, the maximum shear strength was 269 MPa. By comparison, the joint using BNi-2 had an average shear strength of 476 MPa.

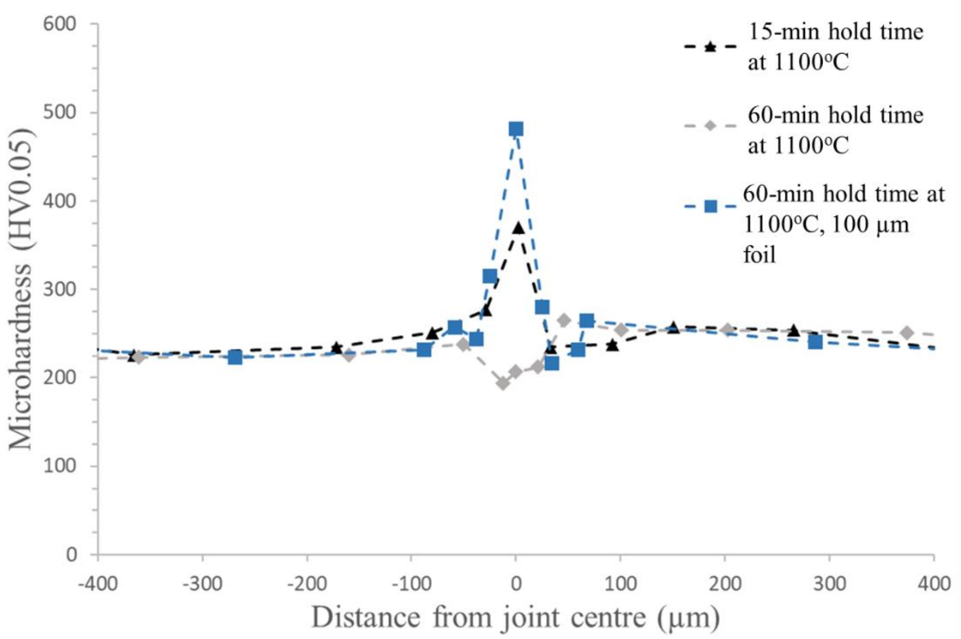

Fig. 15. Microhardness (HV0.05) profiles for different brazed joints (15-minute hold time at 1100°C, 60-minute hold time at 1100°C and 15-minute hold time at 1100°C using 100 µm thickness foil).

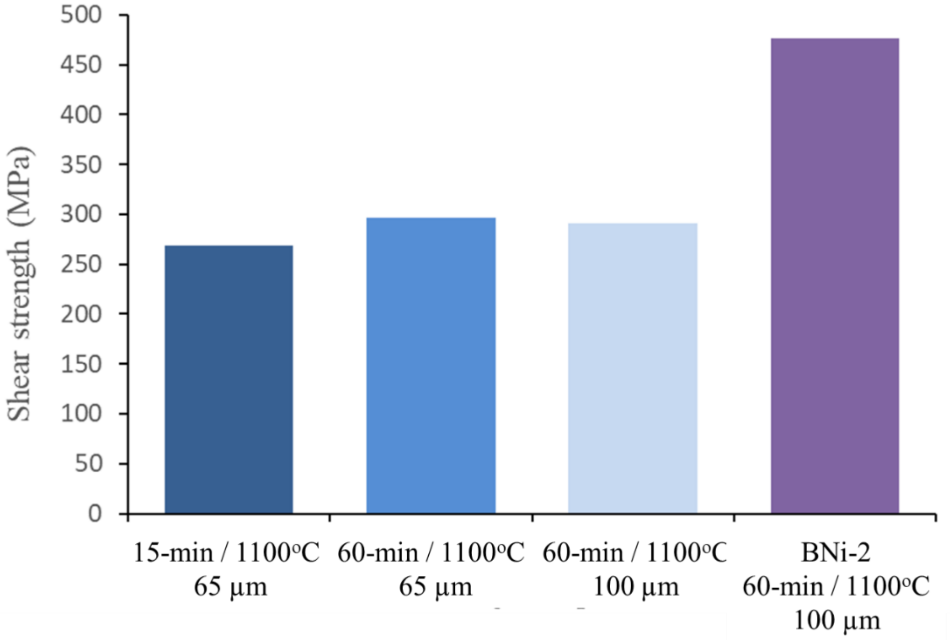

Fig. 16. Comparison of shear strengths of each joint using NiCrFeGeB filler alloy.

In the case of many HEA and MPEA studies, the aim has been to achieve a single (or occasionally dual) phase microstructure, either FCC or BCC, in order to achieve superior mechanical properties. In other cases, secondary precipitates may be intentionally sought in order to strike a balance between ductility and strength. However, the as-cast microstructure of the NiCrFeGeB MPEA in the present study was observed to possess multiple phases, two of which were likely undesirable intermetallic-type phases. As evidenced by the high microhardness measurement, this as-cast state was particularly hard and brittle due to these phases. This is despite, according to the TC predictions and empirical thermodynamic parameters in Equations (1) – (3), a majority FCC or mixed BCC/FCC microstructure, respectively, might have been predicted. A possible cause of this intermetallic-consisting microstructure could be found when looking at the ΔH_{mix} values for specific binary pairs, in this case the Ni-Ge, Cr-Ge and Fe-Ge pairs. These values are -23.5, -18.5 and -15.5 kJ mol^{-1} respectively, all very negative compared to those for the binary pairs between Ni, Cr and Fe. Therefore, despite a small, slightly positive average ΔH_{mix}, this is not sufficient for solid solution formation due to the dominance of the extreme values for binary pairs with Ge. Indeed, this also applies for explaining the presence of borides in the as-cast state.

Considering this, it appears that TC was unable to capture all the resulting phases accurately. First of all, the predictions of Cr(Fe)-boride phase stand up well to the microstructural observations, though EDS did demonstrate the presence of some Fe in solution in these phases in the as-cast state not captured by TC. Nonetheless, the ability to predict the abundance of this phase is understandably useful for such alloy design applications. The other phases predicted by TC, however, were clearly not borne out in the experimental observations and demonstrates a limitation of the CALPHAD approach for such alloys, and of this SSOL4 database in particular, in that the lack of experimentally verified binary systems in the database has resulted in TC treating the Cr and Ge as entirely segregated from the other phases. While perhaps less surprising in the case of Ge given that assessed binary data is not available in SSOL4, it is more surprising that the Cr content was predicted to be completely separate from the Ni and Fe content. We see instead from the observations of the as-cast state that, aside from the aforementioned Cr(Fe)-borides, the Cr is also in each other phase observed, and the Ge is present in each phase apart from the Cr(Fe)-borides.

It is also worth noting how the predicted solidus and liquidus temperatures differ from those measured via DSC. In the case of the solidus temperature, TC predicted 816ºC, a significant discrepancy of approximately 200ºC. Meanwhile, the liquidus prediction is in much more agreement with the measured liquidus, with TC predicting 1062ºC versus the DSC-measured 1055ºC. Apparently, the prediction of the Cr and Ge segregation into the BCC_A2 phase at approximately 950ºC, and then the Ge segregation into DIAMOND_A4 phase may have depressed the prediction of the solidus temperature. Despite this discrepancy, it is still considered that TC can be useful in predicting trends on liquidus temperature, if not the exact temperatures. It is also worth noting that TC predictions are for equilibrium-state conditions (i.e. infinitely slow cooling), which is clearly not the case for the rapid cooling that occurs following arc-melting. This, in addition to the aforementioned lack of complete experimentally-validated databases, means TC should be used with caution in such cases, and is better used for investigating broader changes resulting from composition changes, rather than for precise predictions.

A marked change in microstructure occurs when this alloy is applied to the brazing on IN718 in this study. Brazing or transient liquid phase bonding (TLPB) is considered to be comprised of a series of sequential steps in most models, which have been discussed at greater length elsewhere [6]. Typically, these steps are:

- Base metal dissolution / Liquid Homogenisation
- Isothermal Solidification
- Solid Homogenisation

The microstructures resulting from the described brazing cycles can be understood by considering these steps in the context of the presented results.

In each case, there has been to some extent dissolution of the base metal, as indicated on figs 11(a) and (b). The degree to which base metal dissolution occurs is a function of brazing temperature (a constant in this study), composition of filler and base metal (a constant), hold time, and initial joint width. Upon reaching the brazing temperature, the NiCrFeGeB is fully molten, and during the whole heating stage, the concentrations of MPD elements Ge and B in the solid base metal and molten filler metal follow the solidus and liquidus lines respectively. Therefore, as the concentration of Ge and B in the liquid decreases until it reaches liquidus composition, a corresponding increase in width of the liquid occurs until the solid immediately adjacent to the liquid achieves its solidus composition. At this point, dissolution of the base metal ceases and the concentrations at the solid-liquid interface maintains this equilibrium.

After the base metal dissolution has completed, cross-diffusion of the MPD elements from filler metal and base metal elements occurs, resulting in the liquidus temperature of the melt increasing and the onset of isothermal solidification. It is considered that in this case B is the dominant diffusing element as its reported diffusion coefficient in Ni ($6.22\text{x}10^{-11}$ m^2s^{-1} as used in [9,40]) is orders of magnitude greater than for Ge ($4.5\text{x}10^{-14}$ m^2s^{-1}[33]). This is backed up by the presence of GB-borides in the base metal at a greater distance away from the joint region, especially in the case of the 15-minute hold time. When a critical amount of the B has diffused into the base metal, grains of solidifying liquid form at the solid-liquid interface. It is believed that at this stage the Ni-Ge-Nb phases formed (white contrast on Fig. 12), owing to Ge rejection from the forming Ni-rich solid solution, and the large negative mixing enthalpies between Ni, Ge and Nb. The grain sizes of the solid solution here are notably smaller compared to those that eventually form towards the joint centre as isothermal solidification proceeds. Similar findings were reported by Ghaderi *et al.* [9], who attributed this to boride formation in the region close to the base metal providing a barrier to grain growth. In this case it is presumed that the Ni-Ge-Nb phase similarly hindered grain growth. This formation of the phase largely ceases abruptly and larger grains form, indicating Nb presence only in this region that was dissolved initially.

In the case of the 15-minute hold time, the isothermal solidification progresses to an almost complete stage, but as seen in Fig. 12 some residual Ni-Ge-Nb phase is observed within the IS zone after brazing, again seemingly resulting from rejection from the now larger solid solution grains. In the case of the 60-minute hold time, only fine GB borides are observed in the IS zone, suggesting the prolonged hold time was sufficient for a greater degree of back-diffusion to occur after IS has completed. Several modelling approaches to estimating the time for isothermal solidification have been put forward and employed. Gale & Wallach [41] and later Ojo *et al.* [42] found good agreement between calculations based on Equation (4) and experimental observations.

$$C_S - C_M = (C_0 - C_M)\left\{erf\,\frac{w}{\sqrt{4Dt_f}}\right\} \quad (4)$$

Where C_S, C_M, and C_0 are the MPD (B) solubility limit in the base metal, concentration in the base metal, and concentration in the filler metal respectively; w is the half-width of the brazed joint; D is the MPD (B) diffusivity in the base metal; and t_f is the time for isothermal solidification. This approach is derived from Fick's second law of diffusion and treats B as the sole solute in a simple Ni-B filler metal. This approach has, however, not been applied to cases where a HEA or MPEA is used as the filler metal. Nonetheless, it is considered appropriate to use in this case due to the evidence of B being the dominant diffusing element. The values used for each term in Equation (4) are as follows:

- C_S = 0.3 at.% [41] (based on Ni-B phase diagram from [43])
- C_M = 0.0628 at.%
- C_0 = 2.5 at.%
- w = 65 µm (based on width following base metal dissolution)
- D = $6.22\text{x}10^{-11}$ m^2s^{-1} [9,40]

Using Equation (4), the expected time for IS to complete based only on B diffusion is approximately 30 minutes. This is in reasonable agreement with the experimental observations, with the 15-minute hold time being insufficient to complete IS, whereas an extra approximately 30 minutes for continued diffusion and homogenisation was allowed in the case of the 60-minute hold time.

Lastly, the different hold times had clear effects on the degree of homogenisation seen in the brazed joints. A notable difference between the 15-minute and 60-minute hold times was the presence, or lack, of Cr(Fe)-borides apparently retained from the as-cast state. While the borides phases were observed post-braze for the 15-minute hold time with only slight size reduction, in the case of the 60-minute hold, these borides were apparently dissolved due to diffusion processes over this hold time. The retention or dissolution of these borides can be understood by considering the effect of time and temperature on the diffusion processes, and the driving force provided by the steep concentration gradient between the B-rich borides and the B-lean ISZ. The dissolution of the borides appears to have been a relatively sudden evolution, as they are only slightly reduced after the 15-minute hold time, but for the 60-minute hold time (in which IS completed), the borides were able to completely dissolve. This could be explained by the increased time for B diffusion away from the joint. Perhaps surprisingly, the B released from this dissolution did not form a significant amount of boride phases in what is usually presented as a diffusion-affected zone (DAZ). In fact, the 15-minute hold time sample exhibited a greater abundance of Nb-Mo borides in the base metal than for the 60-minute hold time sample (which in turn exhibited a greater abundance than for the 60-minute + homogenisation sample). This suggests not only that these Nb-Mo borides eventually dissolved due to increased hold time (and then to an even greater degree with subsequent homogenisation), but these borides likely formed before the completion of IS rather than after, similar to findings in [9, 44] and contrary to previous assumptions [45]. It appears that only the Ni-Ge-Nb phase discussed above remained largely unchanged by either increasing the hold time or even homogenisation.

The effect of increased joint width for this filler metal was investigated through use of a 100 µm foil. Despite being held for 60 minutes at the same temperature, in the case of the 100 µm foil the borides were still evident post-brazing, albeit apparently reduced in size suggesting partial dissolution over the course of the braze cycle. While the initial joint width (defined by the initial foil thickness) will have an effect on the time needed to achieve complete isothermal solidification, it is not immediately apparent why the borides were not dissolved completely in this case. However, when considering the fact that the increased foil thickness results in a greater diffusion distance for B into the IN718 base metal, it can be understood that an increased concentration of B still remained in the melt when isothermal solidification commenced. Thus, the concentration gradient and hence the driving force for diffusion of B from boride into ISZ was diminished, allowing the borides to remain.

The sample using the 100 µm foil also showed differences to both 65 µm foil samples in the concentration of the Ni-Ge-Nb phase (caused by base metal dissolution) and the Nb-Mo borides along grain boundaries in the base metal (caused by outward B diffusion). The concentration of the former phase is reduced at the interface with the base metal, instead observed in greater concentration within the joint due to incomplete IS. The concentration of the Nb-Mo borides, however, is increased. It is possible that the increased joint width led to a lesser degree of base metal dissolution, resulting in less of the Ni-Ge-Nb phase. An increased degree of boride dissolution then resulted in diffusion of now-freed B, producing the increase in GB Nb-Mo boride concentration observed.

Of particular note also is the chemistry of the final ISZ in each case. As determined by the EDS analysis, the initial microstructure of the as-cast state of this alloy possessed not just the Cr(Fe)-boride intermetallic, but also a Cr/Ge-rich intermetallic phase. Rather, this appeared to be a stable phase which would probably be undesirable in the final joint. However, unlike the Cr(Fe)-borides this phase was not retained in the final microstructure. This is attributed to the large concentration gradient of Ge that existed between the NiCrFeGeB alloy and the IN718 base material, providing a high driving force for diffusion. In addition, as already mentioned, the solubility of Ge in the base metal is likely significantly greater than for B. Indeed, the grains in the ISZ were found by EDS to contain Ge in a concentration likely to be at the solubility limit. The composition of this ISZ is approximately, as expected, a HEA- or MPEA-like Ni(41)-Cr(25)-Fe(20)-Ge(10)-X(bal.) (in at.%) solid solution, with X being a mixture of base metal elements Al, Mo, Nb and Ti. Calculation of average VEC (= 7.92, using Equation (3)), suggests that this would be more likely to possess a desirable FCC solid solution structure.

In terms of mechanical properties, the shear strengths measured in this study are generally in line with expectation. The greatest shear strength was demonstrated for the case of the 60-minute hold time using the 65 µm foil, likely due to the completion of IS, complete boride dissolution and greater degree of homogenisation. The weakest shear strength was that of the 15-minute hold time using 65 µm foil, likely owing to the retained borides in the joint microstructure. The 60-minute hold time using 100 µm foil had the second highest measure shear strength, despite also possessing retained borides and having the largest joint width (hence least completion of IS). This sample did, however, possess a lower concentration of the Ni-Ge-Nb phase at the base metal interfaces as compared to both the samples that used 65 µm foils. This perhaps counteracted some of the detrimental effect of the retained boride phases, enough to achieve a strength greater than that for the 15-minute hold time, but not greater than that for the 60-minute hold time. Compared to the commercially available AWS BNi-2 filler metal, which achieved an average shear strength of 476 MPa in this study, the shear strengths achieved by the NiCrFeGeB filler metal in each trial was weaker, the highest being 296 MPa. In the literature, strengths of often over 500 MPa may be reached for BNi-2, using comparable brazing cycles. Pouranvari *et al*. achieved a shear strength of approximately 580 MPa when brazing IN718 with AWS BNi-2 at 1100°C with a 60-minute hold time, and the ISZ had a comparatively low hardness of 150 - 200 HV0.01 (increasing towards the joint centre) [46]. Nonetheless, this is a promising result when considering further optimisation that may be made to the alloy. Indeed, the findings suggest that the joint width in the NiCrFeGeB-IN718 joints does not have a large impact on the shear strength, and may be less sensitive to joint width than current filler metals such as BNi-2. This may have a potential benefit in situations where joint gap is hard to control, such as in repair, or in the joining of components with rough surface finish, such as additively manufactured parts.

Conclusions

In the present study, a novel NiCrFeGeB MPEA-derived filler metal was designed using TC software and empirical thermodynamic parameters employed in the design of HEAs. The designed alloy was used, in the form of 65 µm thick foil, to braze Ni-based superalloy IN718 at 1100°C for both 15 minutes and 60 minutes. The stability under approximate service conditions (700°C for 100 hours) was also investigated. A further trial was conducted at 1100°C for 60 minutes using a 100 µm thick foil to investigate the effect of increased joint width. The main findings can be summarised as:

- TC predictions of the as-cast NiCrFeGeB alloy microstructure had mixed accuracy. While Cr-borides were captured by the predictions, the lack of experimentally established data for Ge-containing binary systems appeared to limit the accuracy of the predictions. Predictions for the alloy solidus temperature were significantly different to that measured by DSC, while the liquidus prediction differed from that measured by only a 3°C. TC is best used to investigate broad trends during alloy development rather than to use for precise predictions.

- Contrary to most of the TC predictions and empirical thermodynamic parameters, the as-cast alloy was characterised by Cr(Fe)-borides and a Cr-Ge-rich intermetallic phase, in addition to two other phases, one Ni-rich and one Ge-rich. This is likely due to the very negative ΔH_{mix} between binary pairs of Ni, Cr and Fe with Ge and B, which overrules the average ΔH_{mix} of all binary pairs which was calculated as slightly positive.

- Base metal dissolution resulted in the formation of a Ni-Ge-Nb rich phase in the vicinity of the interfaces with the base metal in all samples.

- Isothermal solidification was completed to varying degrees depending on hold time and joint width. IS was incomplete for the 15-minute hold time and the 100 µm thickness foil samples, both exhibiting residual rejected Ni-Ge-Nb phase in the joint. IS was completed for the 60-minute hold time sample, with IS grains spanning the original gap width. These grains (in all samples) possessed an FCC Ni-rich, HEA-like composition. In the case of the 15-minute hold time and the 100 µm thickness foil samples, Cr(Fe)-borides, apparently retained from the as-cast microstructure, were observed post-braze. This was attributed to the insufficient time at temperature for the former case, and to the increased joint width in the latter case.

- Shear strengths of the NiCrFeGeB brazed joints ranged from 269 MPa (15-minute hold, 65 µm foil) to 296 MPa (60-minute hold, 65 µm foil). Using the increased thickness 100 µm foil resulted in only a small decrease in joint shear strength.

Acknowledgements

LH gratefully acknowledges the financial support of VBC Group and the Engineering and Physical Sciences Research Council (EPSRC) UK, through the Centre for Doctoral Training in Advanced Metallic Systems.

References

[1] C. Briant & E. Hall: *Welding Research Supplement*, 1990, pp. 60–67.

[2] D. Bose, A. Datta, A. Rabinkin & N. J. De Cristofaro: *Welding Research Supplement*, 1986, pp. 23–30.

[3] M. Salmaliyan & M. Shamanian: *Heat and Mass Transfer*, 2019, vol. *55*(8), pp. 2083–2093.

[4] X. J. Yuan, M. B. Kim & C. Y. Kang: *Materials Science and Technology*, 2011, vol. *27*(7), pp. 1191–1197.

[5] M. Abdelfatah & O. A. Ojo: *Materials Science and Technology*, 2009, vol. *25*(1), pp. 61–67.

[6] W. F. Gale & D. A. Butts: *Science and Technology of Welding and Joining*, 2004, vol. *9*(4), pp. 283–300.

[7] A. Ghasemi & M. Pouranvari: 2019, *Science and Technology of Welding and Joining*, vol. *23*(5), pp. 441–448.

[8] A. Amirkhani, B. Beidokhti, K. Shirvani, & M. R. Rahimipour: *Journal of Materials Processing Technology*, 2019, vol. *266*, pp. 1–9.

[9] S. Ghaderi, F. Karimzadeh, & A. Ashrafi: *Journal of Manufacturing Processes*, 2020, vol. *49*, pp. 162–174.

[10] A. Yarmou Shamsabadi, R. Bakhtiari & B. G. Eisaabadi: *Journal of Alloys and Compounds*, 2016, vol. *685*, pp. 896–904.

[11] J. Chen, V. Demers, E. L. Cadotte, D. Turner & P. Bocher: *Journal of Materials Engineering and Performance*, 2017, vol. *26*(2), pp. 547–553.

[12] K. A. Rozman, M. A. Carl, M. Kapoor, N. Doğan, J. A. Hawk: *Materials Science and Engineering A*, 2019, vol. *768*

[13] S. Y. Wang, Y. Sun, X. Y. Hou, C. Y. Cui, X. F. Sun & Y. Z. Zhou: *Materials Letters*, 2020, vol. *258*, pp. 126730

[14] M. K. Dinkel, P. Heinz, F. Pyczak, A. Volek, M. Ott, E. Affeldt, A. Vossberg, M. Göken, R. F. Singer: *TMS Proceedings of the International Symposium on Superalloys*, 2008, pp. 211–220.

[15] B. Laux, S. Piegert & J. Rösler: *Metallurgical and Materials Transactions A,* 2009, vol. 40A, pp. 138–149.

[16] J. W. Yeh, S. K. Chen, S. J. Lin, J. Y. Gan, T. S. Chin, T. T. Shun, C. H. Tsau, S. Y. Chang: *Advanced Engineering Materials*, 2004, vol. *6*(5), pp. 299-303

[17] D. B. Miracle: *Nature Communications*, 2019, vol. *10*(1), pp. 1–3.

[18] P. –K. Huang, J. –W. Yeh, T. –T. Shun, S. –K. Chen: *Advanced Engineering Materials*, 2004, vol. *6(1)*, pp. 74-78.

[19] D. B. Miracle & O. N. Senkov: *Acta Materialia*, 2017, vol. *122*, pp. 448–511.

[20] X. Gao, Y. Lu, B. Zhang, N. Liang, G. Wu, G. Sha, J. Liu & Y. Zhao: *Acta Materialia*, 2017, vol. *141*, pp. 59–66.

[21] Y. Zou, J. M. Wheeler, H. Ma, P. Okle & R. Spolenak: *Nano Letters*, 2017, vol. *17*(3), pp. 1569–1574.

[22] O. N. Senkov, J. M. Scott, S. V. Senkova, D. B. Miracle & C. F. Woodward: *Journal of Alloys and Compounds*, 2011, vol. *509*(20), pp. 6043–6048.

[23] X. W. Qiu, Y. P. Zhang, L. He & C. G. Liu: *Journal of Alloys and Compounds*, 2013, vol. *549*, pp. 195–199.

[24] C. Shang, E. Axinte, W. Ge, Z. Zhang & Y. Wang: *Surfaces and Interfaces*, 2017, vol. *9*, pp. 36–43.

[25] B. Gorr, M. Azim, H. J. Christ, T. Mueller, D. Schliephake & M. Heilmaier: *Journal of Alloys and Compounds*, 2015, vol. *624*, pp. 270–278.

[26] D. Bridges, S. Zhang, S. Lang, M. Gao, Z. Yu, Z. Feng & A. Hu: *Materials Letters*, 2018, vol. *215*, pp. 11-14

[27] W. Tillmann, L. Wojarski, M. Manka & C. Timmer: *Proceedings from the International Brazing & Soldering Conference*, 2018, pp. 142–148.

[28] M. Gao, B. Schneiderman, S. M. Gilbert & Z. Yu: Z: *Metallurgical and Materials Transactions A: Physical Metallurgy and Materials Science*, 2019, vol. *50*(11), pp. 5117–5127.

[29] S. Jin, C. Leinenbach, J. Wang, L. I. Duarte, S. Delsante, G. Borzone, A. Scott & A. Watson: *Calphad: Computer Coupling of Phase Diagrams and Thermochemistry*, 2012, vol. 38, pp. 23-34.

[30] Y. Q. Liu & Y. Du: *Computer Coupling of Phase Diagrams and Thermochemistry*, 2010, vol. 34, pp. 25-36.

[31] H. Okamoto: *Journal of Phase Equilibria and Diffusion*, 2008, vol. *29*, pp. 292.

[32] G.V. Raynor & V.G. Rivlin: *Phase Equilibria in Fe Ternary Alloys*, The Institute of Metals, London, 1988, pp. 316-332.

[33] R. Rettig, S. Steuer & R. F. Singer: *Journal of Phase Equilibria and Diffusion*, 2011, vol. *32*(3), pp. 198–205.

[34] Y. Zhang, Y. J. Zhou, J. P. Lin, G. L. Chen & P. K. Liaw: *Advanced Engineering Materials*, 2008, vol. *10*(6), pp. 534–538.

[35] M. C. Troparevsky, J. R. Morris, Y. Wang, A. R. Lupini & G. Malcolm: *Journal of the Minerals, Metals and Materials Society*, 2015, vol. *67*(10), pp. 2350–2363.

[36] S. Guo, C. Ng, J. Lu & C. T. Liu: *Journal of Applied Physics*, 2011, vol. *109*, pp. 103505.

[37] S. Guo & C. T. Liu: *Progress in Natural Science: Materials International*, 2011, vol. *21*(6), pp. 433–446.

[38] K. Matsu, Y. Miyazawa, Y. Nishi & T. Ariga: *Materials Transactions*, vol. *48*(5), pp. 1055–1059.

[39] W. C. Liu, M. Yao, Z. L. Chen & S. G. Wang: *Journal of Materials Science*, 1999, vol. *34*, pp. 2583–2586.

[40] M. Pouranvari, A. Ekrami & A. H. Kokabi: *Journal of Alloys and Compounds*, 2013, vol. *563*, pp. 143–149.

[41] W. F. Gale & E. R. Wallach: *Materials Science and Technology (United Kingdom)*, 1991, vol. *7*(12), pp. 1143–1148.

[42] O. A. Ojo, N. L. Richards & M. C. Chaturvedi: *Science and Technology of Welding and Joining*, 2004, vol. *9*(6), pp. 532–540.

[43] T. B. Massalski, J. L. Murray & L. H. Bennet: *Binary alloy phase diagrams: Volume 1* In *ASM International*, ASM, Metals Park, Ohio, 1986, pp. 366-371

[44] W. F. Gale & E. R. Wallach: *Metallurgical Transactions A*, 1991, vol. *22*, pp. 2451–2457.

[45] I. Tuah-Poku, M. Dollar & T. B. Massalski: *Metallurgical Transactions A*, 1988, vol. *19*, pp. 675–686.

[46] M. Pouranvari, A. Ekrami & A. H. Kokabi: *Materials Science and Technology (United Kingdom)*, 2014, vol. *30*(1), pp. 109–115.

11.8 Electron Probe Microanalysis with Wavelength Dispersive Spectroscopy of B-containing phases in brazed joints

As detailed in the previous chapter, at least two phases were believed to be boride phases, one of which was likely to be Cr-boride phase retained from the as-cast state of the NiCrFeGeB filler metal, the other being possibly a GB boride phase. In order to confirm that these phases were indeed B-containing, Electron Probe Microanalysis with Wavelength Dispersive Spectroscopy (EPMA (WDS)) was used to map an area of a separate joint brazed with the NiCrFeGeB filler metal for 15 minutes at 1100^{o}C (using foil thickness of approximately 65 μm), and in keeping with the 15-minute hold time braze cycle described in Section 11.7. Preparation of base metal and filler metal was also the same as described in Section 11.7. The EPMA was conducted at an accelerating voltage of 5 kV for B measurement, enhancing the sensitivity to the light element, and 15 kV for other elements.

Fig. 11.11 shows EPMA (WDS) maps of a typical section of the brazed joint, with the legend showing relative abundance of elements (light contrast represents most abundant). The blocky Cr-rich phase seen in the joint region (marked ‘Cr-B’), which was presumed to be a Cr-boride phase, was confirmed to also be rich in B. Furthermore, the Nb-rich GB phase (marked ‘Nb-B’) was also confirmed as being B-rich. It was also observed that some instances of the previously mentioned light contrast Ni, Ge, Nb-rich phase in the joint region (see Fig. 12 in Section 11.7) also contain B, as indicated by the encircled region in Fig. 11.11.

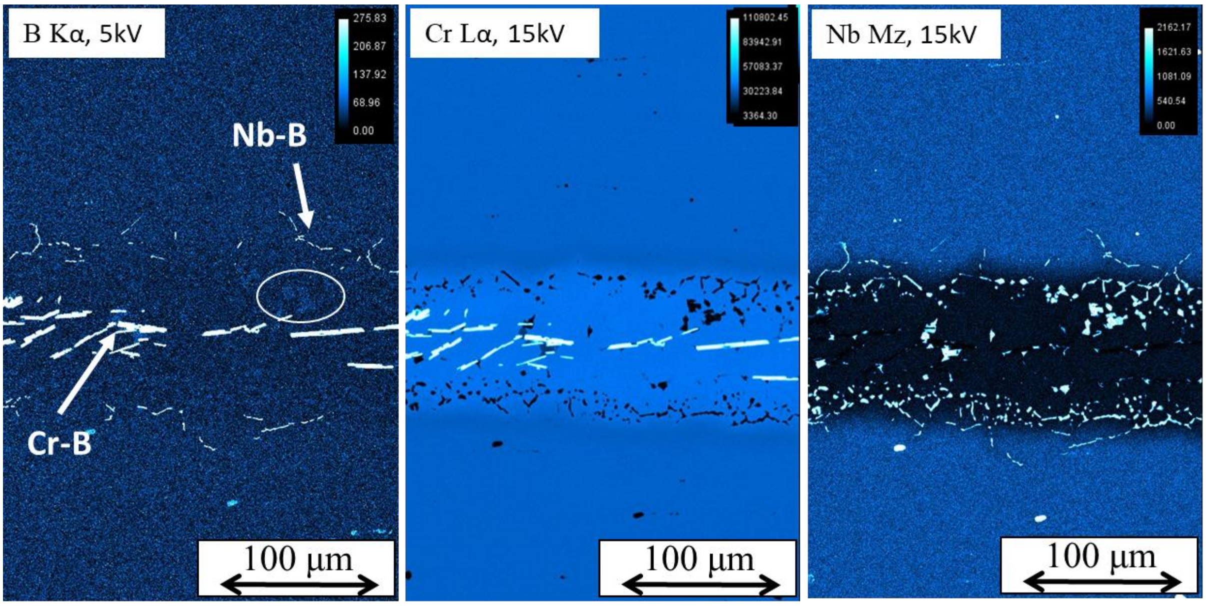

Figure 11.11: EPMA (WDS) maps showing distribution of B, Cr and Nb, allowing confirmation of Cr-boride and Nb-boride phases formed in the vacuum brazing of IN718 with the developed NiCrFeGeB filler metal (15 minutes, 1100^{o}C).

11.9 NiCrFeGeB filler metal powder

In Section 11.7, the successful application of the developed NiCrFeGeB filler metal composition for the brazing of Inconel 718 was demonstrated. The extreme hardness and high degree of brittleness, however, meant that production of foil-thin pieces of the alloy, of suitable size for brazing, was difficult and not time-efficient. As mentioned previously, typically such foils would be produced using the melt-spinning technique, but in the absence of melt-spinning facilities in place at the time of this work, alternatives were considered.

Firstly, attrition milling was considered an option for producing powder from bulk as-cast alloy. Recently, the Royce Translational Centre (RTC) was equipped with a Union Process HD01 CE attrition mill. The attrition milling technique relies on rapid vibration of grinding medium (usually a ceramic or steel) in the form of balls of various sizes (typical sizes for this model is less than 5 mm). The attrition mill is most effective when attempting to grind coarse broken pieces, roughly the size of the grinding media and smaller, down to finer sizes. Attempting this technique with approximately 30 g of pre-crushed alloy failed to reduce the size of the pieces, attributed to an unsuitable amount of material being used, as the mill is designed to be most effective when the grinding chamber is at least half full. For the scope of this work, this was unfeasible as it would require several hundred grams of alloy.

Other routes to powder production exist, however. One such route, detailed in Chapter 7, is gas atomisation. While in theory this technique works with any quantity of material, in practice many external gas atomisation services generally handle hundreds of kilograms of material at one time for efficiency, or are otherwise unable or unwilling to handle experimental alloys such as the developed NiCrFeGeB alloy. Fortunately, gas atomisation services were provided by Arcast Inc. (ME, USA), who were able to trial gas atomisation of smaller quantities (hundreds of grams) of experimental material. Therefore, 350 g of NiCrFeGeB alloy was prepared in the form of 3 x 100 g and 1 x 50 g ingots via arc-melting. As previously, the operating current used was 400 A, and initially 7 x 50 g ingots were produced, with homogeneity improved by flipping and re-melting 5 times followed by magnetic stirring. 6 of these ingots were combined to produce 3 x 100 g ingots, which were again re-melted 3 times followed by magnetic stirring. The yield from the gas atomisation process conducted by Arcast Inc. was approximately 250 g (with losses from powder unable to be collected from the equipment). Investigation of the microstructure of the gas atomised alloy is discussed in the next section.

11.10 NiCrFeGeB Powder Brazing Trial

The size distribution of the received NiCrFeGeB alloy powder was analysed using a Mastersizer 3000, before which extremes in large sizes were sieved out using a 90 µm gap size sieve (Fischer Scientific). From a 20 g sample of powder, the size distribution was determined from an average of 10 measurements. This method uses the refractive index of a material, and as this was not known for this developed alloy, the value for Ni-based superalloy IN718 was used, 1.958 [203]. Table 11.5 reports the D90, D50 and D10 values for this sample (taken as representative of the powder as a whole), and the average full size distribution is shown in Fig. 11.12. The following section will detail brazing trials using this powder to braze Inconel 718, and a comparison to findings from brazing using the NiCrFeGeB foils in Section 11.7.

Fig. 11.13 shows SEM BSE micrographs of the as-received NiCrFeGeB brazing alloy powder. Microstructure of individual particles was not consistent from one to the next, with some exhibiting larger blocky Cr-boride intermetallics, as in Fig. 11.13(a), with clear cracks occurring presumably as a result of stresses surrounding the boride phases following rapid cooling. Others exhibited much finer Cr-boride intermetallics, as in Fig. 11.13(b).

Table 11.5: Particle size distribution obtained from Mastersizer 3000.

Interval	Size (µm)
D90	102
D50	56.3
D20	25.4

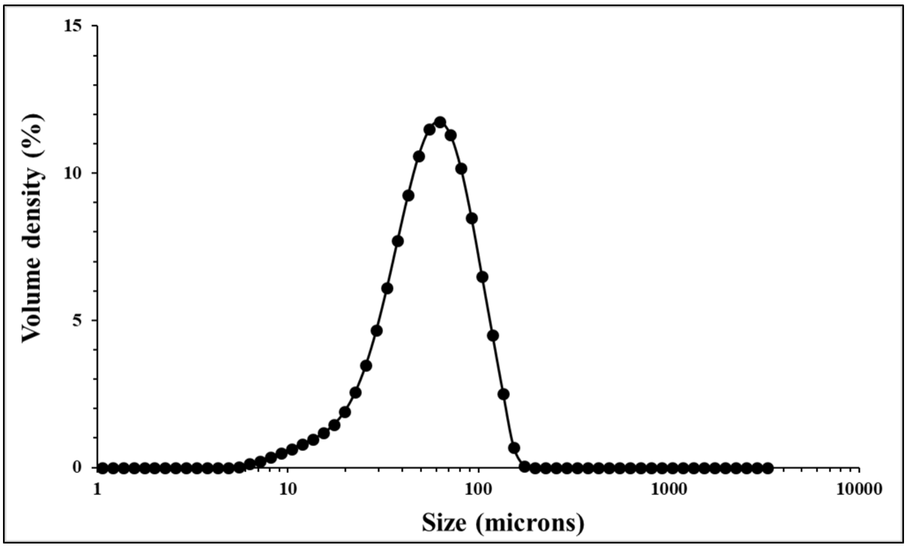

Figure 11.12: Particle size distribution of NiCrFeGeB powder obtained from Mastersizer 3000.

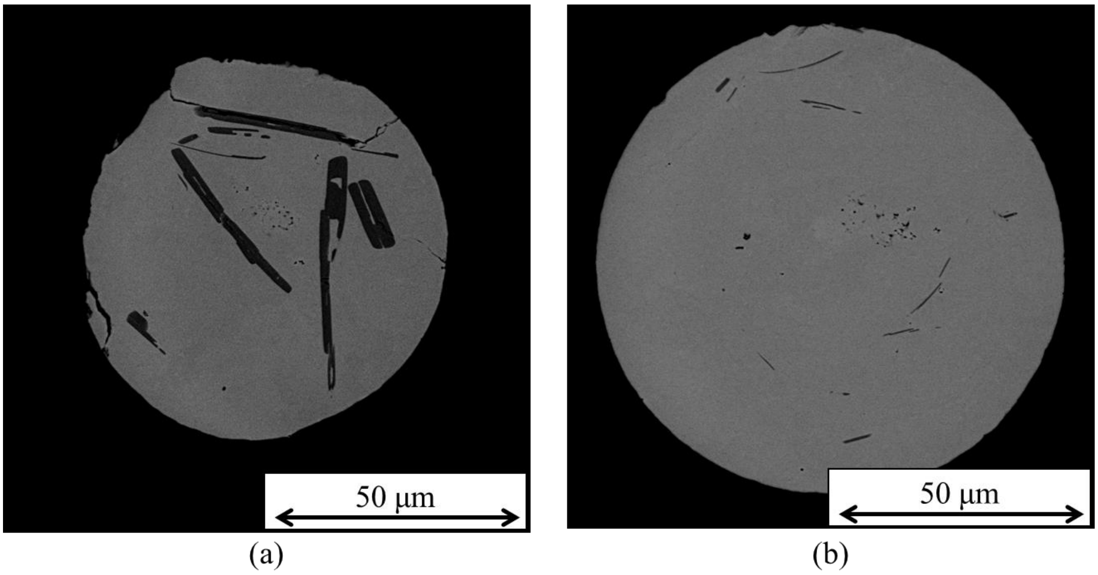

(a) (b)

Figure 11.13: SEM (BSE) micrographs of typical NiCrFeGeB powder particles (a) containing Cr-boride phase, with noticeable cracking, and (b) dispersion of much finer boride phases.

To produce useable brazing alloy paste from this powder, it was combined with a commercial organic binder material (VBC 4841 Braze Binder, supplied by VBC Group, Loughborough). 30 g of brazing paste was produced by combining powder with binder in a 12:1 weight percentage ratio, and then stirring manually. While this ratio is not defined by any particular standard, ratios ranging from 10:1 to 14:1 are commonly used in industry, giving a consistency that is easily extruded from a plunger in order to apply the paste. Paste was inserted into a plunger to allow direct and controlled application of brazing paste to a surface for brazing.

The base alloy for this study was again Inconel 718. As with the trials described earlier in this chapter, 8 mm ø, 5 mm height stubs of IN718 were electron discharge machined from IN718 plate, and 25 x 25 x 3.7 mm IN718 tokens were sectioned from plate, to which the stubs were to be brazed. Surface preparation of the bonding surfaces of the stubs and tokens involved grinding with p1200 SiC grit paper followed by treatment in an ultrasonic bath in acetone for 10 minutes. Brazing alloy paste was then applied via plunger directly on the bonding surface of the stubs, which were then placed down onto the tokens, with a weight of 10 g applied to each. The brazing trials consisted of two brazing trials based on those described in Section 11.7; (a) 1100^{o}C for 15 minutes, and (b) 1100^{o}C for 60 minutes. Ramp rate up to temperature was 15^{o}C min^{-1} with a 15-minute equalisation hold at 1010^{o}C, in each case. Post-brazing, joints were furnace cooled to 900^{o}C before gas quenching. Microstructural analysis of the joints was conducted by SEM in BSE mode (FEI Inspect 50, operated at 20 keV), along with EDS analysis (Aztec software). Microhardness profiles of the joints were performed using a Struers Durascan indentor with 0.05 k-g load (HV0.05) and 15 s dwell time.

Typical sections of the 15-minute hold time sample is shown in the SEM BSE micrograph in Fig. 11.14, with Fig. 11.14(a) showing a section displaying voids, and Fig. 11.14(b) showing a section free of voids. The presence of such voids may indicate poor flowing of the filler metal paste (thus inadequately filling any regions with less paste applied prior to brazing), or they could be a result of the presence of air bubbles within the filler metal paste (while every care was taken to remove these, it is difficult to guarantee their absence). The voids could potentially also be a sign that more filler metal paste was required. The voids, which tended to be between 50 – 100 μm in size, were not found along the interfaces with the base metal, which may lend more credence to the air bubbles or need for more paste explanations, rather than the poor flowing. Indeed, the NiCrFeGeB alloy, when used in foil form as in Section 11.7, did not exhibit any noticeable problems with flow, and the addition of binder to the NiCrFeGeB powder may be expected to improve flow.

The majority of the joint was apparently void free, as in Fig. 11.14(b), in which five distinct phases were observed, appearing largely comparable to the microstructure observed in Fig. 11 from Section 11.7. These include Cr-boride phases (marked *i*), Ni-, Ge- and Nb-rich light contrast observed in the joint region (marked *j*), Ni-, Ge-, Nb- and Cr-rich light contrast phase observed mostly at the interface with the base metal, but also occasionally within the joint region (marked *k*), Ni-rich solid solution (marked *l*), and GB Nb-borides (marked *m*). EDS analysis confirmed that these phases are similar in composition to those observed for the joints brazed using the NiCrFeGeB foil as in Fig. 11 from Section 11.7, and point scan measurements are summarised in Table 11.6 (average of five measurements). The Cr boride phase typically range in sizes from 5 – 30 μm in length. Again, EDS was unable to measure B content due to its limitations in detecting light elements.

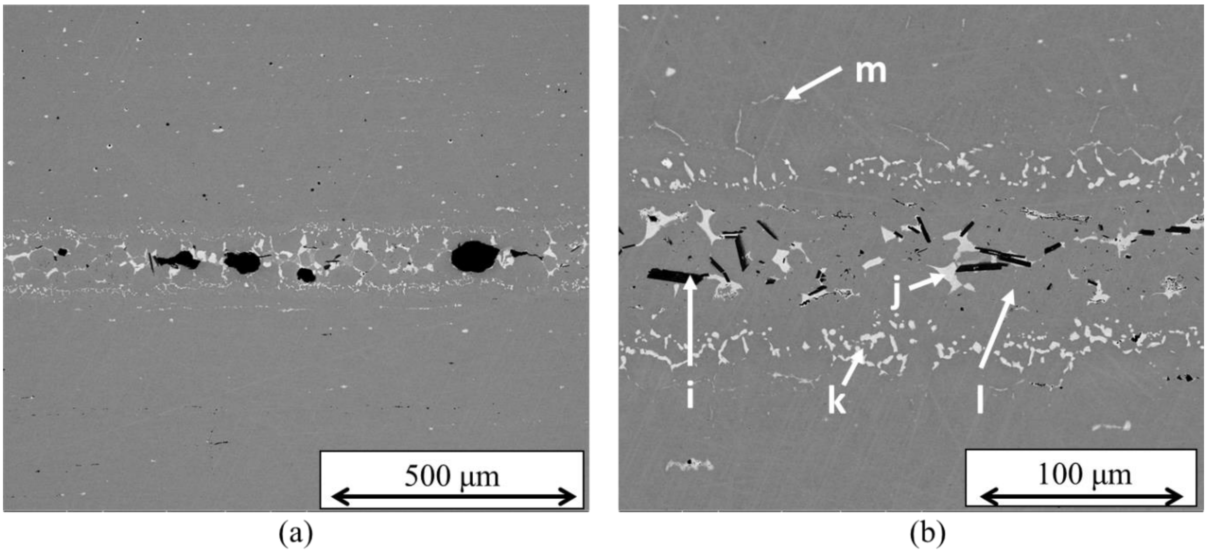

Figure 11.14: SEM (BSE) micrographs of typical section of IN718 brazed with developed NiCrFeGeB filler metal powder for 15 minutes at 1100°C, (b) region displaying microvoids potentially formed from outgassing, and (b) area free of voids, as seen across the majority of the sample.

Table 11.6: EDS measurements (average of 5) of composition of phases identified in Fig. 11.13, in atomic percent.

	Ni	**Cr**	**Fe**	**Ge**	**Nb**	**Mo**	**Ti**	**Al**
i	2.5	87.1	8.0	1.0	0.1	0.9	0.3	0.1
j	49.0	3.6	4.7	22.5	17.0	0.5	2.3	0.4
k	31.4	15.3	11.1	18.7	15.9	6.2	1.3	0.2
l	39.6	25.5	21.2	11.7	0.4	0.7	0.3	0.6
m	3.8	1.7	1.6	1.2	81.9	1.1	8.4	0.3

Fig. 11.15 shows an SEM BSE micrograph of a typical section of a joint following brazing at 1100°C for 60 minutes. As with the joint produced with a 15-minute hold time, EDS point scan measurements (in Table 11.7) distinguished at least six phases present, matching those seen in joints produced so far using the NiCrFeGeB filler metal. These are the Cr boride intermetallic (marked *n*), Ni-, Ge- and Nb-rich light contrast phase (marked *o*), Ni-, Ge-, Nb- and Cr-rich light contrast phase (marked *p*), Ni-rich solid solution (marked *q*), and grain boundary Nb borides (marked *r*), the latter being to small to accurately measure with EDS point scanning. There were also instances of blocky Nb-rich phase towards the base metal interface (possibly also Nb boride or carbide phase).

However, the joint produced for the 60-minute hold time appears to be notably wider than in the case of the 15-minute hold time (approximately 200 µm versus 60 µm). Given the similar distribution of the above phases, it is believed that this increased width is a result of excess filler metal applied and/or insufficient downward pressure applied to the joint. This resulted in some microstructural differences compared to the 15-minute hold time joint. Notably, the 60-minute hold time joint appears to have isothermally solidified solid solution grains originating from the joint centre, rather than just in isothermal solidification fronts originating at the interface with the base metal. However, the presence of the light contrast Ni, Ge and Nb containing phase apparently surrounding these solid solution grains indicates that isothermal solidification was not completed despite the 60-minute hold time due to the increased joint width (this time appeared to be sufficient for the joints using NiCrFeGeB foils of approximately 65 µm foils). This would suggest the formation of the light contrast phase is formed due to rejection from the growing isothermally solidified solid solution phase. The size of the Cr boride intermetallics appears to have remained somewhat larger as compared with those observed in the 15-minute hold time joint, with typical length ranging from 15 – 40 µm, although some smaller sizes were also observed below 10 µm. This is perhaps a result of lower driving force for diffusion with higher B content still in the joint due to the longer diffusion distances. The concentration of phases observed at the interface with the base metal also appear somewhat altered apparently as a result of the increased joint width, with a greater concentration of the light contrast Ni, Ge, Nb and Cr rich phase observed for the 15-minute hold time joint, and a comparatively reduced concentration for the 60-minute hold time. This could point to a decreased extent of base metal dissolution due to the increased initial joint width, due to the further diffusion distance for elements B and Ge. While this might be expected to also result in lower Nb content particularly towards the joint centre, the Nb here is not thought to have diffused, rather the advancing isothermal solidification fronts at the base metal-joint interface have pushed the remaining melt, enriched in rejected Nb, inwards until encountering outward-solidifying fronts forming at the joint centre. Furthermore, it is possible that this Ni, Ge and Nb-containing phase observed in these joints is related to the orthorhombic δ Ni_3Nb phase that forms from transformation of metastable γ″ in Nb-containing superalloy such as IN718 (see Chapter 2, Section 2.2).

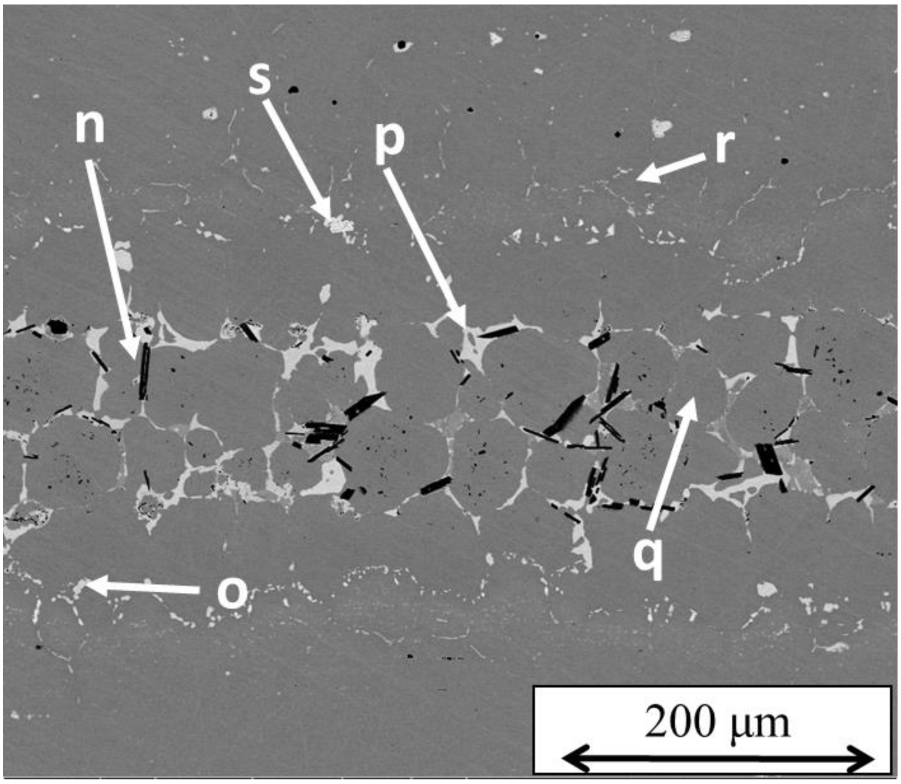

Figure 11.55: SEM (BSE) micrographs of typical section of IN718 brazed with developed NiCrFeGeB filler metal powder for 60 minutes at 1100ºC,.

Table 11.7: EDS measurements (average of 5) of composition of phases identified in Fig. 11.14, in atomic percent.

	Ni	Cr	Fe	Ge	Nb	Mo	Ti	Al
n	2.5	87.1	8.0	1.0	0.1	0.9	0.3	0.1
o	49.0	3.6	4.7	22.5	17.0	0.5	2.3	0.4
p	31.4	15.3	11.1	18.7	15.9	6.2	1.3	0.2
q	39.6	25.5	21.2	11.7	0.4	0.7	0.3	0.6
s	3.8	1.7	1.6	1.2	81.9	1.1	8.4	0.3

The composition of the isothermally solidified grains, as was discussed in Section 11.7, was observed to be a Ni-rich MPEA-like solid solution, with the Ge reduced from the higher initial concentration in the filler metal down to what may be the solubility limit in a single phase Ni-Cr-Fe-Ge system. While the mechanical properties of this solid solution phase are not fully established in this work, in Section 11.7, the solid solution phase (which was continuous across the joint width due to completion of isothermal solidification) resulted in a decrease in microhardness even compared to the base metal, possibly indicating increased ductility which could be of benefit to the overall joint mechanical properties. It is promising to see the formation of an isothermally solidified MPEA-like solid solution phase following the sufficient diffusion of the MPD element, in this case B. As was the case in Section 11.7, the reduced Ge content of this phase due to rejection encouraged the formation of the Ni, Ge and Nb containing phases, whose properties are also not known, but is unlikely to be desirable if only for the tying up of Nb that would otherwise be required in the base metal matrix for formation of γ'' intermetallic. Furthermore, the outward diffusion of B resulted in the formation of Nb-borides at grain boundaries in the base metal.

Mechanical testing was on brazed joints using the NiCrFeGeB filler metal powder, with hold times of 15 and 60 minutes at 1100°C, in order to investigate the effect of holding time. The test method used was that described previously (Chapter 10, Section 10.4, Fig. 10.12). Three joints for each hold time were shear tested in this manner, and Fig. 11.16 shows the average joint shear strength for the 15- and 60-minute hold times (with error determined from the standard deviation). The joints brazed for the longer hold time of 60 minutes exhibited an increased average joint shear strength of 332 ± 15 MPa, compared to 257 ± 26 MPa for the 15-minute hold time. In each case, failure occurred along the brazed seam. Currently, the average joint gap for each hold time is not determined, and although in the microstructural analysis of joints brazed at 1100°C for 15- and 60-minute hold times (as in Fig. 11.14 and Fig. 11.15 respectively) it was observed that the latter exhibited greater joint width, it is not known if this was representative of all such joints. If it was representative, it might be expected that shear strength would decrease for the 60-minute hold time joints, due to isothermal solidification being incomplete even after 60 minutes according to Fig. 11.15. As it stands, assuming the difference in joint widths between Fig. 11.14 and Fig. 11.15 is not representative of all samples, it appears that the longer hold time was beneficial to joint shear strength. This same trend was observed in Section 11.7, where, for hold times of 15 and 60 minutes using 65 μm thickness NiCrFeGeB foils, shear strengths of 269 MPa and 292 MPa were measured, respectively. However, as reported in Section

11.7, joints brazed with commercially available BNi-2 achieved a shear strength of 476 MPa following a hold time of 60 minutes at 1100°C, using the same test method.

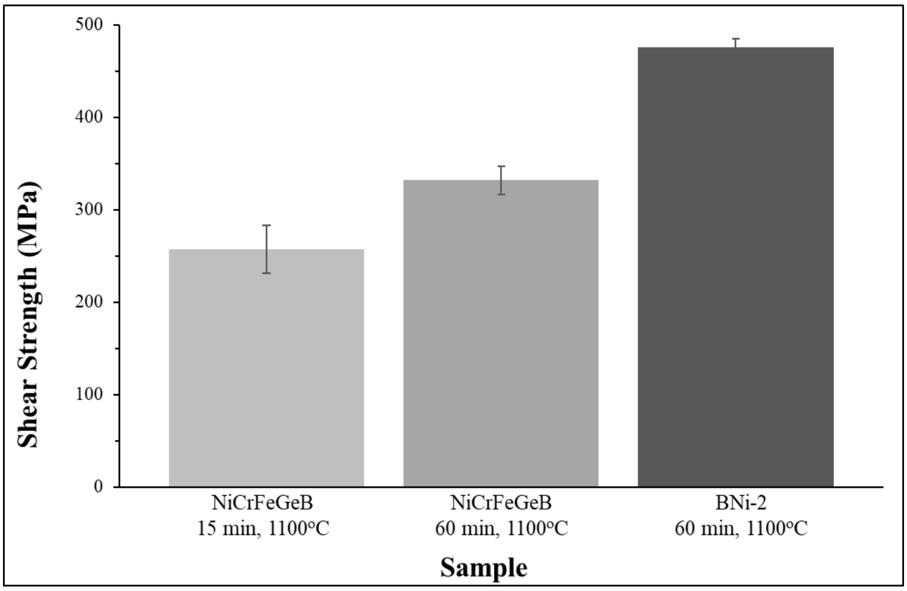

Figure 11.16: Average shear strengths of vacuum brazed IN718-NiCrFeGeB powder joints, brazed at 1100°C for 15 minutes and 60 minutes, and IN718-BNi-2 foil joints, brazed at 1100°C for 60 minutes.

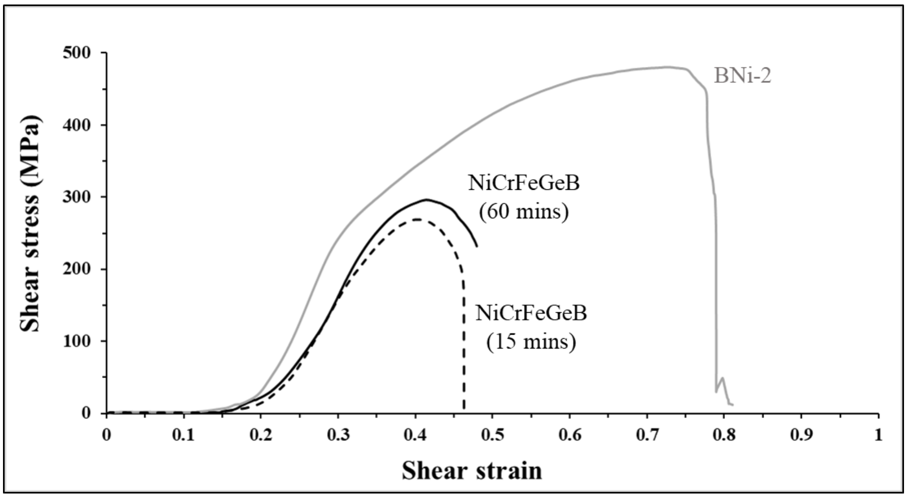

Figure 11.17: Example stress-strain curves of IN718-NiCrFeGeB powder joints, at both brazing conditions, and compared to an example curve for a IN718-BNi-2 joint (brazed at 1100°C for 60 minutes, 50 µm foil).

Example stress-strain curves of joints brazed with both NiCrFeGeB and BNi-2 filler metals are shown in Fig. 11.17. This gives some indication as to the nature of the joints giving rise to the greater shear strength exhibited when using the BNi-2 filler metal. The curve for the BNi-2 filler metal shows a large plastic regime before failure, showing a larger amount of plastic deformation was sustained before failure. In contrast, the curves for the NiCrFeGeB filler metal exhibit much shorter plastic regimes before failure, and so comparatively little plastic deformation can be sustained. This seems to even be the case for the 60-minute hold time joint, where isothermal solidification would be expected to have progressed much further, if not completed, and despite this only a marginally increased plastic regime was observed. The ductility of the primary isothermally solidified MPEA-like NiCrFeGe phase may therefore be limited. However, for both filler metals the yield strength was comparable, in the region of 250 MPa.

11.1 Chapter summary & implications

This section has primarily been concerned with the use of Ge as an MPD element for inclusion in a Ni-Cr-Fe-based MPEA filler metal, for the brazing of Ni-based superalloy IN718. Informed by what was discussed in Section 8.4, Chapter 9, and Section 10.1, initial investigations using TC software were conducted, primarily to attempt optimisation in order to encourage FCC solid solution formation without sacrificing liquidus temperature. As a measure of the usefulness of TC in such optimisation, both equiatomic NiCrFeGe and TC microstructure-optimised NiCrFeGe were fabricated, and compared with the predictions. As already mentioned, TC predictions represent the equilibrium case, and so predicted phases and phase composition may differ from those observed for the rapidly-cooled as-cast ingots. The as-cast equilibrium NiCrFeGe alloy was defined by three distinct phases, with two of the phases containing over 10 at. % of each element. These included a Cr-rich, Ni-lean phase identified via XRD as being similar to a Cr_3Ge intermetallic phase, as well as two probable BCC solid solution phases.

The most notable difference between these observations and TC predictions was the lack of Ge segregation at lower temperatures that was predicted. The plausibility of this prediction was disputable when considering empirical thermodynamic parameters such as the mixing enthalpy, ΔH_{mix}, for which the Ni-Ge, Cr-Ge and Fe-Ge binary pairs all have very negative values, suggesting the formation of ordered compounds would be preferred. Furthermore, the final room temperature phases were predicted as including segregated pure Cr, Fe and Ge, with only a Ni-Fe solid solution. Only at higher temperatures did TC predict the solidification of two solid solution phases (Ni, Fe-rich FCC and Cr, Ge-rich BCC), which are somewhat more in line with the observed microstructure. When also considering the parameters δr and average VEC, which were 10.15 % and 7.00 respectively, a single solid solution phase would not be expected according to typically proposed design ‘rules’ such as those in [139], even without noting the very negative average ΔH_{mix} of -16.88 kJ mol^{-1}, dominated by the binary Ge-containing pairs. However, the apparent formation of two solid solutions as opposed to solely intermetallic compounds suggests that such design rules, which were proposed by cataloguing phase formation for generally more common HEAs and MPEAs using mostly transition and refractory metals, may not fully capture the reality when using less common alloying additions such as Ge.

TC was then used to identify a composition that would maximise the FCC solid solution molar fraction, but Ge content was maintained at 25 at. % in order to ensure a low liquidus temperature. The optimised Ni(bal.)-Cr(15.6)-Fe(29.5)-Ge(25) composition was fabricated, and was observed to possess two solid solution phases, of similar composition to those in the equiatomic case, and which were observed to be of BCC crystal structure rather than FCC. At the same time, the presence of the Cr_3Ge-like phase was greatly reduced to only a few instances observed. Therefore, the optimisation process apparently resulted in increased solid solution while decreasing the Cr_3Ge-like intermetallic, but the solid solutions predicted to form were incorrectly predicted to be of FCC crystal structure in the first place. When comparing microhardness measurements, as a basic indication as to their mechanical properties, the optimisation process resulted in a significant reduction in hardness, apparently as a result of almost complete suppression of the Cr_3Ge-like intermetallic. When considering the change in calculated empirical thermodynamic parameters, the optimised composition moved the values of ΔH_{mix}, δr and average VEC only slightly more towards values that would predict a single solid solution phase. As such, according to these parameters the microstructure may not have been expected to change substantially, in the case of the two BCC solid solution phases observed this holds. Again however, the fact that, despite the still very negative average ΔH_{mix} value, solid solution phases formed and the intermetallic Cr_3Ge-like phase was reduced, which suggests HEA design rules often proposed may be suitable only for a narrow range of possible HEAs if less common elements such as Ge are considered.

It was also clear that, regardless of the microstructure that may be achievable for the NiCrFeGe system, the use of Ge as a sole MPD element was unlikely to achieve a sub-1100ºC as desired. However, the use of Ge in conjunction with another MPD, B, was considered, following on from what was learnt in Chapter 8. In using a reduced (as compared to current commercial B-containing filler metals) B content, and a slightly reduced Ge content, a desirably low liquidus could be obtained. Furthermore, the reduced B content would require less time at temperature to fully diffuse away, potentially resulting in a joint formed primarily of an MPEA-like NiCrFeGe composition with an increased liquidus temperature, and the potential for solid solution strengthening benefits purported for MPEA and HEA systems. Indeed, the work in Sections 11.1 – 11.4 shows that solid solutions in the NiCrFeGe system can form, perhaps contrary to often proposed HEA/MPEA design rules.

The design of a NiCrFeGeB filler metal was reported in Section 11.7, which contains a journal article currently under review for publication. When fabricating the filler metal via arc-melting, the primary effect of the addition of 2.5 at. % B was to result in the formation of a Cr-boride phase, with no observed evidence of other boride phases (though this Cr-boride phase did have some amount of Fe in solution). Other phases appeared to be similar to those observed in the NiCrFeGe alloys discussed in Sections 11.1 – 11.4, which included a Cr, Ge-rich phase similar to a Cr_3Ge intermetallic, as well as two BCC solid solution phases (Ni, Ge-rich and Ni, Ge, Fe-rich). The developed composition was found to possess a high microhardness of 773 ± 10 HV1, due to the presence of the Cr_3Ge-like intermetallic as well as the Cr-type borides.

When used to vacuum braze IN718 superalloy at 1100ºC, the expected B diffusion occurred as evidenced by a reduction in the size of Cr-borides in the joint (which were retained from the as-cast state), and observation of probably Nb-borides at the grain boundaries of the IN718 in the vicinity of the joint interface. It was found that, when brazing at 1100ºC for 15 minutes and 60 minutes, using NiCrFeGeB foils of approximately 65 μm thickness, complete isothermal solidification was not accomplished for the former but was for the latter. In fact, calculations in Section 11.7 suggest that approximately 30 minutes at temperature would be required for complete isothermal solidification for such a joint thickness using the NiCrFeGeB filler metal. In the case of the completely isothermally solidified joint, the joint contained primarily a Ni-rich NiCrFeGe solid solution. While the exact nature of this phase is not known, it is expected to be FCC crystal structure according to TC predictions, empricial thermodynamic parameters, and considering phase diagrams. In the case of the incomplete isothermal solidification, in addition to the NiCrFeGe solid solution, interdendritic regions of a Ni, Ge, Nb-rich phase which was likely solidified final liquid in the joint, enriched in Ge and Nb due to rejection from the advancing isothermally solidifying phase. In both 15-minute and 60-minute hold times, a separate Ni,Ge, Nb-rich phase was observed at the interface with the IN718 base metal. It is believed that dissolution of the base metal due to B, and to a lesser extent, Ge diffusion during heating, resulted in a widening of the liquid phase and introduced base metal elements to the liquid, Nb in particular. The diffusion of B also resulted in the formation of Nb-boride phase along grain boundaries in the IN718 following both brazing cycles.

In terms of the mechanical performance of the joints brazed using the developed NiCrFeGeB filler metal, there was an increase in joint shear strength for the 60-minute hold time as compared to the 15-minute hold time (292 MPa versus 269 MPa). However, this was still substantially lower than was achieved when using the commercially available BNi-2 filler metal under the same conditions (60 minutes at 1100°C), which achieved 476 MPa. However, considering potential optimisation of the composition of this filler metal (see Chapter 12), it is deemed promising that the shear strength achieved are comparable to that of a commercial filler metal. Furthermore, the BNi-2 filler metal was supplied as melt-spun foil of thickness 50 µm; this represents the widely used form of this filler metal, having been used and optimised as such in industry for decades. Considering that such a foil thickness was not achieved for the NiCrFeGeB filler metal, it might be expected that further optimisation of its production may be benficial to the mechanical properties, to say nothing of the increased capacity for testing this would result in.

As such, it was of interest to explore the production of greater quantities of useable forms of the developed NiCrFeGeB filler metal. This was realised in the production of filler metal powder via gas atomisation. When IN718 was again brazed for 15 and 60 minutes at 1100°C using this powder, the resulting microstructure was largely comparable than observed when using the foil (despite an increased gap width being inadvertently produced in the case of the analysed 60-minute joint). Further mechanical testing of the alloy was made possible, and average joint shear strengths of 332 ± 15 MPa and 257 ± 26 MPa were recorded for the 60-minute and 15-minute braze times respectively. While comparisons using powdered BNi-2 filler metal were not made during this project (and in fact there would not be expected to be differences in strength due to using either foils or powders), but it is expected that the shear strength of the joints using powdered NiCrFeGeB powder measured here would still be somewhat below that achievable for BNi-2.

When compared microstructurally to a BNi-2 brazed joint (for examples, see [58,78,98]), the NiCrFeGeB brazed joints appear to have some potential advantages. The phases observed at the interface with the base metal in the NiCrFeGeB brazed joints were observed to be relatively sparse when compared to phases, primarily borides and carbides, often observed in the so-called DAZ when using BNi-2. Furthermore, while the 15-minute braze time was not sufficient for isothermal solidification when using the NiCrFeGeB filler metal, there was no continuous centreline band of athermally solidified eutectic phases that are often observed for BNi-2 joints that have insufficient time for isothermal solidification. The reason for this weaker shear strength is believed to be due to decreased ductility of the isothermally solidified MPEA-like NiCrFeGe solid solution phase, as compared to the primary γ-Ni solid solution often formed for isothermally solidified joints of BNi-2. This is evidenced by the lower displacement at failure achieved during the shear testing; at approximately 2 mm on average for the NiCrFeGeB joints, this is approximately half that achieved for BNi-2 joints. A further contribution may well be the tying up of Nb, the element responsible for formation of strengthening Ni_3Nb γ″ phase in IN718, in some of the phases observed post braze, including the GB Nb-borides and Ni, Ge, Nb-rich phases.

The final chapter of this work follows, in which the main conclusions and implications for both the developed NiCrMnIn and NiCrFeGeB filler metals is summarised, and the potential future work on these alloys is explored.

12. Conclusions & Future Work

This research was aimed at developing Ni-based brazing filler metals of novel compositions, and investigated the potential for use of primarily two alternative MPD elements, to discourage excessively brittle intermetallic formation in the final brazed joint. At the same time, it was also an objective that developed compositions may be used under similar brazing conditions as current commercially available Ni-based brazing filler metals; as such, liquidus temperatures below 1100°C were aimed for, as well as primarily FCC microstructures.

12.1 Main Findings & Conclusions

Initially, this research involved identification, via consideration of phase diagrams, elements that would act as MPD elements in a binary Ni system, while also having some degree of solid solubility in Ni, and not known as forming particularly brittle intermetallic phases with Ni. These were, namely, In and Ge. Ultimately, while both In and Ge were considered as requiring too high a content to achieve a liquidus low enough for feasible use as a binary filler metal alloy, being unattractive for both microstructural and economic reasons. When used in conjunction with a small B weight percentage (as compared to that found in current commercial B-bearing filler metals), lower liquidus temperatures were achievable in the Ni-10-(1,2,3)B systems fabricated, and indeed a sub-1100°C was achieved for 3 wt.% B, but this was not deemed to represent an improvement in terms of the tendency for boride formation. While not fabricated, the Ni-Ge-B system was judged likely to have the same limitations, and so a further strategy was needed.

At the same time, this was used as an opportunity to assess the accuracy of TC predictions for such systems, which were without experimentally verified data in the SSOL4 database. Of the two systems, the Ni-In appeared to show greater deviation from the established phase diagram, whereas Ni-Ge TC predictions showed much better agreement within the range Ni-(0-10 wt.%)Ge. Furthermore, phases predicted by TC were only FCC A1 solid solutions, in clear contrast to the phase diagrams. Overall, these results suggest that quantitative TC predictions should be made with caution, and phase diagrams should be consulted and used in conjunction. TC can prove useful in showing overall trends in solidus and liquidus temperatures (whether an element can be expected to decrease/increase these), and so is of some use for the design of alloys requiring a liquidus such as those for current Ni-based brazing filler metals.

Chapters 10 and 11 detail the development of NiCrMnIn (composition in at. % of 50-9-25-16) and NiCrFeGeB (composition in at.% of 30.5-25-18-25-2.5) MPEA filler metals, with the aim of reaching lower liquidus temperatures than for sole novel MPD addition, and to potentially take advantage of purported promising mechanical properties of such alloys. The latter achieved a very low liquidus temperature of 966°C, but due to high volatility of elements Mn and In, as well as observed liquation during brazing, this filler metal was found to be unsuitable for vacuum brazing. However, belt furnace brazing of IN718 was successful, albeit with poor mechanical properties. When applied to the belt furnace brazing of W-carbide drill tips to EN24 steel drill bits, taking advantage of the low liquidus, probable FCC-type microstructure and ability of Mn to react with W, the NiCrMnIn was again successful. TC predictions, meanwhile, again showed discrepancies, particularly in the phases formed and their composition. Most notably, In was predicted to form a BCC phase with Cr, despite expectations when considering ΔH_{mix} values. Their preference for segregation instead was observed. Again, however, TC proved more useful in optimising this composition for a low liquidus temperature, and indeed the sub-1000^{o}C liquidus shows this. But it is again noted that the exact liquidus value predicted was significantly greater than measured, and so TC can be used for general trends rather than quantitatively.

Meanwhile, the use of Ge as MPD in a NiCrFeGe system was also investigated. As a further investigation of TC as an alloy design and optimisation tool for such systems, it was used in an attempt to optimise the equiatomic NiCrFeGe composition towards one that would promote FCC solid solution. What was found, however, was that while solid solution was promoted, it was in the form of two apparently BCC phases, while a Cr, Ge-rich intermetallic phase was suppressed. This was deemed to be due to TC having predicted that Ge would completely segregate from other elements at lower temperatures in the equilibrium case, whereas observations confirmed Ge relatively evenly distribute between the two phases. The Ge content of the phases therefore promoted the BCC crystal structure over FCC, which was not captured by TC predictions.

The developed NiCrFeGeB composition achieved a promising liquidus temperature of 1055^{o}C, with a B content of 2.5 at. %, representing a substantial reduction as compared to, for example, BNi-2 which has approximately 14 at. % B, and thus reduced concentration of boride phases was expected. When used in the vacuum brazing of IN718, the NiCrFeGeB filler metal was successful in both foil and powder form. For a joint gap of approximately 65 μm, isothermal solidification was achieved for a brazing hold time of 60 minutes at 1100^{o}C, and calculations suggest isothermal solidification may have been completed in as short a time as 30 minutes. The small B content meant that relatively little in the way of borides was observed. However, owing to base metal dissolution, rejection and diffusion of Ge, and the highly negative mixing enthalpy of binary pairs of Ni, Ge and Nb, phases rich in these elements were observed at the base metal interface. When brazed for just 15 minutes at 1100^{o}C, isothermal solidification was incomplete, and such phases were then also observed in the joint region. The isothermal solidification of a NiCrFeGe MPEA-like solid solution provided an intermetallic free joint centre for the 60 minutes brazing time, though where isothermal solidification was not complete, remaining Cr-boride phases were observed in the joint, apparently left over from the fabrication of the filler metal.

In terms of mechanical performance, the NiCrFeGeB MPEA filler metal achieved a joint shear strength in excess of 300 MPa for the 60 minutes at 1100^{o}C braze cycle. This was somewhat lower than the 476 MPa achieved using BNi-2 under identical conditions, and stress-strain curves suggest limited capacity for plastic deformation in the NiCrFeGe MPEA-like solid solution phase. Nonetheless, this is considered a promising result and one which could justify further optimisation of composition and brazing parameters for this filler metal.

As such, the main findings of this research can be summarised as:

- Elements In and Ge are not suitable for use as sole MPDs in a binary Ni alloy, allowing the removal of brittle phase forming elements such as B, Si or P, due to not achieving a suitably low liquidus temperature.
- The strategy of combining the use of MPD elements with concepts such as HEAs and MPEAs has been shown to be effective in achieving a liquidus temperature comparable with current commercially used Ni-based filler metals, allowing its use in typical brazing cycles.
- For the brazing of Ni-based superalloys, the developed NiCrFeGeB filler metal shows promise, with isothermal solidification achievable well within typical brazing times. Comparatively small boride concentration at base metal interface was observed along with an isothermally solidified MPEA-like solid solution phase in the joint region.

- Joint shear strength using this filler metal was inferior to that when using AWS BNi-2 under the same conditions, due largely to limited plastic deformation capacity.
- TC can be useful as a tool for designing alloys for a low liquidus, though predictions of phase composition and quantitative temperature values should be taken with caution. Phase diagrams and empirical thermodynamic parameters can be useful aids to make up for the shortfalls of TC in such an endeavour. More complete databases, including assessed experimental data for a greater variety of binary and ternary systems is encouraged to open up more possibilities for design of novel filler metals, and alloys in general.

12.2 Future Work

In terms of future work, there are several recommendations that may be made. Firstly, this work has demonstrated the need for more complete thermodynamic assessment of binary and ternary alloy systems for use in CALPHAD software such as Thermo-Calc. This could allow exploration of largely unexplored compositions, which could be of enormous benefit the design of novel brazing filler metals even outside the Ni-based filler metals. The demand for greater jet engine efficiency in the future, for example, will in turn demand alloy performance at yet higher temperatures. New filler metals capable of withstanding such temperatures are therefore likely to be needed, and must be designed. In addition, while the advent of HEAS and MPEAs has promised the potential for discovering new alloys with superior properties in the vast compositional space now opened up, such discoveries have been rather limited to alloys sharing a select few elements in general. Therefore, the assessment of yet more binary and ternary systems will be needed to allow the design of new HEAs and MPEAs, particularly as compositions move away from equiatomic and the sole aim of achieving a single phase solid solution. In addition, DICTRA calculations could be used to model diffusion phenomena across such joints as were presented in this work, and thus inform brazing parameters used when trialling such developed filler metals.

With regards to the particular MPEA filler metals developed as part of this research, the NiCrMnIn filler metal could offer some potentially promising microstructural features that may be beneficial for the joining of W-carbide to tool steel, as compared to joints analysed that used the conventional Cu-filler metal. It is believed that further optimisation of the composition to encourage a softer FCC solid solution, perhaps sacrificing somewhat the low liquidus, could result in this MPEA filler metal being a viable option for this application. Furthermore, this alloy could warrant trialling in the brazing of a wider range of tool materials and carbides (or other ceramics used in such applications), where the greater strength of Ni over other used elements such as Cu could be of benefit.

The NiCrFeGeB MPEA filler metal may also warrant further optimisation of composition. For example, this may be done to enhance the ductility of the isothermally solidified NiCrFeGe MPEA-like solid solution formed as a result of the B diffusion. Ideally, if Ge can also be reduced without compromising on the achieved low liquidus, this would represent both a cost benefit, and may help reduce the tying up of Nb from the base metal. Nonetheless, the promising initial results from this filler metal would warrant its trialling on various other Ni-based superalloys. Important assessments may also be made of the high temperature strength of joint brazed using this alloy, and it may be interesting to investigate any benefits to high temperature strength that the possession of an MPEA-like joint region may incur. Likewise, the performance of the joints brazed with this alloy in corrosive and oxidising envFements would be of interest, and comparisons with joints produced with commercial alloys would be valuable as an indicator as to the usefulness of HEA or MPEA-like filler metals for such applications. It would also be of interest to investigate the use of this filler metal for the brazing of other superalloys, such as those containing γ' rather than γ''. This may be particularly interesting when considering the possibility of forming Ge-containing γ'. Fractography of failed joints following shear testing would also be of benefit, in order to correlate microstructural features with failure mechanisms. Particularly for the NiCrFeGeB filler metal, which exhibited several phases when used to braze IN718, fractography could aid understanding as to consequences such phases have on the joint mechanical properties. Outside of brazing, alloys such as this one, with a high hardness measured, could see use in wear-resistant materials and coatings.

As for the design strategy detailed in this work, it need not stop at considering In and Ge as novel MPD elements, nor at Ni-based filler metals. Such a strategy could be employed to develop filler metals for existing and future brazing applications. It could be of particular use for designing filler metals for the brazing of dissimilar materials, as well as HEAs which may see use as future structural materials in applications such as cryogenics and fusion reactors.

References

[1] Yan, G., Nagarajan, B., Bhowmik, A., Chyn Tan, S., Xu, R., & Tan, M. J. (2019). Induction transient liquid phase bonding of Inconel 718 with the Ni-based sintered brazing preform. *Applied Surface Science*, *473*(October 2018), 1024–1037.

[2] Bobzin, K., Öte, M., & Hebing, J. (2020). Approaches and possibilities for reducing residual stresses in induction brazed cemented carbide/steel joints. *Welding in the World*, *64*(9), 1579–1587.

[3] Khorram, A., Fakhraei, O., & Torkamany, M. J. (2016). Laser brazing of Inconel 718 and Inconel 600 with BNi-2 Ni-based filler metal. *International Journal of Advanced Manufacturing Technology*, 1–10.

[4] Sun, B. J., & Xiao, B. (2017). Mechanical properties of diamond grinding discs brazed in a continuous-belt tunnel furnace or vacuum furnace. *International Journal of Advanced Manufacturing Technology*, *89*(5–8), 1379–1386.

[5] The British Standards Institute. (2016). *Brazing — Filler metals (ISO 17672:2016)*

[6] Gale, W. F., & Butts, D. A. (2004). Transient liquid phase bonding. *Science and Technology of Welding and Joining*, *9*(4), 283–300.

[7] Shapiro, A., Flom, Y., Moxson, V. S., & Duz, V. A (2013). Cost-effective sintered brazing foils for joining Ti alloys and ceramics. *Proceedings from Brazing, High Temperature Brazing, and Diffusion Bonding, 10th International Conference,* 18th – 20th June, Aachen, pp. 7 – 10.

[8] Holländer, U., Bach, Fr.-W., Möhwald, K., Kirchberg, S., & Ziegmann, G (2013). Injection molding – characterization and application of polymer bonded Ni based braze metal preforms for high temperature brazing processes. *Proceedings from Brazing, High Temperature Brazing, and Diffusion Bonding, 10th International Conference,* 18th – 20th June, Aachen, pp. 11 – 16.

[9] Reed, R. C. (2006). The Superalloys: Fundamentals and Applications. In *The Superalloys: Fundamentals and Applications*, xiii

[10] Geddes, B., Leon, H., & Huang, X. (2010). Superalloys: Alloying and Performance. In *ASM International*.

[11] Donachie, M. J., & Donachie, S. J. (2002). Superalloys: A Technical Guide. ASM International, 2008. p.1

[12] Nganbe, M., & Heilmaier, M. (2009). High temperature strength and failure of the Ni-base superalloy PM 3030. *International Journal of Plasticity*, *25*(5), 822–837.

[13] Yuan, Y., Kawagishi, K., Koizumi, Y., Kobayashi, T., Yokokawa, T., & Harada, H. (2014). Creep deformation of a sixth generation Ni-base single crystal superalloy at 800°C. *Materials Science and Engineering A*, *608*, 95–100.

[14] Tharappel, J. T., & Babu, J. (2018). Welding processes for Inconel 718 - A brief review. *IOP Conference Series: Materials Science and Engineering*, *330*(1).

[15] Liu, W. C., Yao, M., Chen, Z. L., & Wang, S. G. (1999). Nb segregation in Inconel 718. *Journal of Materials Science*, *34*, 2583–2586.

[16] Lynch, J. F., Feinstein, L., Huggins, R. A. (1959). Brazing by the diffusion controlled formation of a liquid intermediate phase. *Welding Journal*, 38(2), 85 – 89.

[17] Owczarski, W. A. (1962). Eutectic brazing of Zircaloy 2 to Type 304 Stainless steel. *Welding Journal*, 42(2), 78 – 83.

[18] The Materials Information Society. (1992). ASM Handbook Volume 3 - Alloy Phase Diagrams. In *ASM Handbook*.

[19] Singleton, M. F., & Nash, P. (1991). Phase diagrams of binary Ni alloys. *ASM International*, 1991.

[20] Okamoto, H. (2010). Ni-P (Ni-P). *Journal of Phase Equilibria and Diffusion*, *31*(2), 200–201.

[21] Duvall, D., Owczarski, W. A., & Paulonis, D. F. (1974). TLP boding: A new method for joining heat resistant alloys. In *Welding Journal* (Vol. 53, Issue 4, pp. 203–214).

[22] Knotek, O., & Lugscheider, E. (1976). Brazing Filler Metals Based on Reacting Ni-Cr-B-Si Alloys. *Welding Research Supplement*, *55*, 314–318.

[23] Lugscheider, E., Knotek, O., & Klohn, K. (1978). Development of Ni-Cr-Si Base Filler Metals. *9th International AWS-WRC Brazing Conference*, 319–324.

[24] Lugscheider, E., Knotek, O., & Klöhn, K. (1979). Melting behaviour of Ni-Cr-Si alloys. *Thermochimica Acta*, *29*(2), 323–326.

[25] Lugscheider, E., Klohn, K., & Burchard, W. (1980). Structure of Low-P Alloyed Ni-Cr-Si Brazed Stainless Steel Joints. *11th International AWS-WRC Brazing Conference*, 283–288.

[26] Lugscheider, E., & Cosack, T. (1988). High-Temperature Brazing of Stainless Steel with Low-P Ni-Based Filler Metal. *Supplement to the Welding Journal*, *October*, 215–221.

[27] Briant, C., & Hall, E. (1990). The microstructure and corrosion resistance of Ni-based filler metals with high Cr contents. *Welding Research Supplement*, *February*, 60–67.

[28] Rabinkin, A., Wenski, E., & Ribaudo, A. (1998). Brazing stainless steel using a new MBF-series of Ni-Cr-B-Si amorphous brazing foils. *Welding in the World*, *41*(6), 466–478.

[29] Takemoto, T., & Okamoto, I. (1984). Effect of Composition on the Corrosion Behavior of Stainless Steels Brazed With Ag-Base Filler Metals. *Welding Journal (Miami, Fla)*, *63*(10), 300–307.

[30] Schaefer, R. P., Flynn, J. E., & Doyle, J. R. (1971). Brazing Filler Metal Evaluation for an Aircraft Gas Turbine Engine Application. *Welding Research Supplement*, *9*, 394–400.

[31] Roberts, P. (2013). Industrial Brazing Practice. In *Industrial Brazing Practice*.

[32] Bose, D., Daita, A., Rabinkin, A., & De Cristofaro, J. (1986). High strength Ni-Pd-Cr brazing alloys. *Welding Journal*, *Supplement*(January), 23S-29S.

[33] Baranowski, M., & Senkara, J. (2019). Brazing of selected heat-resisting alloys using Ni-Pd filler metal. *Welding Technology Review, 91*(10), 51–58.

[34] Baranowski, M., & Senkara, J. (2019). Brazing of selected heat-resisting alloys using Ni-Pd filler metal. *Welding Technology Review, 91*(10), 51–58.

[35] Lugscheider, E., & Cosack, T. (1988). High-Temperature Brazing of Stainless Steel with Low-P Ni-Based Filler Metal. *Supplement to the Welding Journal*, *October*, 215–221.

[36] Hartmann, T., & D. Nuetzel. (2009). New amorphous brazing foils for exhaust gas applications. *Proceedings of the 4th International Brazing and Soldering Conference*, 26th – 29th April, Orlando, 110–117.

[37] Tomio, A., Sagara, M., Doi, T., Amaya, H., Otsuka, N., & Kudo, T. (2015). Role of alloyed Mo on corrosion resistance of austenitic Ni-Cr-Mo-Fe alloys in H2S-Cl- envFements. *Corrosion Science*, *98*, 391–398.

[38] Way, M., Willingham, J., & Goodall, R. (2020). Brazing filler metals. *International Materials Reviews*, *65*(5), 257–285.

[39] Hartmann, T., & Nuetzel, D. (2010). Ni-Cr-Based Amorphous Brazing Foils for Continuous Furnace Brazing of Stainless Steel. *Proceedings of the 9th International Conference of Brazing, High Temperature Brazing and Diffusion Bonding*. 15th – 17th June, Aachen. 42 - 47

[40] Sandin, T. A., (2006). Development of Active Ni Based Brazing Filler Metals. *Proceedings of the 3rd International Brazing and Soldering Conference*. 24th – 26th June, San Antonio. 367 – 372.

[41] Susukida, K., Tada, K., & Yamazaki, T. (2016). Soldering of diamond using Zn-15Al solder by applying ultrasonic vibration. *Proceedings from Brazing, High Temperature Brazing, and Diffusion Bonding, 11th International Conference,* 7th – 9th June, Aachen, 372 - 377.

[42] Lugscheider, E., & Partz, K.-D. (1983). High Temperature Brazing of Stainless Steel with Ni-Base Filler Metals BNi-2, BNi-5 and BNi-7. *Welding Research Supplement, 6,* 2–6.

[43] Yuan, X. J., Kim, M. B., & Kang, C. Y. (2011). Effects of B and Si on microstructure and isothermal solidification during TLP bonding of a duplex stainless steel using two Ni-Si-B insert alloys. *Materials Science and Technology*, *27*(7), 1191–1197.

[44] Bakhtiari, R., & Ekrami, A. (2012). The effect of gap size on the microstructure and mechanical properties of the transient liquid phase bonded FSX-414 superalloy. *Materials and Design*, *40*, 130–137.

[45] Ivannikov, A. A., Sevryukov, O. N., Vertkov, A. V., Penyaz, M. A., Misnikov, V. E., Kochnov, Y. O., Morokhov, P. V., & Lyublinskiy, I. E. (2017). High-temperature brazing of Mo to 12Cr18Ni10Ti steel with the CTEMET 1301 rapidly quenched Ni brazing alloy. *Welding International*, *31*(10), 767–772.

[46] Lu, C., Zhang, J., Duan, T., & Liu, C. (2016). Microstructure evolution and brazing mechanisms of the Ti2AlC/Ni joints using Ni based filler alloy. *Journal of the European Ceramic Society*, *36*(14), 3319–3327.

[47] Mohammed Hadian, A., & Drew, R. A. L. (1996). Strength and Microstructure of Si Nitride Ceramics Brazed with Ni-Cr-Si Alloys. *Journal of the American Ceramic Society*, *79*(3), 659–665.

[48] Wu, X., Chandel, R. S., Li, H., Seow, H. P., & Wu, S. (2000). Induction brazing of Inconel 718 to Inconel X-750 using Ni-Cr-Si-B amorphous foil. *Journal of Materials Processing Technology*, *104*(1), 34–43.

[49] Henhoeffer, T., Huang, X., Yand, S., Au, P., & Nagy, D. (2010). Microstructure and high temperature tensile properties of wide gap brazed Co based superalloy X-40. *Materials Science and Technology, 26*(4), 431–439.

[50] Chen, B., Xiong, H. P., Mao, W., Cheng, Y. Y., & Wu, X. (2015). Dissimilar joining of P/M superalloy and single crystal superalloy using Ni–Cr–B brazing alloy. *Welding in the World*, *59*(6), 911–915.

[51] Ghomi, M. K., Nategh, S., & Mirdamadi, S. (2016). Microstructural evolution during the transient liquid-phase bonding of dissimilar Ni-based superalloys of IN738LC and Nimonic 75. *Materials and Technology, 50*(3), 365–371.

[52] Khakian, M., Nategh, S., & Mirdamadi, S. (2015). Effect of bonding time on the microstructure and isothermal solidification completion during transient liquid phase bonding of dissimilar Ni-based superalloys IN738LC and Nimonic 75. *Journal of Alloys and Compounds*, *653,* 386–394.

[53] Sadeghian, A., Arhami, F., & Mirsalehi, S. E. (2019). Phase formation during dissimilar transient liquid phase (TLP) bonding of IN939 to IN625 using a Ni-Cr-Fe-Si-B interlayer. *Journal of Manufacturing Processes*, *44*(May), 72–80.

[54] Miyazawa, Y., & Ariga, T. (1992). Brazing of Inconel 600 and SUS304 stainless steel with used of rapidly solidified Ni-base brazing foil. *Materials Transactions (Japanese Institute of Metals), 33*(5), 509–518.

[55] Baharzadeh, E., Shamanian, M., Rafiei, M., & Mostaan, H. (2019). Properties of IN X-750/BNi-2/SAF 2205 joints formed by transient liquid phase bonding. *Journal of Materials Processing Technology*, *274*(May).

[56] Ojo, O. A., & Aina, O. (2018). On the Effect of Liquid-State Diffusion on Isothermal Solidification Completion Time During Transient Liquid-Phase Bonding of Dissimilar Materials. *Metallurgical and Materials Transactions A: Physical Metallurgy and Materials Science*, *49*(5), 1481–1485.

[57] Hadibeyk, S., Beidokhti, B., & Sajjadi, S. A. (2018). Effect of bonding time and homogenization heat treatment on the microstructure and mechanical properties of the transient liquid phase bonded dissimilar GTD-111/FSX-414 TLP superalloys. *Journal of Alloys and Compounds*, *731,* 929–935.

[58] Ghaderi, S., Karimzadeh, F., & Ashrafi, A. (2020). Evaluation of microstructure and mechanical properties of transient liquid phase bonding of Inconel 718 and nano/ultrafine-grained 304L stainless steel. *Journal of Manufacturing Processes*, *49*(November 2019), 162–174.

[59] Lu, C., Zhang, J., Duan, T., & Liu, C. (2016). Microstructure evolution and brazing mechanisms of the Ti2AlC/Ni joints using Ni based filler alloy. *Journal of the European Ceramic Society*, *36*(14), 3319–3327.

[60] Lee, S., Kang, K.-H., Hong, H. S., Yun, Y., & Woo, S.-K. (2010). Microstructure and interfacial morphologies of brazed NiO-YSZ/316 stainless steel using B-Ni2 brazing alloy. *Materials Testing in Joining Technology*, *52*(4), 257–262.

[61] Lee, S., Kang, K. H., Hong, H. S., Yun, Y., Ahn, J. H., & Woo, S. K. (2011). Interfacial morphologies between NiO-YSZ fuel electrode/316 stainless steel as interconnect material and B-Ni3 brazing alloy in solid oxide fuel cell system: Effect of joint loading during brazing. *Canadian Metallurgical Quarterly*, *50*(1), 72–79.

[62] Tuah-Poku, I., Dollar, M., & Massalski, T. B. (1988). A study of the transient liquid phase bonding process applied to a Ag/Cu/Ag sandwich joint. *Metallurgical Transactions A, 19A*, 675–686.

[63] MacDonald, W. D., & Eagar, T. W. (1992). Transient liquid phase bonding processes. *Annual Review of Materials Science*, *1*(1), 23–46.

[64] Zhou, Y., Gale, W. F., & North, T. H. (2012). Modelling of transient liquid phase bonding. *International Materials Reviews*, *40*(5), 181–196.

[65] Illingworth, T. C., Golosnoy, I. O., Gergely, V., & Clyne, T. W. (2005). Numerical modelling of transient liquid phase bonding and other diffusion controlled phase changes. *Journal of Materials Science*, *40*(9–10), 2505–2511.

[66] Padron, T., Khan, T. I., & Kabir, M. J. (2004). Modelling the transient liquid phase bonding behaviour of a duplex stainless steel using Cu interlayers. *Materials Science and Engineering A*, *385*(1–2), 220–228.

[67] Gale, W. F., & Wallach, E. R. (1991). Influence of isothermal solidification on microstructural development in Ni–Si–B filler metals. *Materials Science and Technology (United Kingdom)*, *7*(12), 1143–1148.

[68] Gale, W. F., & Wallach, E. R. (1991). Microstructural development in transient liquid-phase bonding. *Metallurgical Transactions A*, *22*(10), 2451–2457.

[69] Nakagawa, H., Lee, C. H., & North, T. H. (1991). Modeling of base metal dissolution behavior during transient liquid-phase brazing. *Metallurgical Transactions A*, *22*, 543–555.

[70] Ojo, O. A., Richards, N. L., & Chaturvedi, M. C. (2004). Isothermal solidification during transient liquid phase bonding of Inconel 738 superalloy. *Science and Technology of Welding and Joining*, *9*(6), 532–540.

[71] Nakao Y., Nishimoto K., Shinozaki K., Kang C.Y. (1990) Transient Liquid Insert Metal Diffusion Bonding of Ni-Base Superalloys. In: *North T.H. (eds) Advanced Joining Technologies*. pp. 129 – 144

[72] Sinclair, C. W., Purdy, G. R., & Morral, J. E. (2000). Transient liquid-phase bonding in two-phase ternary systems. *Metallurgical and Materials Transactions A: Physical Metallurgy and Materials Science*, *31*(4), 1187–1192.

[73] Yuan, X. J., Kim, M. B., & Kang, C. Y. (2011). Effects of B and Si on microstructure and isothermal solidification during TLP bonding of a duplex stainless steel using two Ni-Si-B insert alloys. *Materials Science and Technology*, *27*(7), 1191–1197.

[74] Idowu, O. A., Richards, N. L., & Chaturvedi, M. C. (2005). Effect of bonding temperature on isothermal solidification rate during transient liquid phase bonding of Inconel 738LC superalloy. *Materials Science and Engineering A*, *397*(1–2), 98–112.

[75] Abdelfatah, M., & Ojo, O. A. (2009). Formation of eutectic-type microconstituent during transient liquid phase bonding of Ni: influence of process parameters. *Materials Science and Technology*, *25*(1), 61–67.

[76] Binesh, B., & Jazayeri Gharehbagh, A. (2016). Transient Liquid Phase Bonding of IN738LC/MBF-15/IN738LC: Solidification Behavior and Mechanical Properties. *Journal of Materials Science and Technology, 32*(11), 1137–1151.

[77] Ghasemi, A., & Pouranvari, M. (2018). Microstructural evolution mechanism during brazing of Hastelloy X superalloy using Ni–Si–B filler metal. *Science and Technology of Welding and Joining*, *23*(5), 441–448.

[78] Pouranvari, M., Ekrami, A., & Kokabi, A. H. (2013). TLP bonding of cast IN718 Ni based superalloy: Process-microstructure-strength characteristics. *Materials Science and Engineering A*, *568*, 76–82.

[79] Ebrahimzadeh Pilehrood, A., Omidvar, H., Shamsipur, A., & Khakian-Ghomi, M. (2019). Effect of transient liquid phase bonding followed by homogenization on the microstructure and hot tensile behavior of Inconel 738 superalloy. *Journal of Manufacturing Processes*, *48*(October), 110–118.

[80] Amiri, D., Sajjadi, S. A., Bakhtiari, R., & Kamyabi-Gol, A. (2018). The role of TLP process variables in improvement of microstructure and mechanical properties in TLP joints of GTD-111/Ni-Cr-Fe-B-Si/GTD-111 system. *Journal of Manufacturing Processes*, *32*(March), 644–655.

[81] Jalilvand, V., Omidvar, H., Rahimipour, M. R., & Shakeri, H. R. (2013). Influence of bonding variables on transient liquid phase bonding behavior of Ni based superalloy IN-738LC. *Materials and Design*, *52*, 36–46.

[82] Li, W., Jin, T., Sun, X. F., Guo, Y., Guan, H. R., & Hu, Z. Q. (2003). Study of Ni-Cr-Co-W-Mo-B interlayer alloy and its bonding behaviour for a Ni-base single crystal superalloy. *Scripta Materialia*, *48*(9), 1283–1288.

[83] Ghasemi, A., & Pouranvari, M. (2019). Intermetallic phase formation during brazing of a Ni alloy using a Ni–Cr–Si–Fe–B quinary filler alloy. *Science and Technology of Welding and Joining*, *24*(4), 342–351.

[84] Malekan, A., Farvizi, M., Mirsalehi, S. E., Saito, N., & Nakashima, K. (2020). Holding time influence on creep behavior of transient liquid phase bonded joints of Hastelloy X. *Materials Science and Engineering A*, *772*(August 2019), 138694.

[85] Shamsabadi, A. Y., Bakhtiari, R., & Eisaabadi B., G. (2016). TLP bonding of IN738/MBF20/IN718 system. *Journal of Alloys and Compounds*, *685*, 896–904.

[86] Binesh, B., & Jazayeri Gharehbagh, A. (2016). Transient Liquid Phase Bonding of IN738LC/MBF-15/IN738LC: Solidification Behavior and Mechanical Properties. *Journal of Materials Science and Technology*, *32*(11), 1137–1151.

[87] Cook, G. O., & Sorensen, C. D. (2011). Overview of transient liquid phase and partial transient liquid phase bonding. In *Journal of Materials Science* (Vol. 46, Issue 16, pp. 5305–5323).

[88] Sun, Y., Liu, J., Li, B., Li, H., & Jin, T. (2014). Microstructure evolution of single crystal superalloy DD5 joints brazed using AWS BNi-2 filler alloy. *Materials Research Innovations*, *18*(sup4), S4-341-S4-346.

[89] Steuer, S., & Singer, R. F. (2014). Suppression of boride formation in transient liquid phase bonding of pairings of parent superalloy materials with different compositions and grain structures and resulting mechanical properties. *Metallurgical and Materials Transactions A: Physical Metallurgy and Materials Science*, *45*(8), 3545–3553.

[90] Jamaloei, A. D., Khorram, A., & Jafari, A. (2017). Characterization of microstructure and mechanical properties of dissimilar TLP bonding between IN718/IN600 with BNi-2 interlayer. *Journal of Manufacturing Processes*, *29*, 447–457.

[91] Zhang, L. X., Sun, Z., Xue, Q., Lei, M., & Tian, X. Y. (2016). Transient liquid phase bonding of IC10 single crystal with GH3039 superalloy using BNi2 interlayer: Microstructure and mechanical properties. *Materials and Design*, *90*, 949–957.

[92] Pouranvari, M., Ekrami, A., & Kokabi, A. H. (2018). Role of base-metal composition in isothermal solidification during diffusion brazing of Ni-based superalloys. *Science and Technology of Welding and Joining*, *23*(1), 13–18.

[93] X. Wu, R. S. Chandel, H. L. (2001). Evaluation of transient liquid phase bonding between Ni base superalloys. *J. of Mater. Sci*, *36*(6), 1539–1546.

[94] Liu, J.-D., Jin, T., Zhao, N.-R., Wang, Z.-H., Sun, X.-F., Guan, H.-R., & Hu, Z.-Q. (2010). Bonding behaviour of Ni base single crystal to polycrystal superalloys by transient liquid phase method. *Science and Technology of Welding and Joining*, *15*(3), 194–198.

[95] Ye, Y., Zou, G., Long, W., Jia, Q., Bai, H., Wu, A., & Liu, L. (2019). Diffusion brazing repair of IN738 superalloy with crack-like defect: microstructure and tensile properties at high temperatures. *Science and Technology of Welding and Joining*, *24*(1), 52–62.

[96] Yan, G., Bhowmik, A., Nagarajan, B., Song, X., Tan, S. C., & Tan, M. J. (2019). Bonding temperature effects on the wide gap transient liquid phase bonding of Inconel 718 using BNi-2 paste filler metal. *Applied Surface Science*, *484*(January), 1223–1233.

[97] Arhami, F., & Mirsalehi, S. E. (2019). The effect of heat treatment sequence on microstructure and mechanical properties of diffusion brazed IN-939 superalloy. *Journal of Materials Processing Technology*, *266*(June 2018), 351–362.

[98] Pouranvari, M., Ekrami, A., & Kokabi, A. H. (2013). Transient liquid phase bonding of wrought IN718 Ni based superalloy using standard heat treatment cycles: Microstructure and mechanical properties. *Materials and Design*, *50*, 694–701.

[99] Amirkhani, A., Beidokhti, B., Shirvani, K., & Rahimipour, M. R. (2019). Two-step heating transient liquid phase bonding of Inconel 738LC. *Journal of Materials Processing Technology*, *266*(October 2018), 1–9.

[100] Pouranvari, M., Ekrami, A., & Kokabi, A. H. (2014). Aging response of transient liquid phase bonded wrought IN718 superalloy: Influence of post-bond heat treatment. *Science and Technology of Welding and Joining*, *19*(2), 105–110.

[101] Luo, Y., Zhang, Q., Jiang, W., Zhang, Y., Hao, M., & Tu, S. T. (2017). The microstructure, mechanical properties and fracture behavior of hastelloy C276-BNi2 brazed joint. *Materials and Design*, *115*, 458–466.

[102] Hartmann, T., & Marsilius, M. (2016). Brazing joint properties of Ni-Cr-Si-B-P amorphous brazing foils at elevated temperatures. *Proceedings of the 11th International Conference of Brazing, High Temperature Brazing and Diffusion Bonding,* 7th to 9th June 2016, Aachen, 239–244.

[103] Pouranvari, M., Ekrami, A., & Kokabi, A. H. (2013). Solidification and solid state phenomena during TLP bonding of IN718 superalloy using Ni-Si-B ternary filler alloy. *Journal of Alloys and Compounds*, *563*, 143–149.

[104] Pouranvari, M. (2015). Solid solution strengthening of transient liquid phase bonded Ni based superalloy. *Materials Science and Technology*, *31*(14), 1773–1780.

[105] Gypen, L. A., & Deruyttere, A. (1977). Multi-component solid solution hardening - Part 1 Proposed model. *Journal of Materials Science*, *12*(5), 1028–1033.

[106] Roth, H. A., Davis, C. L., & Thomson, R. C. (1997). Modeling solid solution strengthening in Ni alloys. *Metallurgical and Materials Transactions A: Physical Metallurgy and Materials Science*, *28*(6), 1329–1335.

[107] Hartmann, T., & Nuetzel, D. (2012). Cr Containing Amorphous Brazing Foils and Their Resistance to Automotive Exhaust Gas Condensate. *Proceedings of the 5th International Brazing and Soldering Conference, Las Vegas, Nevada, USA.*

[108] Riggs, B., Alexandrov, B., Benatar, A., & Xu, R. (2017). Metallurgical characterisations of CMSX-4 vacuum-brazed with BNi-2 and BNi-9. *Science and Technology of Welding and Joining*, *22*(3), 227–235.

[109] Pouranvari, M., Ekrami, A., & Kokabi, A. H. (2013). Phase transformations during diffusion brazing of IN718/Ni-Cr-B/IN718. *Materials Science and Technology (United Kingdom)*, *29*(8), 980–984.

[110] Gale, W. F., & Wallach, E. R. (1990). Wetting of Ni-Alloys by Ni Based Brazes. *Materials Science and Technology*, *6*, 170–175.

[111] Murray, J. L. (1987). *Phase diagrams of binary Ti alloys.* ASM International

[112] Guo, C., & Du, Z. (2005). *Intermetallics*. 525 – 534.

[113] Laux, B., Piegert, S., & Rösler, J. (2009). Braze alloy development for fast epitaxial high-temperature brazing of single-crystalline Ni-based superalloys. *Metallurgical and Materials Transactions A: Physical Metallurgy and Materials Science*, *40*(1), 138–149.

[114] Piegert, S., Laux, B., & Rösier, J. (2012). Design of a braze alloy for fast epitaxial brazing of superalloys. *IOP Conference Series: Materials Science and Engineering*, *33*, 012028.

[115] Dinkel, M. K., Heinz, P., Pyczak, F., Volek, A., Ott, M., Affeldt, E., Vossberg, A., Göken, M., & Singer, R. F. (2008). New B and Si free single crystal-diffusion brazing alloys. *Proceedings of the International Symposium on Superalloys*, 211–220.

[116] Wang, T., Jin, Z., & Zhao, J. C. (2001). *Metallkd, 92*(5), 441–446.

[117] Zheng, Y., & Ruan, Z. (1990). Microstructure and performance of Ni-Hf brazing filler alloy. *Acta Metallurgica Sinica (English Edition)*, *3*(5), 335–340.

[118] Lugscheider, E., & Humm, S. (2002). High-temperature brazing of superalloys and stainless steels with novel ductile Ni-Hf-based filler metals. *Advanced Engineering Materials*, *4*(3), 138–142.

[119] Miglietti, W. M., Curtis, R., Hall, B., & Lazarin, C. M. (2000). Liquid phase diffusion bond repair of westinghouse 501F, Row3 vanes. *Proceedings of the ASME Turbo Expo*.

[120] Wiglietti, W. (2003). US 65,520,401 B1: Diffusion Bonding of Gaps. In *Patent Application Publication.* US

[121] Huang, X. (2010). US 2010/00384 12 A1: Low-melting B-free braze alloy compositions. In *Patent Application Publication*. US.

[122] Miglietti, W., & Du Toit, M. (2010). High Strength, Ductile Braze Repairs for Stationary Gas Turbine Components—Part I. *Journal of Engineering for Gas Turbines and Power*, *132*(8).

[123] Miglietti, W., & Du Toit, M. (2010). High Strength, Ductile Braze Repairs for Stationary Gas Turbine Components—Part II. *Journal of Engineering for Gas Turbines and Power, 132*(8).

[124] Ivannikov, A. A., Sevryukov, O. N., Penyaz, M. A., & Popov, N. S. (2018). Development of Ni-based filler metal for producing high-strength joints in critical products from heat-resistant materials. *Non-Ferrous Metals, 45*(2), 43–49.

[125] Ivannikov, A. A., Kalin, B. A., Sevryukov, O. N., Penyaz, M. A., Fedotov, I. V., Misnikov, V. E., & Tarasova, M. S. (2018). Study of the Ni–Si–Be system as a base to create B-free brazing filler metals. *Science and Technology of Welding and Joining, 23*(3), 187–197.

[126] White, S. J., Corcoran, E. C., Thompson, W. T., Lewis, B. J., Palleck, S., Goodyear, H., Harmsen, J. G., & Dimayuga, F. (2015). Thermodynamic considerations in the use of Ni-Be alloy to braze Zircaloy-4. *Journal of Nuclear Materials, 465*, 42–53.

[127] Lugscheider, E., & Pelster, H. (1983). Ni-Au and Ni-Pd Filler Metals of Low Precious Metal Content. *Welding Research Supplement, October*, 261–266.

[128] Zhang, G. D., Yu, S. F., Li, Z. Y., Fu, C. Y., & Lu, W. J. (2001). Influence of Cu on amorphous Ni based brazing alloy. *Science and Technology of Welding and Joining*, *6*(2), 103–107.

[129] Nishimoto, K., Saida, K., & Shinohara, Y. (2003). Computer aided alloy design of insert metal for transient liquid phase bonding of γ/γ′/β type high Al Ni base superalloy. *Science and Technology of Welding and Joining*, *8*(1), 29–38.

[130] Shi, K., Tsunoda, T., Shohji, I., Matsu, K., & Taguchi, Y. (2016). Microstructure and electrochemical corrosion behavior of Fe-Cr system alloys as substitutes for ni-based brazing filler metal. *Acta Metallurgica Sinica (English Letters)*, *29*(8), 697–706.

[131] Fusner, E. W., Hope, A. T., & Lippold, J. C. (2014). Development of high-Cr, Ni-based filler metals using combined computational and experimental techniques. *Welding Journal*, *93*(5), 171–182.

[132] Persson, U., & Bornegard, N. (2016). New Ni based brazing alloy suitable for very corrosive envFements. *Proceedings of the 11th International Conference of Brazing, High Temperature Brazing and Diffusion Bonding*. 7th – 9th June, Aachen. 42 – 47.

[133] Yeh, J. W., Chen, S. K., Lin, S. J., Gan, J. Y., Chin, T. S., Shun, T. T., Tsau, C. H., & Chang, S. Y. (2004). Nanostructured high-entropy alloys with multiple principal elements: Novel alloy design concepts and outcomes. *Advanced Engineering Materials*, *6*(5), 299-303+274.

[134] Cantor, B., Chang, I. T. H., Knight, P., & Vincent, A. J. B. (2004). Microstructural development in equiatomic multicomponent alloys. *Materials Science and Engineering A*, *375–377*(1-2 SPEC. ISS.), 213–218.

[135] Murty, B. S., Yeh, J. W., & Ranganathan, S. (2014). High Entropy Alloys. *High Entropy Alloys*, *January*, 159–169.

[136] Miracle, D. B., & Senkov, O. N. (2017). A critical review of high entropy alloys and related concepts. *Acta Materialia*, *122*, 448–511.

[137] Pickering, E. J., & Jones, N. G. (2016). High-entropy alloys: a critical assessment of their founding principles and future prospects. *International Materials Reviews*, *61*(3), 183–202.

[138] Poletti, M. G., & Battezzati, L. (2014). Electronic and thermodynamic criteria for the occurrence of high entropy alloys in metallic systems. *Acta Materialia*, *75*, 297–306.

[139] Guo, S., & Liu, C. T. (2011). Phase stability in high entropy alloys: Formation of solid-solution phase or amorphous phase. *Progress in Natural Science: Materials International*, *21*(6), 433–446.

[140] Chanda, B., & Das, J. (2019). An assessment on the stability of the eutectic phases in high entropy alloys. *Journal of Alloys and Compounds*, *798*, 167–173.

[141] Hume-Rothery, W., & Powell, H. M. (1935). On the Theory of Super-Lattice Structures in Alloys, *Zeitschrift für Kristallographie - Crystalline Materials*, 91(1), 23-47.

[142] Mizutani, U. (2012). Hume-Rothery rules for structurally complex alloy phases. *MRS Bulletin*.

[143] Wu, C. S., Tsai, P. H., Kuo, C. M., & Tsai, C. W. (2018). Effect of atomic size difference on the microstructure and mechanical properties of high-entropy alloys. *Entropy*, *20*(12).

[144] Kube, S. A., Sohn, S., Uhl, D., Datye, A., Mehta, A., & Schroers, J. (2019). Phase selection motifs in High Entropy Alloys revealed through combinatorial methods: Large atomic size difference favors BCC over FCC. *Acta Materialia*, *166*, 677–686.

[145] Zhang, Y., Zhou, Y. J., Lin, J. P., Chen, G. L., & Liaw, P. K. (2008). Solid-solution phase formation rules for multi-component alloys. *Advanced Engineering Materials*, *10*(6), 534–538.

[146] Troparevsky, M. C., Morris, J. R., Wang, Y., Lupini, A. R., & Malcolm, G. (2015). Beyond Atomic Sizes and Hume-Rothery Rules : Understanding and Predicting High-Entropy Alloys. *Journal of the Minerals, Metals and Materials Society*, *67*(10), 2350–2363.

[147] Zhang, K., & Fu, Z. (2012). Effects of annealing treatment on phase composition and microstructure of CoCrFeNiTiAl x high-entropy alloys. *Intermetallics*, *22*, 24–32.

[148] Leong, Z., Huang, Y., Goodall, R., & Todd, I. (2018). Electronegativity and enthalpy of mixing biplots for High Entropy Alloy solid solution prediction. *Materials Chemistry and Physics*, *210*, 259–268.

[149] Guo, S., Ng, C., Lu, J., & Liu, C. T. (2011). Effect of valence electron concentration on stability of fcc or bcc phase in high entropy alloys. *Journal of Applied Physics*, *109*, 103505.

[150] Tsai, M. H., Tsai, K. Y., Tsai, C. W., Lee, C., Juan, C. C., & Yeh, J. W. (2013). Criterion for sigma phase formation in Cr- and V-Containing high-entropy alloys. *Materials Research Letters*, *1*(4), 207–212.

[151] Fang, W., Yu, H., Chang, R., Zhang, X., Ji, P., Liu, B., Li, J., Qu, X., Liu, Y., & Yin, F. (2019). Microstructure and mechanical properties of Cr-rich Co-Cr-Fe-Ni high entropy alloys designed by valence electron concentration. *Materials Chemistry and Physics*, *238*(October 2018), 121897.

[152] Yang, S., Lu, J., Xing, F., Zhang, L., & Zhong, Y. (2020). Revisit the VEC rule in high entropy alloys (HEAs) with high-throughput CALPHAD approach and its applications for material design-A case study with Al–Co–Cr–Fe–Ni system. *Acta Materialia, 192*, 11–19.

[153] Pickering, E. J., Muñoz-Moreno, R., Stone, H. J., & Jones, N. G. (2016). Precipitation in the equiatomic high-entropy alloy CrMnFeCoNi. Scripta Materialia, 113, 106–109.

[154] Patel, D., Richardson, M. D., Jim, B., Akhmadaliev, S., Goodall, R., & Gandy, A. S. (2020). Radiation damage tolerance of a novel metastable refractory high entropy alloy V2.5Cr1.2WMoCo0.04. *Journal of Nuclear Materials, 531*, 152005.

[155] Gandy, A. S., Jim, B., Coe, G., Patel, D., Hardwick, L., Akhmadaliev, S., Reeves-McLaren, N., & Goodall, R. (2019). High temperature and ion implantation-induced phase transformations in novel reduced activation Si-Fe-V-Cr(-Mo) high entropy alloys. *Frontiers in Materials, 6* (June).

[156] Zhang, T., Zhao, R. D., Wu, F. F., Lin, S. B., Jiang, S. S., Huang, Y. J., Chen, S. H., & Eckert, J. (2020). Transformation-enhanced strength and ductility in a FeCoCrNiMn dual phase high-entropy alloy. *Materials Science and Engineering A*, *780*(February).

[157] Zhang, M., Zhou, X., Wang, D., Zhu, W., Li, J., & Zhao, Y. F. (2019). AlCoCuFeNi high-entropy alloy with tailored microstructure and outstanding compressive properties fabricated via selective laser melting with heat treatment. *Materials Science and Engineering A*, *743*(August 2018), 773–784.

[158] Qin, G., Wang, S., Chen, R., Gong, X., Wang, L., Su, Y., Guo, J., & Fu, H. (2018). Microstructures and mechanical properties of Nb-alloyed CoCrCuFeNi high-entropy alloys. *Journal of Materials Science and Technology*, *34*(2), 365–369.

[159] Li, Z., Pradeep, K. G., Deng, Y., Raabe, D., & Tasan, C. C. (2016). Metastable high-entropy dual-phase alloys overcome the strength-ductility trade-off. *Nature*, *534*(7606), 227–230.

[160] Li, Z., Körmann, F., Grabowski, B., Neugebauer, J., & Raabe, D. (2017). Ab initio assisted design of quinary dual-phase high-entropy alloys with transformation-induced plasticity. *Acta Materialia*, *136*, 262–270.

[161] Lim, K. R., Lee, K. S., Lee, J. S., Kim, J. Y., Chang, H. J., & Na, Y. S. (2017). Dual-phase high-entropy alloys for high-temperature structural applications. *Journal of Alloys and Compounds*, *728*, 1235–1238.

[162] Ghassemali, E., Sonkusare, R., Biswas, K., & Gurao, N. P. (2017). In-situ study of crack initiation and propagation in a dual phase AlCoCrFeNi high entropy alloy. *Journal of Alloys and Compounds*, *710*, 539–546.

[163] Liao, Y., & Baker, I. (2008). Microstructure and room-temperature mechanical properties of Fe30Ni20Mn35Al15. *Materials Characterization*, *59*(11), 1546–1549.

[164] Jain, R., Rahul, M. R., Jain, S., Samal, S., & Kumar, V. (2018). Phase Evolution and Mechanical Behaviour of Co–Fe–Mn–Ni–Ti Eutectic High Entropy Alloys. *Transactions of the Indian Institute of Metals*, *71*(11), 2795–2799.

[165] Gao, X., Lu, Y., Zhang, B., Liang, N., Wu, G., Sha, G., Liu, J., & Zhao, Y. (2017). Microstructural origins of high strength and high ductility in an AlCoCrFeNi2.1 eutectic high-entropy alloy. *Acta Materialia*, *141*, 59–66.

[166] Asoushe, M. H., Hanzaki, A. Z., Abedi, H. R., Mirshekari, B., Wegener, T., Sajadifar, S. V., & Niendorf, T. (2021). Thermal stability, microstructure and texture evolution of thermomechanical processed AlCoCrFeNi2.1 eutectic high entropy alloy. *Materials Science and Engineering A*, *799*(May 2020), 140012.

[167] Wu, Z., Parish, C. M., & Bei, H. (2015). Nano-twin mediated plasticity in carbon-containing FeNiCoCrMn high entropy alloys. *Journal of Alloys and Compounds*, *647*, 815–822.

[168] Li, J., Gao, B., Wang, Y., Chen, X., Xin, Y., Tang, S., Liu, B., Liu, Y., & Song, M. (2019). Microstructures and mechanical properties of nano carbides reinforced CoCrFeMnNi high entropy alloys. *Journal of Alloys and Compounds*, *792*, 170–179.

[169] Rogal, Ł., Kalita, D., Tarasek, A., Bobrowski, P., & Czerwinski, F. (2017). Effect of SiC nano-particles on microstructure and mechanical properties of the CoCrFeMnNi high entropy alloy. *Journal of Alloys and Compounds*, *708*, 344–352.

[170] Jia, B., Liu, X., Wang, H., Wu, Y., & Lu, Z. (2018). Microstructure and mechanical properties of FeCoNiCr high-entropy alloy strengthened by nano-Y2O3 dispersion. *Science China Technological Sciences*, *61*(8), 695–698.

[171] Lin, D., Xu, L., Li, X., Jing, H., Qin, G., Pang, H., & Minami, F. (2020). A Si-containing FeCoCrNi high-entropy alloy with high strength and ductility synthesized in situ via selective laser melting. *Additive Manufacturing*, *35*(February), 101340.

[172] Joy, J., Jadhav, M., Sahane, D., Davis, D., & Singh, S. (2019). Elemental effect on formation of solid solution phase in CoCrFeNiX and CoCuFeNiX (X = Ti, Zn, Si,Al) high entropy alloys. *Materials Science and Technology (United Kingdom)*, *35*(14), 1700–1707.

[173] Tillmann, W., Wojarski, L., Ulitzka, T., Ulitzka, H., Manka, M., (2019). Brazing of high temperature materials using melting range optimized filler metals based on the high-entropy alloy CoCrCuFeNi. *Proceedings from Brazing, High Temperature Brazing, and Diffusion Bonding, 12th International Conference*, 21st – 23rd May, Aachen, pp. 1 – 6.

[174] Tillmann, W., Ulitzka, T., Wojarski, L., Manka, M., Ulitzka, H., & Wagstyl, D. (2020). Development of high entropy alloys for brazing applications. *Welding in the World*, *64*(1), 201–208.

[175] Bridges, D., Zhang, S., Lang, S., Gao, M., Yu, Z., Feng, Z., & Hu, A. (2018). Laser brazing of a Ni-based superalloy using a Ni-Mn-Fe-Co-Cu high entropy alloy filler metal. *Materials Letters*, *215*, 11–14.

[176] Gao, M., Schneiderman, B., Gilbert, S. M., & Yu, Z. (2019). Microstructural Evolution and Mechanical Properties of Ni-Base Superalloy Brazed Joints Using a MPCA Filler. *Metallurgical and Materials Transactions A: Physical Metallurgy and Materials Science*, *50*(11), 5117–5127.

[177] Wang, G., Yang, Y., He, R., Tan, C., Huttula, M., & Cao, W. (2020). A novel high entropy CoFeCrNiCu alloy filler to braze SiC ceramics. *Journal of the European Ceramic Society*, *40*(9), 3391–3398.

[178] Song, Y., Liu, D., Hu, S., Song, X., & Cao, J. (2019). Graphene nanoplatelets reinforced AgCuTi composite filler for brazing SiC ceramic. *Journal of the European Ceramic Society*, *39*(4), 696–704.

[179] Tillmann, W., Wojarski, L., Manka, M., & Timmer, C. (2018). Eutectic high entropy alloys – A novel class of materials for brazing applications. *Proceedings from the International Brazing & Soldering Conference*, 15th – 18th April. New Orleans. 142–148.

[180] Zhang, L. X., Shi, J. M., Li, H. W., Tian, X. Y., & Feng, J. C. (2016). Interfacial microstructure and mechanical properties of ZrB2--Si--CC ceramic and GH99 superalloy joints brazed with a Ti-modified FeCoNiCrCu high-entropy alloy. *Materials and Design*, *97*, 230–238.

[181] Spencer, P. J. (2008). A brief history of CALPHAD. *Calphad: Computer Coupling of Phase Diagrams and Thermochemistry*, *32*(1), 1–8.

[182] Saunders, N., & Miodownik, A. P. (1998). CALPHAD. In *CALPHAD Calculation of Phase Diagrams A Comprehensive Guide*.

[183] Kroupa, A. (2013). Modelling of phase diagrams and thermodynamic properties using Calphad method - Development of thermodynamic databases. *Computational Materials Science*, *66*, 3–13.

[184] Redlich, O., & Kister, A. T. (1948). Algebraic representation of thermodynamic properties and the classification of solutions. Industrial & Engineering Chemistry, 40(2), 345-348.

[185] Ruiz-Vargas, J., Siredey-Schwaller, N., Bocher, P., & Hazotte, A. (2013). Microstructure Development during isothermal brazing of Ni/BNi-2 couples. *Journal of Materials Processing Technology*, *213*(12), 2074–2080.

[186] Piegert, S., Laux, B., & Rösier, J. (2012). Design of a braze alloy for fast epitaxial brazing of superalloys. *IOP Conference Series: Materials Science and Engineering*, *33*, 012028.

[187]Snell, R. (2017). *The Development of Novel Ag Brazing Alloys*. (PhD Thesis)

[188] Chen, H. L., Mao, H., & Chen, Q. (2018). Database development and Calphad calculations for high entropy alloys: Challenges, strategies, and tips. *Materials Chemistry and Physics*, *210*, 279–290.

[189] Gorsse, S., & Tancret, F. (2018). Current and emerging practices of CALPHAD toward the development of high entropy alloys and complex concentrated alloys. *Journal of Materials Research*, *33*(19), 2899–2923.

[190] Wu, M., Wang, S., Huang, H., Shu, D., & Sun, B. (2020). CALPHAD aided eutectic high-entropy alloy design. *Materials Letters*, *262*, 127175.

[191] Zhang, C., Zhang, F., Diao, H., Gao, M. C., Tang, Z., Poplawsky, J. D., & Liaw, P. K. (2016). Understanding phase stability of Al-Co-Cr-Fe-Ni high entropy alloys. *Materials and Design*, *109*, 425–433.

[192] Zhang, B., Gao, M. C., Zhang, Y., Yang, S., & Guo, S. M. (2015). Senary refractory high entropy alloy MoNbTaTiVW. *Materials Science and Technology (United Kingdom)*, *31*(10), 1207–1213.

[193] Ma, D., Yao, M., Pradeep, K. G., Tasan, C. C., Springer, H., & Raabe, D. (2015). Phase stability of non-equiatomic CoCrFeMnNi high entropy alloys. *Acta Materialia*, *98*, 288–296.

[194] Tapia, A. J. S. F., Yim, D., Kim, H. S., & Lee, B. J. (2018). An approach for screening single phase high-entropy alloys using an in-house thermodynamic database. *Intermetallics*, *101*(June), 56–63.

[195] Zhang, B., Gao, M. C., Zhang, Y., & Guo, S. M. (2015). Senary refractory high-entropy alloy CrxMoNbTaVW. *Calphad: Computer Coupling of Phase Diagrams and Thermochemistry*, *51*, 193–201.

[196] Waldner, P. & Ipser, Herbert. (2002). Thermodynamic modeling of the Ni–In system. Zeitschrift für Metallkunde. 93. 825-832.

[197] Jin, S., Leinenbach, C., Wang, J., Duarte, L. I., Delsante, S., Borzone, G., Scott, A., & Watson, A. (2012). Thermodynamic study and re-assessment of the Ge-Ni system. *Calphad: Computer Coupling of Phase Diagrams and Thermochemistry*, *38*, 23–34.

[198] Swartzendruber, L. J., Itkin, V. P., & Alcock, C. B., (1991) Phase Diagrams of Binary Ni Alloys, *P. Nash, Ed., ASM International*, pp. 110–132.

[199] Raynor, G. V., and Rivlin, V. G., (1988) Phase Equilibria in Fe Ternary Alloys, The Institute of Metals, London.

[200] Takeuchi, A., & Inoue, A. (2005). Classification of bulk metallic glasses by atomic size difference, heat of mixing and period of constituent elements and its application to characterization of the main alloying element. *Materials Transactions*. 46(12). 2817 – 2829.

[201] F. R. Boer and D. G. Perrifor, (1998). Cohesion in Metals, *(Elsevier Science Publishers)* B.V., Netherlands

[202] Voiculescu, I., Geanta, V., Binchiciu, H., Iovanas, D., & Stefanoiu, R. (2017). Dissimilar Brazed Joints between Steel and W Carbide. *IOP Conference Series: Materials Science and Engineering*, *209*(1).

[203] Nguyen, Q. B., Nai, M. L. S., Zhu, Z., Sun, C. N., Wei, J., & Zhou, W. (2017). Characteristics of Inconel Powders for Powder-Bed Additive Manufacturing. *Engineering*, *3*(5), 695–700.